

NANOSTRUCTURED SURFACES USING THERMAL NANOIMPRINT LITHOGRAPHY:  
APPLICATIONS IN THIN MEMBRANE TECHNOLOGY,  
PIEZOELECTRIC ENERGY HARVESTING AND  
TACTILE PRESSURE SENSING

by

BHARGAV PRADIP NABAR

Presented to the Faculty of the Graduate School of  
The University of Texas at Arlington in Partial Fulfillment  
of the Requirements  
for the Degree of

DOCTOR OF PHILOSOPHY

THE UNIVERSITY OF TEXAS AT ARLINGTON

DECEMBER 2013

Copyright © by Bhargav P Nabar

All Rights Reserved

## Acknowledgements

To my advisor, Dr. Zeynep Celik-Butler, I owe a heartfelt debt of gratitude for giving me the opportunity to work on projects at the cutting edge of research in nanotechnology. I thank her for her patience, her guidance and constant support and encouragement to try new ideas. I would also like to extend a special vote of thanks to Dr. Donald Butler for serving on the dissertation committee and for his many insightful suggestions and generous guidance.

I would like to thank my graduate committee members, Dr. J.C.Chiao, Dr. Weidong Zhou and Dr. Dereje Agonafer not only for feedback and direction but also for helping me develop the background and the skills I needed for my research through the various excellent courses at UTA.

I must thank Dr. Nader Hozhabri, Dennis Bueno, Richard Chambers, Richard Wells, Eduardo Maldonado and Paul Logan for going out of the way to help me with my every need during the time I spent at Nanofab.

I cherish the company of the many researchers at Nanofab and would like to thank them for the many informative discussions, sharing of expertise and for their warm friendship.

Finally I would like to thank my parents and family for their support and encouragement without which this endeavor would not be possible.

This work was supported in part by the UTA/UTD/TI/THRE Medical Technology Research Program and in part by the National Science Foundation under Grant No: NSF-IIS-1208623.

November 20, 2013

## Abstract

# NANOSTRUCTURED SURFACES USING THERMAL NANOIMPRINT LITHOGRAPHY: APPLICATIONS IN THIN MEMBRANE TECHNOLOGY, PIEZOELECTRIC ENERGY HARVESTING AND TACTILE PRESSURE SENSING

Bhargav P Nabar, PhD

The University of Texas at Arlington, 2013

Supervising Professor: Zeynep Celik-Butler

Nanoimprint lithography (NIL) is emerging as a viable contender for fabrication of large-scale arrays of 5-500 nm features. The work presented in this dissertation aims to leverage the advantages of NIL for realization of novel Nano Electro Mechanical Systems (NEMS). The first application is a nanoporous membrane blood oxygenator system. A fabrication process for realization of thin nanoporous membranes using thermal nanoimprint lithography is presented. Suspended silicon nitride membranes were fabricated by Low-Pressure Chemical Vapor Deposition (LPCVD) in conjunction with a potassium hydroxide-based bulk micromachining process. Nanoscale features were imprinted into a commercially available thermoplastic polymer resist using a pre-fabricated silicon mold. The pattern was reversed and transferred to a thin aluminum oxide layer by means of a novel two stage lift-off technique. The patterned aluminum oxide was used as an etch mask in a  $\text{CHF}_3/\text{He}$  based reactive ion etch process to transfer the pattern to silicon nitride. Highly directional etch profiles with near vertical sidewalls and excellent  $\text{Si}_3\text{N}_4/\text{Al}_2\text{O}_3$  etch selectivity was observed. One-micrometer-thick porous membranes with varying dimensions of  $250 \times 250 \mu\text{m}^2$  to  $450 \times 450 \mu\text{m}^2$  and pore diameter of 400 nm have been engineered and evaluated. Results indicate that the

membranes have consistent nanopore dimensions and precisely defined porosity, which makes them ideal as gas exchange interfaces in blood oxygenation systems as well as other applications such as dialysis. Additionally, bulk – micromachined microfluidic channels have been developed for uniform, laminar blood flow with minimal cell trauma. NIL has been used for ordered growth of crystalline nanostructures for sensing and energy harvesting. Highly ordered arrays of crystalline ZnO nanorods have been fabricated using a polymer template patterned by thermal nanoimprint lithography, in conjunction with a low temperature hydrothermal growth process. Zinc Oxide nanorods were characterized to determine their piezoelectric response to an applied force. An atomic force microscope operating in the force spectroscopy mode was used to apply forces in the nN range. In contrast to previously published reports using lateral tip motion (C-AFM), the action of the tip in our experiment was perpendicular to the plane of the nanorods, allowing a more defined tip – nanorod interaction. Voltage pulses of a positive polarity with amplitude ranging from hundreds of  $\mu\text{V}$  to few mV were observed. The tip – nanorod interaction was modeled using commercial solid modeling software and was simulated using finite element analysis. Comparison of the results yielded useful observations for design of piezoelectric energy harvesters/sensors using ZnO nanorods. A nanoelectromechanical (NEMS) piezoelectric energy harvester using crystalline ZnO nanowires is developed. The device converts ambient vibrations into usable electrical energy for low power sensor applications. This is accomplished by mechanical excitation of an ordered ZnO nanorod array using a suspended bulk micromachined proof mass. The device is capable of generating up to 14.2 mV single polarity voltage under an input vibration of amplitude 1 g ( $9.8 \text{ m/s}^2$ ) at a frequency of 1.10 KHz. Finally, large area arrays of ordered ZnO piezoelectric nanorods are developed on flexible substrates towards self-powered sensing skin for robots. The sensor array is designed to measure tactile

pressure in the 10 kPa– 200 kPa range with 1 mm spatial resolution. A voltage signal in the range of few mV is observed in response to applied pressure. This work represents the first demonstration of perfectly ordered, vertically aligned, crystalline ZnO nanorod arrays, fabricated in polyimides to ensure conformity to non-planar surfaces such as a robot's. The sensors are self-packaged using a flexible substrate and a superstrate. In addition to the novelty of the sensor structure itself, the work includes an innovative low-temperature hydrothermal ZnO growth process compatible with the temperature restrictions imposed by the polyimide substrate/superstrate.

## Table of Contents

Acknowledgements .....	iii
Abstract .....	iv
List of Illustrations .....	xii
List of Tables .....	xxii
List of symbols .....	xxiii
Chapter 1 Introduction.....	1
1.1 The necessity and advantages of nanofabrication .....	1
1.2 Nanofabrication techniques and current state – of – the – art .....	3
1.3 Nanoimprint lithography (NIL).....	5
1.3.1 Overview of NIL process. ....	5
1.3.2 Nanoimprint mold .....	6
1.3.3 Nanoimprint resists.....	7
1.3.4 Nanoimprinting equipment .....	7
1.4 Application of NIL to present research .....	8
1.5 Dissertation layout .....	11
1.5 Summary .....	12
Chapter 2 Design and fabrication of a membrane blood oxygenation system using a nanoporous Si <sub>3</sub> N <sub>4</sub> membrane.....	14
2.1 Introduction .....	14
2.1.1 Blood oxygenation systems – Necessity and current trends .....	14
2.1.2 Requirements for a blood oxygenator system.....	16
2.1.3 Nanoporous membranes .....	17
2.2 Blood oxygenator design .....	19
2.2.1 Blood oxygenator structure .....	19

2.2.2 Blood channel design considerations .....	20
2.2.3 Gas channel and gas exchange interface design .....	25
2.3 Blood channel microstructure fabrication .....	26
2.3.1 Fabrication of blood channels using surface micromachining .....	26
2.3.2 Fabrication of blood channel microstructures using bulk micromachining .....	34
2.4 Fabrication of gas exchange microstructure with integrated nanoporous silicon nitride membrane.....	37
2.4.1 Silicon nitride growth and backside patterning.....	37
2.4.2 Nanoimprint lithography and pattern reversal process.....	37
2.4.3 Silicon nitride membrane and nanopore fabrication.....	39
2.5 A discussion on the development of the two stage lift – off process and the anisotropic reactive ion etch process. ....	42
2.6 Summary .....	51
Chapter 3 Low temperature growth and characterization of piezoelectric properties of crystalline ZnO nanorods using atomic force microscopy .....	52
3.1 Introduction .....	52
3.1.1 Zinc oxide nanostructures – an overview.....	52
3.1.2 Piezoelectric properties of ZnO .....	53
3.1.3 Crystalline ZnO nanorod growth techniques .....	56
3.1.3.1 Vapor – Liquid – Solid (VLS) process.....	56
3.1.3.2 Hydrothermal growth.....	56
3.1.3.3 Hydrothermal growth with NIL assisted template – our method of choice.....	58



3.2 An experiment to observe the piezoelectric response of crystalline ZnO nanorods.....	59
3.2.1 Overview of the experiment.....	59
3.2.2 Sample preparation .....	61
3.2.3 Experimental setup for characterization .....	64
3.2.4 Characterization results.....	66
3.3 Diameter and density controlled low temperature growth of crystalline ZnO nanorods.....	77
3.3.1 Motivation .....	77
3.3.2 Ordered arrays of ZnO nanorods using thermal nanoimprint lithography. ....	77
3.3.3 Effect of hydrothermal growth solution concentration on diameter of ZnO nanorods.....	78
3.3.4 Effect of seed layer deposition temperature.....	79
3.3.5 Fabrication of rows of ordered ZnO nanorods using NIL and conventional photolithography.....	84
3.4 Force spectroscopy characterization of the nanorod array using the Bruker Dimension FastScan AFM system.....	85
3.5 Summary .....	86
Chapter 4 A novel NEMS vibration energy harvester using crystalline ZnO nanorods .....	88
4.1 Vibration energy harvesting introduction, principle of operation, review of the state – of – the – art.....	88
4.2 Design of a NEMS vibration energy harvester using piezoelectric ZnO nanorods.....	93

4.2.1 Z - axis vibration energy harvester .....	93
4.2.1.1 Principle of operation and design .....	93
4.2.1.2 Analysis of operation using finite element methods.....	95
4.2.1.3 Z – axis energy harvester - device behavior results and discussion .....	99
4.2.2 Lateral motion vibration energy harvester .....	101
4.2.2.1 Principle of operation and design .....	101
4.2.2.2 Evaluation of device performance using finite element modeling.....	102
4.2.2.3 Lateral motion energy harvester - device behavior results and discussion .....	104
4.2.3 Vibration energy harvester with bulk - micromachined proof - mass .....	108
4.2.3.1 Principle of operation and design .....	108
4.2.3.2 Evaluation of device performance using finite element modeling.....	111
4.3 Fabrication process development for bulk - micromachined proof - mass energy harvester .....	117
4.4 Summary .....	118
Chapter 5 Self-powered tactile pressure sensors using NIL – ordered arrays of piezoelectric ZnO nanorods on flexible substrates .....	121
5.1 Introduction to tactile pressure sensing, review of the current state-of- the-art .....	121
5.2 Sensor structure, principle of operation and FEM simulation.....	123

5.3 Fabrication of tactile pressure sensors on a polyimide based flexible substrate .....	131
5.4 Frequency domain and time domain characterization of ZnO nanorods .....	137
5.5 Summary .....	151
Chapter 6 Conclusion.....	152
6.1 Nanoimprint lithography as an enabling technology.....	152
6.2 Development of a novel membrane blood oxygenator with a nanoporous silicon nitride membrane.....	152
6.3 Characterization of piezoelectric response of crystalline ZnO nanorods and low temperature NIL assisted hydrothermal growth .....	153
6.4 Development of a NEMS vibration energy harvester using ordered ZnO nanorods.....	155
6.5 Design, fabrication and characterization of tactile pressure sensors on flexible substrates using piezoelectric ZnO nanorods .....	156
References.....	158
Biographical Information .....	175

## List of Illustrations

Figure 1-1 Steps involved in thermal nanoimprint lithography.....	6
Figure 1-2 Silicon mold used for the nanoimprint lithography process. (a) SEM image, (b) AFM image.....	9
Figure 1-3 Nanoimprint lithography as an enabling technology for development of nanoporous membranes (left) and ordered arrays of ZnO nanostructures (right).....	10
Figure 2-1 Schematic representation of nanoporous membrane blood oxygenator. ....	19
Figure 2-2 Components and assembly of micro blood oxygenator. ....	20
Figure 2-3 Blood channel "tree" distribution structure. ....	21
Figure 2-4 Transition in channel depth from 40 $\mu\text{m}$ at the inlet to 10 $\mu\text{m}$ at the oxygenation area.....	21
Figure 2-5 Gradual transition in net channel cross - section area from 40000 $\mu\text{m}^2$ to 480000 $\mu\text{m}^2$ .....	22
Figure 2-6 Bifurcations in the channel structure. ....	23
Figure 2-7 (a) Bifurcations at each and every step. (b) Inverted "V" shaped distribution network.....	24
Figure 2-8 75° bifurcation at the inlet channels to reduce flow stagnation. ....	25
Figure 2-9 (a) Cross section of the gas channel structure showing gas exchange chambers and gas exchange membrane (b) Zoomed in cross section view of gas channel structure (c) Top view of gas channel structure. ....	25
Figure 2-10 Process flow for surface micromachined blood channel structure .....	27
Figure 2-11 (a) Microscope image (b) SEM image of patterned 20 $\mu\text{m}$ thick sacrificial layer.....	28
Figure 2-12 (a) Microscope image showing the first and second stage sacrificial layers. (b) Magnified image of second stage sacrificial layer. ....	29

Figure 2-13 Microscope images of sacrificial layer (a) before process temperature correction. (b) after process temperature correction.....	30
Figure 2-14 (a) Microscope image (b) SEM image of patterned second stage sacrificial layer.....	30
Figure 2-15 (a) Microscope image (b) SEM image of patterned third stage sacrificial layer.....	31
Figure 2-16 (a) Microscope image (b) SEM image of patterned flange sacrificial layer. ...	31
Figure 2-17 a) SEM image of cross section at the blood channel inlet. (b) Higher magnification image showing the structural and sacrificial layers. ....	32
Figure 2-18 (a) SEM image of blood channels with patterned etch holes (b) SEM image side view. ....	33
Figure 2-19 SEM images of collapsed membranes after sacrificial layer removal. ....	34
Figure 2-20 (a) CoventorWare solid model (b) SEM of bulk micromachined first stage microchannels. ....	36
Figure 2-21 (a) CoventorWare solid model (b) SEM of bulk micromachined second stage microchannels. ....	36
Figure 2-22 (a) CoventorWare solid model (b) SEM of bulk micromachined third stage oxygenation area microchannels. ....	37
Figure 2-23 Schematic illustration of the nanoporous membrane fabrication process.....	40
Figure 2-24 SEM images at different stages of the fabrication process. ....	41
Figure 2-25 Percentage error in nanopore dimension as a function of aluminum oxide to chromium thickness ratio. ....	44
Figure 2-26 (a) Chromium lift-off stage showing “mushroom” shaped pillars. Inset: Magnified image (b) Nanoimprint resist after residual resist ashing showing positive sidewall profile.....	45

Figure 2-27 Effect of bottom electrode RF power on the nanopore etch profile. ....	45
Figure 2-28 Effect of process pressure on the nanopore etch profile.....	46
Figure 2-29 Effect of process gas chemistry on nanopore etch profile (a)CF <sub>4</sub> /O <sub>2</sub> (b) CHF <sub>3</sub> . .....	47
Figure 2-30 Reactive ion etch profile of nanopores in a 1 μm thick silicon nitride layer on silicon. ....	48
Figure 2-31 (a) Wafer layout and sampling location nomenclature. (b) Individual die .....	48
Figure 2-32 Point defects on a 10 μm x 10 μm sample area of a suspended silicon nitride membrane. ....	49
Figure 3-1 Voltage generated in ZnO nanorod after application of a bending force. ....	55
Figure 3-2 Voltage generated in ZnO nanorod after application of a compressive force. ....	55
Figure 3-3 An example of a force plot obtained using a TESP type tip interacting with a ZnO nanorod array.....	61
Figure 3-4 Schematic illustration of the test sample preparation process.....	63
Figure 3-5 (a) SEM image of ZnO nanorods (top view). (b) SEM image of ZnO nanorods (side view) (c) AFM tapping mode image of ZnO nanorod array. (d) XRD scan showing the dominant (0002) ZnO peak. (e) EDAX scan from top of a single ZnO nanorod.....	63
Figure 3-6 (a) Schematic, (b) Photograph showing experimental setup for mechanical deflection and measurement of generated piezoelectric voltage from ZnO nanorods. ....	64
Figure 3-7 Voltage vs time plots for different pulse widths obtained from sampling the signal generator output using the nanovoltmeter – LabVIEW program module. ....	66
Figure 3-8 (a) Force plot from one nanorod – tip interaction event. (b) Schematic for forward and reverse polarity connections in separate experiments conducted to verify the origin of the observed signal. (c) Voltage signals recorded by the nanovoltmeter in forward and reverse polarity experiments.....	68

Figure 3-9 (a) Voltage recorded by nanovoltmeter in response to manual probing of the nanorod array. Sample force plots corresponding to positive (b), and negative (c) polarity voltage spikes. ....	69
Figure 3-10 (a) Simulated displacement ( $\mu\text{m}$ ) of AFM tip in response to an applied force. (b) Simulated voltage (volts) generated in a ZnO nanorod in response to lateral displacement. ....	71
Figure 3-11 Probe positions for force spectroscopy on the nanorod array.....	71
Figure 3-12 (a) an example plot of the piezoelectric signal as a result of the manually triggering the AFM tip to extend into the nanorod array. (b-e) Voltage generated as a result of manually triggering the AFM tip for different trigger voltages .....	73
Figure 3-13 (a) an example plot of the piezoelectric signal as a result of the triggering the AFM tip to extend into the nanorod array at a frequency of 1 Hz. (b-e) Voltage generated as a result of triggering the AFM tip at 1 Hz for different trigger voltages at five different trigger voltages.....	74
Figure 3-14 (a) Force plot from a single tip-nanorod interaction (b) Corresponding voltage signal from the nanovoltmeter.....	75
Figure 3-15 Schematic showing an equivalent model for the ZnO nanorod array – AFM tip interaction.....	76
Figure 3-16 Ordered growth of ZnO nanorod arrays using NIL.....	78
Figure 3-17 ZnO nanorods grown with NIL patterned thermoplastic template at different equimolar concentrations. (a) 20 mM (b) 40 mM (c) 65 mM (d) 100 mM .....	79
Figure 3-18 EDAX spectrum for ZnO seed layer showing presence of Zn and O.....	80
Figure 3-19 XRD spectrum from PLD deposited seed layer at (a) Room temperature (b) 200°C (c) 400°C .....	80

Figure 3-20 SEM images of ZnO nanorods grown using a NIL patterned template at a solution concentration of 40 mM. (a) Top view and (b) side view of nanorods grown on seed layer deposited at 400 °C. (c) Top view and (d) side view of nanorods grown on seed layer deposited at room temperature .....	82
Figure 3-21 SEM images of ZnO nanorods grown using a NIL patterned template at a solution concentration of 85 mM. (a) Top view and (b) side view of nanorods grown on seed layer deposited at 400 °C. (c) Top view and (d) side view of nanorods grown on seed layer deposited at room temperature. ....	83
Figure 3-22 SEM images (a) photolithography-patterned seed layer coated with NIL patterned template layer (b) higher magnification image.....	84
Figure 3-23 SEM images of rows of ordered ZnO nanorods grown using the hydrothermal growth process. (a) Top view (b) Side view .....	85
Figure 3-24 AFM image of the nanorod sample with the FastScan AFM system. ....	85
Figure 3-25 Force plots corresponding to each of the probe points shown in Fig. 3-24. .	86
Figure 4-1 Mass spring damper system.....	92
Figure 4-2 Schematic description of z – axis energy harvester under z - axis vibration ..	94
Figure 4-3 Solid model of z - axis energy harvester .....	94
Figure 4-4 Cross section view of z - axis energy harvester model .....	95
Figure 4-5 HEXA 3 model meshed with extruded brick elements .....	96
Figure 4-6 Simulated displacement for HEXA 3 Model under 2 g –ve z - direction acceleration .....	96
Figure 4-7 A proof - mass compressing a nanorod array of 6 x 6 nanorods .....	97
Figure 4-8 Stiffness of nanorod array vs. number of nanorods .....	98
Figure 4-9 Lateral motion energy harvester design .....	101



Figure 4-10 Cross sectional view of lateral motion energy harvester showing the position of the nanorod array.....	102
Figure 4-11 (a) Top view of nanorod array (green) and electrode (blue) (b) Cross sectional side – view of the nanorod array and electrode.....	102
Figure 4-12 Left - Simplified solid model for simulation of the lateral motion energy harvester. Right – Cross section.....	103
Figure 4-13 (a) Top view of the simplified solid model of lateral motion energy harvester with membrane electrode hidden (b) with membrane electrode.....	103
Figure 4-14 FEM boundary conditions, meshing and loading for the simplified lateral energy harvester model .....	104
Figure 4-15 (a) Lateral motion design under 1 g acceleration in +ve x direction (The proof - mass is hidden) (b) Displacement simulation for a simplified z - axis design for comparison.....	105
Figure 4-16 Calculated resonance frequency for different nanorod lengths and different proof - mass sizes. ....	106
Figure 4-17 Nanorod array stiffness as a function of array pitch .....	107
Figure 4-18 Nanorod array stiffness as a function of Nanorod array area for an array pitch of 0.5 $\mu\text{m}$ .....	107
Figure 4-19 Schematic of the bulk micromachined proof - mass energy harvester design, showing operation under applied vibrations.....	109
Figure 4-20 Schematic of the nanorod – tooth interaction.....	110
Figure 4-21 Structure and assembly of the bulk micromachined proof - mass energy harvester design.....	110
Figure 4-22 Cross section view of the assembled bulk micromachined proof - mass energy harvester design with dimensions.....	111

Figure 4-23 (a) Quarter model of top substrate, meshed. (b) Spring arm dimensions, displayed in Table 4-4. ....	112
Figure 4-24 (a) Vertical displacement (b) von Mises stress in response to 2 g acceleration applied to proof - mass. ....	112
Figure 4-25 (a) Lateral bending of 8 $\mu\text{m}$ long nanorod rows (b) Nanorod deformation exaggerated, tooth hidden. ....	114
Figure 4-26 (a) Variation of vertical stiffness and (b) lateral bending stiffness with nanorod row length. ....	115
Figure 4-27 Electric potential generated on a single ZnO nanorod when subjected to lateral bending. ....	117
Figure 4-28 Top wafer fabrication process flow. ....	119
Figure 4-29 Fabrication of bottom wafer. ....	120
Figure 5-1 Tactile sensor structure consisting of a substrate, superstrate, fill layer, nanorod array and electrodes. ....	124
Figure 5-2 Simulation results showing nanorod compression in response to applied pressure for different sensor cross section area (a) 2.15 $\mu\text{m}$ x 2.15 $\mu\text{m}$ (b) 5.13 $\mu\text{m}$ x 5.13 $\mu\text{m}$ . ....	125
Figure 5-3 Nanorod compression in response to applied tactile pressure for different thicknesses of flexible substrate. (a) 5 $\mu\text{m}$ substrate – 5 kPa pressure (b) 20 $\mu\text{m}$ substrate – 5 kPa pressure (c) 35 $\mu\text{m}$ substrate – 5 kPa pressure (d) 5 $\mu\text{m}$ substrate – 500 kPa pressure (e) 20 $\mu\text{m}$ substrate – 500 kPa pressure (f) 35 $\mu\text{m}$ substrate – 500 kPa pressure. ....	126
Figure 5-4 Voltage generated by a single nanorod in response to axial compression (a) 5 kPa (b) 500 kPa. ....	127

Figure 5-5 CoventorWare solid model showing the different sensor designs (a) TSS (b) TS9_100 (c) TS25_50 (d) TS49_30.....	128
Figure 5-6 Single die layout showing the AAL44, SD16 and AAS44 arrays.....	129
Figure 5-7 Bondpad nomenclature for individual sensor addressing .....	130
Figure 5-8 Sensor nomenclature. ....	130
Figure 5-9 (a) Tactile sensor fabrication process flow.....	132
Figure 5-10 Deposition and patterning of Al <sub>2</sub> O <sub>3</sub> pressure distribution plate (a) AAL44 (b) SD16 (c) AAS44.....	133
Figure 5-11 Photolithography for definition of the top electrode using negative photoresist NR9 1500PY (a) 30 μm (b) 50 μm (c) 100 μm (d) 500 μm (e) Patterned Cr/Au layer after lift-off.....	133
Figure 5-12 Patterned ZnO/Ti layer (a) 30 μm x 30 μm (b) 50 μm x 50 μm (c) 100 μm x 100 μm (d) 500 μm x 500 μm area .....	134
Figure 5-13 SEM image of NIL patterned nanoimprint resist template on ZnO seed layer (a) Top view (b) Side view.....	134
Figure 5-14 SEM images of ordered ZnO nanorod arrays Left – Top view, Right – Side view. (a-b) 500 μm x 500 μm (c-d) 100 μm x 100 μm (e-f) 50 μm x 50 μm (g-h) 30 μm x 30 μm .....	135
Figure 5-15 SEM images of exposed nanorod tips embedded in polyimide after plasma etch.....	136
Figure 5-16 Microscope images after Au/Ti bottom electrode deposition and lift-off(a) TS49_30 (b) TS25_50 (c) TS9_100 (d) TSS (e) AAS44 array .....	136
Figure 5-17 Microscope images after deposition of flexible substrate (a) TS49_30 (b) TS25_50 (c) TS9_100 (d) Photograph of tactile sensor arrays on flexible substrate after removal of silicon base wafer.....	137

Figure 5-18 (a) Modified micromanipulator station used for characterization of tactile pressure sensors (b) Zoomed in photograph showing a sample under test along with the nano - positioner, load cell and probe (c) SEM image, top view of flat - tipped tungsten probe (d) SEM image side view of tungsten probe.....	138
Figure 5-19 (a) Schematic of the characterization setup used for frequency domain characterization of tactile pressure sensor (b) An example plot from the signal analyzer showing sensor signal, and various noise components.....	139
Figure 5-20 Sensor response at 100 kPa and 200 kPa at different probe frequencies..	140
Figure 5-21 Micrographs showing the tactile sensor array being probed. R1C1 is connected to the measurement apparatus (a) Probe not engaged (b) R1C1 probed (c) R1C2 probed (d) R1C3 probed (e) R1C4 probed (f) Frequency domain plot corresponding to a-e .....	141
Figure 5-22 Tactile sensor response when subjected to a cyclic load in the 10 – 200 kPa range (a)TSS (b) TS9_100 (c) TS25_50 (d) TS49_30 .....	142
Figure 5-23 Averaged results from probing the different sensor designs at different pressure values multiple times. The error bars at each data point show standard deviation. (a) TSS (b) TS9_100 (c) TS25_50 (d)TS49_30. ....	143
Figure 5-24 Sensitivity of tactile pressure sensors as a function of the number of nanorod arrays in each sensor design. ....	144
Figure 5-25 Tactile sensor response when subjected to a cyclic load in the 10 – 200 kPa range after deposition of 18 $\mu$ m substrate polyimide (a)TSS (b) TS9_100 (c) TS25_50 (d) TS49_30.....	145
Figure 5-26 Averaged results from probing the different sensor designs after deposition of 18 $\mu$ m substrate polyimide at different pressure values multiple times. (a) TSS (b) TS9_100 (c) TS25_50 (d)TS49_30.....	145

Figure 5-27 Sensitivity of tactile pressure sensors as a function of the number of nanorod arrays in each sensor design after deposition of 18 $\mu\text{m}$ thick substrate.....	146
Figure 5-28 SD16 sensor response after being tapped manually using a hex key. ....	148
Figure 5-29 Time domain response from the different tactile sensors in the 10 – 50 kPa pressure range. ....	149
Figure 5-30 Time domain response from the different tactile sensors in the 10 – 50 kPa pressure range. ....	150

## List of Tables

Table 2-1 KOH wet etch process parameters.....	35
Table 2-2 Etch rate and etch uniformity over a 3” Si wafer using a KOH wet etch process .....	35
Table 2-3 Defect occurrences in 10 $\mu\text{m}$ x 10 $\mu\text{m}$ sample areas on a single wafer.....	49
Table 2-4 Variation in nanopore diameter across a 3” diameter wafer.....	50
Table 3-1 Process temperature for different nanorod growth techniques .....	58
Table 3-2 Variation of ZnO grain size with substrate temperature .....	81
Table 4-1 z – axis energy harvester designs and dimensions.....	95
Table 4-2 Calculation of spring constants and resonance frequencies for the z – axis harvester designs.....	100
Table 4-3 Calculation of spring constants and resonance frequencies for the z – axis and lateral energy harvester designs .....	105
Table 4-4 Spring arm design – simulation results.....	113
Table 4-5 Vertical, lateral displacement, and spring constants for different row lengths	114
Table 4-6 Calculation of lateral displacement and resonance frequency .....	116
Table 5-1 Sensor designs, nomenclature and dimensions.....	128
Table 5-2 Sensor addressing for a single die .....	131

## List of symbols

$A$	Area of cross section
$A_{int}$	Surface area of the interface
$b$	Damping constant
$D$	Electric displacement density ( $C/m^2$ )
$d_{cant}$	Deflection of the AFM cantilever
$D_{int}$	Diffusion constant (dependent on solubility of gas, temperature and permeability of the interface)
$d_z$	Vertical displacement
$E$	Electric field (V/m)
$e$	Piezoelectric stress coefficient ( $C/m^2$ )
$F$	Force
$g$	Acceleration due to earth's gravity. ( $9.8 m/s^2$ )
$i$	Denotes the direction of electric field
$j$	Denotes the direction of strain
$k$	Spring constant
$K_{cant}$	Stiffness of the AFM cantilever
$K_x$	Lateral stiffness
$K_z$	Vertical stiffness
$L_r$	Length of nanorod rows
$m$	Mass of the proof-mass
$mM$	millimolar
$P$	Pressure
$S_v$	AFM cantilever sensitivity (nm/V)
$T_{int}$	Thickness of the interface

$TL1$	Template layer 1
$TL2$	Template layer 2
$V_{gas}$	Volume of gas diffused across the interface / unit time
$V_t$	Trigger voltage (V)
$Y$	Young's Modulus
$\epsilon$	Dielectric permittivity (F/m)
$\epsilon$	Strain
$\sigma$	Stress



## Chapter 1

### Introduction

#### 1.1 The necessity and advantages of nanofabrication

It was nearly half a century ago that Dr. Richard Feynman delivered his iconic “There’s plenty of room at the bottom” lecture at Caltech [1]. In the lecture, he introduced the world of the ultra – small, the thousandth of a millionth of a meter. This was a time when the “simple” germanium transistor represented the pinnacle of scientific progress in electronics. Dr. Feynman expounded the importance and advantages of manufacturing machines and devices at the nanometer scale – nanofabrication. He envisioned technologies that we know today as electron beam lithography (EBL), that would revolutionize the areas of information storage, computing, medicine, fluidics and self-assembly. He further predicted that by the year 2000, nanomanufactured devices and nanofabrication processes would be at the forefront of research and development. Today, examples of such improved - performance devices abound in recent literature. Applications can be found in diverse areas such as sensing, biotechnology, fluidics, optics and photonics to name a few.

The ability to precisely control the placement or define features at nanoscale dimensions is of immense importance to the realization of different next generation devices. In addition to the advantages of miniaturization and higher packing density, nanofabrication also results in substantial device performance enhancements by taking advantage of the significant differences in the laws of physics at the nanoscale.

Some of the advantages of nanostructuring are higher sensitivity to applied forces owing to enhanced compliance, greater mass resolution and fast response times. This has led to the development of nanomechanical sensors with the capability to resolve forces upto 10 pN [2]. Nanofabricated atomic force microscope (AFM) probes have the ability to resolve the forces necessary for stretching [3] and rupturing [4] hydrogen bonds in biological molecules. Nano devices capable of measuring a few zeptograms of mass have been reported [5].

Biosensing applications using nanoporous membranes benefit tremendously from nanofabrication [6]. One significant advantage is the drastic reduction in the sample size necessary for analysis. Additional advantages include faster processing, enhanced accuracy and higher portability [7]. Precise control over length, size and shape significantly improve detection and analytical capabilities of such sensors [8]. Bio – imaging of living cells without subjecting the cells to any adverse effects has been enabled using nanofabricated devices [9]. Replication of the physiological and natural environment is possible with nanofabricated devices. This important feature has its own advantages such as enabling real time study of live cells under different environments, modulation of topography and density of cell adhesion sites and fabrication of 3-D nanostructures that can closely mimic in-vivo conditions [10].

Nanophotonics is an area where nanofabrication techniques are used extensively. Fabrication of photonic crystals is facilitated by nanofabrication techniques such as nanoimprint lithography and laser interference lithography which can produce large area ordered arrays of nanoscale features. Such nanostructured surfaces exhibit interesting physical properties such as the ability to influence the generation and propagation of light on-chip. The flexibility offered by nanofabrication to tune nanostructure geometries results in novel types of filters, couplers, lasers and waveguides [11].

The advantages of the altered laws of physics at nanoscale are readily evident in the development of nanofabricated fluidic devices. These devices benefit from higher surface to volume ratio making surface and interfacial forces dominant. Also the size of the devices is frequently comparable to the size of the proteins or DNA being analyzed. This results in unique phenomena such as capillary induced negative pressure, diffusion limited reactions and surface charge governed ion transport [12].

## 1.2 Nanofabrication techniques and current state – of – the – art

The quest to fulfill Moore's law for semiconductor devices is driving a revolution in the way microchips are designed and fabricated. The importance and contribution of lithography techniques in keeping Moore's law relevant cannot be overstated. The International Technology Roadmap for Semiconductors (ITRS) lists critical dimension control, overlay accuracy, defect control and process cost as the four key parameters that a next generation lithography technique needs to address [13]. The requirements of the current and upcoming technology nodes i.e. beyond 32 nm half pitch, present significant challenges to conventional optical lithography systems. The wavelength of the light source and the absorption spectrum of the photoresists used for the process dictate the maximum achievable resolution. Sub-50 nm resolution has been achieved by means of optical lithography using the 193 nm and 248 nm wavelengths [14, 15]. Evidently, to obtain an even greater resolution, light sources that emit at even lower wavelengths need to be explored. EUV (Extreme UV) [16] and X-ray lithography [17] have demonstrated the necessary resolving capabilities and are important candidates for industrial integration.

These advances in optical lithography, in theory, can meet many of the requirements set by the industry. The ITRS however identifies several issues that are hampering widespread adoption. Cost of ownership of the sophisticated optical equipment and photomask manufacturing is significant. Technology extendibility is a concern as the industry demands a technology that does not render equipment unusable after one or two nodes. Other identified issues are, high complexity of masks with resultant slow throughput, alignment issues, critical dimension control and fab logistics [18]. Issues related to source power, highly specialized photomasks, have been recognized for EUV technologies for the past five years [19].

Several non-optical lithography technologies have been explored for their feasibility towards nanometer – scale patterning. Some, like EBL [20] and Focused Ion Beam Lithography [21] have been in use successfully for a few decades. Other techniques such as soft lithography

[22] and AFM lithography [23] rely on mechanical contact between the substrate and a patterning medium such as a mold or AFM tip. These technologies address many of the aforementioned drawbacks associated with optical lithography. The main limitation of these techniques is that pattern definition on the substrate is serial in nature i.e. each feature is 'written' one after another. As such, throughput is extremely low and meeting mass fabrication requirements of the semiconductor industry is all but impossible.

Research in 'bottom-up' lithography techniques is gaining significant momentum. Self-assembly methods based on polymers [24], nanoparticles [25] and DNA [26] are potential candidates for next generation lithography. Other methods such as device transfer [27] offer an edge over others for fabrication on flexible substrates. Such methods however, are presently at research stage and require substantial refinements before being introduced for mass fabrication.

Interest in efficient lithography techniques is not limited to the semiconductor industry. The primary advantage of sub –micron fabrication in the IC industry is scaling i.e. increased transistor density resulting in greatly improved performance. In recent times, researchers in different areas such as biotechnology [28], photonics [29] and computation [18] have demonstrated a new class of devices that leverage nanoscale feature sizes to achieve unique physical effects not observed at the micron scale. A common requirement for these devices is patterning a large area array of nanoscale features. At the research stage, these prototype and proof-of-concept devices do not place as stringent demands on the fabrication technology as the industry, mainly in terms of yield. A technology that has low equipment and material costs and high throughput for rapid prototyping is desirable. A welcome advantage is such a technology meeting industrial production standards in which case porting the process from the laboratory to an industrial foundry is greatly simplified.

### 1.3 Nanoimprint lithography (NIL)

Nanoimprint lithography (NIL) was developed by Professor Stephen Chou at Princeton [30] as a possible solution to some of the issues listed above. Pattern definition in NIL is accomplished by means of controlled mechanical deformation of the resist material and contrast is achieved by curing the resist by either elevated temperature or UV exposure. The chief advantage of NIL is throughput. Large area arrays of nanoscale features can be patterned in a single process run, thus greatly reducing process times as compared to single write techniques such as EBL. The most important metric for any lithography system is the resolution. Two nm wide isolated features [31] and 6 nm half pitch grating lines [32] have been successfully demonstrated using NIL. Additionally, the costs associated with NIL in terms of equipment and materials are lower than optical lithography systems of comparable resolution [33].

#### *1.3.1 Overview of NIL process.*

A characteristic that makes NIL attractive is conceptual simplicity. The process starts with spin coating of the nanoimprint resist on the substrate to be patterned. The resist is then baked at an elevated temperature to remove all solvent. Next, the substrate is brought into physical contact with the nanoimprint mold that serves as the 'mask' for the NIL process. The mold contains the inverse topography of the desired pattern defined on its surface. The mold and the substrate are then placed in a specialized piece of equipment known as a nanoimprinter; akin to an aligner or stepper in photolithography. The mold and substrate are then subjected to mechanical force; and depending on the type of NIL technique, thermal (Thermal NIL) or UV (Step and flash imprint or SFIL) curing. When the resist has been deformed by the mold and cured, the mold and resist are separated. To facilitate easy separation, anti-adhesion coatings are typically applied to the mold surface. Figure 1 is a pictorial description of the process to simplify understanding.

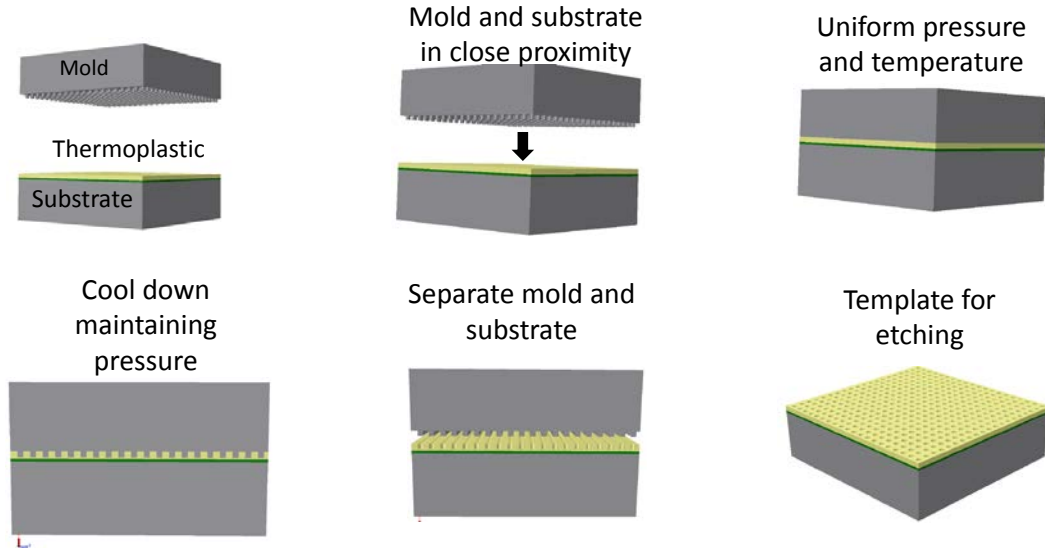


Figure 1-1 Steps involved in thermal nanoimprint lithography

### 1.3.2 Nanoimprint mold

A critical component of the NIL process is the nanoimprint mold. The mold is either a hard substrate (silicon wafer) a nano-patterned surface ( $\text{SiO}_2$ ,  $\text{Si}_3\text{N}_4$ ) on a hard substrate, or a soft substrate (PDMS). For the UV based step and flash imprint (SFIL) NIL, the mold material is quartz. A common requirement for the mold material is hardness and mechanical strength. The mold features should not deform, buckle or collapse during imprinting, so as to achieve faithful reproduction of features. The mold is typically patterned using EBL or laser interference lithography, followed by reactive ion etching to define nanoscale features. As mentioned before, the pattern on the mold is complementary to the pattern desired on in the nanoimprint resist. To prevent damage to the mold during physical contact, the thickness of the mold features is designed such that a layer of resist remains in the imprinted features after NIL. This resist known as residual resist helps cushion the mold and prevents any damage due to friction. The mold surface contains a significant number of nanoscale features in the form of protrusions and troughs. This increases the effective surface area of the mold and can cause the imprint resist to stick to the mold during separation. A popularly used solution to this problem is coating the mold with a fluoropolymer that reduces the surface energy.

### *1.3.3 Nanoimprint resists*

Nanoimprint resists vary according to suit the type of NIL process in use. For thermal NIL, the resists are thermoplastics. These are available dissolved in solvents for deposition on the substrate by spin coating. A baking step is usually necessary to drive out the solvent after spin coating, resulting in a uniform thin film on the substrate. During the imprinting process, the resist is heated beyond its glass transition temperature resulting in a decrease in its Young's modulus and viscosity. The mold is then impressed into the resist by applying a uniform pressure. Keeping the pressure constant, the temperature is ramped down below the glass transition temperature to preserve the imprinted pattern on in the resist. The 'curing' step in this process is essentially the reduction in temperature below the glass transition point.

For UV - based NIL processes such as Step – and – Flash – Imprint (SFIL), the resists used have an important addition – a photoinitiator and crosslinker compound, that crosslinks under UV exposure to provide mechanical stability to the resist. UV curable NIL resists typically have a lower viscosity than thermal resists. The mold used is a quartz mold, owing to its transparency to UV wavelengths. After the mold is impressed on the resist, the area is flooded with UV light that causes the resist to crosslink and harden. The curing necessary for pattern preservation occurs by means of the UV exposure step.

### *1.3.4 Nanoimprinting equipment*

Equipment for NIL i.e. nanoimprinters, borrow several concepts from established semiconductor fabrication tools such as mask aligners and wafer bonders. In NIL, the viscous resist is required to flow under an applied pressure at a specific temperature and conform to the features on the impressing mold. Evidently, the NIL equipment must be capable of precisely maintaining stable pressures and temperatures. In NIL, the mechanism for exerting pressure on the mold and substrate has to allow for relative movement between the two due to the viscous flow of the resist in between. However excessive relative motion has to be prevented in order to preserve pattern integrity. This is accomplished by including a compliant system such as a

membrane sandwiched in an air cushion, or a compliant material with low Young's modulus to account for the non-flatness of the surfaces. In a UV NIL system, the pressures used are lower than those in thermal NIL; hence, stability is achieved using molds fabricated from UV transparent compliant materials such as PDMS. In cases where hard quartz molds are used, the role of maintaining stable operating environment is taken over by the resist.

#### 1.4 Application of NIL to present research

Taking into account the several advantages of NIL in the foregoing discussion, the amount of attention NIL has received over the past decade seems reasonable. It is not, however, completely without shortcomings. The chief limitation is imposed by the mold. Since the mold used for NIL is manufactured using other lithography techniques such as EBL, the maximum achievable resolution is limited by the patterning technique used to make the mold. In this sense, NIL is not a stand-alone lithography technique, but a means to greatly enhance throughput, reduce operation costs and improve process simplicity of other lithography techniques. These advantages are significant and hence in spite of its dependence on other lithography techniques, NIL has been added to the ITRS as a candidate for future IC production.

Thermal NIL was chosen for its relative simplicity and has been used in all the applications in this research. All nanoimprinting was done using the Nanonex NXB 200 nanoimprinter at the Nanofab facility at UT Arlington.

A three-inch (100) silicon wafer patterned with pillar shaped structures of 200 nm in diameter, 500 nm pitch and 120 nm in height was acquired from NILT technologies, Denmark ([www.nilt.com](http://www.nilt.com)). The mold was coated with NXT 100 anti-adhesion layer from Nanonex Inc to facilitate separation of the mold from the nanoimprint resist after imprinting without damage. (Fig. 2).



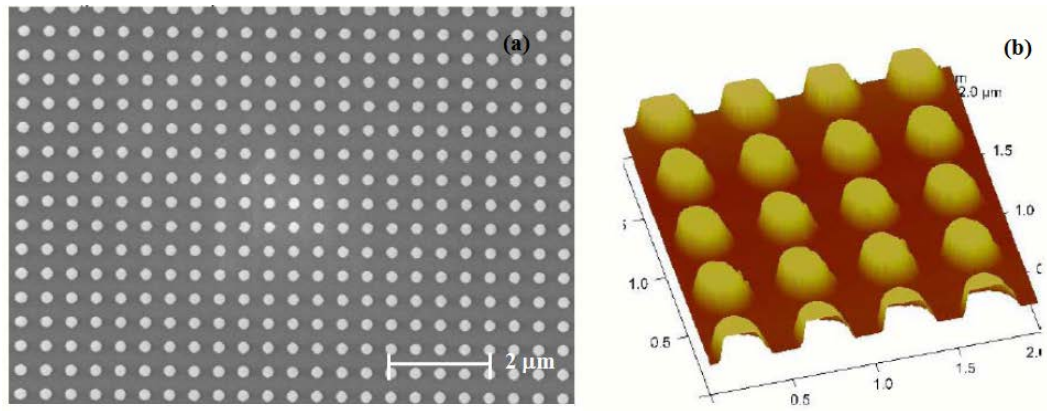


Figure 1-2 Silicon mold used for the nanoimprint lithography process. (a) SEM image, (b) AFM image. (Image courtesy of NILT Denmark)

Thermal NIL was the enabling technology for the applications presented in this research (Fig.3). The first application, a thin gas transfer membrane for a micro blood oxygenation system, required a technique for large scale fabrication of high aspect ratio sub – micron features (nanopores) with control over feature placement. Uniform pore dimensions and distribution was necessary to ensure uniformity of gas transfer at the gas – liquid interface. Using thermal NIL in conjunction with an innovative two step lift – off patterning process, a 1  $\mu\text{m}$  thick  $\text{Si}_3\text{N}_4$  membrane was patterned with a uniform array of well-defined 0.4  $\mu\text{m}$  nanopores. The two step lift off process extends the pattern transfer capabilities of NIL and was used with a specially formulated reactive ion assisted etch process to fabricate high aspect ratio nanostructures.

The second application involved fabrication of an ordered array of nanostructures for vibration energy harvesting and tactile pressure sensing. Using solution growth techniques, high quality crystalline metal compound nanostructures can be grown on specially treated substrates. NIL provides a means to precisely define growth sites for these nanostructures at submicron scale in terms of growth site dimensions and spacing. This is accomplished by using NIL to fabricate a template on top of the specially treated “seed” layer that results in a contrast pattern of lattice constants on the growth surface. Nanostructure growth occurs only at sites

where the lattice constant of the nano – material being deposited matches the lattice constant on the seed surface. This results in patterned growth of the nanostructure, and allows a great degree of control over growth site placement over a large area. In this research, ordered growth of zinc oxide nanostructures has been demonstrated. The resultant Nano Electro Mechanical System (NEMS) devices were shown to have improved performance, uniformity and repeatability.

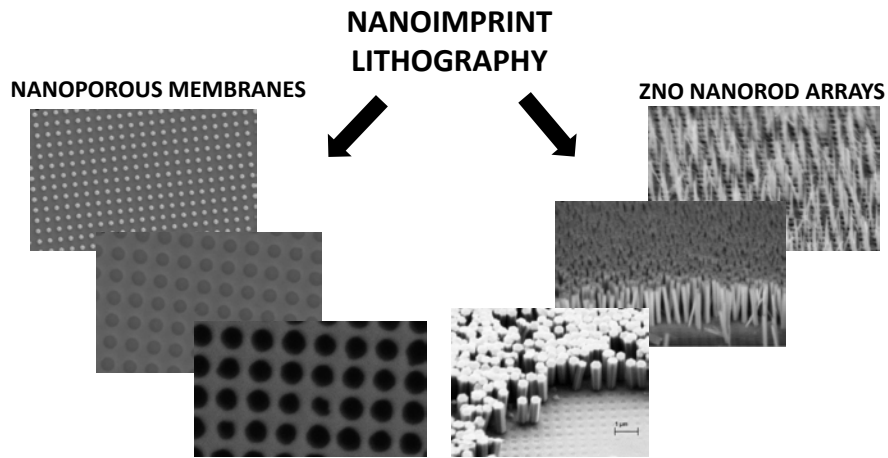


Figure 1-3 Nanoimprint lithography as an enabling technology for development of nanoporous membranes (left) and ordered arrays of ZnO nanostructures (right)

The gist of this dissertation could be summarized as follows,

- For the first time, a technique has been developed for realizing a thin nanoporous silicon nitride membrane with superior pore diameter uniformity and pore placement accuracy as compared to the state-of -the-art PCTE membranes with faster large – area throughput than E-beam lithography.
- An innovative two -stage lift-off technique has been introduced, that significantly enhances the pattern transfer capabilities of nanolithography processes.
- A novel, fully integrated, NEMS device capable harvesting energy from frequently encountered environmental vibrations has been designed, fabricated and tested using highly efficient crystalline ZnO nanorods.

- First demonstration of a large area array of tactile sensors on a flexible substrate using NIL – ordered crystalline ZnO nanorods. The sensors are self-generating and fully packaged in polyimide for environmental protection. A spatial resolution lower than 1 mm is demonstrated which is in theory limited only by photolithography.

### 1.5 Dissertation layout

The content of this dissertation is divided into six chapters. The first chapter introduces thermal nanoimprint lithography which is the underlying technology used extensively in this research. Advantages of using NIL are presented and the general benefits of using nanofabrication methods towards improving existing micro devices are discussed.

Chapter 2 presents a novel blood oxygenation system incorporating a nanoporous silicon nitride membrane fabricated using NIL. A brief review of the operation and state – of – the- art in blood oxygenation systems is presented for reference. Design aspects of the microfluidic channel structure designed for this application are discussed and fabrication details as well as scanning electron and microscope images of the completed devices are included. The chapter also presents a novel two step lift – off fabrication technique developed to mitigate some of the shortcomings of the nanoimprint resist. Nanoporous silicon nitride membranes were successfully fabricated using the developed techniques and scanning electron and microscope micrographs are presented as evidence. A qualitative analysis of the fabrication process is also included.

Chapter 3 delves into the material properties of a zinc oxide (ZnO) nanorods with specific emphasis on piezoelectric properties. The chapter starts with a literature review about the recent surge of interest in ZnO nanostructure technology and devices utilizing them. A review of nanoscale mechanical probing using atomic force microscopy is also provided. The chapter then describes an experiment conducted to study and verify the piezoelectric properties of crystalline ZnO nanostructures using AFM. It also explores the low temperature hydrothermal

growth technique of growing ZnO nanorods and effects of the different experiment parameters in nanorod growth. Finally, a technique using NIL to accomplish template assisted, ordered growth of crystalline ZnO nanorods is presented.

Chapter 4 describes the development of a novel vibration energy harvester system using NIL ordered arrays of ZnO nanorods. A literature review of the prominent energy harvesting methodologies, their advantages and shortcomings is presented. Design criteria for an ambient environment vibration energy harvester system are described and a NEMS device designed to fulfill the criteria is presented. Real time operation is mimicked using a finite element simulation and the results are presented.

Chapter 5 describes the design, simulation, fabrication and characterization of a NEMS tactile pressure sensor employing piezoelectric ZnO nanorods fabricated on a flexible substrate. These sensors were developed specifically to meet the demands of mobile robotic systems. An overview of the state – of – the –art in tactile pressure systems for robotics is presented. This is followed by a description of the sensor design, principle of operation and performance evaluation using finite element model (FEM) simulations. Fabrication of the sensor systems is described with Scanning Electron Microscope (SEM) and microscopic micrographs presented as evidence. The chapter concludes with real –time frequency and time domain characterization.

Chapter 6 summarizes the body of this dissertation and presents an outlook for future work on this subject.

## 1.5 Summary

The ability to manufacture objects at nanoscale is driving a revolution in the way next generation devices and systems are designed. The unique and extraordinary physical and chemical properties of nanomaterials and nanostructures has enabled the development of novel devices with fantastic capabilities. With the semiconductor industry as the main driver, novel nanofabrication techniques are being developed and perfected leading to a revolution in the

areas of sensing, actuation, photonics, medicine etc. This research concentrates on one such method, i.e. thermal nanoimprint lithography (NIL), that enables the fabrication of large area arrays of submicron features. This is a relatively economical technique that offers fast experiment times, ease of operation, and high yield. NIL has been extensively utilized for the development of novel nanostructured devices presented in this research. Nanoporous silicon nitride membranes with a large area array of high aspect ratio, uniform diameter submicron features have been successfully developed. NIL has also been used for template assisted ordered growth of ZnO nanostructures. This has enabled novel applications in nanostructure characterization, and development of Nano Electro Mechanical System (NEMS) vibration energy harvesting devices. Finally, NIL – template assisted growth of ZnO nanostructures has been instrumental towards the development of fully packaged tactile pressure sensors on flexible substrates.

## Chapter 2

### Design and fabrication of a membrane blood oxygenation system using a nanoporous $\text{Si}_3\text{N}_4$ membrane

#### 2.1 Introduction

##### *2.1.1 Blood oxygenation systems – Necessity and current trends*

Lung disease is America's number three killer and responsible for one in seven deaths [34]. Approximately 150,000 people are afflicted with Acute Respiratory Disease Syndrome (ARDS), a form of lung disease, each year in the United States [35]. The mortality rate associated with ARDS is as high as 50% [36]. Acute and chronic respiratory problems are a significant health care challenge [37]. Another form of lung disease, Chronic Obstructive Pulmonary Disease (COPD) which includes emphysema and chronic bronchitis affects about 10 million adults per year in the United States with a mortality rate of 40% [38]. Chronic lung disease causes lung damage and reduces the lung's gas exchange capabilities thus impairing one's ability to perform daily tasks [39].

Treatment associated with these diseases involves the use of mechanical ventilator systems [40] that have a number of shortcomings. Some of the problems associated with ventilator usage include lung damage due to excessive pressure applied to lung tissue (barotrauma), distension of lung tissue (volutrauma), and damage to parenchyma due to toxic levels of oxygen used for effective ventilator support [41]. Another area that necessitates an effective lung assistance system is lung transplantation. The average waiting time for lung transplant is 1-1.5 years with a mortality rate of 11.3 % for waiting patients [42]. There is currently no system that can replace or augment the human lung for weeks or months [43].

Some of the issues associated with ventilator systems are addressed by the oxygenator system first developed in 1953 [44]. Oxygenator systems work by oxygenation and de-oxygenation of blood using specialized apparatus outside the patient's body and thus work independent of the patient's lungs. This allows a reparably damaged lung to rest and heal.

Oxygenator systems offer an improved form of treatment for acute and chronic lung disease and provide a short term solution for sustaining lung transplant patients [34].

Oxygenator systems are based on two main modes of operation – direct contact between gas and blood as in the case of bubble oxygenators and film oxygenators and systems where blood and gas are separated by a thin membrane known as Extra Corporeal Membrane Oxygenators or ECMO. Bubble type oxygenators are the simpler of those mentioned, and work by bubbling gas directly into the blood. These are also inherently efficient at gas transfer on account of the large surface area of bubbles. Removal of bubbles and foam is a major issue associated with bubble oxygenators and necessitates a holding arterial reservoir for the bubbles to dissolve completely. The major disadvantage of this type of oxygenator is hemolysis or trauma to red blood corpuscles due to the bubbling process. This limits the usage of the bubble oxygenator to a few hours [45]. Film type oxygenators work by drawing the blood in thin film and exposing it to gas. This approach reduces hemolysis but a large volume of blood is necessary to prime the device.

Membrane based oxygenator systems provide a possible solution to each of the problems listed previously. These systems are similar in principle to the alveoli found in human lungs. The blood and gas are separated by a thin permeable membrane and oxygenation occurs by diffusion. Current membrane blood oxygenators are realized using hollow fiber membranes (HFM). The HFM's are suspended in a chamber and blood is introduced to the chamber. The HFM's carry the gas (pure or diluted oxygen) to be diffused into the blood and also carry away the carbon dioxide that diffuses out of the blood. This configuration offers the advantages of reduced cell trauma, reduced thrombogenesis and gas transfer rates comparable to bubble oxygenators. The HFM's used in current oxygenators are polymer tubes with wall thickness of 20 – 50  $\mu\text{m}$ , outer diameter of 200 – 400  $\mu\text{m}$  and pore diameter of 0.1  $\mu\text{m}$  with 30 – 50% porosity [34]. They are not however completely without shortcomings. To provide adequate gas transfer rates, approximately a meter-squared of HFM area is necessary [46].

This high contact area raises issues of biocompatibility and hemocompatibility [47]. Moreover, present systems are complex, expensive and require systemic anticoagulation and labor intensive patient monitoring [41]. Additionally, they are bulky and therefore limited to use in intensive care units [43].

### 2.1.2 Requirements for a blood oxygenator system

The human lung is very efficient at gas exchange in a range of scenarios. An optimal oxygenation system therefore, could be realized by mimicking the properties possessed by the human lung. Gas diffusion at the alveoli occurs according to Fick's law [46].

$$V_{gas} = \left( \frac{A_{int}}{T_{int}} \right) * D_{int} * (P_1 - P_2) \quad (2-1)$$

Where

$V_{gas}$  : Volume of gas diffused across the interface / unit time

$A_{int}$  : Surface area of the interface

$T_{int}$  : Thickness of the interface

$D_{int}$  : Diffusion constant (dependent on solubility of gas, temperature and permeability of the interface)

$P_1 - P_2$  : Difference in pressure across the interface

From Eq. 2-1, it is evident that a large surface area of interaction along with a small interface thickness will greatly improve the diffusion properties of the oxygenation system. The human lung has an interface area equivalent to that of a tennis court i.e. 100-150 m<sup>2</sup> [48]. The interfacial distance between blood and gas at the alveoli is about 1 – 2 μm [49]. The human lung supplies O<sub>2</sub> and CO<sub>2</sub> at a rate of 200-250 ml/min under resting conditions and is capable of 10-20 times the rate under conditions of exercise [50]. In addition other requirements include minimizing resistance to blood flow, reducing the priming volume ensuring easy de –bubbling at setup and minimizing blood activation and thrombogenicity [34].

A solution to the aforementioned requirements could be found in the field of semiconductor fabrication technology. Semiconductor and MEMS fabrication frequently involves



realization of structures within the micro or nanometer range. A variety of materials can be micromachined and their surface properties tailored by means of various thin film deposition techniques. In addition, the oxygenator components can be miniaturized to make the device portable or implantable. Other advantages are scaling and mass fabrication that can significantly reduce the costs associated with such a device. The device developed in the present research utilizes this approach.

A few examples of microfabricated oxygenation systems can be found in literature [51, 52]. These utilize standard semiconductor fabrication techniques for construction of hollow conduits for blood and gas transport. An important component of the membrane oxygenator is the gas exchange interface i.e. the membrane. The membranes used in the aforementioned research are made from PDMS which is inherently permeable to O<sub>2</sub> and CO<sub>2</sub>, and, is biocompatible. However, the thickness of the PDMS membranes reported is 15 - 64 μm. As stated previously, the membrane needs to be thin (1 – 2 μm) for efficient gas transfer. Also, the fabrication procedure for the PDMS membranes provides no control over the porosity, uniformity of pore diameter and pore placement. These issues in membrane fabrication are addressed in the present work.

### *2.1.3 Nanoporous membranes*

Nanoporous membranes fabricated from organic and inorganic materials have garnered widespread interest in the scientific community. Such membranes are primarily used for selective mass transfer [53-55]. Owing to their unique physical properties at nanometer scale dimensions, nanoporous membranes also find applications such as biosensing and chemical sensing [56-59].

Typical requirements for porous membranes are precise pore placement, uniform pore density over a wide area and mechanical robustness to withstand frequently encountered differential pressures and cyclic loadings. Pore blockage during either fabrication or operation and subsequent impedance to matter transfer is another common problem for porous

membranes that needs to be addressed. Additional application-specific requirements such as pore depth, pore diameter, membrane surface energy and surface texture place stringent demands on the fabrication process. A number of techniques have been developed to meet these constraints with each offering unique advantages and drawbacks.

Fabrication of porous membranes using electron beam lithography [60] and focused ion beam [61] has been reported. Porous membranes with a pore diameter of 50 nm and 1.8  $\mu\text{m}$  have been achieved. These techniques offer significant advantages in terms of pore placement precision and the fabricated pores offer unimpeded mass transfer. Nevertheless, large-area production is not possible and as such, these techniques are impractical in terms of cost and time for mass fabrication of high pore density membranes.

Heavy ion track etching is an established technique used to fabricate nanoporous membranes from organic polymers such as PCTE [62]. However, the inherent random nature of the heavy ions in the plasma environment precludes the formation of well-defined arrays of nanopores.

As stated previously, nanoimprint lithography (NIL), provides an excellent solution to each of the shortcomings of the processes discussed above. NIL draws on the strengths of each of these processes and offers the advantage of being able to simultaneously fabricate a large number of nano-scale features with precise dimensions, high aspect ratio, and accurate placement. Combined with conventional CMOS pattern transfer techniques, mass fabrication of wide-area arrays of nanometer features with high aspect ratios is achievable at a fraction of the cost as compared to the other processes. This makes NIL the method of choice for fabrication of nanoporous membranes in this present work.

In this work, a fabrication technique is presented for a bulk micromachined, nanoporous silicon nitride membrane containing a wide-area, highly periodic array of high-aspect ratio, through-membrane, straight-walled nanopores. NIL is used in conjunction with a pattern reversal lithography technique, which is also described herein. Using the described process, 1

$\mu\text{m}$ -thick nanoporous silicon nitride membranes having a pore diameter of 400 nm with a pitch of 500 nm have been successfully fabricated.

## 2.2 Blood oxygenator design

### 2.2.1 Blood oxygenator structure

The basic structure of the blood oxygenator system developed in this research is shown in Figure 2-1. It consists of three distinct sub - systems – (a) blood transport system, (b) gas transport system and (c) gas exchange interface.

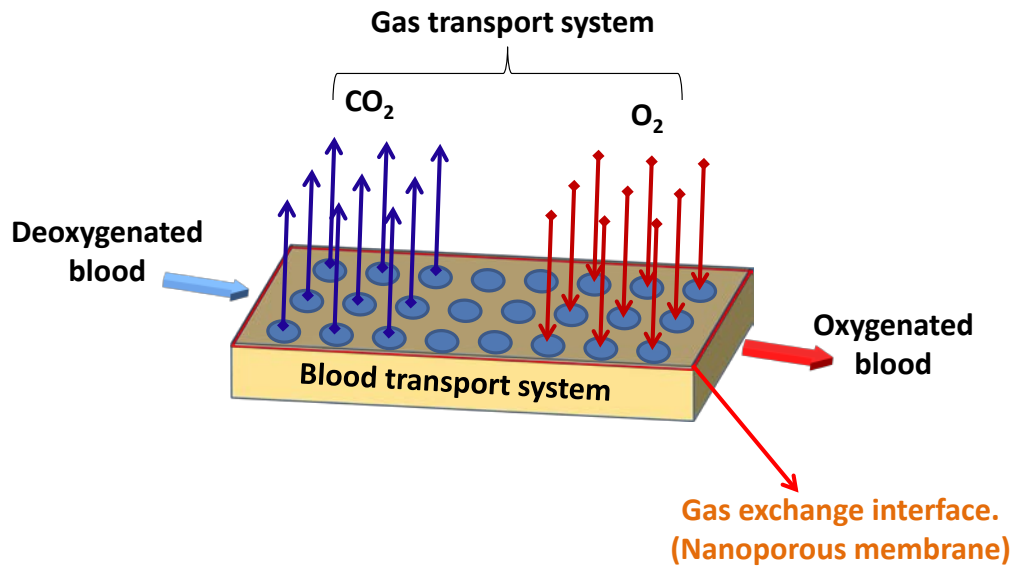


Figure 2-1 Schematic representation of nanoporous membrane blood oxygenator.

These were realized using a combination of bulk and surface micromachining techniques. The micro blood-oxygenator module consists of a bulk micromachined blood channel structure fabricated on a single silicon wafer. The gas exchange interface and gas channel structures were fabricated on another silicon wafer. The structures on these two wafers are aligned and mechanically clamped to realize the blood oxygenator. Figure 2-2 depicts the micro blood oxygenation system.

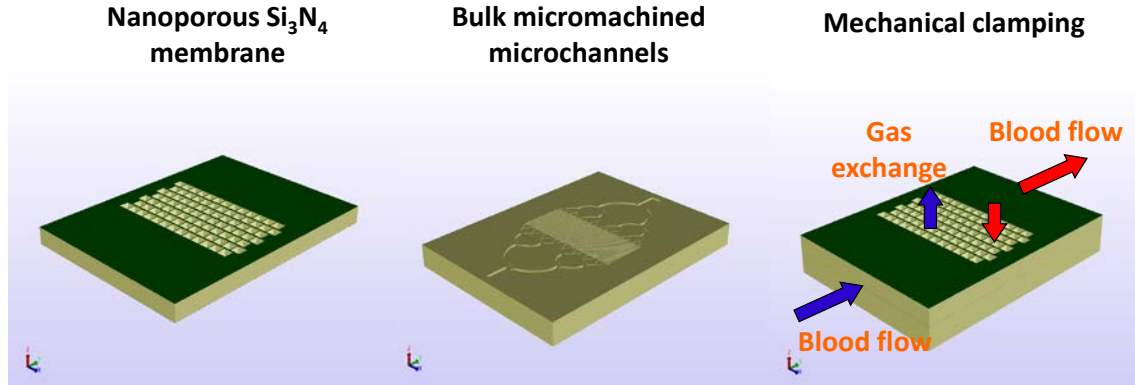


Figure 2-2 Components and assembly of micro blood oxygenator.

### 2.2.2 Blood channel design considerations

A tree structure (Fig. 2-3) was employed to distribute the blood flow from a single inlet to multiple oxygenation channels. Post oxygenation, the blood is collected via an identical tree structure, and is directed to a single outlet.

The blood channels in the oxygenation area are designed to be  $10\mu\text{m}$  in height to allow a single file of RBC's ( $8\mu\text{m}$  diameter) to traverse through them. This would ensure that all the blood passing through the device (and not just the upper surface) would be uniformly oxygenated. The inlet and outlet are designed to be  $40\mu\text{m}$  in height to allow for the insertion of tubing which would introduce blood to the device and carry blood away from it. To meet this specification, the channel height dimensions are reduced in three steps i.e.  $40\mu\text{m}$  to  $20\mu\text{m}$  to  $10\mu\text{m}$ . This helps to reduce vortices and disturbances in the flow which can cause platelet accumulation. The transition in height from the inlet to the oxygenation channel is shown in Figure 2-4.

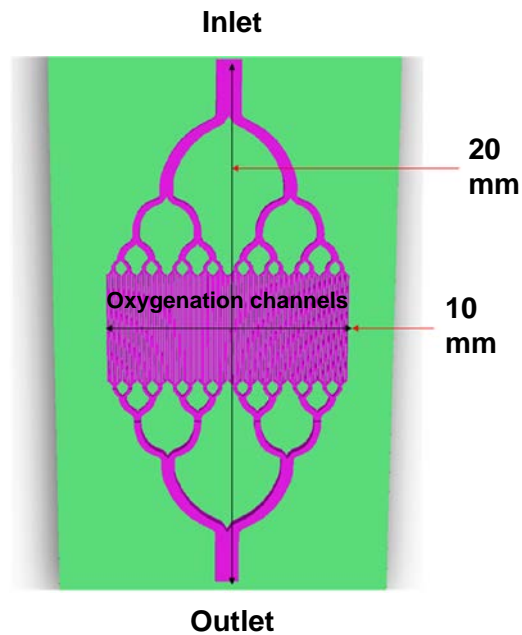


Figure 2-3 Blood channel "tree" distribution structure.

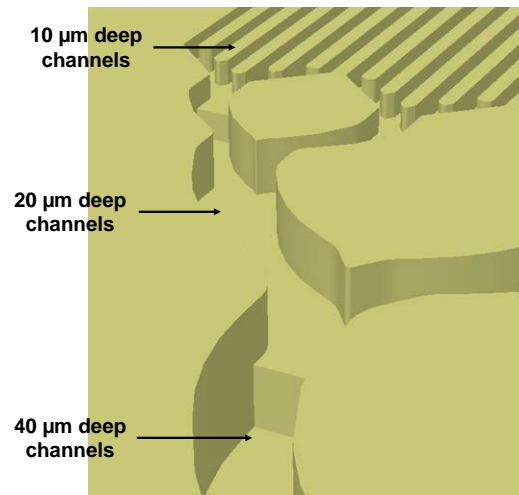


Figure 2-4 Transition in channel depth from 40 μm at the inlet to 10 μm at the oxygenation area.

The net channel cross sectional area, defined as the total area of all channels incident to a bifurcation stage, is gradually increased from the inlet to the oxygenation area. As a result, for a constant inlet blood pressure, the pressure of the blood in the channels drops progressively and gradually as the blood reaches the oxygenation area. This gradual increase and decrease in cross section area (5% from the previous stage) helps maintain a laminar flow.

Post oxygenation, the net channel cross sectional area decreases progressively towards the outlet, and the inlet and outlet blood pressures are same. This is depicted in Figure 2-5.

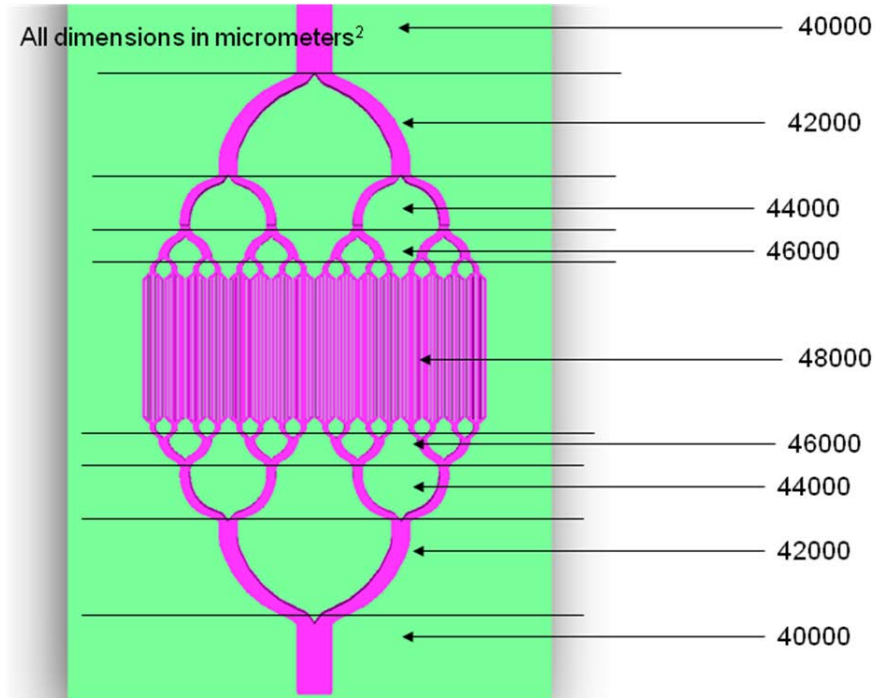


Figure 2-5 Gradual transition in net channel cross - section area from 40000  $\mu\text{m}^2$  to 480000  $\mu\text{m}^2$ .

The channel branches in the tree structure have a curved shape to facilitate smooth flow of blood. In addition, the junctions at each bifurcation are filleted with different radii of curvature to avoid cell trauma and platelet accumulation associated with sharp edges. Figure 2-6 depicts the curvature which was employed at the sharp edges of the channel. Care was taken to ensure that the radius of curvature of each fillet is substantially greater than the diameter of the RBC.

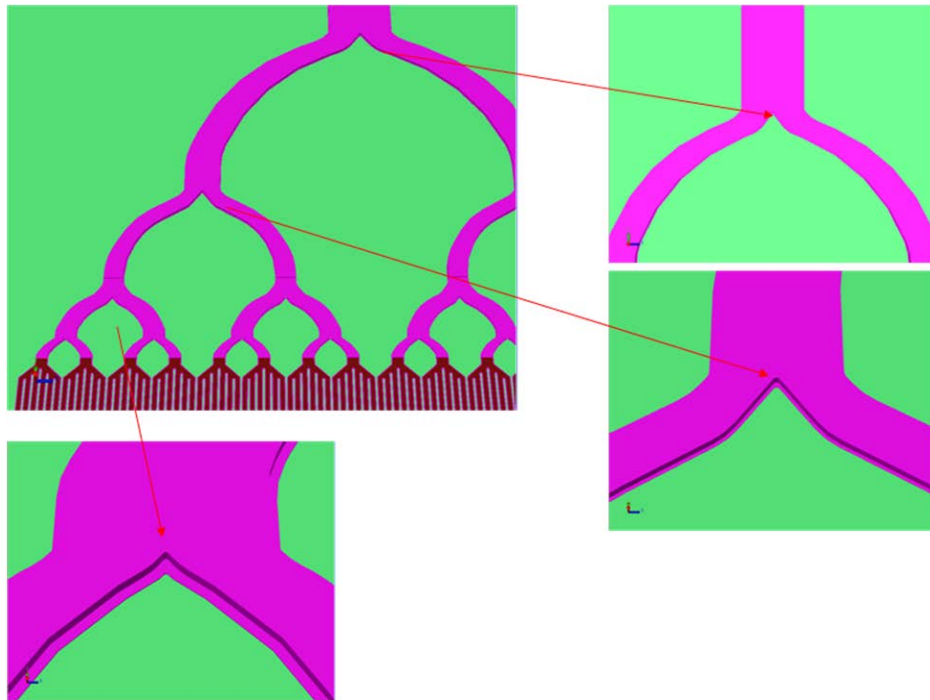


Figure 2-6 All bifurcations in the channel structure were designed with rounded corners to minimize cell trauma.

To extract the highest oxygenation efficiency from the device, it is imperative to ensure that most of the blood channels in the oxygenation area have blood flowing through them. To this effect, the design of the blood channel structure incorporates the following features,

- Channel branching at each stage prior to the oxygenation area is restricted to two branches (bifurcation). The two branches at each junction present identical flow conditions to the blood arriving at the junction, which could help minimize preferential flow in a particular part of the device.
- The blood channel branch arriving at a junction runs normal to the junction for a few microns. This should allow sufficient time for the blood flow vector to present itself to the junction in a normal fashion, thus ensuring that the angle of any subsequent branch does not aid the incoming flow vector which could result in preferential flow in the aiding branch. This is shown in Figure 2-7(a).

- At the blood oxygenation area the bifurcating channel structure is discarded in favor of an inverted 'V' shaped distribution structure which helps in reducing the device dimensions. A bifurcating structure up to the blood oxygenation area if employed would result in the tree structure becoming impractically long and occupying real estate on the wafer during fabrication. The inverted 'V' shaped distribution effectively distributes the flow in each of the six channels, at the same time makes the device compact. This is depicted in Figure 2-7(b).

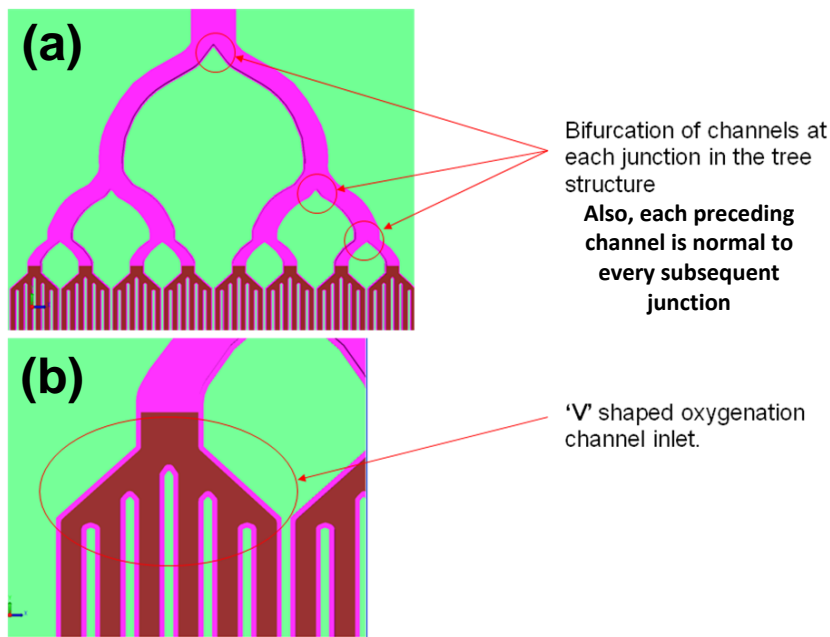


Figure 2-7 (a) Bifurcations at each and every step. (b) Inverted "V" shaped distribution network.

Flow stagnation is a major concern in a blood flow system chiefly because it can cause platelets to accumulate in the stagnation areas forming thrombi which can cause blockage at that point, or emboli which could cause blockage in subsequent channels of a lower dimension. Such blockage would adversely affect the functionality of the device and would reduce oxygenation efficiency. The chief locations of concern in this regard are the junctions in the tree structure, and the design incorporates a filleted 'V' bifurcation at an optimum angle of  $75^{\circ}$  to mitigate this problem. This is depicted in Figure 2-8. Also the junction areas are optimized such that there is sufficient separation between the two microfluidic events of flow branching and



channel height transition to avoid flow vortices, at the same time ensuring that the separation does not cause stagnation areas.

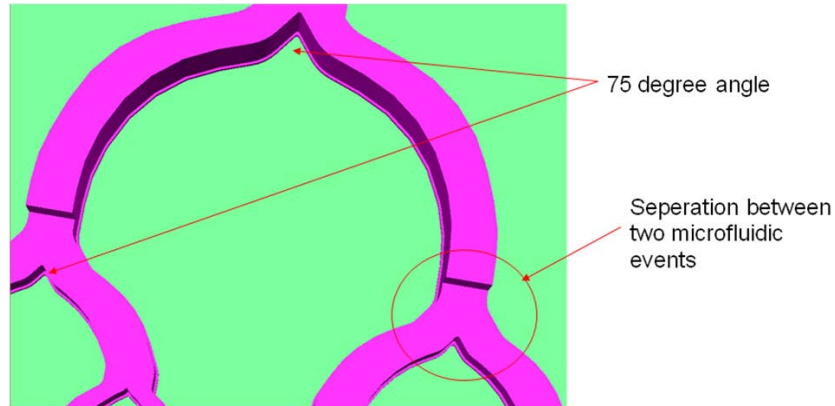


Figure 2-8 75o bifurcation at the inlet channels to reduce flow stagnation.

### 2.2.3 Gas channel and gas exchange interface design

As mentioned before, the gas channel structure is bulk micromachined from a single silicon wafer and incorporates the gas exchange interface i.e. a nanoporous silicon nitride membrane. It consists of a series of individual chambers for gas exchange, each containing a nanoporous membrane. The chambers are arranged in a staggered formation to cover the entire blood channel oxygenation area. A solid model is shown in Figure 2-9.

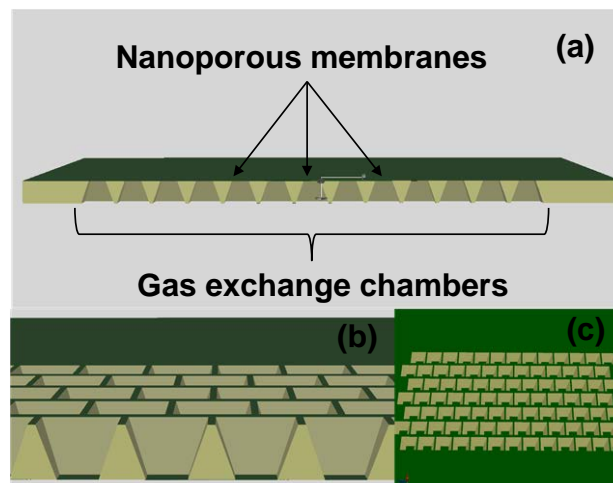


Figure 2-9 (a) Cross section of the gas channel structure showing gas exchange chambers and gas exchange membrane (b) Zoomed in cross section view of gas channel structure (c) Top view of gas channel structure.

## 2.3 Blood channel microstructure fabrication

### 2.3.1 Fabrication of blood channels using surface micromachining

Surface micromachining, as the name implies, consists of microstructure fabrication on the surface of a silicon substrate primarily by means of thick and thin film deposition techniques such as spin coating, evaporation, sputtering and chemical vapor deposition, followed by patterning techniques such as photolithography, wet etching and dry etching.

Fabrication of a microchannel structure serving as the blood transport mechanism was attempted using aforementioned surface micromachining techniques. The technique could be described as comprising of three chief steps. Step 1 consists of fabrication of the desired microstructure on the surface of the silicon wafer using a material that serves as a 'sacrificial layer' i.e. the material only serves as an aid during the fabrication process. In step 2, the 'structural layer', i.e. the material that possesses the desired surface and mechanical properties for the microchannel structure is deposited on top of the sacrificial layer in a conformal fashion. Step 3 involves removal or 'sacrificing' of the sacrificial layer using chemical etching techniques, leaving the structural layer in-place on the surface of the silicon wafer.

The structural material which in this case is silicon nitride ( $\text{Si}_3\text{N}_4$ ), forms the gas exchange membrane as well as the sidewalls of the microchannel structure. The sacrificial material chosen for this particular application was negative photoresist NR4-8000P and negative photoresist NR9-1000P, manufactured by Futurrex Corp. Photoresist is particularly attractive as a sacrificial layer primarily due to ease of deposition, patterning and importantly, removal.

A step by step description of process flow development using the proposed techniques and materials is presented below. Each step in the process flow is elaborated along with experimental results. Characterization of obtained results was carried out using optical and scanning electron microscopy (SEM), and contact profilometry.

A process flow for surface micromachined microchannels is shown in Figure 2-10.

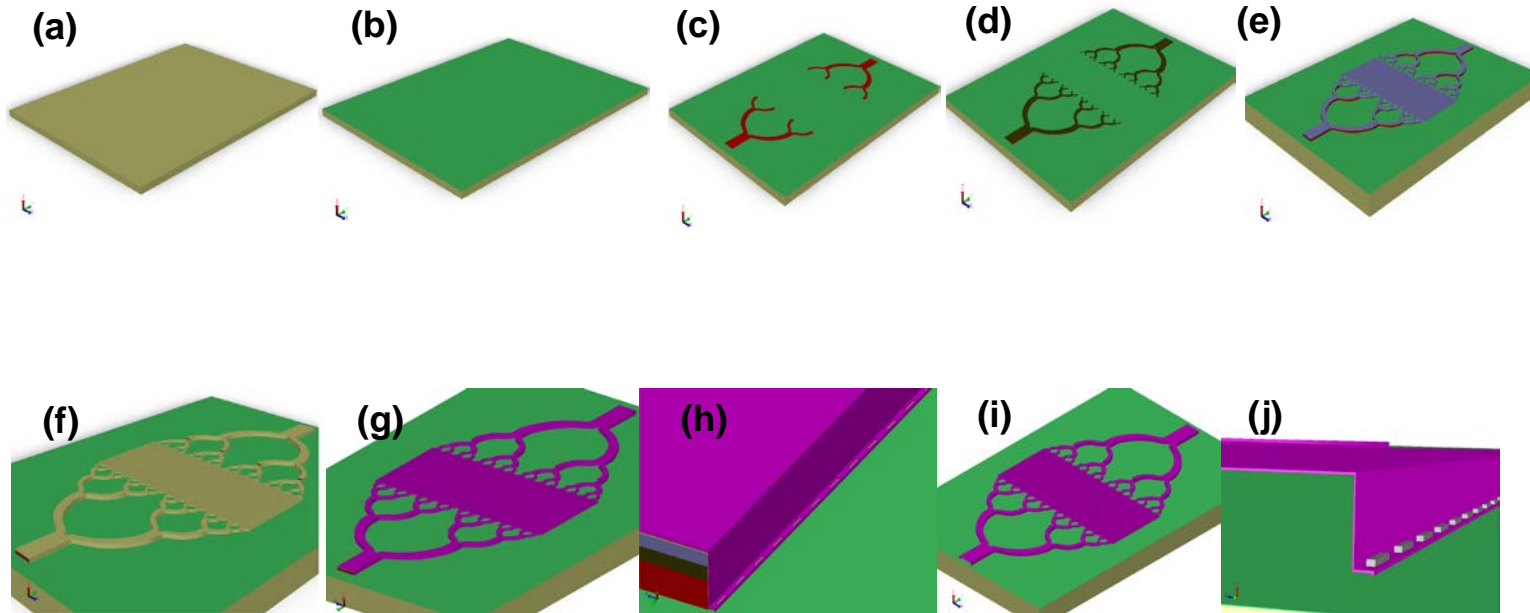


Figure 2-10 Process flow for surface micromachined blood channel structure (a) Si wafer cleaned with standard RCA clean. (b) Sputter deposition of 500 nm  $\text{Si}_3\text{N}_4$  to improve surface hydrophilicity. (c) Photolithographic deposition and patterning of 20  $\mu\text{m}$  thick NR4 8000P photoresist. (d) Photolithographic deposition and patterning of 10  $\mu\text{m}$  thick NR4 8000P photoresist. (e) Photolithographic deposition and patterning of 9  $\mu\text{m}$  thick NR4 8000P photoresist. (f) Photolithographic deposition and patterning of 1  $\mu\text{m}$  thick NR9 1000P photoresist. (g) Sputter deposition of 1  $\mu\text{m}$  thick  $\text{Si}_3\text{N}_4$  as structural layer. (h) Patterning etch holes in the structural layer using RIE. (i) Removal of sacrificial layer. (j) Plugging of etch holes with  $\text{SiO}_2$  to complete fabrication of blood channels.

Step 1: Deposition of base silicon nitride.

A thin layer of silicon nitride forms the base layer of the microchannel structure. Silicon nitride was sputter deposited on the surface of a 3" silicon wafer. An AJA Orion sputter system was used to sputter a 500 nm thin film of silicon nitride for a duration of 300 minutes. RF power was maintained at 150 W with Ar as the primary sputter gas at a pressure of 2.8mT. N2 was added to improve stoichiometry.

Step 2: Deposition of first stage sacrificial layer.

The first sacrificial layer is a 20 $\mu$ m thick film composed of NR4-8000P photoresist. The photoresist is spin coated on the substrate at 1000 RPM for a duration of 40 seconds. The photoresist is baked at 150 C for a duration of 60 seconds and subsequently exposed to UV light using an OAI model 806 aligner. Thereafter it is post baked at 100 C for a duration of 60 seconds to improve adhesion to the substrate and developed using developer RD6. The process results in a sacrificial layer microstructure on the substrate comprising of the first and second bifurcation stages and having a thickness of 20 $\mu$ m (Fig. 2-11).

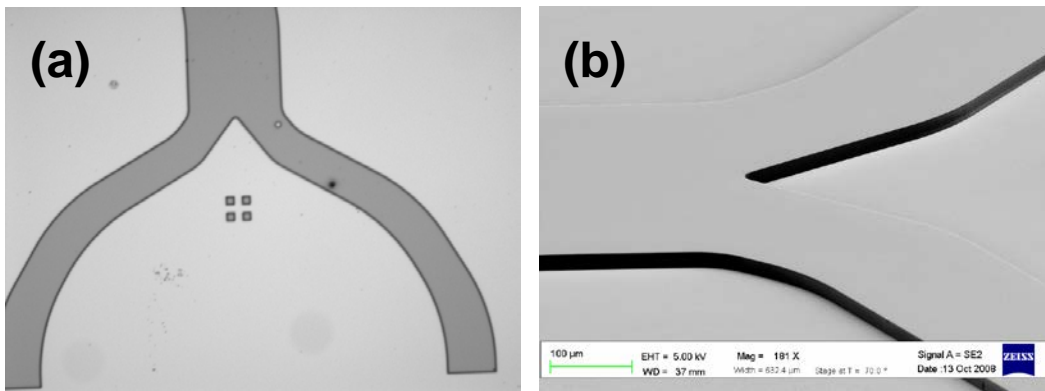


Figure 2-11 (a) Microscope image (b) SEM image of patterned 20  $\mu$ m thick sacrificial layer.

Step 3: Deposition of second stage sacrificial layer

The second stage sacrificial layer consists of a spin coated layer of 10 $\mu$ m thick NR4-8000P photoresist patterned to stack on top of the first sacrificial layer for a total thickness of 30 $\mu$ m and to form the third and the fourth bifurcation stages for a thickness of 10 $\mu$ m. The pre-

bake and post-bake temperatures were kept the same as in case of stage 1. The results are shown in Figure 2-12.

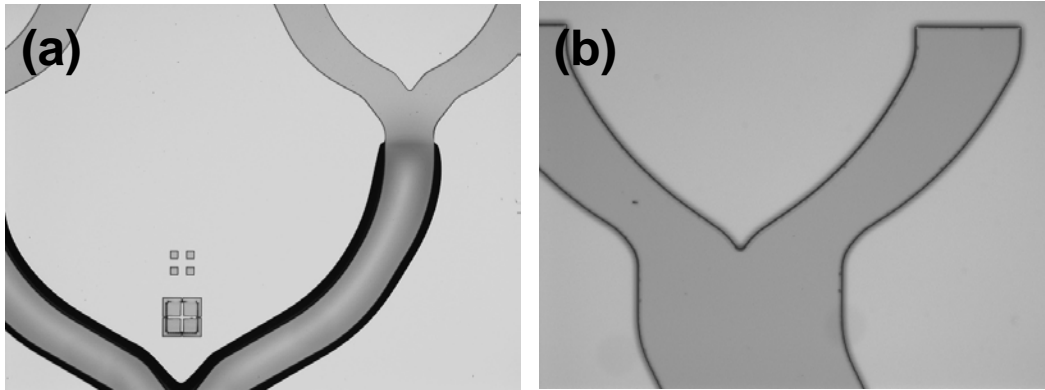


Figure 2-12 (a) Microscope image showing the first and second stage sacrificial layers. (b)

Magnified image of second stage sacrificial layer.

The pictures show that 10 $\mu$ m second stage sacrificial layer has been patterned correctly; however the earlier deposited 20 $\mu$ m sacrificial layer has deformed underneath the recent 10 $\mu$ m layer leading to a net increase in the linewidth.

An investigation into the cause of the deformation of the 20 $\mu$ m layer revealed that the pre-bake and the post bake processes for the subsequent 10 $\mu$ m layer caused the pre-deposited 20 $\mu$ m layer to overheat, resulting in deformation as shown in Figure 2-13(a).

To overcome this problem, the pre - bake temperature was dropped from 150 C to 90 C and the pre-bake time was increased to 120 seconds. The lower temperature did not cause the pre-deposited 20 $\mu$ m photoresist to deform, at the same time allowing an extended time for the solvent in the upper 10 $\mu$ m layer to evaporate. As a result, precise feature dimensions for both , the pre-deposited 20 $\mu$ m layer and the subsequent 10 $\mu$ m layer could be achieved (Fig. 2-13(b), Fig. 2-14).

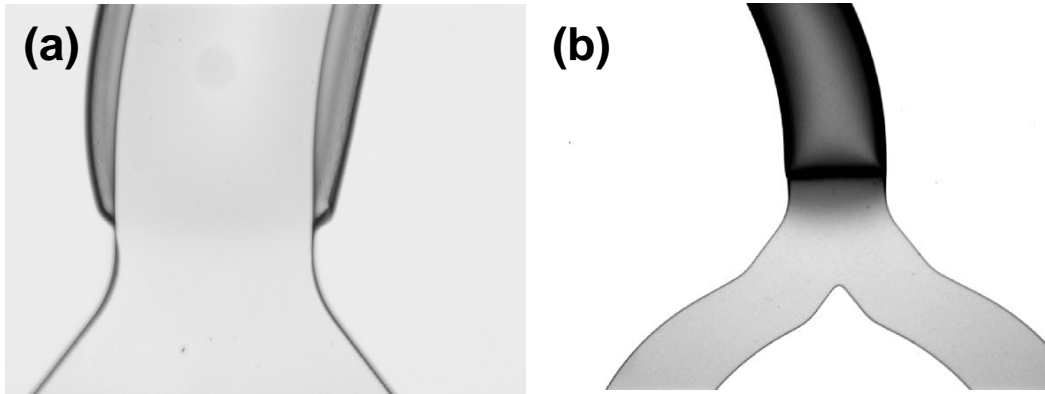


Figure 2-13 Microscope images of sacrificial layer (a) before process temperature correction. (b) after process temperature correction.

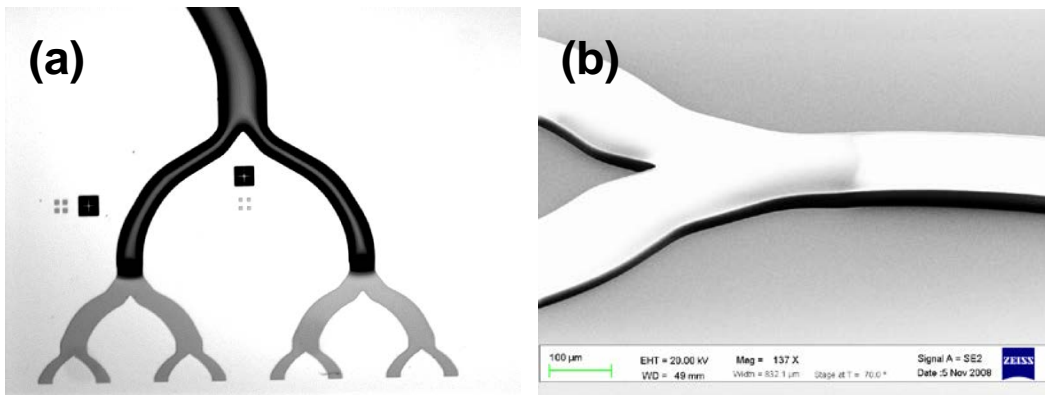


Figure 2-14 (a) Microscope image (b) SEM image of patterned second stage sacrificial layer.

#### Step 4 : Deposition of third stage sacrificial layer.

The third stage sacrificial layer adds the oxygenation area microchannels (50µm width) to the existing structure. The third stage is deposited by spin coating a 5 µm NR4 – 8000P layer on top of the first and the second stages. This step raises the stack thickness of the first stage to 35 µm, the second stage to 15 µm, and the third stage to 5 µm. The pre-bake temperature is 90 C for 2 minutes. This is sufficient to drive out solvent from the 5 µm top layer without damaging the lower layers. The post bake temperature is 100 C for 10 seconds. The results of the third stage deposition are shown in figure 2-15.

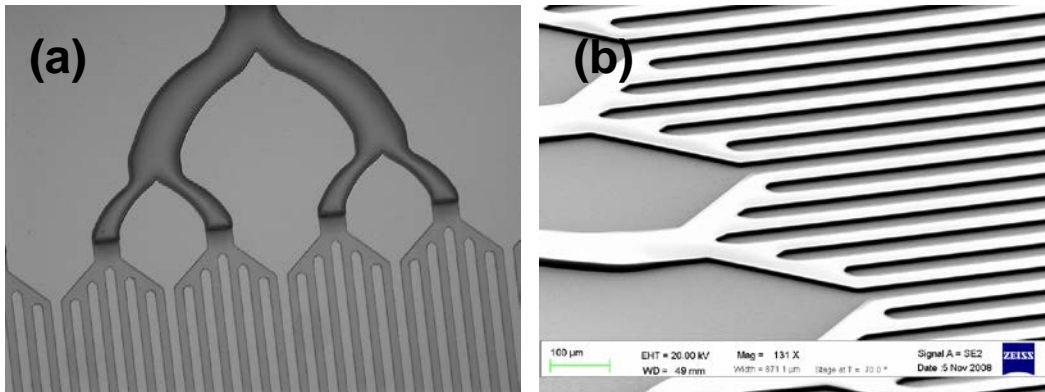


Figure 2-15 (a) Microscope image (b) SEM image of patterned third stage sacrificial layer.

Step 5: Deposition of 5  $\mu\text{m}$  flange layer.

The sacrificial layer forming the 1  $\mu\text{m}$  thick flange on both sides of each microchannel was spin coated on top of the existing structure at 3000 RPM for duration of 40 seconds. The photoresist used for this purpose was the NR71 - 6000P negative resist. The pre bake temperature and time were once again adjusted such that the previous stages were not damaged in any manner. The 5  $\mu\text{m}$  layer was patterned such that it exceeded the entire existing feature dimension by 15  $\mu\text{m}$  on each side of each channel. As a result, in addition to a 5  $\mu\text{m}$  thick, 15  $\mu\text{m}$  wide flange, the thickness of each previously deposited stack was increased by 5  $\mu\text{m}$  such that, the first stage thickness was 40 $\mu\text{m}$ , the second stage thickness was 20 $\mu\text{m}$  and the third stage thickness was 10  $\mu\text{m}$ . The fully fabricated four stage sacrificial layer is shown in Figure 2-16.

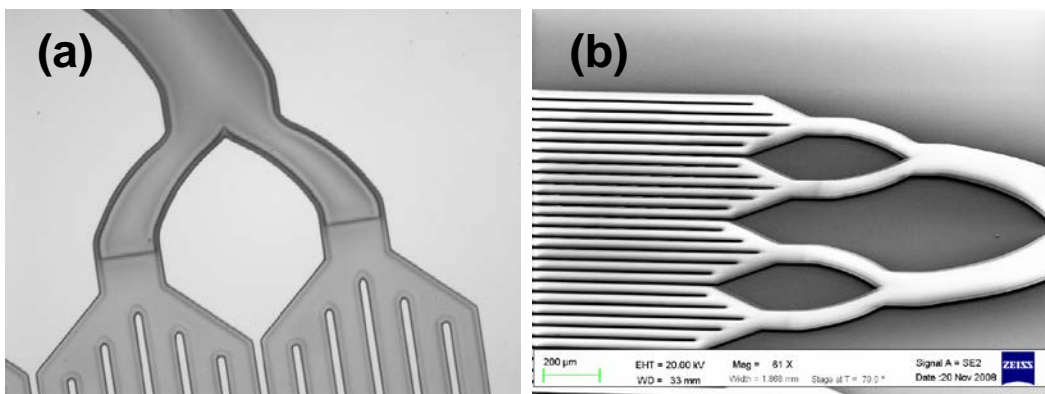


Figure 2-16 (a) Microscope image (b) SEM image of patterned flange sacrificial layer.

Step 6: Deposition of the membrane silicon nitride (structural layer).

The structural layer is a 1  $\mu\text{m}$  silicon nitride ( $\text{Si}_3\text{N}_4$ ) that forms the gas exchange membrane as well as the sidewalls of the microchannel structure. Silicon nitride was sputter deposited on the surface of a 3" silicon wafer. An AJA Orion sputter system was used to sputter a 1  $\mu\text{m}$  thin film of silicon nitride for a duration of 10 hours. RF power was maintained at 150 W with Ar as the primary sputter gas at a pressure of 2.8mT.  $\text{N}_2$  was added to improve stoichiometry. Figure 2-17 shows the cross-section SEM micrographs of the inlet microchannel. A thin layer of silicon nitride is visible over the bulk of the photoresist sacrificial layer.

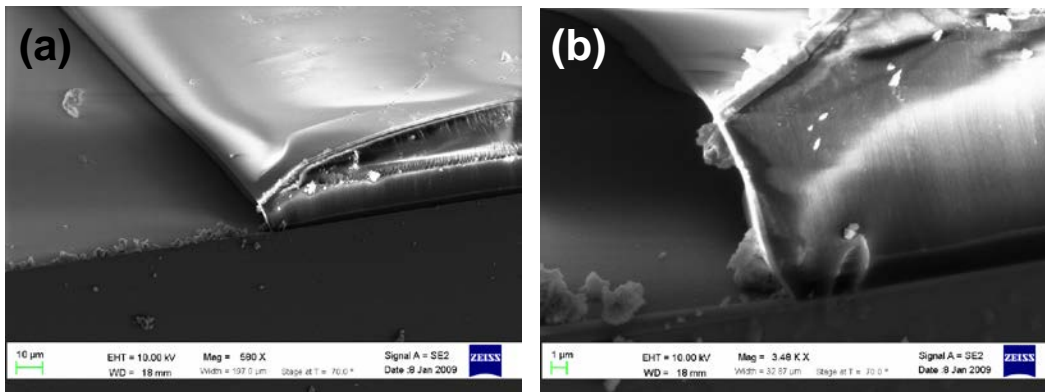


Figure 2-17 a) SEM image of cross section at the blood channel inlet. (b) Higher magnification image showing the structural and sacrificial layers.

Step 7: Fabrication of etch holes over the flanges.

Since the sacrificial photoresist is entirely covered by silicon nitride, etch holes need to be cut into the nitride layer in order to facilitate easy removal of the sacrificial layer. The etch holes are fabricated over the flanges built for this special purpose. A dry etch recipe was developed for etching silicon nitride using the Technics Series 800 Micro RIE tool. Negative photoresist NR9 3000P (3  $\mu\text{m}$ ) was used as the masking material. A steady etch rate of 30 nm/min with good etch uniformity was obtained at a chamber pressure of 130 mT with 100 W RF power.  $\text{CF}_4$  was used as the etchant gas at a flow rate of 10 sccm. The results after the etch process are shown in Figure 2-18.



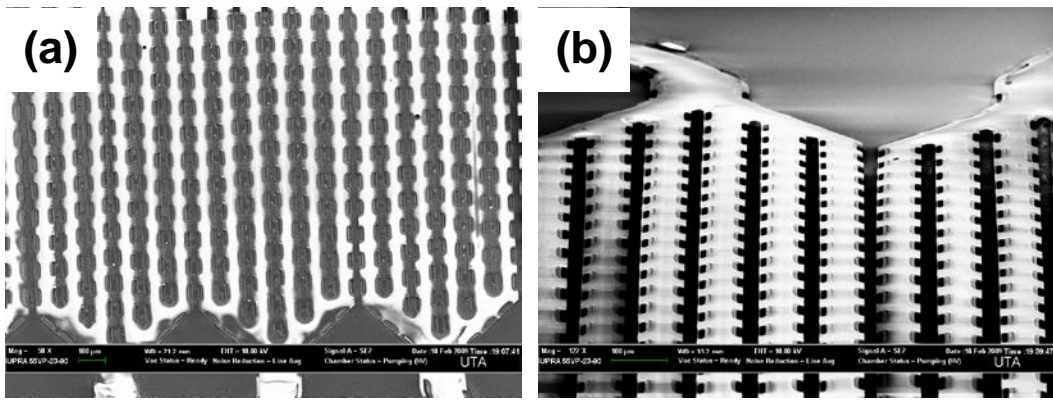


Figure 2-18 (a) SEM image of blood channels with patterned etch holes (b) SEM image side view.

Step 8: Removal of the sacrificial layer.

Removal of the sacrificial photoresist was attempted by placing the fabricated samples in an acetone bath for a period of 6 hours. The photoresist was removed by the acetone; however the silicon nitride channel structure lifted off the wafer along with the photoresist (Fig. 2-19). An investigation into the possible cause of this occurrence revealed that the sidewalls of the silicon nitride structure were very thin and hence not robust enough to support the membrane after removal of the photoresist. Therefore at that point, the limitations of the surface micromachining technique became evident. Even with good step coverage, the sidewalls were not robust enough to support the membrane after sacrificial layer removal. A different fabrication approach was therefore deemed necessary in order to fabricate microchannels with robust sidewalls capable of supporting the membrane structure after release. Bulk micromachining was identified as a possible solution to the problem, and a new process was developed based on this approach.

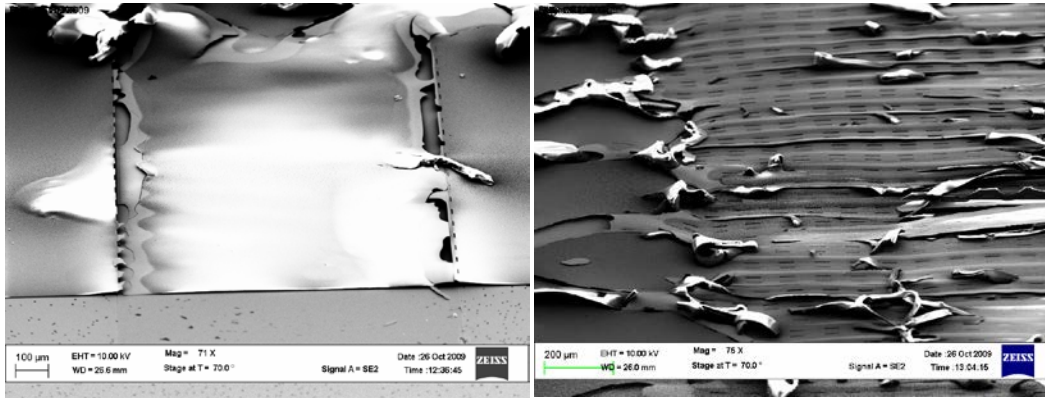


Figure 2-19 SEM images of collapsed membranes after sacrificial layer removal.

### 2.3.2 Fabrication of blood channel microstructures using bulk micromachining

Bulk micromachining involves microstructure fabrication by means of patterning and etching the silicon substrate referred to as the 'bulk'. Generally, microstructures fabricated using bulk micromachining utilize the substrate as a structural material as opposed to surface micromachining wherein the chief role of the bulk is to provide mechanical support during fabrication. Thin film deposition techniques are used in bulk micromachining mainly to alter the surface properties or as auxiliary structural layers, however the substrate plays a dominant role in device operation.

The process flow for microchannel fabrication using bulk micromachining techniques differs considerably from surface micromachining. In this approach, the microchannel structures are fabricated into the substrate as opposed to fabrication on the top of the substrate as in the case of surface micromachining. This approach results in microchannels with robust sidewalls capable of surviving the fabrication process. A major part of the supporting microchannel structure is fabricated from bulk silicon and as such is benefited from the inherent mechanical strength afforded by the bulk.

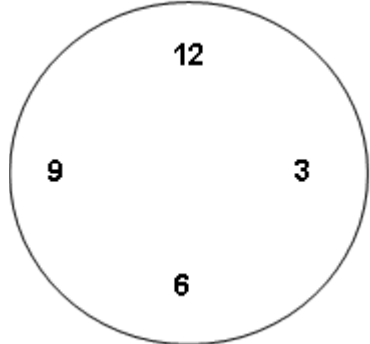
As described above, a major part of the bulk micromachining comprises of patterning and etching the silicon substrate. Microchannels were etched into the silicon substrate using a potassium hydroxide (KOH) based wet etch process. Low pressure chemical vapor deposited (LPCVD) Si<sub>3</sub>N<sub>4</sub> was used as a hard mask for the KOH etch. The silicon nitride was patterned

using conventional photolithography and RIE. The wet etch process was initially characterized for etch rate and etch uniformity.

Table 2-1 KOH wet etch process parameters

Etchant composition	30 % KOH solution in DI water at 80°C
Hard mask	LPCVD Si <sub>3</sub> N <sub>4</sub> (1 μm)
Silicon etch rate	1.76 μm/min
Hard mask etch rate.	negligible

Table 2-2 Etch rate and etch uniformity over a 3" Si wafer using a KOH wet etch process

Wafer sampling position	Feature size	1000 μm	525μm	275 μm
	Position	Etched depth		
	12	18.60	18.60	18.60
	6	18.00	18.10	18.10
	9	18.50	18.50	18.50
	3	18.30	18.30	18.30
	Average	18.35	18.38	18.38
	%SD	1.44	1.21	1.21

Step 1: First stage 20 μm etch.

A 20 μm deep trench was etched into the silicon substrate. The trench consisted of the first and second bifurcation stages (Fig. 2-20).

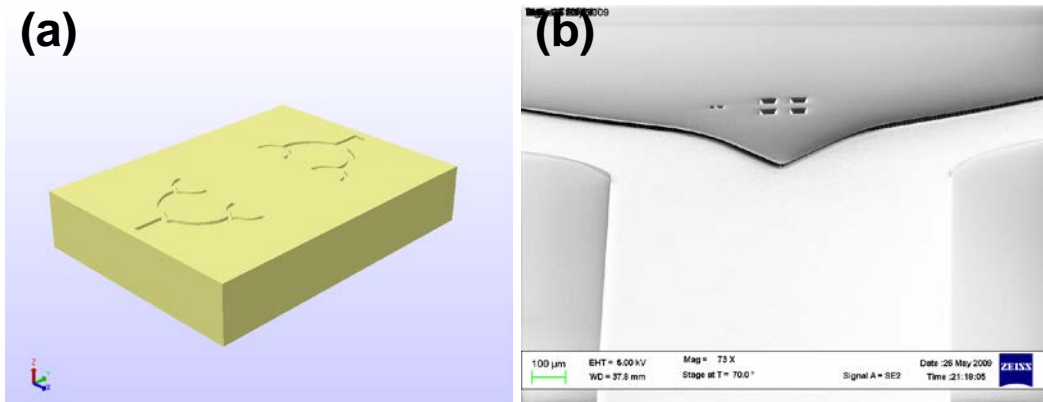


Figure 2-20 (a) CoventorWare solid model (b) SEM of bulk micromachined first stage microchannels.

Step 2: Second stage 10  $\mu\text{m}$  etch.

Step 2 involves fabrication of the third and fourth bifurcation stages. Trenches consisting of the third and fourth bifurcation stages were etched into silicon to a depth of 10  $\mu\text{m}$  with the same etch equipment and process as described in step 1. Control of the etch depth was achieved by etching up to a calculated time based on the etch rate (Fig. 2-21).

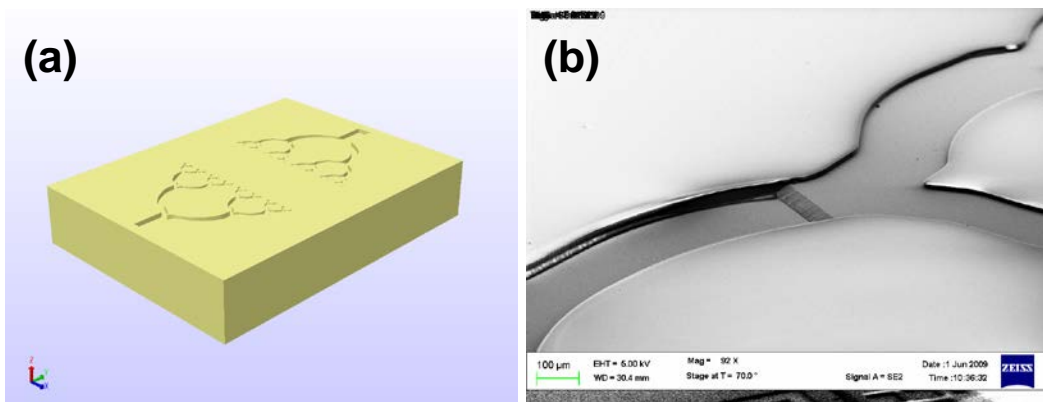


Figure 2-21 (a) CoventorWare solid model (b) SEM of bulk micromachined second stage microchannels.

Step 3 : Fabrication of third stage – 10  $\mu\text{m}$  oxygenation area microchannels

10  $\mu\text{m}$  deep oxygenation area microchannels are fabricated using the KOH etch process described above and the etch depth controlled by timing the etch based on the previously observed etch rate (Fig. 2-22)

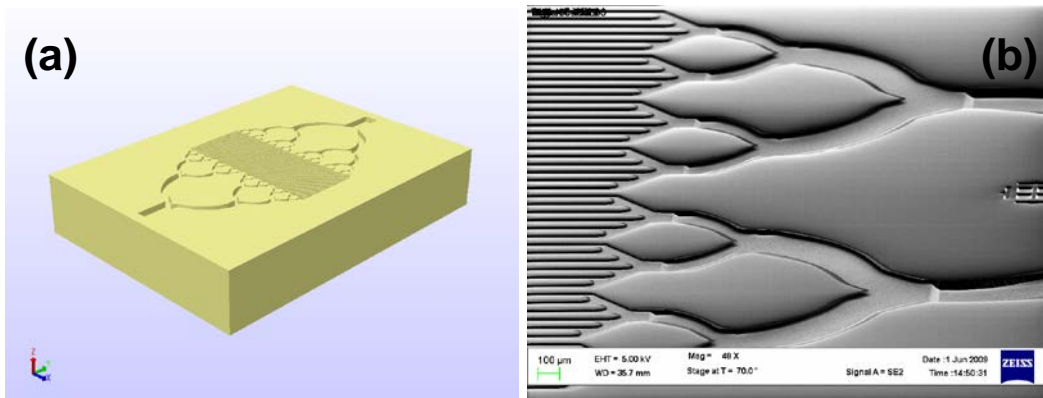


Figure 2-22 (a) CoventorWare solid model (b) SEM of bulk micromachined third stage oxygenation area microchannels.

## 2.4 Fabrication of gas exchange microstructure with integrated nanoporous silicon nitride membrane

### 2.4.1 Silicon nitride growth and backside patterning.

The process started with the deposition of a thin silicon nitride ( $\text{Si}_3\text{N}_4$ ) layer. The  $\text{Si}_3\text{N}_4$  was deposited using Low-Pressure Chemical Vapor Deposition (LPCVD) on both sides of a 3" (100) silicon wafer at a temperature of 835° C and pressure of 250 mTorr. Dichlorosilane (100 sccm) and ammonia (20 sccm) were used as the process gases, resulting in growth of a  $1 \pm 0.05$   $\mu\text{m}$  thick low-stress  $\text{Si}_3\text{N}_4$  at a rate of 200 nm/hr. Next, NR9 3000P photoresist from Futurrex Inc was spin-coated on the backside to achieve a thickness of 3  $\mu\text{m}$ , followed by a pre-bake and UV- exposure to define the membrane windows. After a post -exposure, the resist was developed using RD6 developer. The pattern transferred from the photomask to the photoresist consisted of arrays of square shaped features having dimensions  $250 \times 250$   $\mu\text{m}^2$ ;  $350 \times 350$   $\mu\text{m}^2$  and  $450 \times 450$   $\mu\text{m}^2$ . These patterns were transferred from the photoresist to the underlying silicon nitride by means of a fluorine-based reactive ion etch (RIE) process, using tetrafluoromethane ( $\text{CF}_4$ ) at 130 mTorr pressure, and 100 W RIE power. An etch rate of 30 nm/min was obtained.

### 2.4.2 Nanoimprint lithography and pattern reversal process

Nanoimprinting step started with spin-coating a 180 nm-thick NXR 1025 thermal imprint resist from Nanonex Inc on the front-side silicon nitride. The wafer was then baked at 150 C for

3 min on a hotplate to drive out all the solvent. The silicon nanoimprint mold was placed in contact with the nanoimprint resist and both wafers were loaded into a Nanonex NXB 200 nanoimprinter. The wafers were heated to a temperature of 130° C and were compressed at an initial pressure of 120 psi. After holding the pressure constant for a few seconds, it was increased to 200 psi and thermal resist was imprinted for 30 seconds. Thereafter the temperature was slowly reduced to room temperature, allowing the resist to solidify. The wafers were subsequently separated without much difficulty owing to the anti-adhesion layer coated on the silicon mold. The resultant features are schematically illustrated in Fig. 2-23(a). SEM photo is shown in Fig. 2-24(a).

The imprinting process resulted in an intentional residual resist with a thickness of 60-70 nm due to the difference in the thermal imprint resist thickness and the features on the mold. This residual resist was etched in a reactive ion etcher in Ar/O<sub>2</sub> plasma, at a pressure of 11 mTorr and with RF power of 40 W at 13.56 MHz to realize an anisotropic etch profile. Figs. 2-23(b) and 2-24(b) depict the structures at the end of this stage.

Next, an 85 nm chromium layer was deposited on the thermal imprint resist in an electron beam evaporator, at a chamber pressure of 2.0 x10<sup>-8</sup> mTorr (Fig. 2-23(c)). The deposition rate was maintained at a constant 0.15 nm/sec rate by means of controlling the electron beam current. This serves as an intermediary layer to transfer the pattern from the thermal resist to the aluminum oxide (Al<sub>2</sub>O<sub>3</sub>) mask layer. The Cr film was then patterned by means of a lift-off process in acetone bath, resulting in Cr pillars of 210 nm in diameter and 85 nm in height as shown in Figs. 2-23(d) and 2-24(c). After that, a thin film of Al<sub>2</sub>O<sub>3</sub> was sputtered on top of the chromium pillars in an ultra-high vacuum RF magnetron sputter deposition system. The process pressure was set to 5.0 mTorr and the deposition was carried out at a RF power of 150.0 W. A total of 55 nm of Al<sub>2</sub>O<sub>3</sub> was deposited at a deposition rate of 1.04 nm/min (Fig. 2-23(e)). Next, the Al<sub>2</sub>O<sub>3</sub> was patterned by means of a second lift-off process, by placing the wafer in a CR 1020 Cr etchant bath. The process resulted in an array of circular patterns in the

aluminum oxide layer having a diameter of 250 nm (Figs. 2-23(f) and 2-24(d)). The aluminum oxide layer was thus patterned over the entire area of the 3" wafer except for 2 mm wide handling space along the wafer periphery.

#### *2.4.3 Silicon nitride membrane and nanopore fabrication.*

The wafer was then subjected to a through-the-wafer potassium hydroxide (KOH) anisotropic wet etch process. The nanostructured aluminum oxide on the front side was protected from the KOH by clamping the wafer in a fixture specifically designed for the purpose. A steady etch rate of 1.2  $\mu\text{m}/\text{min}$  was obtained at a temperature of 85.0° C. The LPCVD  $\text{Si}_3\text{N}_4$  was used as the etch stop. Suspended silicon nitride membranes having dimensions 250x250  $\mu\text{m}^2$ , 350x350  $\mu\text{m}^2$  and 450x450  $\mu\text{m}^2$  were thus obtained (Figs. 2-23(g) and 2-24(f)).

The patterned  $\text{Al}_2\text{O}_3$  layer was used as the etch mask for the subsequent  $\text{Si}_3\text{N}_4$  membrane etch. Using this mask, the 1- $\mu\text{m}$  thick  $\text{Si}_3\text{N}_4$  membrane was patterned in fluorine-based RIE process with an inductively coupled plasma (ICP) generator at a process pressure of 11 mTorr. The ICP power was set to 4500 W and the wafer chuck was supplied with RF power of 35 W. The process gases used were trifluoromethane ( $\text{CHF}_3$ ) and helium (He). The etch process yielded a vertical etch rate of 63.8 nm/min for the LPCVD silicon nitride with sufficient anisotropy. 400 nm wide, 1 $\mu\text{m}$  deep pores were obtained as a result of this etch process, as depicted in Fig. 2-23(h).

The complete fabrication process is schematically illustrated in Figure 2-24. The SEM photos of nanoporous membrane reveal excellent periodicity and uniformity. From the SEM photos of the nanopores on the front-side (Fig. 2-24(e)) and the back-side (Fig. 2-24(g)), it is clear the pores are all the way through the membrane.

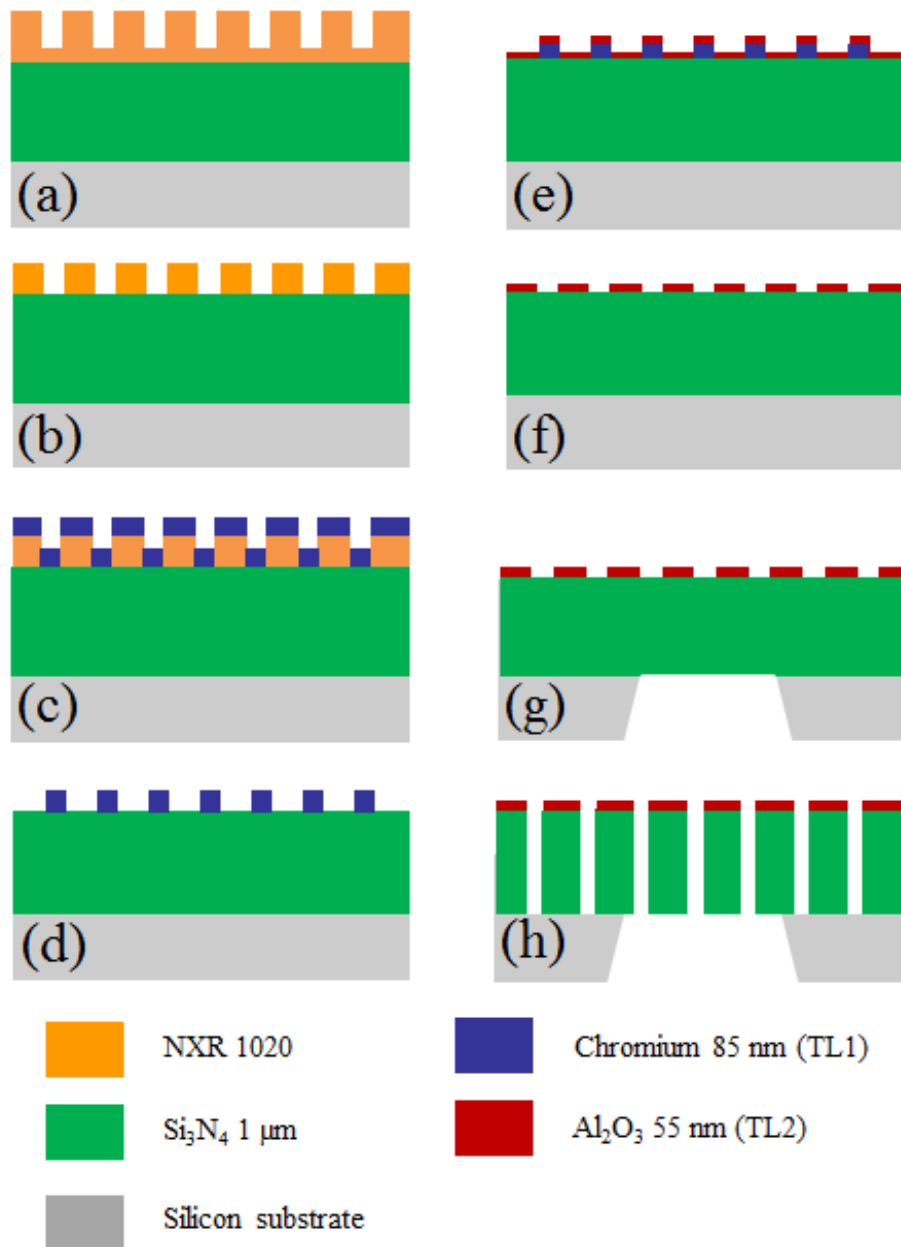


Figure 2-23 Schematic illustration of the nanoporous membrane fabrication process. (a) NXR1020 spin coating and nanoimprinting, (b) Residual resist ashing, (c) Chromium evaporation, (d) Chromium lift-off, (e) Aluminum oxide deposition, (f) Aluminum oxide lift-off, (g) Backside KOH etch, (h) Reactive ion etch to realize nanopores.



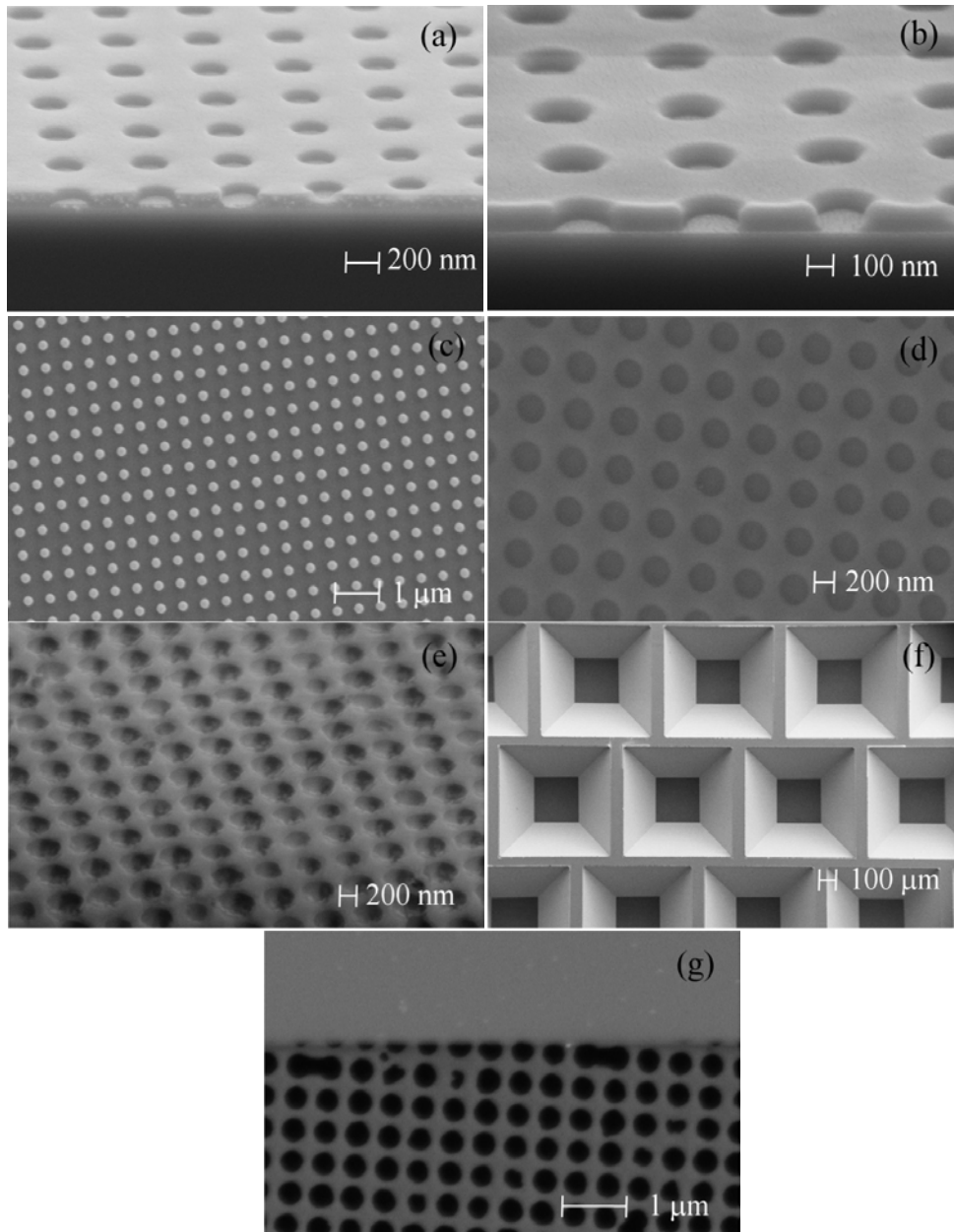


Figure 2-24 SEM images at different stages of the fabrication process. (a) NXR 1025 after nanoimprinting, (b) after residual resist ashing, (c) chromium lift-off, (d) aluminum oxide lift-off, (e) suspended nanoporous membrane from front side, zoomed-in view, (f) nanoporous membranes from backside, (g) zoomed-in image of suspended nanoporous membrane from the backside. The solid gray strip at the top is silicon.

## 2.5 A discussion on the development of the two stage lift – off process and the anisotropic reactive ion etch process.

The two stage lift-off pattern reversal technique described here was developed for two chief reasons. Firstly, the nanoimprint resist did not possess sufficient selectivity over  $\text{Al}_2\text{O}_3$  in a fluorine based RIE process. Attempts to etch  $\text{Al}_2\text{O}_3$  in a wet etch process with dilute hydrofluoric acid resulted in severe undercutting of the nanoimprint resist causing it to delaminate from the  $\text{Al}_2\text{O}_3$  layer during the etch. Therefore, it was concluded that a direct etch process would not be a feasible option for patterning of the  $\text{Al}_2\text{O}_3$  layer. Indirect patterning using a conventional lift-off process would mean that the polarity of the silicon mold would have to be reversed, effectively necessitating fabrication of a new mold with holes instead of pillars. Such a mold, however, is harder to use due to difficulties in cleaning it, and would most likely to have a shorter life-time than a pillar mold because it would be more challenging to separate it from the resist after the nano-imprint process

Pattern reversal techniques for photolithography have been well established. These techniques were developed to provide an extra degree of flexibility to the process design engineer. By varying the photoresist processing parameters, the same photomask can be used for direct and reverse pattern transfer. The NIL pattern reversal technique accomplishes the same outcome by reversing the polarity of the pattern on the nanoimprint mold with the help of an intermediate etch mask deposited on the substrate. The pattern reversal is accomplished by means of two consecutive liftoff pattern transfer processes. This is illustrated in Figure 2-23. The patterned nanoimprint resist is coated with a thin film of template layer 1 (TL1). The first lift-off process is a conventional lift-off process that results in a mirror image of the mold pattern on the template layer 1. Next, the patterned template layer 1 is coated with a thin film of template layer 2 (TL2). The sample is then placed in an etchant to remove TL1. This results in patterning of TL2 by means of a lift-off. If this method were to be analogized to a conventional lift-off process, TL1 would be the “lift-off resist” and the etchant would be the “resist remover”.

The selection of TL2 is primarily governed by the requirements imposed by its function in the device or the fabrication process. In the present case, high etch selectivity over silicon nitride in a fluorine based RIE process necessitated the selection of aluminum oxide as TL2. The two-stage lift-off process, however, imposes another important requirement on the selection of TL2, mainly that it should have sufficiently high etch resistance to the chemical etchant used to remove TL1. A non-trivial etch rate for TL2 in the etchant can cause pattern distortion, as the removal process for TL1 is isotropic. Thus, TL1 has to be chosen such that it readily dissolves in a wet etchant that has a very low etch rate for TL2. In the present case,  $\text{Al}_2\text{O}_3$  exhibited a negligible etch rate in CR 1020, the etchant used for removing chromium (etch rate 0.2 nm/sec).

The thickness of TL1 could also be influenced by its role in the device/process. In addition, the ratio of thicknesses of TL2 to TL1 has been found to influence pattern transfer accuracy. As is observed in conventional lift-off processes, a high TL2 to TL1 thickness ratio leads to a larger error in the pattern dimension (Fig. 2-25).

This error could possibly stem from a conformal deposition of sputtered aluminum oxide on chromium. For a successful lift-off, any deposition of aluminum oxide on the sidewalls of the chromium pillar would first need to be removed for the etchant to access and dissolve chromium. Therefore, the time required for lift-off would be greater, considering that  $\text{Al}_2\text{O}_3$  has a very slow etch rate in CR1020. It was observed that for  $\text{Al}_2\text{O}_3$  to Cr thickness ratios greater than 0.4, the time required to dissolve Cr coated with  $\text{Al}_2\text{O}_3$  was considerably more compared to that necessary to dissolve bare Cr of the same thickness. Moreover, ultrasonic agitation was necessary to achieve lift-off uniformity over the entire wafer. The greater time spent by the wafer in the etchant could cause pattern distortion of the  $\text{Al}_2\text{O}_3$ . In general, the ideal method for deposition of TL2 would be one that is non-conformal, such as thermal or electron beam evaporation. In addition, if a lower thickness ratio of TL2 to TL1 can be tolerated, the resulting thinner sidewall would be easier to remove thus minimizing the error.

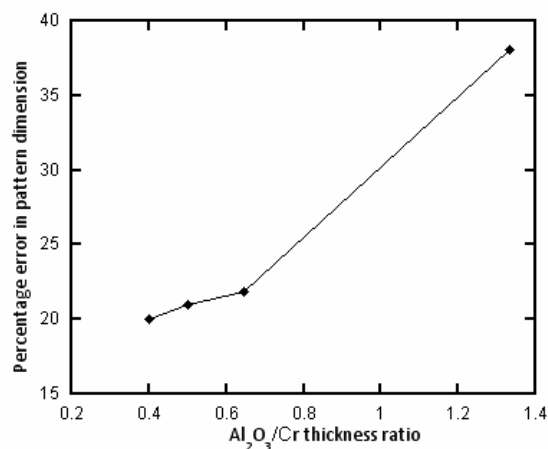


Figure 2-25 Percentage error in nanopore dimension as a function of aluminum oxide to chromium thickness ratio.

The sidewall profile of the Cr pillars was observed in a SEM by tilting the sample to 70°. The chromium pillars display a “mushroom” like structure as seen in Figure 2-26(a). The top half of the pillar is noticeably broader than the bottom. This is similar to a negative slope profile or an undercut profile typically observed in the sidewalls of conventional lift-off resists that are optimized for lift-off based patterning. The mushroom structure causes a shadow effect during the deposition of Al<sub>2</sub>O<sub>3</sub>, thus minimizing the formation of an Al<sub>2</sub>O<sub>3</sub> layer on the Cr pillar sidewall. The etchant can then access and remove the Cr in minimal time resulting in more accurate pattern transfer.

The negative sidewall slope in the chromium pillar is possibly an artifact of the Ar/O<sub>2</sub> etching process used for removing the residual resist after nanoimprinting. As seen in Figure 2-26(b), the nanopore in the imprinted resist has a positive sidewall slope after residual resist etching. The positive sidewall slope in the imprint resist translates to a negative sidewall slope in the chromium pillar, resulting in the characteristic mushroom shape. It was observed that a ratio of 0.3 for Al<sub>2</sub>O<sub>3</sub>/Cr thickness resulted in negligible distortion of the pattern dimensions. In addition, the time required for lift-off was significantly shorter and no ultrasonic agitation was necessary. The results point to the conclusion that pattern distortion in TL2 in the two-stage lift-

off process can be limited by engineering of the sidewall profile of TL1 to obtain a negative sidewall slope.

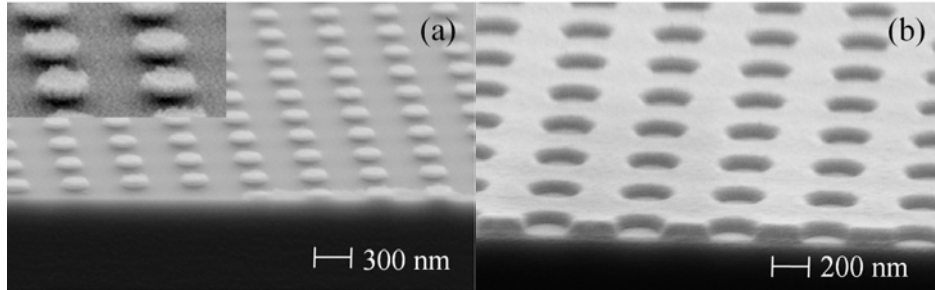


Figure 2-26 (a) Chromium lift-off stage showing “mushroom” shaped pillars. Inset: Magnified image (b) Nanoimprint resist after residual resist ashing showing positive sidewall profile.

Pattern transfer from the aluminum oxide to silicon nitride was achieved using a specially formulated RIE process. Initially,  $CF_4$  was chosen as the primary etch gas and the effect of RF power on the etch profile was observed.

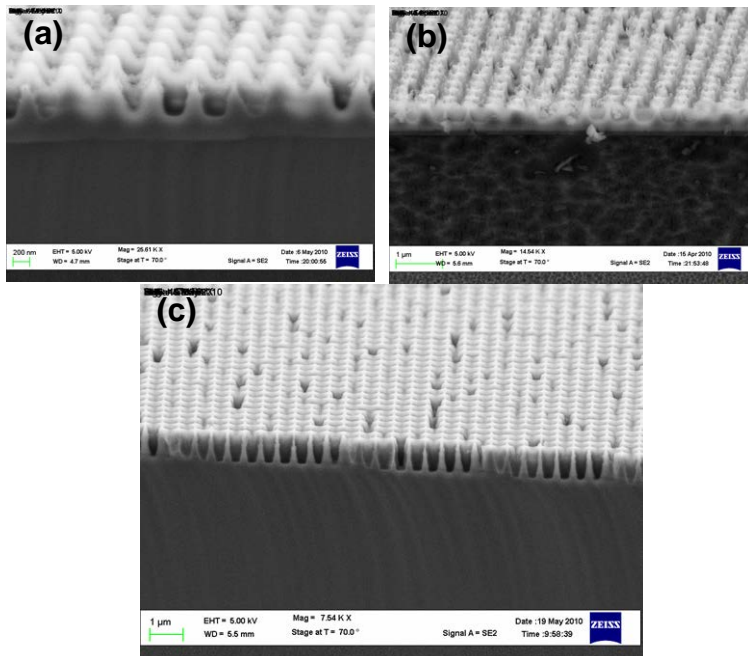


Figure 2-27 Effect of bottom electrode RF power on the nanopore etch profile. (a) 150 W RF power (b) 100 W RF power (c) 35 W RF power. A progressive improvement in etch selectivity is observed, with reduction in RF power.

It was observed that at higher RF power, the directionality was adequate, but the selectivity suffered drastically (Fig. 2-27). On the other hand at lower RF powers, even though excellent directionality was observed, the  $\text{Si}_3\text{N}_4$  exhibited a low etch rate; thus lowering the net selectivity over alumina. Another observation was the occurrence of “rounded” sidewalls at the nanopore bottom. Since the etch gas flow rate was kept low to minimize lateral etching, transport of volatile etch products suffered causing the etch rates at the bottom of the nanopores to drop, resulting in the rounded bottom profile.

Addition of helium facilitated efficient transport of the reactant species and removal of volatile etch products. A low chamber process pressure further improved the directionality, while independent control of the plasma density with the inductively coupled plasma generator improved selectivity (Fig. 2-28).

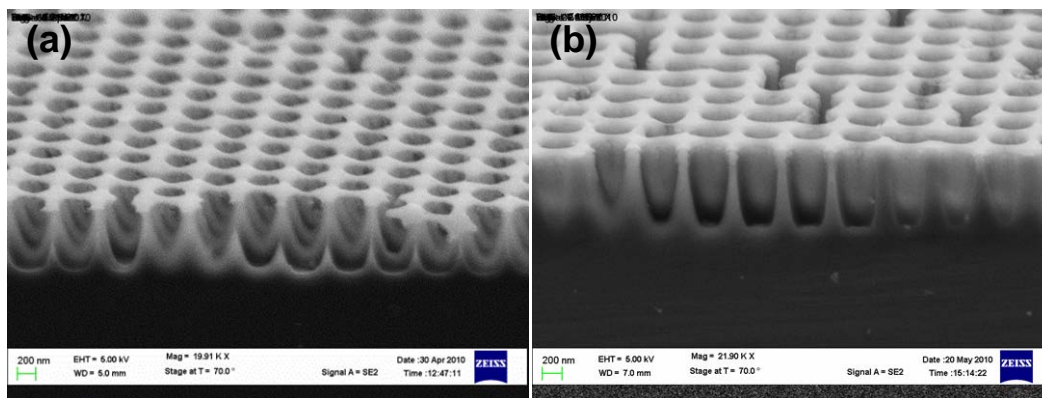


Figure 2-28 Effect of process pressure on the nanopore etch profile (a) 50 mTorr (b) 11 mTorr.

A significant improvement in directionality is observed with reduction in the process pressure due to an increase in the mean free path.

Trifluoromethane ( $\text{CHF}_3$ ) was then selected as the primary etchant gas providing a source of fluorine radicals, while helium was added for dilution and to improve anisotropy (Fig. 2-29). It was assumed that usage of a fluorine deficient fluorocarbon such as trifluoromethane as opposed to tetrafluoromethane ( $\text{CF}_4$ ) would limit the availability of fluorine radicals per unit volume of chamber atmosphere thus lowering the lateral etch rate and improving anisotropy [63].

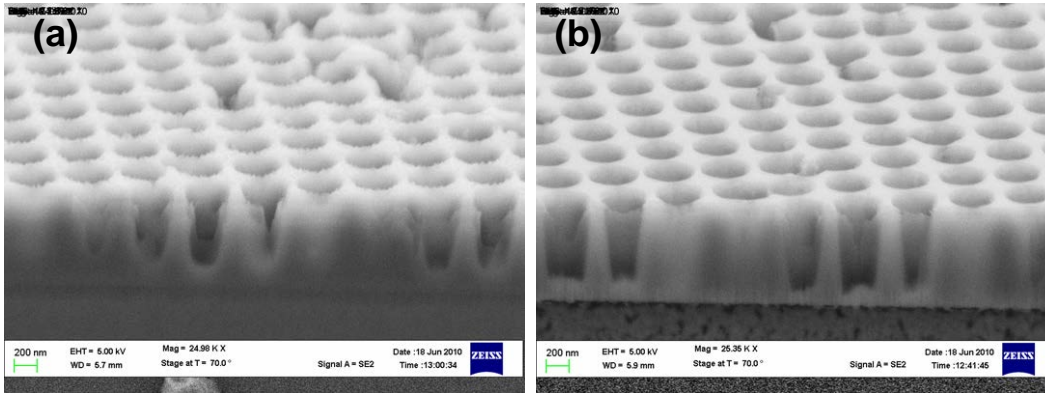


Figure 2-29 Effect of process gas chemistry on nanopore etch profile (a)CF<sub>4</sub>/O<sub>2</sub> (b) CHF<sub>3</sub>. An

improvement in the sidewall as well as the bottom profile is observed along with an improvement in directionality and selectivity.

As shown in Figure 2-30, near vertical sidewalls for the nanopores were obtained (sidewall angle 89.4°). The vertical to lateral etch rate ratio was 12.76 resulting in cylindrical pores with pore diameter of 400 nm and separation of 100 nm. The etch selectivity of Si<sub>3</sub>N<sub>4</sub> to Al<sub>2</sub>O<sub>3</sub> was found to be 24.75: 1. To the best of our knowledge, the highest reported selectivity for silicon dioxide over silicon nitride is 30:1 in plasma etch process [64]. Our results demonstrate the practicality of Al<sub>2</sub>O<sub>3</sub> as an alternative mask for Si<sub>3</sub>N<sub>4</sub> in a fluorine based RIE process.

Post- fabrication, the nanoporous membranes were examined for cracks and point defects. Fig 2-31(a) shows membrane placement and sampling locations on a 3" diameter wafer.

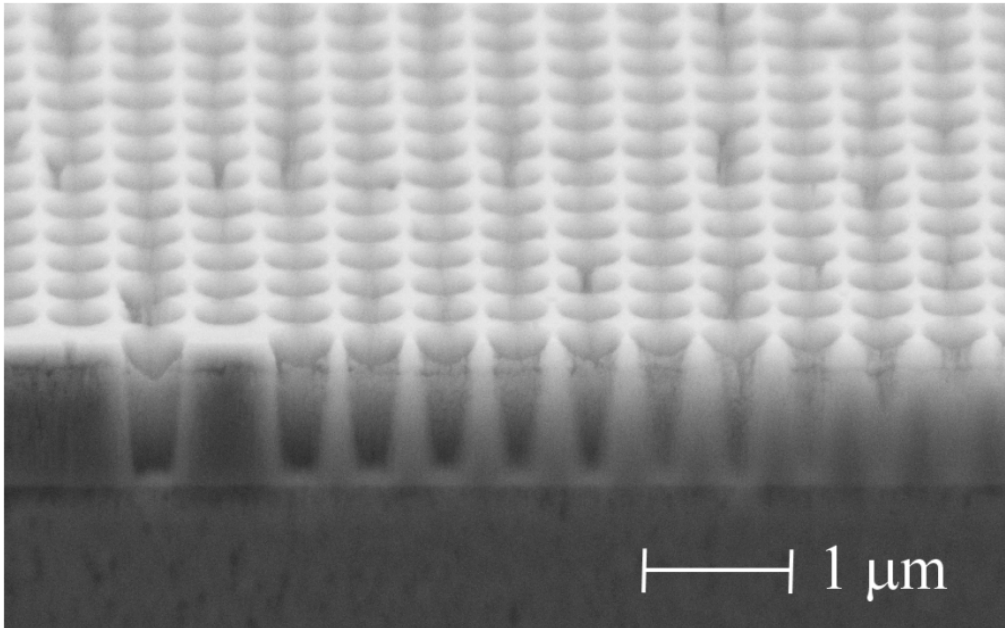


Figure 2-30 Reactive ion etch profile of nanopores in a 1  $\mu\text{m}$  thick silicon nitride layer on silicon.

Figure 2-31(b) shows an individual die on the wafer. Each die contains 91 suspended nanoporous membranes for a total of 364 membranes on the entire wafer. Each of the membranes was examined under a Nomarski microscope. All 364 membranes were found to be intact after the completion of the process.

A single membrane from each die - identified according to the nomenclature presented in Figure 2-31 was imaged using a scanning electron microscope for point defects. An area of  $10\ \mu\text{m} \times 10\ \mu\text{m}$  was chosen for characterization. Figure 2-32 shows the different point defects identified.

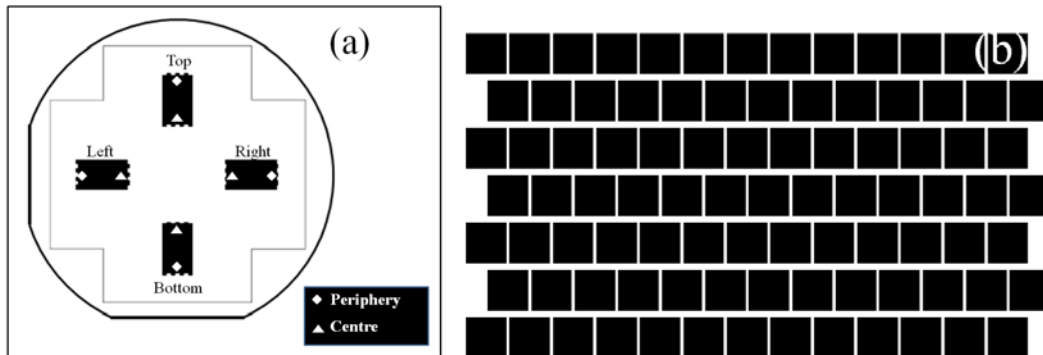


Figure 2-31 (a) Wafer layout and sampling location nomenclature. (b) Individual die



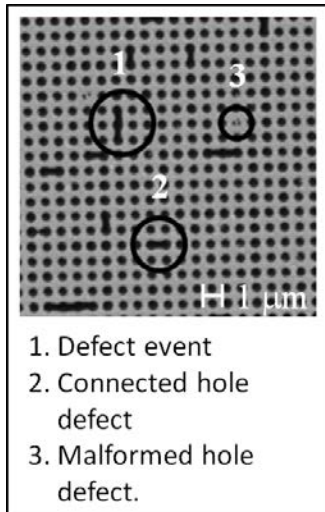


Figure 2-32 Point defects on a 10 μm x 10 μm sample area of a suspended silicon nitride membrane.

Observations at different points on the wafer as outlined by the nomenclature in Figure 2-31 and Figure 2-32 yielded the results shown on Table 2-3.

Table 2-3 Defect occurrences in 10 μm x 10 μm sample areas on a single wafer.

	Position of the Sample Area			
	Top	Bottom	Left	Right
Total no. of pores	400	400	400	400
Defect events	13	27	24	22
Connected pores (a)	28	70	63	56
Malformed pores (b)	2	0	1	1
Total no. of damaged pores (a+b)	30	70	64	57
% damaged pores	7.5	17.5	16	14.25
Wafer average % damaged pores	13.81			
% Standard deviation in no of damaged pores across wafer	27.66			

The areal defect density was calculated as,

$$\frac{\text{Area of a single pore} \times \text{average number of defective pores}}{\text{Sample area}} \quad (2-2)$$

Accordingly, the areal defect density for the sampled areas was found to be 0.064. The observed standard deviation was significant at 27 % and suggests that the detected point defects are the result of randomly occurring process variations not inherent to the process design. Some of the identified process variations are local non uniformities in nanoimprint resist thickness from particulate residue and variations in the thickness of the nanoimprint resist after residual resist etching. Other reasons include artifacts from the nanoimprinting process due to local failure of the anti-adhesion layer after repeated use and variations in the thickness of the Cr/Al<sub>2</sub>O<sub>3</sub> resulting in improper lift-off. A significant reduction in the occurrences of point defects is thought to be possible by improving process environment and equipment repeatability such as found in a commercial foundry.

The membranes were further characterized for variations in pore diameter across the wafer. The diameter was measured from images taken with a scanning electron microscope. The sampling locations were as illustrated in Fig. 2-31(a). A summary of the observations is presented in Table 2-4.

Table 2-4 Variation in nanopore diameter across a 3" diameter wafer

	Position							
	Top		Bottom		Left		Right	
	Centre	Edge	Centre	Edge	Centre	Edge	Centre	Edge
Average Diameter(nm)	387	382	389	383	384	389	387	384
Wafer Average (nm)	385.63							
% S.D	0.71							

As is evident from the percent standard deviation, the variation in nanopore diameter is quite insignificant. The observations listed in Table 2-4 also include human and instrument error in scanning electron microscopy, stemming from image focusing and diameter judgment from the obtained image using software based analysis tools. As such, excellent uniformity in nanopore diameter is observed across a 3" wafer. This observation suggests that within the limits of reasonable process latitude, variation in nanopore diameter is more tolerant of the process variations listed previously. This demonstrates the efficacy of the two-step lift-off pattern transfer process towards pattern size uniformity over a large area.

## 2.6 Summary

Microfabrication techniques developed for the semiconductor industry offer means to realize novel next generation devices in other areas of science and engineering. The present work describes a novel membrane blood oxygenator designed to mimic the human lung in terms of performance while improving on present day oxygenators in terms of gas transfer efficiency. Miniaturization and scaling techniques used in the semiconductor fabrication industry are fully utilized to realize a microstructure that is robust and compact enough to be used as an implantable device.

The gas exchange interface i.e. the membrane is the most important aspect of the membrane oxygenator and was the special focus of this research. Nanoporous silicon nitride membranes were fabricated using thermal nanoimprint lithography. A novel two stage lift-off process to accomplish pattern transfer from nanoimprint resist to silicon nitride is reported. A highly directional fluorine based reactive ion etch process for defining nanoscale dimensions was developed and optimized. Viability of amorphous aluminum oxide as a suitable etch mask for reactive ion etching of silicon nitride was demonstrated. Nanoporous membranes of 1  $\mu\text{m}$  thickness with highly ordered nanopores of 400 nm diameter were achieved. The developed membranes are thinner and offer much higher control over porosity and in turn gas transfer than those found in present literature.

## Chapter 3

### Low temperature growth and characterization of piezoelectric properties of crystalline ZnO nanorods using atomic force microscopy

#### 3.1 Introduction

##### 3.1.1 Zinc oxide nanostructures – an overview

Zinc oxide nanostructures have attracted global interest on account of their multitude of unique properties. The zinc oxide structure consists of alternating planes of  $\text{Zn}^{2+}$  and  $\text{O}^{2-}$  stacked in the c –axis direction. The crystal structure is wurtzite in nature and lacks a center of symmetry. As a result ZnO possesses piezoelectric and pyroelectric properties. In addition, ZnO is a wide band-gap semiconductor (3.3 eV) which makes it suitable for short wavelength optoelectronic applications [65].

ZnO crystals exhibit fast growth in the  $\pm[0001]$  directions in order to maximize area on the low energy side surfaces, thereby maintaining a stable structure. This property results in a family of nanostructures known as nanorods which are characterized by diameters up to few hundreds of nanometers and lengths of few tens of microns.

Piezoelectric properties of ZnO nanowires and their applications in environmental energy harvesting have been brought into focus by the work of Wang et al [66]. Recent computational [67-69] and experimental work [70] into piezoelectric properties of ZnO nanorods suggests that due to nanoscale surface effects, ZnO nanostructures may exhibit different piezoelectric properties than bulk ZnO. This observation coupled with recent findings that propose a dependence of mechanical properties on the size due to surface effects [71] suggest that ZnO nanorods can produce higher strain energy that can be converted to a piezoelectric voltage, as compared to bulk ZnO [72].

ZnO nanowires also find novel applications in nanophotonics such as LED's that produce electroluminescent emissions in the visible spectrum [73]. Development of optically pumped lasers using pulsed-laser-deposited (PLD) ZnO nanowires has also been reported [74].

Several advantages of ZnO nanowires such as better absorption and carrier extraction make them attractive over conventional thin films for photovoltaic applications [75].

Gas sensors with metal oxide semiconductors as the sensing material offer advantages of small dimension, low cost, low power consumption, on-line operation and compatibility with microelectronic processing [65]. ZnO nanowires find application in innovative ethanol sensors [76-78]. Other applications such as oxygen sensing [79, 80] and ammonia sensing [81] have been reported where use of ZnO nanowires improved sensitivity.

### 3.1.2 Piezoelectric properties of ZnO

A piezoelectric material is a non-centrosymmetric material, such that, when subjected to mechanical strain, charge separation occurs within the volume leading to the formation of a dipole of static charges. This phenomenon is explained by the piezoelectric constitutive equation [82]

$$D_i = \sum_j e_{ij} \epsilon_j + \sum_j \epsilon_{ij}^E E_j \quad (3.1)$$

Where,  $D$ : Electric displacement density ( $C/m^2$ )

$e$ : Piezoelectric stress coefficient ( $C/m^2$ )

$\epsilon$ : Normal strain

$\epsilon$ : Dielectric permittivity. ( $F/m$ )

$E$ : Electric field ( $V/m$ )

$i$ : denotes the direction of electric field

$j$ : denotes the direction of strain

Since the applied electric field is 0, the second term in the above equation can be set to 0. Mechanical and piezoelectric properties of ZnO have been reported [83]. These coefficients have been used as material properties for the subsequent FEM analysis

Compliance coefficients of ZnO ( $10^{-12}\text{m}^2/\text{N}$ )

$$\begin{bmatrix} 0 & 0 & 0 & 0 & e_{15} & 0 \\ 0 & 0 & 0 & e_{15} & 0 & 0 \\ e_{31} & e_{31} & e_{33} & 0 & 0 & 0 \end{bmatrix} = \begin{bmatrix} 0 & 0 & 0 & 0 & -0.48 & 0 \\ 0 & 0 & 0 & -0.48 & 0 & 0 \\ -0.573 & -0.573 & 1.32 & 0 & 0 & 0 \end{bmatrix}$$

Piezoelectric stress coefficients of ZnO ( $\text{C}/\text{m}^2$ )

$$\begin{bmatrix} 0 & 0 & 0 & 0 & e_{15} & 0 \\ 0 & 0 & 0 & e_{15} & 0 & 0 \\ e_{31} & e_{31} & e_{33} & 0 & 0 & 0 \end{bmatrix} = \begin{bmatrix} 0 & 0 & 0 & 0 & -0.48 & 0 \\ 0 & 0 & 0 & -0.48 & 0 & 0 \\ -0.573 & -0.573 & 1.32 & 0 & 0 & 0 \end{bmatrix}$$

ZnO dielectric co-efficients under constant strain.

$$\begin{bmatrix} \varepsilon_{11} & 0 & 0 \\ 0 & \varepsilon_{11} & 0 \\ 0 & 0 & \varepsilon_{33} \end{bmatrix} = \begin{bmatrix} 7.57 & 0 & 0 \\ 0 & 7.57 & 0 \\ 0 & 0 & 9.03 \end{bmatrix}$$

A FEM model of a single ZnO nanorod bent using a 1000 nN force was simulated in ANSYS software. The nanorod was modeled as a cylinder 300 nm in diameter, 2  $\mu\text{m}$  in length. Displacement was restricted at the bottom of the nanorod; also the bottom was electrically grounded. The force was applied as a point force to a node on the top face of the nanorod, perpendicular to the Z-axis. Figure 3-1 shows the voltage generated in the nanorod.

The simulation shows that a voltage of 0.63 V (Fig.3-1) can be generated by the nanorod under the applied conditions. A similar simulation has been described in [84]. The authors in that publication report a voltage of 0.56 V. Another important observation is that a positive voltage develops on the side under tensile stress, while a negative voltage develops on the side under compressive stress. Therefore, when connecting an electrode to draw the generated voltage, care must be taken to ensure that the electrode does not make contact with both sides at once, to prevent shorting of the nanorod across the diameter [85]. This point has been addressed in the design of the lateral energy harvester described in Chapter 4.

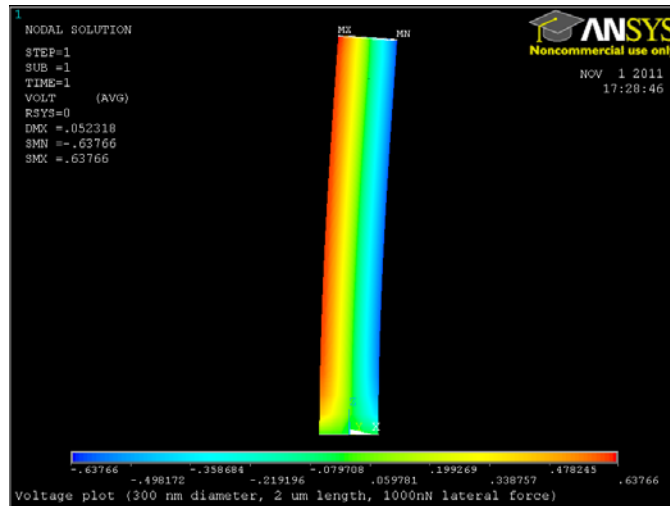


Figure 3-1 Voltage generated in ZnO nanorod after application of a bending force.

Another FEM simulation was performed to observe the potential distribution in the nanorod when subjected to an axial compression. With similar boundary conditions as before, the top of the nanorod was subjected to a pressure load corresponding to a force of 0.2 pN. This force corresponds to a 10  $\mu\text{m}$  thick proof mass axially compressing the nanorod under a Z – axis vibration of amplitude 1 g.

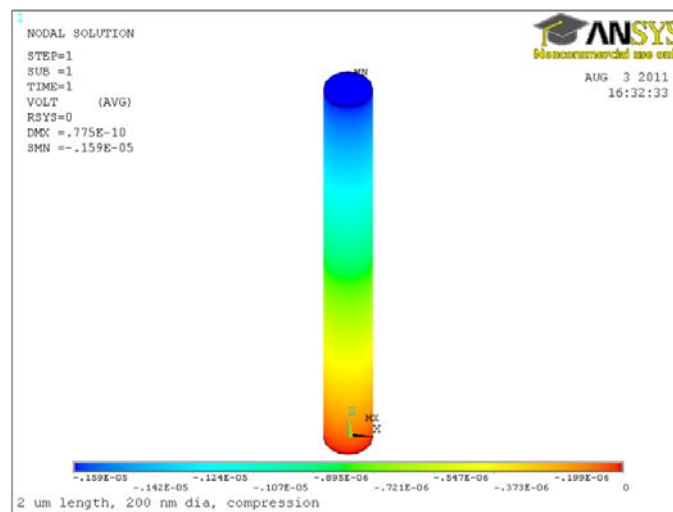


Figure 3-2 Voltage generated in ZnO nanorod after application of a compressive force.

The nanorod generated a potential of  $-1.5 \mu\text{V}$  (Fig.3-2). The potential was set up across the length of the nanorod. This potential distribution can be tapped using a simpler top

and bottom electrode configuration. This configuration formed the basis of the z – axis energy harvester design discussed in Chapter 4.

### 3.1.3 Crystalline ZnO nanorod growth techniques

#### 3.1.3.1 Vapor – Liquid – Solid (VLS) process

The VLS process is based on the principle of supersaturation and precipitation. A metal pad of nano-scale dimensions is deposited on a solid substrate which is typically a semiconductor. The metal is chosen such that it melts at a lower temperature by forming an alloy with the substrate semiconductor as compared to the melting point of the metal. The substrate is placed in a furnace and the temperature is increased causing the metal pad to liquefy. The material to be deposited is then introduced into the furnace in the form of gaseous precursors. For ZnO nanorod growth, Au or Sn [86] is typically used for the metal pads and a mixture of powdered ZnO graphite are evaporated to form the gaseous precursor [87]. At an elevated temperature, the liquid – phase metal exhibits a higher sticking co-efficient than the solid substrate around it. Hence the gas – phase precursor atoms deposit preferentially on to the liquefied metal pad. This process continues until the metal is supersaturated with precursor atoms. At this point the precursor material starts to precipitate resulting in nanorod growth.

It is evident that the liquid –phase metal pad is key to nanorod growth using the VLS process. Nanorod growth occurs only at sites on the substrate where the metal pad is present. This property can be leveraged to achieve patterned, ordered growth of ZnO nanorods. By patterning the nano – scale metal pads using a suitable sub –micron lithography technique, the placement of nanorods can be effectively controlled. Fabrication of ordered arrays of ZnO nanorods using VLS and different approaches for placement control such as flexible metal nanotube membranes [88], e – beam lithography [89], and TEM grids [90] has been reported.

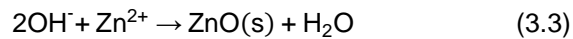
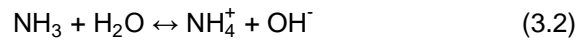
#### 3.1.3.2 Hydrothermal growth

In the hydrothermal technique, the precursors of the material to be deposited are dissolved in an aqueous solution at a particular concentration. The substrate to be coated with



the material is immersed in this 'growth' solution. At elevated temperature, the material of interest is synthesized from the dissolved precursors and precipitates on the substrate in the form of crystalline nanostructures.

The practicality of hydrothermal growth for synthesis of crystalline ZnO nanorods was first demonstrated by Vayssieres using zinc nitrate and hexamethylenetetramine (HMTA) [91]. Since then a number of different precursors have been explored by various researchers in the field. The most popularly used source of  $Zn^{2+}$  ions is zinc nitrate. Thermal decomposition of HMTA releases hydroxyl ions that react with  $Zn^{2+}$  ions to form ZnO [92]. The process is summarized by the following equations [93].



The role of HMTA in ZnO nanorod growth is primarily to supply the hydroxyl ions for the precipitation reaction and also possibly as a kinetic buffer [94]. It is also proposed that HMTA contributes to the anisotropy of crystal growth which results in high aspect ratio nanorods and nanowires [95]. HMTA being a long chain polymer and a non-polar chelating agent preferentially attaches to the non-polar faces of the crystal, thus cutting off the supply of  $Zn^{2+}$  ions to the side faces. The polar (0001) top faces are exposed to the  $Zn^{2+}$  from the solution and hence the crystal can grow only along that direction [93].

Other zinc salts such as zinc chloride [96] and zinc acetate [97] have been explored by different researchers in the field. A comparative study of nanorod growth using zinc nitrate, zinc acetate and zinc chloride has been reported by Akgun et al [98]. It was demonstrated that under similar process conditions, the highest aspect ratio of nanorod dimensions could be achieved using zinc acetate as a source of  $Zn^{2+}$  ions.

A thin film of a material with matching lattice parameters to ZnO could be used to promote growth and attachment of the nanorod to mismatched substrates such as silicon.

Analogous to the VLS process, this seed layer can be patterned using various lithography techniques to achieve patterned and ordered growth at nano and micro scale. Ordered arrays of ZnO nanorods by means of patterning the seed layer have been reported in literature using laser interference lithography [99-101] and e-beam lithography [102].

3.1.3.3 Hydrothermal growth with NIL assisted template – our method of choice

Besides VLS and hydrothermal growth, some of the other methods used for growth of ZnO nanorods include the Vapor-Solid technique and direct deposition using pulsed laser ablation. One of the most important parameters to be taken into consideration for selection of the nanorod growth process was the process temperature, in order for the process to be compatible with low temperature processing necessary when working with organic materials such as polyimides. A review of process temperatures for different growth techniques is presented in Table 3-1.

Table 3-1 Process temperature for different nanorod growth techniques

<b>Process</b>	<b>Process temperature</b>	<b>Reference</b>
VLS	800°C - 1150°C	[88, 103]
VS	500°C	[104]
Hydrothermal growth	95°C	[91]

HD 4100 series polyimides from HD Microsystems Inc. have been used extensively in the applications discussed in Chapters 4 and 5. These polyimides have a glass transition temperature ( $T_g$ ) of 330°C [105]. This limits the maximum process temperature to 330°C and hence, hydrothermal growth is our method of choice for growth of ZnO nanorods. The effect of different hydrothermal process variables on nanorod growth have been examined in section 3.3. We have used PLD deposited polycrystalline ZnO as the seed layer and zinc acetate along with HMTA as a source of zinc ions for hydrothermal growth. Additionally, patterned, ordered arrays of ZnO nanorods have been demonstrated using NIL.

## 3.2 An experiment to observe the piezoelectric response of crystalline ZnO nanorods

### 3.2.1 Overview of the experiment

The piezoelectric response of crystalline ZnO nanorods was determined by means of force spectroscopy using an atomic force microscope (AFM). The force spectroscopy mode allows controlled quantities of force to be applied in the normal direction to a sample using the AFM tip. The force applied by the tip serves as mechanical excitation for ZnO nanorods which causes an electric potential to be generated on the nanorod surface. The tip is coated with a conductive coating that enables the extraction and measurement of the generated electrical signal. The AFM tip therefore, performs the dual role of a mechanical excitation probe and as an electrode for extraction of the generated piezoelectric signal.

Previous studies have investigated piezoelectric properties of ZnO nanowires using conductive atomic force microscopy (C-AFM) [106]. The C-AFM technique involves an AFM tip scanning laterally across the nanorod array, i.e. the motion of the tip is in the same plane as the array. In contrast, we probed the ZnO nanorod array using the advanced force mode, wherein the motion of the AFM tip is perpendicular to the plane of the array. In this mode, the tip extends and retracts into the nanorod array, causing lateral bending of the nanorods. The extension/retraction results in deflection of the tip which is used to determine the force applied on the nanorods. Conversely, by specifying set points for tip deflection, the tip can be made to extend by the requisite amount, thus allowing a degree of control over the magnitude of force applied. The resulting extension – deflection graph known as the force plot is useful not only to determine the magnitude of force, but as will be shown later, provides some insight into the nature of the nanorod – tip interaction. Additionally, in order to verify the rationality of the experimental results, the tip – nanorod interaction was simulated using a computer generated solid model and finite element analysis (FEA). Using the advanced force mode probing technique, voltages up to few mV were observed at output.

Force spectroscopy using an AFM is frequently used for application of force and determination of surface properties of various samples. Application of force magnitudes as low as a few nN has been reported [107, 108]. The AFM tip is physically extended towards the sample, and when the desired magnitude of force is applied to the sample, the tip is retracted. The interaction between the sample and tip is recorded by the AFM's split – photodiode as a voltage signal that corresponds to tip deflection. The vertical extension and retraction of the probe holder containing the tip in order to achieve the aforementioned deflection is also recorded. The tip deflection is plotted on the Y – axis and the vertical deflection on the X – axis of a two dimensional plot that provides a graphical interpretation of the tip – sample interaction known as a force plot. The tip deflection data can be converted to applied force knowing the sensitivity ( $S_v$ ) of the cantilever (slope of the tip –deflection vs probe holder extension plot) and the stiffness of the cantilever ( $K_{cant}$ ) according to Hooke's law, (Eqn. 3.4) and Equation 3.5 [109]. Setting a set - point for the photodiode voltage ( $V_t$ ) allows control over the magnitude of the applied force.

$$F = K_{cant} * d_{cant} \quad (3.4)$$

Hence,

$$F = K_{cant} * S_v * V_t \quad (3.5)$$

Where,

$F$ : Applied force

$d_{cant}$ : deflection of the cantilever

$K_{cant}$ : Stiffness of the AFM cantilever. The TESP type cantilever used in this experiment had a nominal stiffness of 42 N/m

$S_v$ : Cantilever sensitivity. This parameter is determined experimentally determined from the steeply sloped section of the force plot and relates deflection of the cantilever to the photodiode voltage

$V_t$ : Trigger voltage. This voltage serves as the set – point for the cantilever deflection voltage measured by the split – photodiode. The cantilever is

extended towards the sample until the bending of the cantilever is registered by the photodiode as a voltage equal to the trigger voltage

A sample force plot obtained from AFM tip – ZnO nanorod interaction is shown in Figure 3-3.

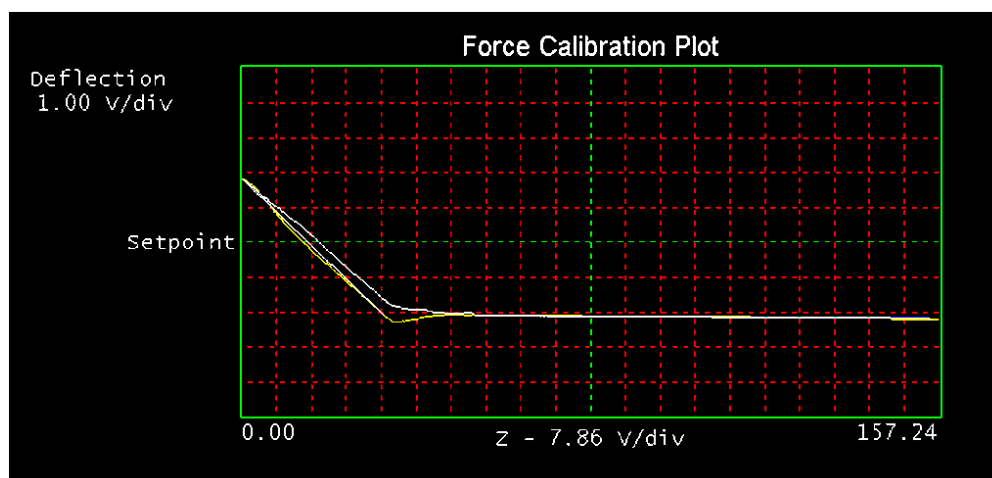


Figure 3-3 An example of a force plot obtained using a TESP type tip interacting with a ZnO nanorod array. The white trace denotes extension of the tip towards the sample and the yellow trace represents retraction. The point at which the trace steeply slopes represents the extent of the nanorod – tip interaction

### 3.2.2 Sample preparation

Crystalline ZnO nanorods were grown on a silicon substrate for the purpose of this experiment using the low temperature hydrothermal growth process. The nanorods were grouped into arrays of 500  $\mu\text{m}$  x 500  $\mu\text{m}$  by means of defining the areas for hydrothermal growth. This was accomplished by patterning the ZnO seed layer using photolithography. In order to extract the piezoelectric signal, the nanorods were grown on top of a patterned Au electrode. As mentioned previously, the AFM tip serves as the other electrode.

The fabrication process is outlined in Figure 3-4. The first step involves deposition of a 200 nm  $\text{Si}_3\text{N}_4$  layer for passivation/planarization on a (100) Si wafer (Fig.3-4(a)). 100 nm of Au with an underlying 30 nm Cr adhesion layer were subsequently deposited and patterned using a

lift-off process to form a bottom electrode 500  $\mu\text{m}$  wide and 1500  $\mu\text{m}$  long (Fig 3-4(b,c)). Then, 30 nm of Ti and 400 nm of ZnO seed layer were put down successively (Fig 3-4(d)) and patterned to form a 500  $\mu\text{m}$  x 500  $\mu\text{m}$  square for defining the nanorod growth area (Fig. 3-4(e)). Arrays of crystalline ZnO nanorods were grown using a low temperature hydrothermal growth process (Fig. 3-4(f)). The sample was placed in an aqueous equimolar solution of Zinc acetate and hexamethylenetetramine (HMTA) for duration of three hours at a temperature of 85°C for nanorod growth. The morphology was examined using SEM and AFM imaging. Crystalline ZnO nanorods grew in a sparse array as seen in Figure 3-5(a-c). The average diameter was 166 nm and the average separation between nanorods was found to be 270 nm. The nanorods were 5 – 6  $\mu\text{m}$  in length. The crystal structure and composition of ZnO nanorods grown using the aqueous growth process were characterized using XRD (Fig. 3-5(d)) and EDAX (Fig. 3-5(e)). The XRD analysis clearly shows the presence of the dominant (0002) peak which indicates that the ZnO nanorods are predominantly c-plane oriented and have wurtzite structure.

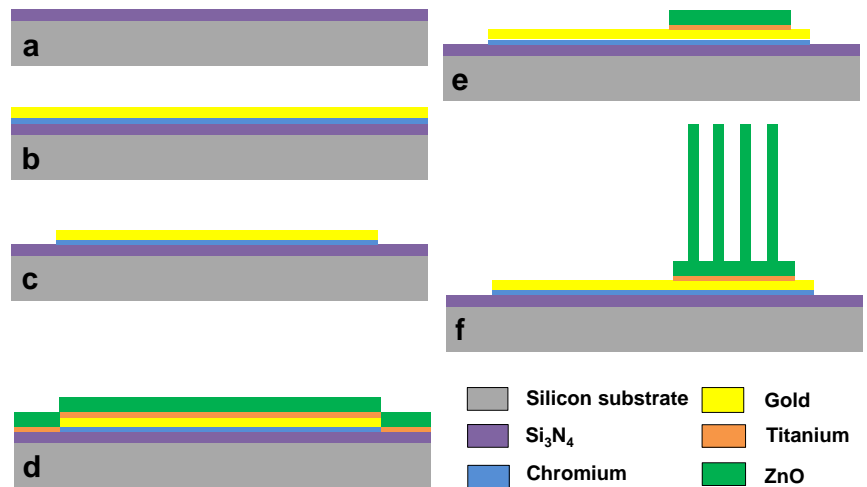


Figure 3-4 Schematic illustration of the test sample preparation process. (a) Passivation silicon nitride is deposited on silicon substrate. (b) Cr/Au deposition. (c) Cr/Au patterning to form the bottom electrode. (d) Deposition of Ti/ZnO seed layer (e) Patterning of Ti/ZnO to form Ohmic contact. (f) Hydrothermal growth of ZnO nanorods.

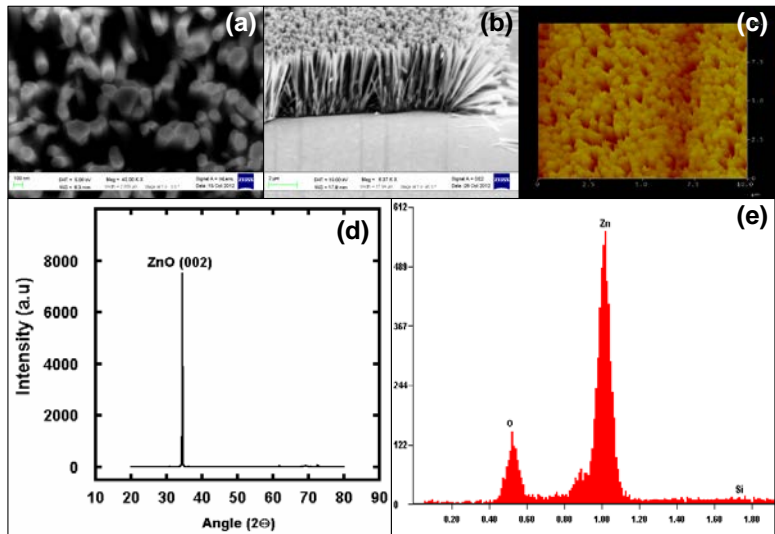


Figure 3-5 (a) SEM image of ZnO nanorods (top view). (b) SEM image of ZnO nanorods (side view) (c) AFM tapping mode image of ZnO nanorod array. (d) XRD scan showing the dominant (002) ZnO peak. (e) EDAX scan from top of a single ZnO nanorod.

### 3.2.3 Experimental setup for characterization

The silicon wafer with as-grown ZnO nanorods was diced into individual dies each containing ten nanorod arrays. The dies were packaged using quad flat pack type packages using Au ball bonding. The sample was probed using a Bruker Dimension D5000 AFM operating in contact mode. The advanced force mode was used to initiate interaction between the AFM tip and ZnO nanorods. A conductive Au coated (30 nm) silicon AFM tip (TESP, Bruker Inc.) acted as the top electrode and a force probe as explained previously. The signal from the AFM tip was extracted using a conductive AFM (C-AFM) probe holder (model DSCMSCH, Bruker Inc) that features a built in lead with electrical contact to the tip. The lead was connected to a sensitive voltmeter (Keithley 2182A nanovoltmeter). The inputs to the nanovoltmeter were from the package and the AFM tip holder. All measurements were carried out across a 1 M $\Omega$  resistor connected across the device. The package, AFM and nanovoltmeter were placed inside a grounded enclosure to shield against stray electromagnetic noise. The experimental setup is shown in Figure 3-6.

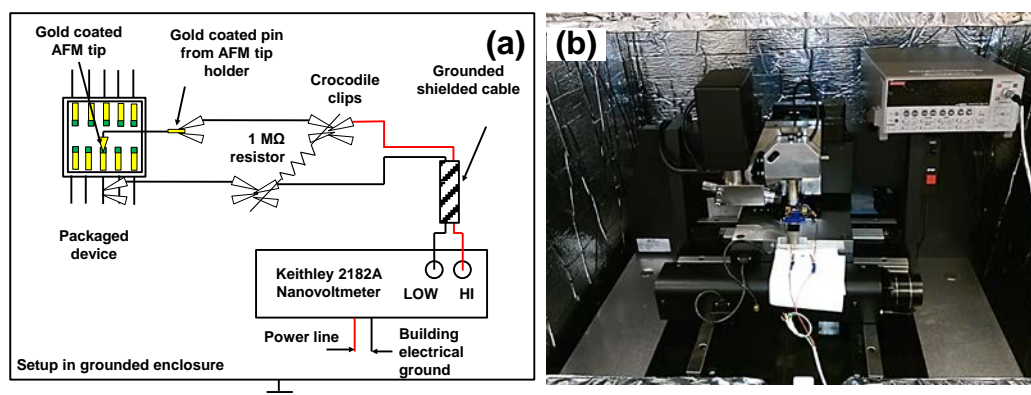


Figure 3-6 (a) Schematic, (b) Photograph showing experimental setup for mechanical deflection and measurement of generated piezoelectric voltage from ZnO nanorods.

The voltmeter used in the experiment (Keithley 2182A) is a highly sensitive voltage measurement instrument capable of resolving voltages up to few nV with excellent SNR. It is however a DC voltmeter optimized for measurement of DC or slow varying signals. The AFM tip



extends and retracts into the nanorod array in a very short amount of time (few hundreds of ms). As the tip also functions as one of the electrodes, the extension - retraction results in making and breaking of electrical contact with the nanorods. Hence, the piezoelectric signal from the nanorods is expected to be in the form of a sequence of short duration voltage spikes, corresponding to the extension and retraction of the tip. Therefore, a software module was developed using LabVIEW software that continuously triggered the nanovoltmeter to measure the voltage signal at its input. The LabVIEW software along with the nanovoltmeter represents a system that capable of measuring a time varying signal with excellent SNR characteristics. In order to ascertain the capabilities of this system, a pulse train similar to that expected from the nanorod sample was input to the nanovoltmeter – LabVIEW combination using a signal generator. The nanovoltmeter was configured such that the ADC integration time was equal to the time period of 1 power line cycle (1 PLC). Some of the other features of the nanovoltmeter, such as line voltage synchronization, analog and digital filters and front - end and back – end amplifier auto-zero algorithms were turned off to to optimize signal acquisition speed. The performance of the nanovoltmeter was verified using an oscilloscope that was fed the same input from the signal generator. The amplitude of the signal was kept constant at 700  $\mu\text{V}$  (limited by the voltage resolution capabilities of the oscilloscope). The frequency of the signal was fixed at 1 Hz (similar to that expected from the AFM tip extension – retraction). The pulse width was varied from 39 ms to 300 ms. The results are shown in Figure 3-7.

It was observed that the pulse shape was distorted for pulse – widths lesser than 150 ms. Up to a minimum pulse - width of 100 ms, the system is capable of accurately resolving the amplitude of the signal under measurement. At 39 ms and 60 ms pulse-width, the system occasionally failed to register the amplitude of the signal accurately. At pulse-widths of 150 ms and higher, the system resolved the rectangular pulse shape with the flat top along with accurate measurement of amplitude. This experiment demonstrates that the system is capable

of resolving a minimum pulse width of 150 ms and up to a minimum of 100 ms if only the amplitude is of interest.

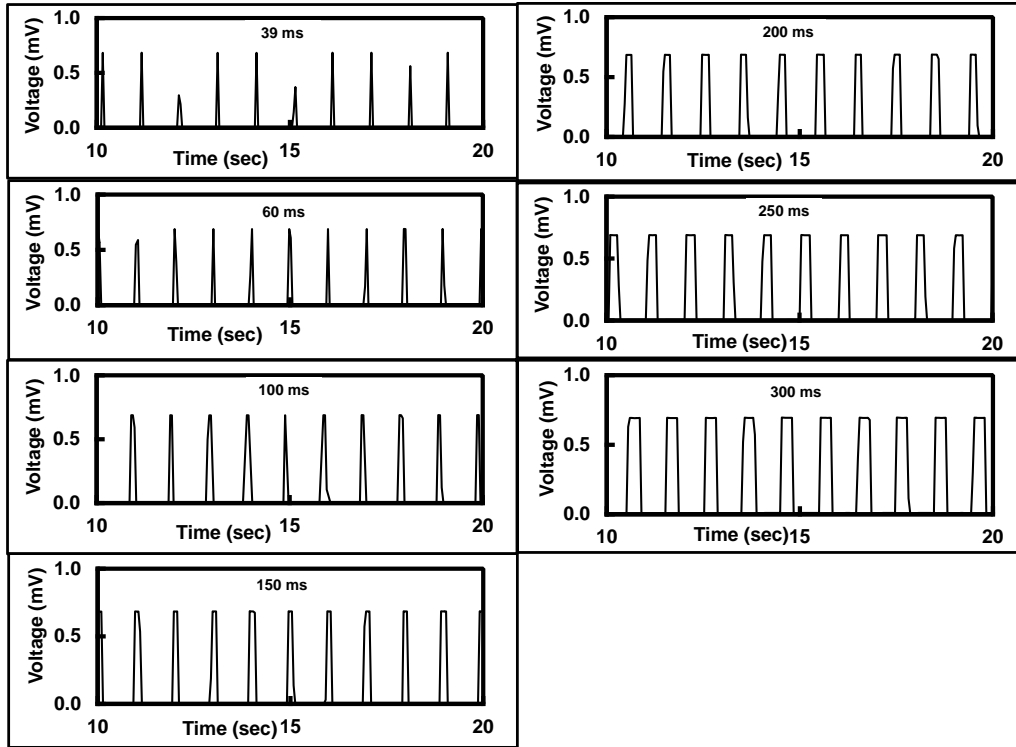


Figure 3-7 Voltage vs time plots for different pulse widths obtained from sampling the signal generator output using the nanovoltmeter – LabVIEW program module. A noticeable improvement in the pulse shape is observed for pulse- widths above 150 ms.

### 3.2.4 Characterization results

With the performance characteristics of the measurement setup established, the ZnO nanorod sample was probed using the AFM in force spectroscopy mode. The first experiment aimed to verify the piezoelectric origin of the observed signal. Figure 3-8(a) shows an example of the force plots obtained from a single nanorod – tip interaction event. In order to verify the origin of the signal, the sample was initially connected in the ‘forward’ fashion. After recording the signal, the sample was next connected in ‘reverse’ fashion (Fig. 3-8(b)). It was expected that

if the observed signal was piezoelectric in origin, the polarity of the signal would be different in the forward and reverse connection experiments. On the other hand, if the observed signal was simply the result of a change in contact resistance due to the sliding of the tip against the nanorods, the polarity of the signal in both cases would be same. Figure 3-8(c) shows voltage generated as a result of the AFM tip interacting with the ZnO nanorods. The AFM tip was made to extend and retract at a frequency of 1 Hz. Voltage spikes were observed as the result of the AFM tip bending the nanorods. The voltage spikes were positive in polarity when the device was connected in the 'forward' fashion. When the polarity of the device was reversed, voltage spikes of negative polarity were obtained. This demonstrates an active voltage generation mechanism within the device, as opposed to a possible variation of circuit resistance due to tip-nanorod interaction.

A majority of the observed voltage spikes are positive in forward connection and negative in reverse connection. A number of spikes, opposite in polarity and smaller in magnitude than the majority, are also observed. To investigate the origin of these opposite polarity spikes, the tip was made to interact with the nanorods manually i.e. the tip extended and retracted into the nanorod array in response to a trigger from the AFM operator (Fig. 3-9). The corresponding force plot for each interaction was recorded. Figure 3-9(a) shows sample voltage-time and force plots from this experiment. Figure 3-9(b) is a sample force plot that corresponds to positive voltage spikes while Figure 3-9(c) is a sample force plot for negative voltage spikes. The nature of the force plot reflects the stiffness encountered by the AFM tip when probing the ZnO nanorods.

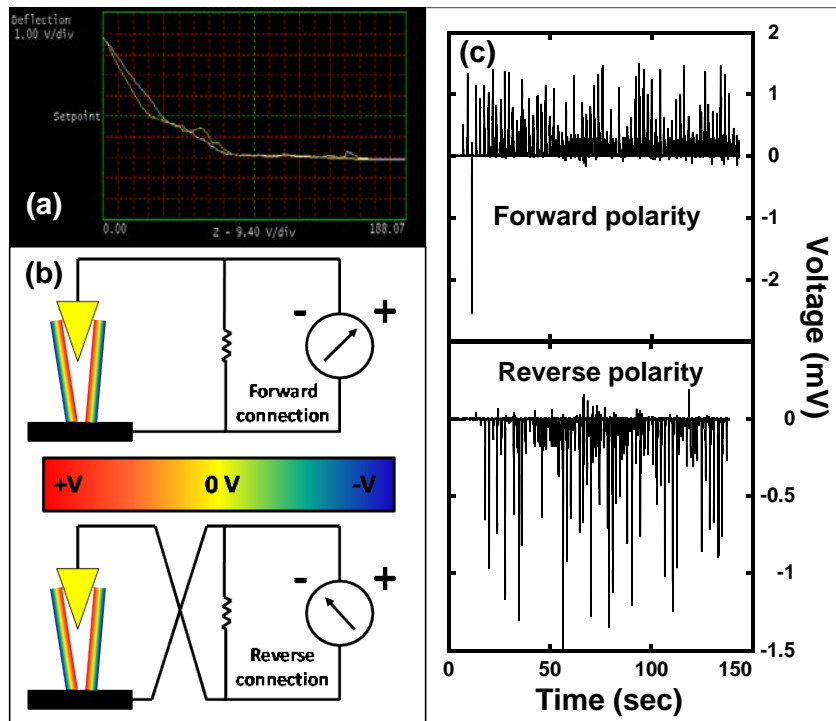


Figure 3-8 (a) Force plot from one nanorod – tip interaction event. The x axis represents z motion of the AFM piezo-actuator column calibrated in Volts. The y axis represents deflection of the AFM tip as detected by the AFM photodiode calibrated in Volts. The white trace is the tip extension while the yellow trace is the tip retraction. (b) Schematic for forward and reverse polarity connections in separate experiments conducted to verify the origin of the observed signal. (c) Voltage signals recorded by the nanovoltmeter in forward and reverse polarity experiments. The tip-nanorod interaction was realized by extension/retraction of the AFM tip into the nanorod array at a frequency of 1 Hz.

When the tip probes between nanorods, the nanorods are bent laterally, generating a positive voltage on the side in contact with the AFM tip. This is registered as a positive voltage spike on the voltage graph. The corresponding force plot (Fig. 3-9(b)) is irregular in nature. It is possible that the tip – nanorod interaction in this case is not smooth, owing to short range forces. The tip, therefore, encounters a variable stiffness when it squeezes in between the nanorods and this is reflected in the irregular nature of the force plot. On the other hand, under

rare circumstances such as the one denoted by the \* mark in Fig. 3-9(a), a negative voltage spike is observed, and the corresponding force plot (Fig. 3-9(c)) is close to ideal. This means that the tip encountered constant vertical stiffness during extension and retraction. It is possible that in this case, the tip rested on the top of a ZnO nanorod, which was then compressed. This interaction is similar to the tip compressing a rigid surface resulting in a force plot that is near ideal in nature. The voltage generated on the compressed top surface is negative which is then registered as a negative voltage spike on the voltage plot.

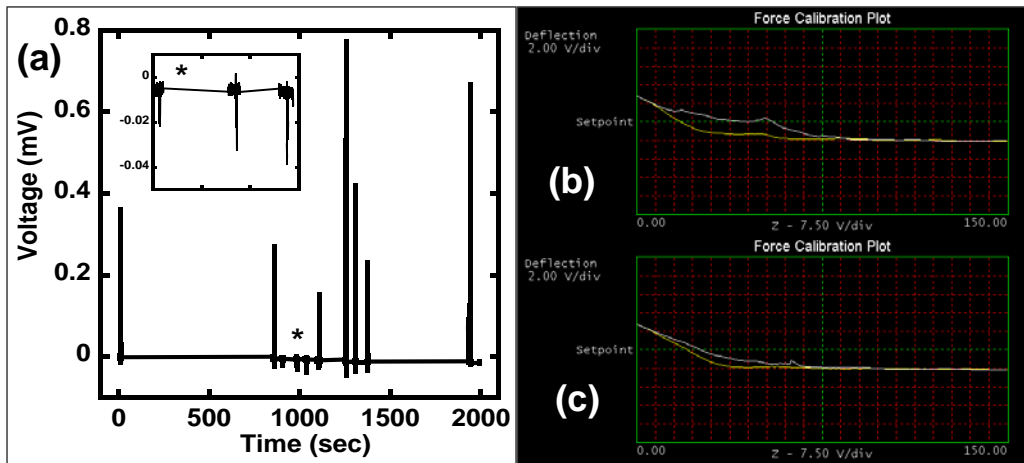


Figure 3-9 (a) Voltage recorded by nanovoltmeter in response to manual probing of the nanorod array. Each voltage spike corresponds to one manually triggered tip-nanorod interaction event. (inset) magnified view of negative polarity voltage spikes. Sample force plots corresponding to positive (b), and negative (c) polarity voltage spikes.

In order to ensure that the obtained results were within theoretical bounds, the AFM tip – nanorod interaction was simulated using finite element methods. The AFM tip was modeled according to the dimensions specified by the manufacturer (TESP, Bruker Inc). The ZnO nanorods were modeled as a regularly spaced array of hexagonal cylinders of diameter 166 nm and height 5  $\mu\text{m}$ . The separation between the adjacent nanorods was set to 270 nm. The material properties used for the simulation were previously published bulk ZnO values [83]. Force was applied to the cantilever at the top surface of the pyramidal tip. The magnitude of this

force was the same as that determined from the AFM force plot. All motion was restricted at the base of the cantilever as well as the base of the nanorods. Contact boundary conditions that allowed for relative movement of two contacting surfaces were defined between the pyramidal tip and nanorods. The finite element problem was solved using the CoventorWare MemMech solver and the lateral displacement of the nanorods was determined (Fig. 3-10(a)). The simulated lateral displacement obtained from CoventorWare was applied to the top face of a single ZnO nanorod modeled using ANSYS (Fig. 3-10(b)). As before, the bottom of the nanorod was restricted from motion and was electrically grounded. The model was solved to find the potential distribution in the nanorod as a result of the applied strain. It was observed that voltage in the range of 6.7 mV – 39.4 mV could be generated for a AFM – applied force in the range of 8.8  $\mu$ N – 47.2  $\mu$ N. This range of force was chosen because it represents the estimated magnitudes of forces that can be applied to the nanorods using trigger voltages in the range of 2V – 6V in the force spectroscopy mode. Note that the force range mentioned includes the force needed to bend the nanorods and the force needed to bend the cantilever. The effect of various short – range and long – range force typically experienced by the AFM tip when interacting with a sample are not included in the simulation. Based on the lateral displacements of the nanorods obtained from the simulation, it is estimated that each nanorod experiences a bending force in the range of 5 nN – 31.2 nN. This estimate assumes that the nanorods are of uniform diameter and are equally spaced as modeled in Figure 3-10(a). In reality, as is observed from the SEM image in Figure 3-5(a), the nanorods density and diameter vary significantly at different positions in the array. As a result, the lateral the vertical stiffness experienced by the AFM tip can differ considerably from the finite element model and making accurate determination of the actual force experienced/nanorod challenging.

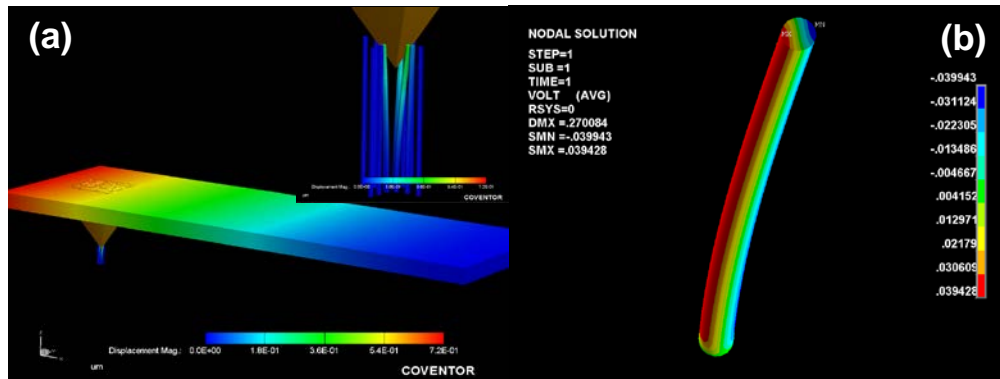


Figure 3-10 (a) Simulated displacement ( $\mu\text{m}$ ) of AFM tip in response to an applied force. The tip laterally displaces four nanorods (166 nm diameter, 5  $\mu\text{m}$  length) that are in direct contact. (inset) magnified view of the tip – nanorod interaction. (b) Simulated voltage (volts) generated in a ZnO nanorod in response to lateral displacement. The tensile side (in contact with the tip) generates a positive voltage, while the compressed side generates a negative voltage

The tip-nanorod interaction was further examined to observe the relation between applied force and generated voltage. Five different locations were probed on the 500  $\mu\text{m}$  x 500  $\mu\text{m}$  array (Fig. 3-11). The AFM tip was manually triggered to interact with the ZnO nanorods five times at each location. Each interaction was observed as a single peak or multiple peaks on the voltage-time plot (Fig. 3-12(a)). This experiment was repeated for different values of trigger voltage which correspond to different magnitudes of the applied force (Fig. 3-12(b-f)).

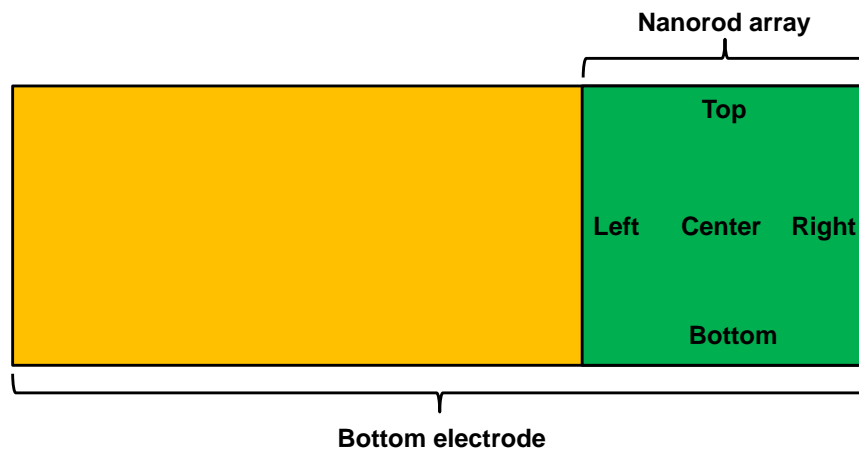


Figure 3-11 Probe positions for force spectroscopy on the nanorod array

A second, similar experiment was carried out with the AFM tip extending and retracting into the nanorod array at a frequency of 1 Hz (Fig. 3-13).

As mentioned previously, it is possible to calculate the force applied by the AFM cantilever from Eqn. 3-5. However, since the force applied is directly proportional to the sensitivity of the system, the magnitude of force determined depends heavily on accurate measurement of the sensitivity parameter  $S_v$ .

$S_v$  is the slope of the tip-nanorod interaction portion of the force plot. Generally, the surface being probed using force spectroscopy is flat as compared to the diameter of the AFM tip and therefore presents a surface of constant stiffness. This results in the surface-tip interaction portion of the force plot having a linear characteristic. Consequently, determination of the slope i.e.  $S_v$  is straightforward and the applied force can be therefore calculated with good accuracy.

The interaction of the AFM tip with the ZnO nanorod array is not as straightforward. When the AFM tip is triggered to extend into the array, the tip forces its way between adjacent nanorods bending them laterally. This interaction is very complex in nature, since the net vertical resistance to translation (i.e. the stiffness presented by the nanorods) experienced by the AFM tip is not constant. The bending stiffness of the nanorods increases progressively as the AFM tip extends further into the array. Additional non – linearity could possibly be introduced by sliding friction, and various short – range and long – range forces. The topography of the nanorods themselves is probably the most significant factor contributing to the non-linearity. Variations in nanorod density, length, diameter and angle of growth with respect to the substrate present a singularly complex surface to the AFM tip. As a result, the tip - nanorod interaction portion of the force plot is frequently observed to be irregular in nature (Fig. 3-14).



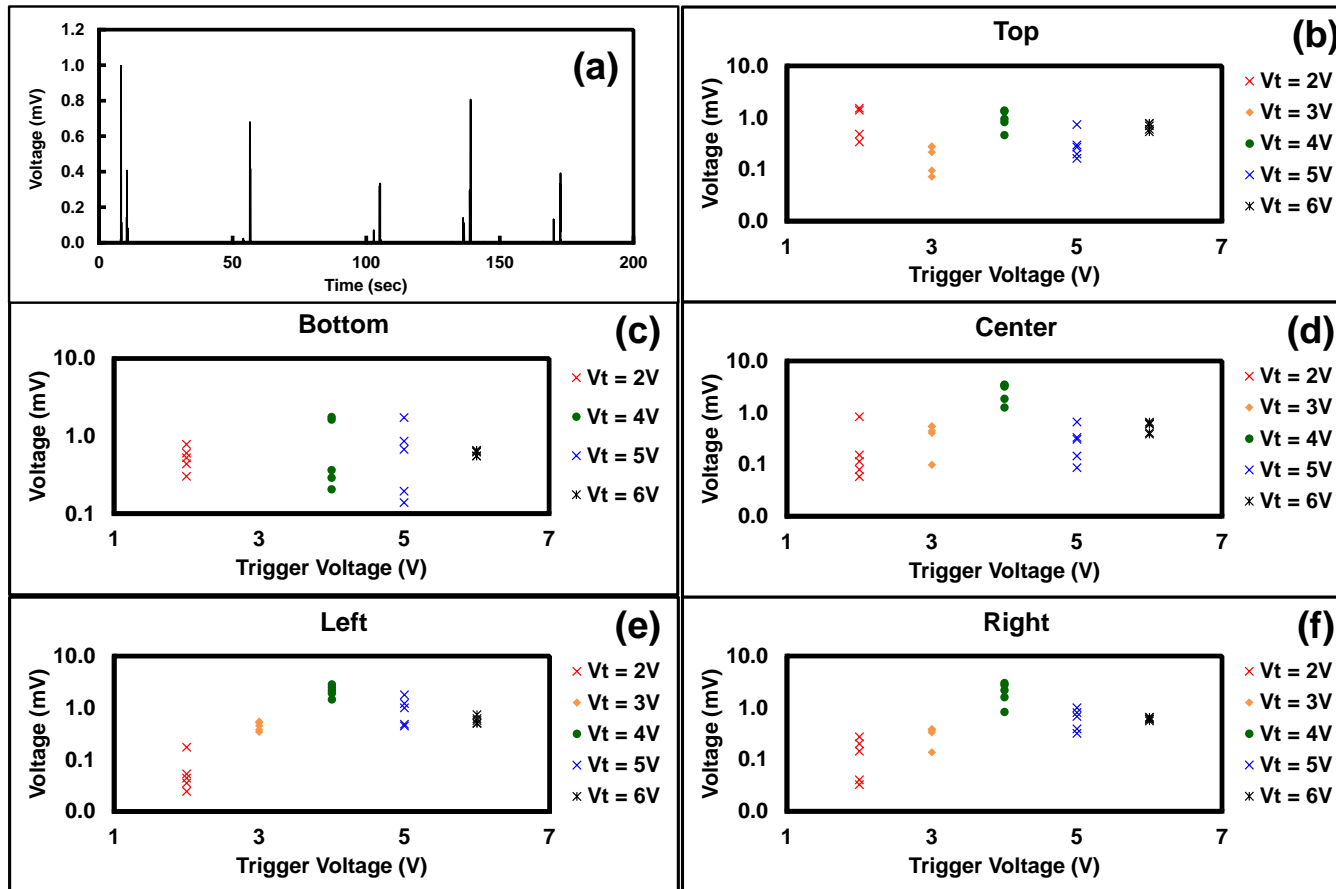


Figure 3-12 (a) an example plot of the piezoelectric signal as a result of the manually triggering the AFM tip to extend into the nanorod array. (b-e) Voltage generated as a result of manually triggering the AFM tip for different trigger voltages, at five different positions on the array as per Figure 3-11

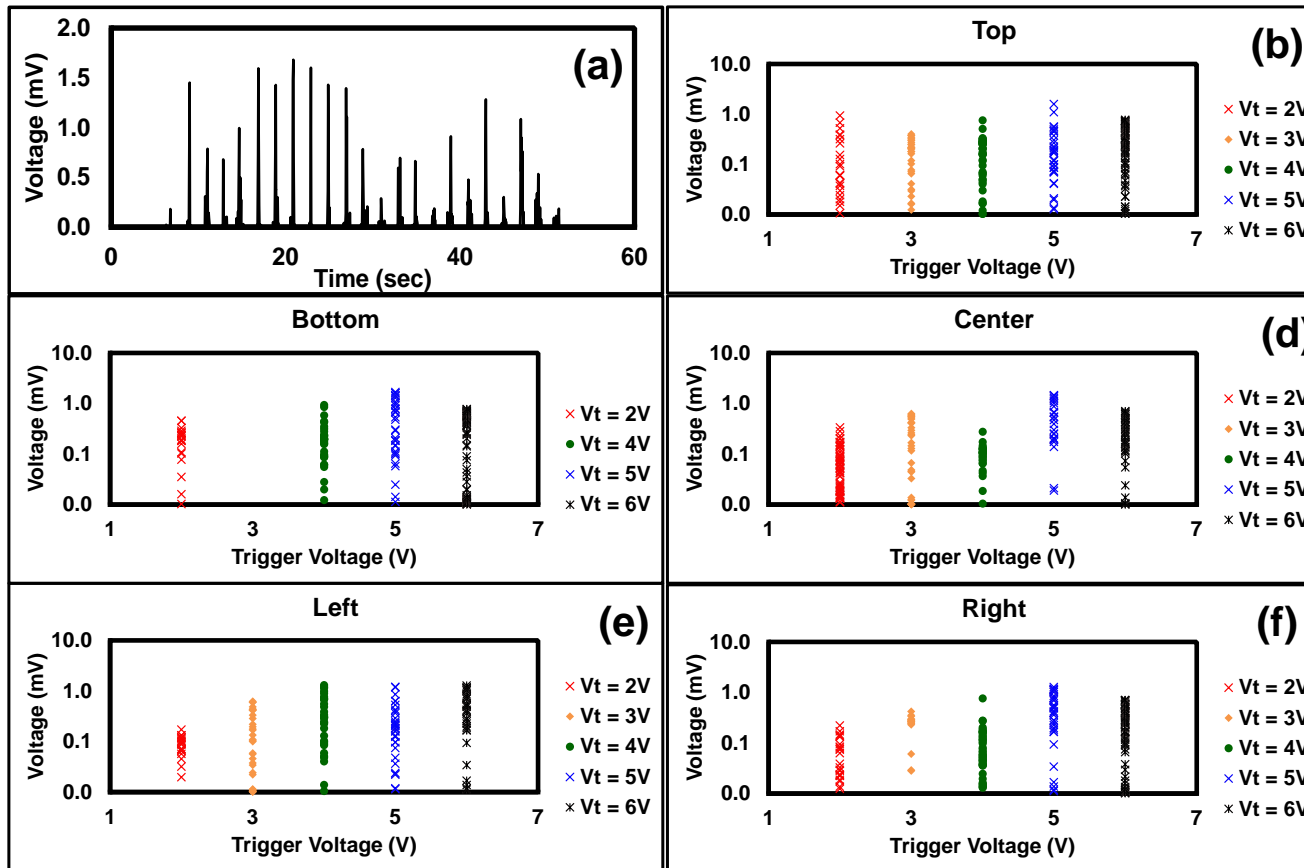


Figure 3-13 (a) an example plot of the piezoelectric signal as a result of the triggering the AFM tip to extend into the nanorod array at a frequency of 1 Hz. (b-e) Voltage generated as a result of triggering the AFM tip at 1 Hz for different trigger voltages at five different positions on the array as per Figure 3-11

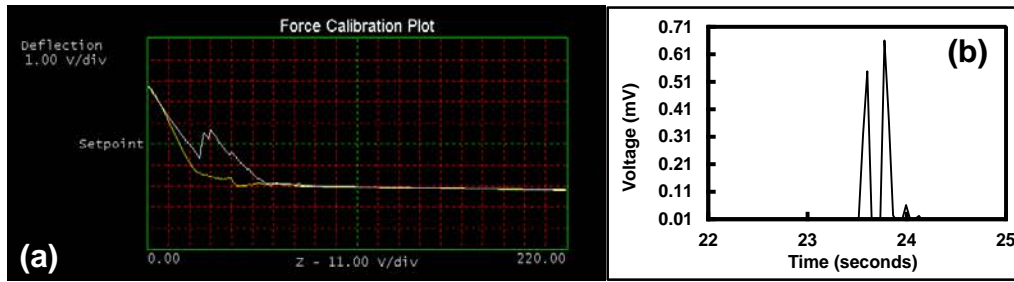


Figure 3-14 (a) Force plot from a single tip-nanorod interaction (b) Corresponding voltage signal from the nanovoltmeter. The irregularity in the extension trace is possibly due to successive bending of two groups of nanorods corresponding to the two voltage peaks seen in (b).

The irregular nature of the force plot precludes the measurement of the slope i.e.  $S_v$  and consequently an accurate determination of the applied force for the particular tip – nanorod interaction event is not possible. In a few instances, however, a smooth force plot is observed and an estimate from those few instances places the applied force in the 8.8 – 47  $\mu\text{N}$  range for trigger voltage of 2 – 6 V.

As seen from Figures 3-12 and 3-13, the magnitude and nature of the experimental tip – nanorod interaction is lower than the simulation estimate. This difference can be attributed to several reasons, one of which is the complexity of the nature of the tip – nanorod interaction. The simulations assume a uniform AFM tip diameter and completely symmetric separation of the nanorods as the tip is pushed into the array, as shown in Fig. 3-10(a). In reality, these differ from the ideal and from experiment to experiment.

The simulations are based on averages for the nanorod dimensions and separation values measured across the fabricated wafer. There is considerable variation, however, from array to array on the wafer. This can cause differences in the lateral stiffness encountered by the AFM tip. A higher lateral stiffness than the one assumed could lower voltage magnitude. Another important reason for the reduced voltage obtained in the experimental results lies in the nature of the electrical contact between the Au coated AFM tip and ZnO. It has been reported that the ZnO - Au contact is a Schottky contact [110]. The simulation assumes an ideal Ohmic

contact with zero contact resistance. Nevertheless, some contact resistance is to be expected owing to miniscule tip – nanorod contact area. The combination of a Schottky barrier and high contact resistance could result in a lower obtained voltage. A third reason, also rooted in the nature of the tip – nanorod interaction, is that the simulation assumes that nanorods will undergo strictly lateral bending resulting in a pure positive voltage extracted from the AFM tip. Considering the random placement of ZnO nanorods, it is likely that the AFM tip vertically compresses some nanorods when it is bending them. The negative voltage generated by the compression could reduce the magnitude of the positive voltage contributed by the lateral bending action, thus resulting in a reduced net voltage at the output (Fig. 3-15).

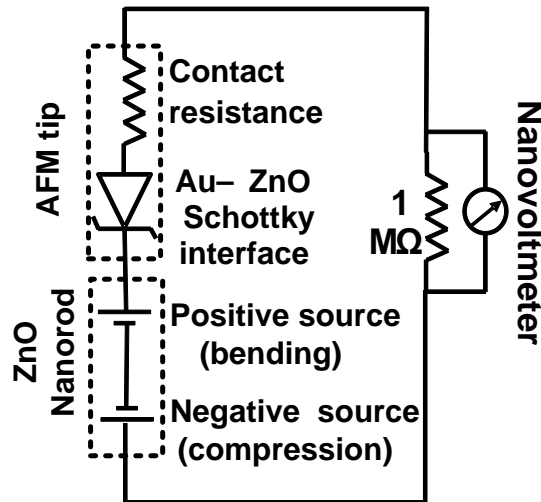


Figure 3-15 Schematic showing an equivalent model for the ZnO nanorod array – AFM tip interaction. It is probable that the AFM tip on some occasions compresses and bends the nanorods simultaneously. This could be represented by two different voltage sources connecting in series. In addition, the Au – ZnO tip interface is represented by a Schottky barrier and contact resistance

Previous studies have noted a similar difference between simulated (hundreds of mV) and experimental (tens of mV) voltages [84]. It is important to note that the observed positive polarity voltage is in response to the vertical motion of the AFM tip with respect to the nanorod array. Song et al. [111] observed a voltage of negative polarity in response to an AFM tip that is

laterally scanned across the array. They also reported an infrequent occurrence of a voltage spike of positive polarity attributed to a breakdown of the ZnO – Pt Schottky barrier. Zhou et al. [112] noted a voltage of positive polarity sensed from the tensile side of a ZnO nanowire. Our observed results (positive voltage spikes) point to a similar conclusion. The much higher frequency of occurrence of the positive voltage spikes is due to the nature of the AFM tip's vertical motion.

### 3.3 Diameter and density controlled low temperature growth of crystalline ZnO nanorods

#### 3.3.1 *Motivation*

In the foregoing discussion involving determination of the magnitude of the force applied to the nanorods, it was observed that an accurate measurement of the sensitivity parameter was not possible due to the complex nature of the nanorod – tip interaction. Moreover, as mentioned, the complexity arose largely due to the randomness of nanorod placement and the variation in topographical characteristics of the nanorods such as diameter and angle of growth with respect to the substrate. These factors directly influence the nanorod density and hence the mechanical, electrical and optical characteristics of any device that employs nanorod arrays. Therefore, control over nanorod diameter, placement and density is of utmost importance for the realization of different types of sensors and MEMS systems.

#### 3.3.2 *Ordered arrays of ZnO nanorods using thermal nanoimprint lithography.*

It has been previously demonstrated that nanorod growth can be restricted to certain areas of the substrate by means of patterning the seed layer using conventional photolithography. This approach provides a means for achieving patterned growth of ZnO nanorods at the micron scale. A similar approach can be used to achieve ordered growth of nanorods at the nano-scale using nanoimprint lithography (NIL). In this approach, the seed layer is masked with a template layer of thermoplastic resist. The resist is patterned using NIL to obtain sub-micron patterns and the residual resist is etched to expose the underlying seed layer for subsequent nanorod growth using the hydrothermal process. It is observed that the areas of

the seed layer that are masked by the thermoplastic resist experience no nanorod growth while the submicron openings where the seed layer is exposed to the growth solution shows nanorod growth (Fig.3-16).

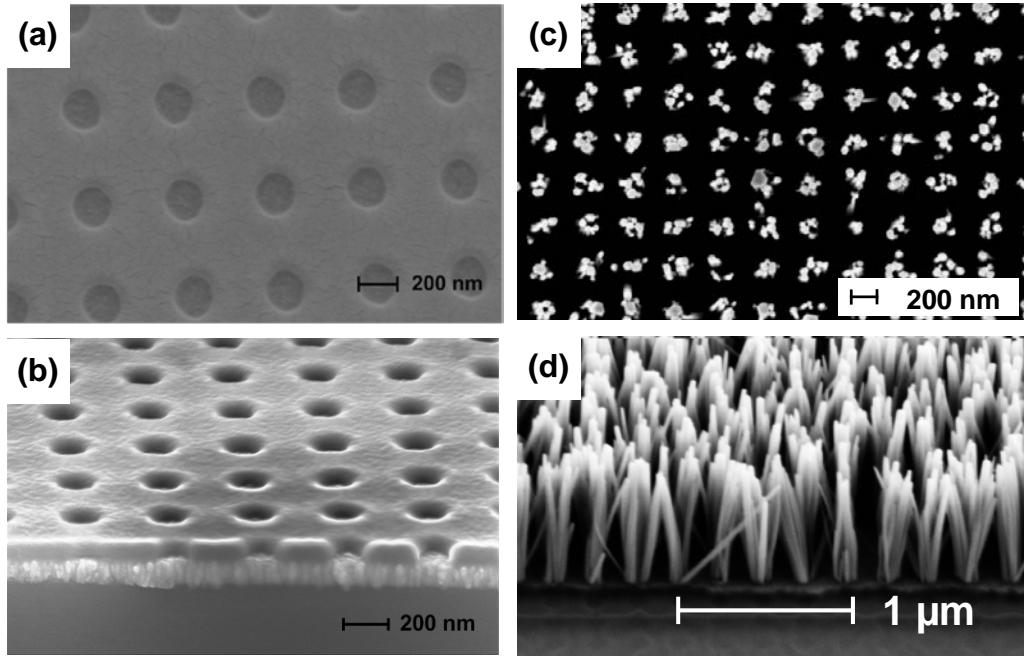


Figure 3-16 Ordered growth of ZnO nanorod arrays using NIL (a)Top view and (b) side view of NIL patterned thermoplastic template on ZnO seed layer. (c)Top view and (d) side view of ZnO nanorods grown after hydrothermal process.

### 3.3.3 Effect of hydrothermal growth solution concentration on diameter of ZnO nanorods

In order to grow a regular ZnO nanorod array with single nanorod per growth site, one approach would be to match the diameter of the nanorod to the diameter of the growth site. Since the diameter of the growth site is fixed by the diameter of the nanoimprint mold, an increase in the nanorod diameter is necessary. Vayssieres [91] observed an increase in nanorod diameter by increasing the concentration of the growth solution constituents while maintaining an equimolar relationship between them. Accordingly, equimolar solutions of Zinc acetate and HMTA were prepared with increasing concentration of the constituents. Hydrothermal growth was carried in 20 mM, 40 mM, 60 mM and 100 mM solutions for a duration of 120 minutes at a constant temperature of 85°C. All samples had a PLD deposited

ZnO seed layer covered with a nano-patterned thermoplastic polymer template. Each sample was examined with SEM (Fig.3-17).

From the SEM images one can conclude that the diameter of ZnO nanorods does indeed increase with an increase in the growth solution concentration. As seen for the 100 mM case, the nanorod diameter increased to such an extent that adjacent nanorods touched each other.

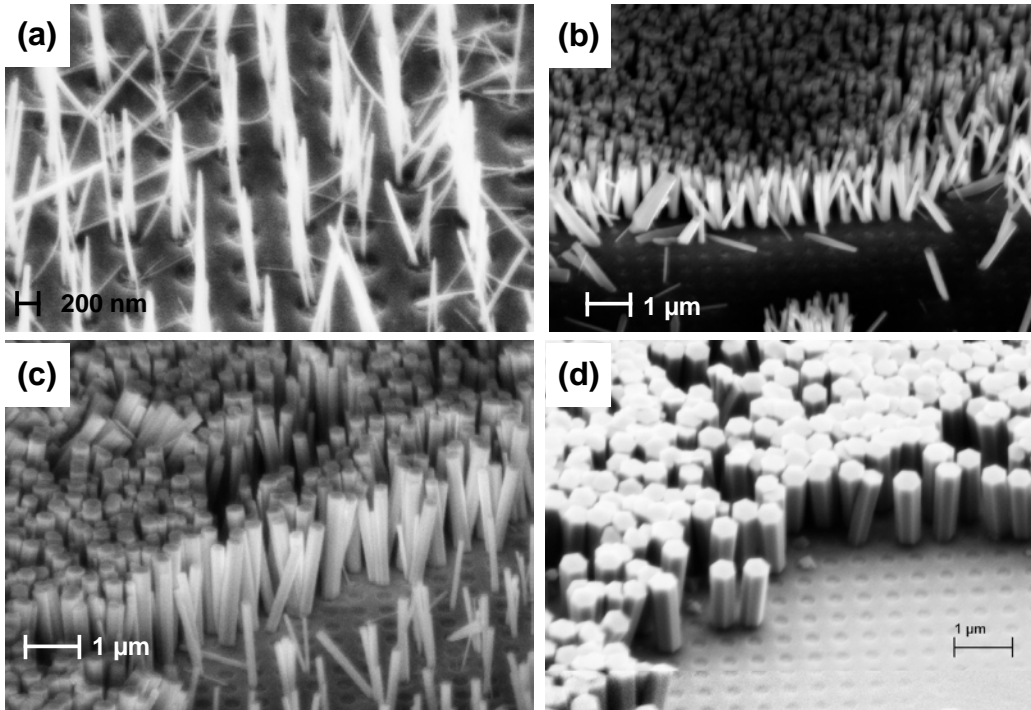


Figure 3-17 ZnO nanorods grown with NIL patterned thermoplastic template at different equimolar concentrations. (a) 20 mM (b) 40 mM (c) 65 mM (d) 100 mM

### 3.3.4 Effect of seed layer deposition temperature

The seed layer for hydrothermal growth was deposited on a 3" (100) silicon wafer using pulsed laser ablation (PLD). A 99.999 % purity ZnO target was ablated using a 248 nm KrF excimer laser at 500 mJ in an oxygen environment. The chamber pressure was maintained at 100 mTorr for all depositions. A deposition rate of 45 nm/ minute was observed. The thickness of the deposited seed layer was measured to be 450 nm. The composition of the film was characterized using Energy Dispersive X-ray Spectroscopy (EDAX) (Fig. 3-18).

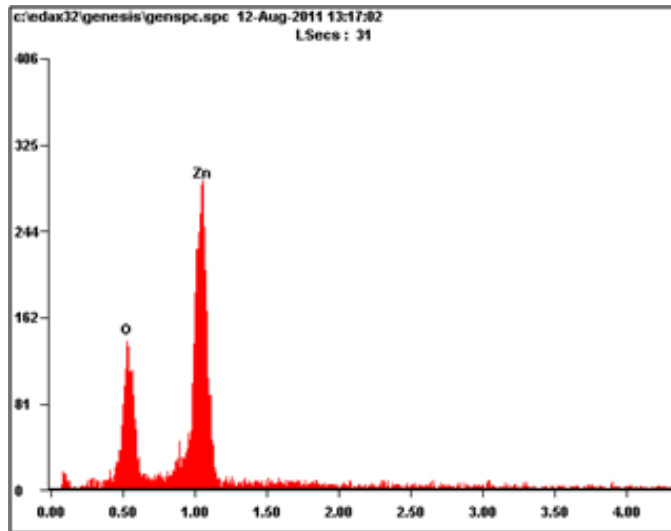


Figure 3-18 EDAX spectrum for ZnO seed layer showing presence of Zn and O

The effect of substrate temperature on the morphology of the deposited film was characterized using X-ray diffraction (XRD). ZnO was deposited while keeping the substrate at 21°C, 200°C and 400°C (in three different depositions). The results are presented below (Fig.3-19).

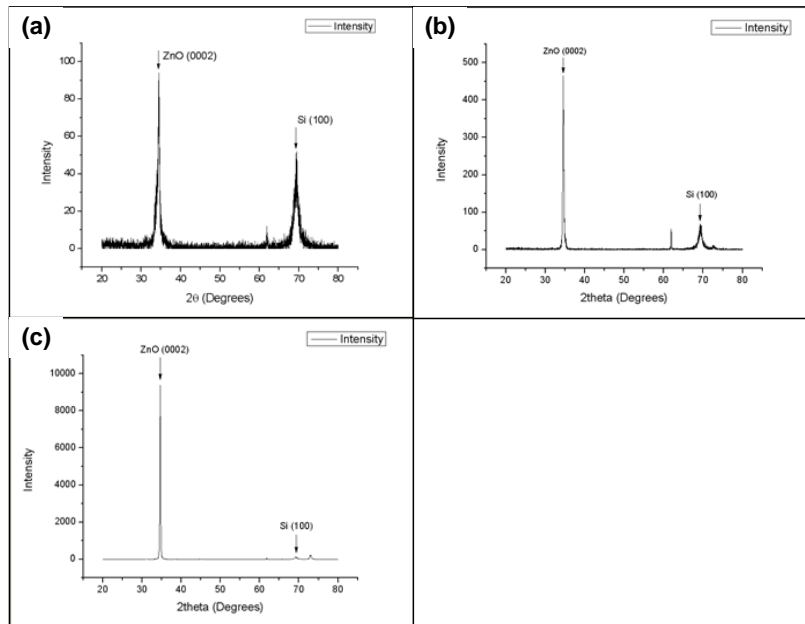


Figure 3-19 XRD spectrum from PLD deposited seed layer at (a) Room temperature (b) 200°C (c) 400°C



The XRD analysis clearly shows the presence of (0002) dominant peak in all samples. This indicates that the ZnO surface is predominantly c-plane oriented and the deposited film has a wurtzite structure. As mentioned before, this orientation of the seed layer is the preferred for subsequent hydrothermal growth of c-plane oriented ZnO nanorods. The Scherrer formulation [113] was used to estimate the grain size of the deposited films at different temperatures (Table. 3-2). It is understood here that this formulation rather than providing the actual grain size, shows the minimum possible grain size for that sample. The estimate is also prone to errors stemming from inherent film strain and instrument calibration.

Table 3-2 Variation of ZnO grain size with substrate temperature

Chamber Pressure (mTorr)	Substrate Temperature C	Bragg Angle ( $2\theta$ ) (degrees)	Cos $\theta$	Peak width (Degrees)	Peak width (Radians)	Grain size ( $\text{\AA}$ )
100	21	34.44453	0.95516	0.64141	0.01119	129.62014
100	200	34.56504	0.95485	0.26981	0.00471	308.24213
100	400	34.65990	0.95461	0.18855	0.00329	441.20002

The results show an increase in grain size with increase in substrate temperature. This is in agreement with results in published literature [114]. The obtained grain sizes were in the range of 12 – 44 nm, which is much lower than the desired diameter of the ZnO nanorods (~200 -250nm). Hence, variation in substrate temperature and the resultant change in grain size was deemed inadequate in terms of influencing the nanorod diameter.

It was observed that increasing the deposition temperature of the seed layer caused the nanorods to grown in a normal fashion to the substrate. The seed layer was deposited by laser ablation of a ZnO target on a 100 silicon wafer in a 100 mTorr  $\text{O}_2$  environment. Two different samples were processed. One sample was kept at room temperature during the seed layer deposition. The other sample was heated to a temperature of 400°C and the ZnO seed layer was deposited. The deposition time for both samples was kept the same, at 10 minutes. Next,

both samples were coated with the thermoplastic template and patterned using NIL. Finally, ZnO nanorods were grown on the samples using the hydrothermal process at 85°C at two different solution concentrations of 40 mM and 85 mM. The results are presented in Figures 3-20 and 3-21

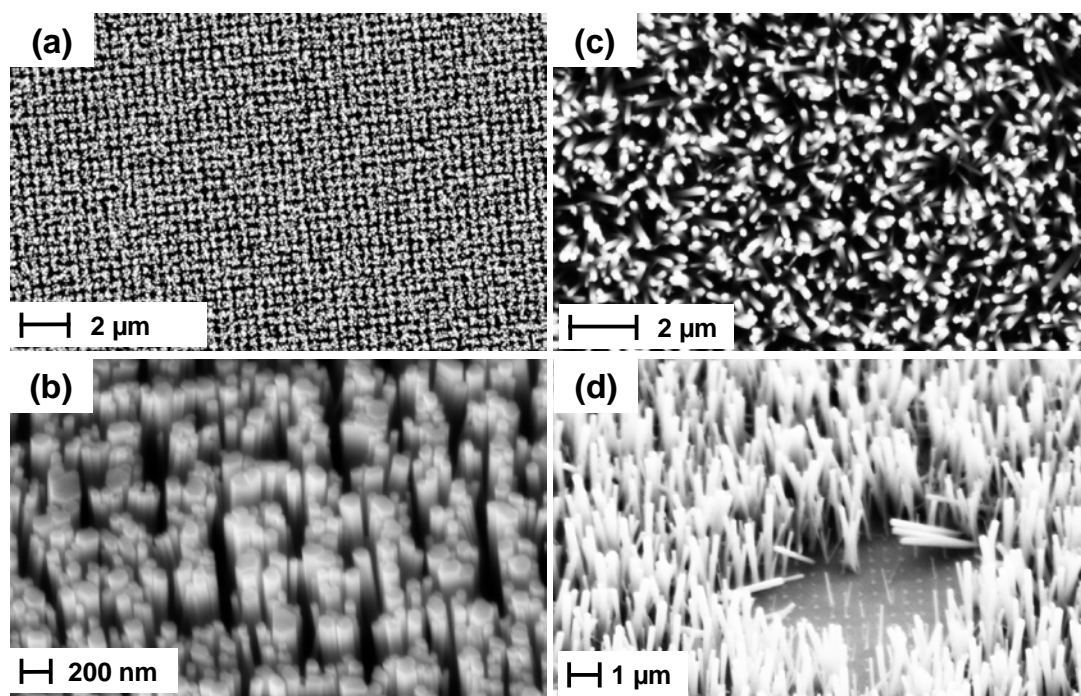


Figure 3-20 SEM images of ZnO nanorods grown using a NIL patterned template at a solution concentration of 40 mM. (a) Top view and (b) side view of nanorods grown on seed layer deposited at 400 °C. (c) Top view and (d) side view of nanorods grown on seed layer deposited at room temperature

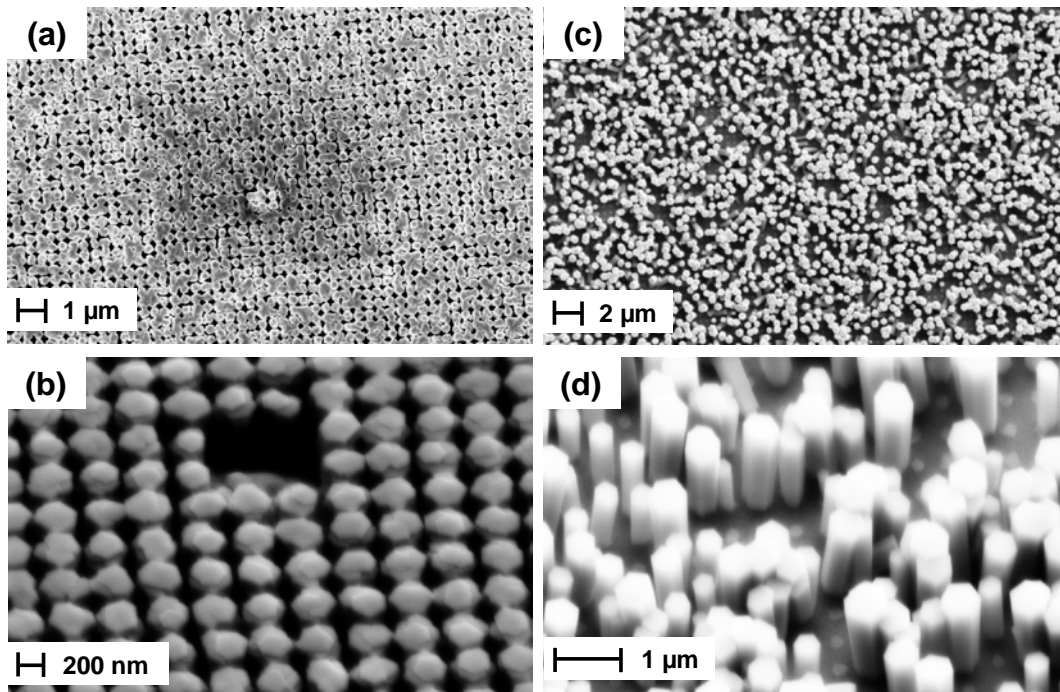


Figure 3-21 SEM images of ZnO nanorods grown using a NIL patterned template at a solution concentration of 85 mM. (a) Top view and (b) side view of nanorods grown on seed layer deposited at 400 °C. (c) Top view and (d) side view of nanorods grown on seed layer deposited at room temperature.

Once again, it is observed that the nanorod diameter increases with increase in the growth solution concentration. More importantly, it is observed that the nanorods grown on seed layer deposited at a higher temperature exhibit improved ordering as compared to the ones grown on seed layer deposited at room temperature. It is also observed that the nanorods grown on seed layer deposited at higher temperature tend to grow in a normal fashion to the substrate as compared to the ones grown on seed layer deposited at room temperature. A possible reason for this growth characteristic could be that orientation of the seed layer grains deposited at higher temperature is more parallel to the substrate as compared to that deposited at room temperature. This experiment demonstrates that seed layer deposition temperature is an important parameter for achieving control over density and placement of nanorods grown using the hydrothermal technique.

### 3.3.5 Fabrication of rows of ordered ZnO nanorods using NIL and conventional photolithography

The previous experiments demonstrate that the different nanorod growth process parameters in conjunction with NIL could be leveraged to obtain ordered growth of ZnO nanorods with some degree of control over nanorod placement and density. These results could be used to alleviate the issues associated with tip-nanorod interaction described in section 3.2.4. It has been already demonstrated that nanorod arrays can be patterned on the micro-scale using conventional photolithography to pattern the seed layer. The approach described in this experiment aims to combine the micro-scale and nano-scale ordering capabilities of photolithography and NIL to realize micro-scale rows of nanorod arrays. The fabrication process starts with patterning of the polycrystalline ZnO seed layer using photolithography and lift-off to create 2  $\mu\text{m}$  wide, 500  $\mu\text{m}$  long rows. The next step involves coating the seed layer with the thermoplastic template, which is followed by NIL and residual resist etching (Fig. 3-22). ZnO nanorods are subsequently grown using the hydrothermal process with an equimolar (30 mM) solution of Zinc Acetate and HMTA at a temperature of 85°C for 120 minutes (Fig. 3-23).

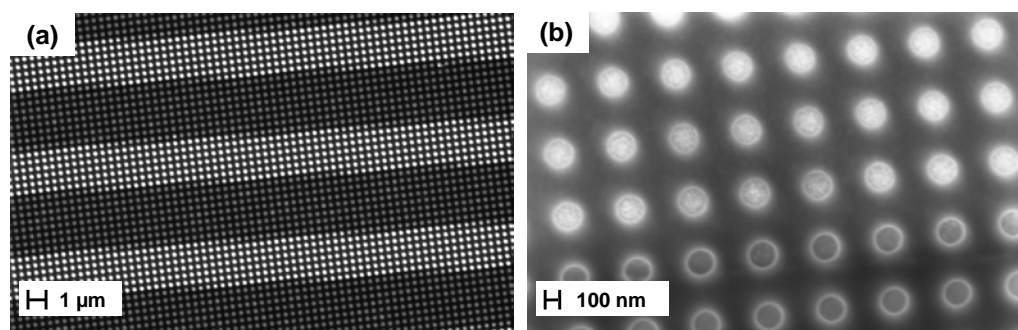


Figure 3-22 SEM images (a) photolithography-patterned seed layer coated with NIL patterned template layer (b) higher magnification image. The ZnO seed layer rows are seen as the lighter band regions in (a) and (b).

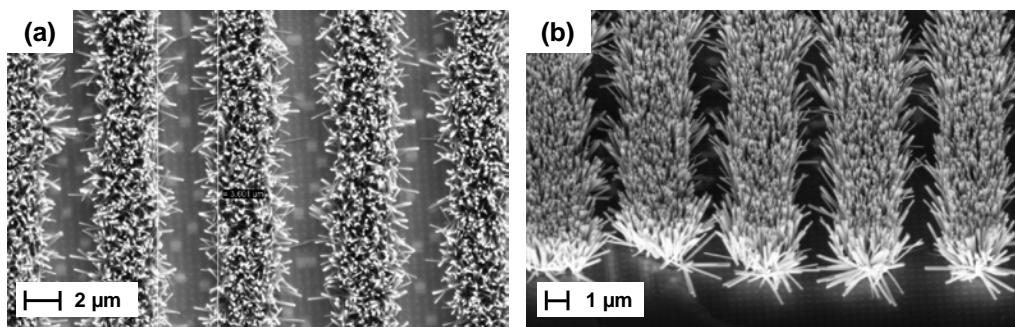


Figure 3-23 SEM images of rows of ordered ZnO nanorods grown using the hydrothermal growth process. (a) Top view (b) Side view

### 3.4 Force spectroscopy characterization of the nanorod array using the Bruker Dimension FastScan AFM system

The newest version of the Bruker AFM systems, i.e. the Bruker FastScan AFM system was used to obtain a force spectroscopy plot from the ZnO nanorod sample. The new AFM system presents a significant advantage over the older D5000 system in the form of closed – loop tip position control. This allowed for accurate placement of the tip at different positions in the nanorod array with nanometer accuracy. The points where the sample was probed at are shown in Figure 3-24.

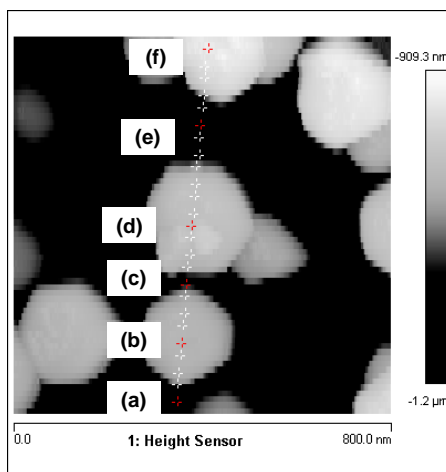


Figure 3-24 AFM image of the nanorod sample with the FastScan AFM system. The red cross marks denote the points at which a force plot was obtained (Image courtesy: Bruker Corporation)

It is consistently observed that the force plot from the gap in between the nanorods is irregular in nature and the force plots obtained from the top flat portion of the nanorods are ideal in nature. This corroborates our earlier finding using the D5000 system as discussed in section 3.2.4.

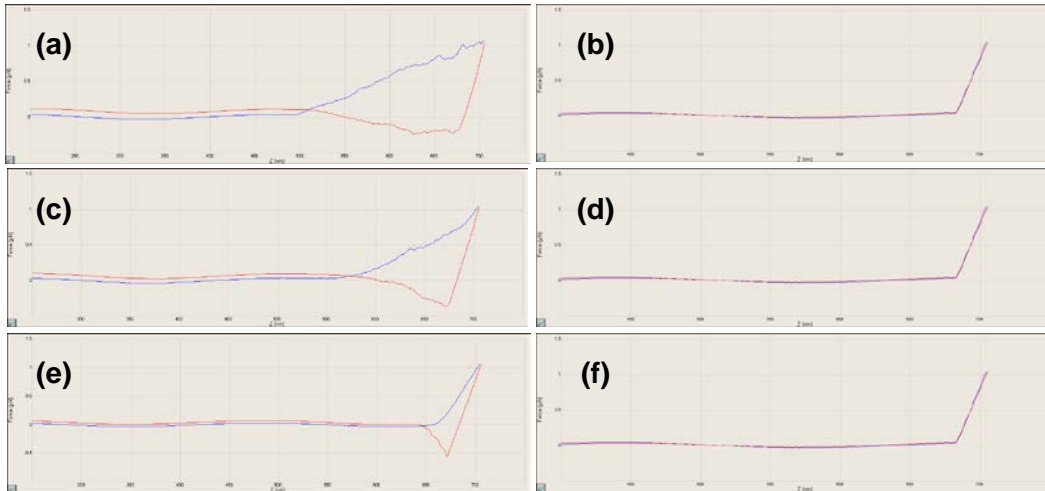


Figure 3-25 Force plots corresponding to each of the probe points shown in Fig. 3-24. Plots obtained using the FastScan AFM system (Courtesy: Bruker Corporation)

### 3.5 Summary

Nanostructures of ZnO have garnered widespread interest in recent times on account of their unique properties. Applications ranging from piezoelectric, photonic, photovoltaic and environmental sensing abound in literature. The present work is geared towards growth and characterization of piezoelectric properties of crystalline ZnO nanorods. An atomic force microscope operating in the advanced force calibration mode (force spectroscopy) was used to apply precisely controlled forces in the nN range. In contrast to previously published reports using lateral tip motion (C-AFM), the action of the tip in our experiment was perpendicular to the plane of the nanorods, allowing a different type of tip – nanorod interaction. Voltage pulses of a positive polarity with amplitude ranging from hundreds of  $\mu\text{V}$  to few mV were observed. The tip – nanorod interaction was modeled using commercial solid modeling software and was simulated using finite element analysis. Comparison of the results yielded useful observations

for design of piezoelectric energy harvesters/sensors using ZnO nanorods. Additionally the effects of process parameters such as solution concentration and seed layer deposition temperature on the morphology of ZnO nanorods were determined. Finally, a NIL based process for ordered growth of ZnO nanorods was developed.

## Chapter 4

A novel NEMS vibration energy harvester using crystalline ZnO nanorods

### 4.1 Vibration energy harvesting introduction, principle of operation, review of the state – of – the – art

Portable devices have become a mainstay of modern living. Advances in semiconductor manufacturing technology have led to an unprecedented miniaturization of a number of systems. While the physical dimensions may have shrunk, the performance and capabilities have improved with each iteration of technology. Starting with the humble handheld calculator of yesteryear, to the multifunctional smartphones of today, capable of computation, communication, imaging and entertainment, portability, compactness and multifunctionality seem to be the technology drivers behind development of consumer electronic systems.

System portability plays a key role in technology development in robotics. Mobile robotic systems are designed for a variety of tasks that include structural health monitoring, hazardous environment operation, human interaction and military defense. Such systems possess an array of specialized equipment such as sensors, actuators computation and communication devices that enable the system to execute its desired operation. The very nature of operation of such systems provides few opportunities for battery replacement. Another related area is wireless sensor networks. These are networks of sensor nodes that are spread over a large area. Each node in the network has limited sensing, communication, processing and energy capabilities. Energy is the most scarcely available resource for the sensor node. These nodes are expected to function without human intervention from weeks to years as human intervention for battery replenishment implies a high network operational cost [115].

Portable devices have made a big impact in the field of medicine. A range of portable devices perform a variety of diagnostic and assistive tasks. Some devices are designed to be implanted or operate completely in – vivo. It is estimated that around 3 million people worldwide use a pacemaker with 60000 implantations per year [116]. Lithium ion batteries used in current



generation pacemakers have a lifetime of 10 years [117] necessitating replacement every decade through surgery. Another cardiac device, the implantable cardioverter defibrillator (ICD) currently uses lithium/silver vanadium oxide batteries that need replacement every 5-10 years, again through invasive surgery [118]. Implantable chemical sensors are being developed that are capable of detecting concentrations of clinically relevant species [119]. Long term operation of devices such as the ones mentioned and others such as neural stimulators, cochlear implants and drug pumps is constrained by the lifetime of their power sources.

As electronic devices increasingly grow more capable, their power requirements also rise. It should be noted though, that modern electronic devices have benefited tremendously from advanced semiconductor technologies such as use of novel materials and scaling which has resulted in drastic reductions in power consumption. Even so, these benefits are overshadowed by the multitasking the devices are expected to perform. As a result, on board power sources i.e. batteries are emerging as one of the most significant limiting factor in development of enhanced devices[120]. Even after several advancements in battery technology, issues related to lower power density, capacity degradation over several charge discharge cycles and safe disposal impose limitations on the performance of the devices that they power. Energy storage capacitors address some of these issues by having higher charge discharge cycles, although their theoretical energy densities are still low [121]. Another energy storage device that is gaining widespread interest is the micro fuel cell. These devices use hydrocarbon based fuels that have much higher energy densities as compared to batteries and capacitors, and do not require re-fueling as frequently as batteries or capacitors need recharging [122]. Nevertheless, the aforementioned power sources are energy storage devices and thus have a finite store of energy that needs to be replenished. This requirement is a serious disadvantage for standalone systems such as wireless sensor networks and medical implantable devices.

Energy harvesting offers a different approach to tackle this issue. Rather than storing pre-generated energy on board, energy harvesting systems generate power by extracting energy from the surrounding environment. The energy sources that these devices tap into are potentially inexhaustible and hence such devices can be used to either power low power devices independently, or augment energy storage devices thus increasing their lifetime. Energy harvesting is not an entirely new concept. Self-winding wrist watches that work by rotation of an inertial mass in response to wrist motion and solar powered calculators are some of the earliest examples of devices that employ energy harvesting. With emergence of a myriad of power-hungry devices in the past couple of decades, interest in energy harvesting technologies is gaining momentum. Several different energy sources are available for harvesting, depending on the environment of the particular application. These include ambient electromagnetic radiation, solar power, ambient thermal gradients, and motion, which includes ambient vibrations, and fluid flow.

Solar energy harvesting using photovoltaic cell arrays is the most mature form of technology [123, 124]. Availability of a constant light source is the primary limiting factor prohibiting widespread use in wireless sensor networks. Additionally photovoltaic devices need to be in the line of sight of the light source, which may not be possible in certain scenarios. Energy harvesters employing the thermoelectric effect have been proposed for scavenging energy from human body heat. These devices employ the Seebeck effect wherein a voltage drop is generated across the thermoelectric material in response to a temperature gradient [125]. The drawback is that, when such devices are deployed at micron scales, the temperature gradients tend to be insignificant and therefore the voltage generated is lower [126]. Energy harvesting from ambient radiation is also hampered by unavailability of significant RF power levels and extraction efficiency using devices that are smaller than the available wavelengths is lower [127]. Kinetic energy either from motion or vibrations is the most abundant form of energy

available [126], and thus forms the focus of the energy harvesting technology used in this research.

Energy harvesters employing ambient vibrations as the energy source have been a subject of significant interest since Roundy et al [128] demonstrated a cantilever based macro scale piezoelectric energy harvesting device for powering wireless sensor nodes. Several different approaches including piezoelectric, electrostatic and electromagnetic energy harvesters [129-131] have been proposed by different researchers in the field. Extensive studies of ambient vibrations from different sources in the environment ranging from milling machines to commercial aircraft have also been reported [128, 132]. An examination of the various studies done to date reveals the following important requirements common to all vibration energy harvesting systems.

- The ability to generate useful electric energy from very low (0.1 – 1 g) vibration amplitudes.
- The device should have a resonant frequency close to the frequency of the incoming vibration. These frequencies are typically in the range of 100 – 4000 Hz.
- With increasing focus on the system – on – chip approach, that consists of the sensor, data processing unit, energy harvesting unit and the data transfer unit on the same chip, energy harvester designs are expected to be integration friendly with existing chip components and should have the lowest possible footprint on the system die.

Regardless of the physics of the device (i.e. piezoelectric, electrostatic or electromagnetic) all vibration energy harvesters can be represented by the mass –spring – damper formulation. Figure 4-1 shows a generic mass spring damper system.

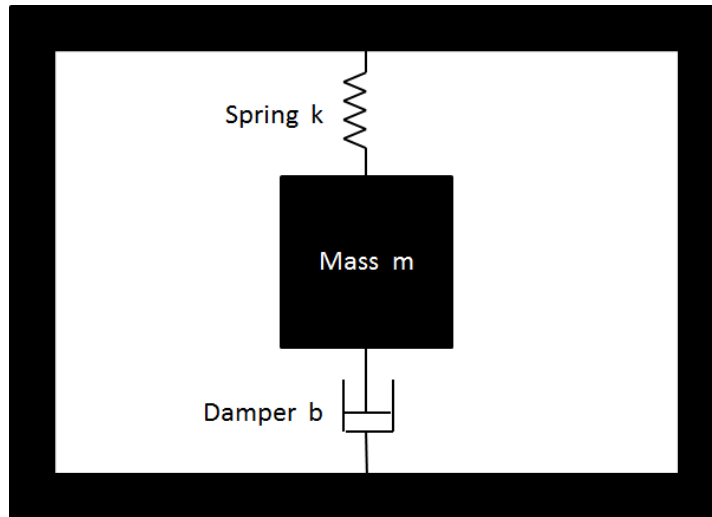


Figure 4-1 Mass spring damper system

When a force  $F$  is applied to this system, the dynamic behavior can be given by the mass spring damper system equation [133].

$$m \frac{d^2 x}{dt^2} + b \frac{dx}{dt} + kx = F(t) \quad (4-1)$$

The resonant frequency of this system is given by,

$$f_{res} = \frac{1}{2\pi} \sqrt{\frac{k}{m}} \quad (4-2)$$

Where,

$m$ : mass of the proof - mass

$b$  : damping constant for the system

$k$  : spring constant of the system

$F$ : applied force

$f_{res}$  : resonance frequency

$x$  : displacement of the proof - mass

Recently, the piezoelectric properties of ZnO nanowires have been brought into focus by the work of Wang et al [134]. As a piezoelectric material, ZnO nanorods offer several advantages such as enhanced piezoelectric effect, superior mechanical properties and high

sensitivity to small forces [135]. Energy harvesting devices using macro scale flexure [136] and ultrasonic agitation [137] have been demonstrated that can generate voltage from few tens to few hundreds of mV.

The energy harvester presented in this research extends the concepts developed in the aforementioned studies to satisfy the requirements necessary for successful operation in a real-world environment. Three different designs employing piezoelectric ZnO nanorods as the energy transduction element are evaluated for performance using finite element modeling. The final design consists of a nanoelectromechanical (NEMS) piezoelectric energy harvester that converts ambient vibrations into usable electrical energy for low power sensor applications. This is accomplished by mechanical excitation of an ordered ZnO nanorod array using a suspended bulk micromachined proof - mass. The device is capable of generating up to 14.2 mV single polarity voltage under an input vibration of amplitude 1 g (9.8 m/s<sup>2</sup>) at a frequency of 1.10 KHz. A process flow for fabrication of such a device is developed. It is shown that the control over nanorod density and placement afforded by NIL is key to successful realization of such a device.

## 4.2 Design of a NEMS vibration energy harvester using piezoelectric ZnO nanorods

### 4.2.1 Z - axis vibration energy harvester

#### 4.2.1.1 Principle of operation and design

The z - axis energy harvester design aims to utilize vibrations normal (hereinafter referred to as the z - axis) to the plane of the device to generate energy. This is achieved by using a mass – spring – damper system to cause mechanical elastic deformation of the ZnO nanorods along their C –axis. The design envisages an electroplated proof - mass suspended by a membrane spring. Such a configuration has been reported to have low stiffness in the z - direction and high stiffness in the planar directions [138]. This property is of special importance because while a low stiffness in the z direction is desirable for inducing maximum strain, a low stiffness in the planar directions can cause the nanorod array to bend; thereby shorting out the

nanorod across its cross section. Figure 4-2 represents a schematic description of the Z axis design.

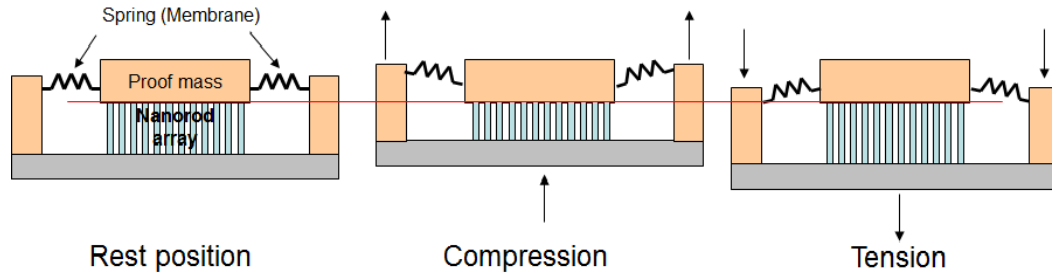


Figure 4-2 Schematic description of z – axis energy harvester under z - axis vibration

A NEMS device was designed around the aforementioned principle of operation (Fig. 4-3 and Fig.4-4). The device consists of a nickel proof - mass seated atop a thin ( $0.5 \mu\text{m}$ ) conductive Au/Al membrane. The membrane and the proof - mass are positioned over an array of ZnO nanorods grown on top of a conductive Au electrode. The membrane is in contact with the tops of the nanorods in the array and acts as the other electrode. In this device structure, the membrane serves the dual purpose of a mechanical spring, pliant in the z - axis, and an electrode for extracting the voltage generated by the nanorods when subjected to compressive forces. Accordingly, the z – axis harvester was modeled and the behavior under an applied acceleration was simulated using CoventorWare software.

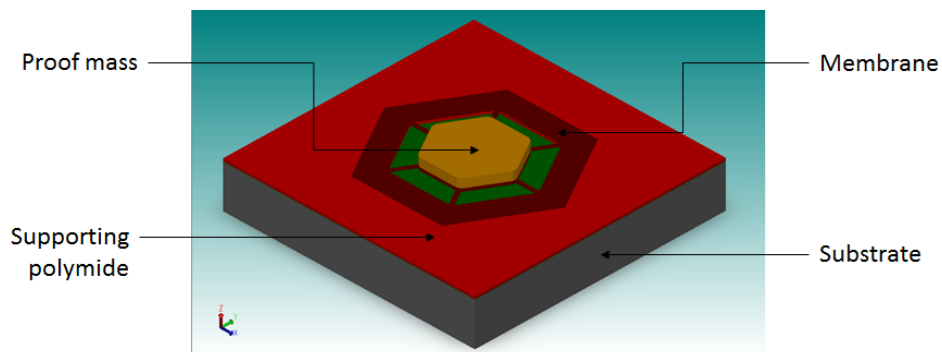


Figure 4-3 Solid model of z - axis energy harvester

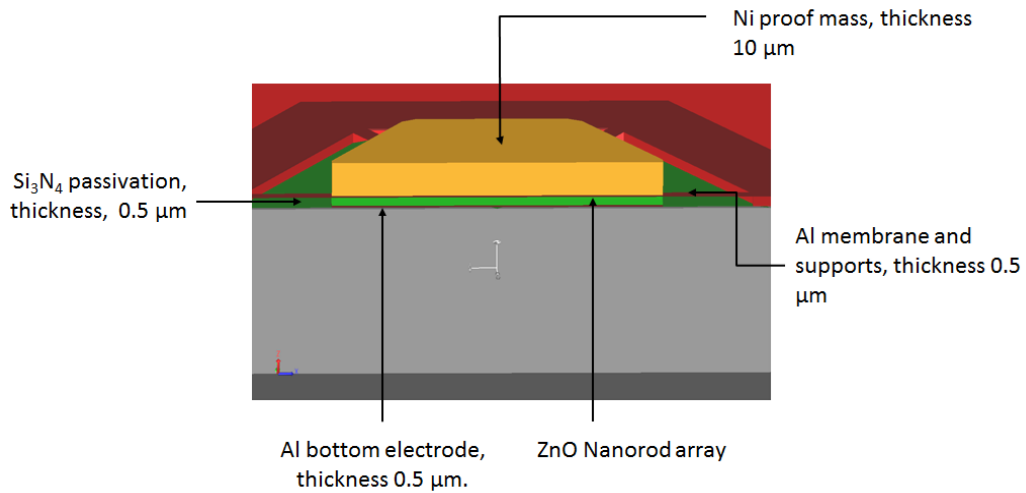


Figure 4-4 Cross section view of z - axis energy harvester model

The design of the membrane structure and consequently the vertical stiffness of the device was varied to observe the effect on device behavior. Accordingly, three different designs were developed (Table 4-1).

Table 4-1 z – axis energy harvester designs and dimensions

Design : HEXA 4	Design HEXA 4A	Design : HEXA 4B
Proof - mass/shuttle plate: Hexagonal, 50 μm leg length.	Proof - mass/shuttle plate: Hexagonal, 25 μm leg length.	Proof - mass/shuttle plate: Hexagonal, 25 μm leg length.
Supports: 6 supports, 25 μm long, 5 μm wide.	Supports: 6 supports, 10 μm long, 5 μm wide.	Supports: 3 supports, 10 μm long, 5 μm wide.

#### 4.2.1.2 Analysis of operation using finite element methods

Each of the models was meshed using polygonal extruded brick elements and simulated for displacement using the CoventorWareMemMech FEM solver. An example is

shown in Figure 4-5. The boundary conditions for the FEM analysis were as follows; an acceleration of 2 g was applied to the proof - mass in the  $-ve$  z direction to simulate the effect of 1 g vibration in addition to gravity. Displacement was restricted in all directions at the bottom of the passivation nitride layer (Fig. 4-6).

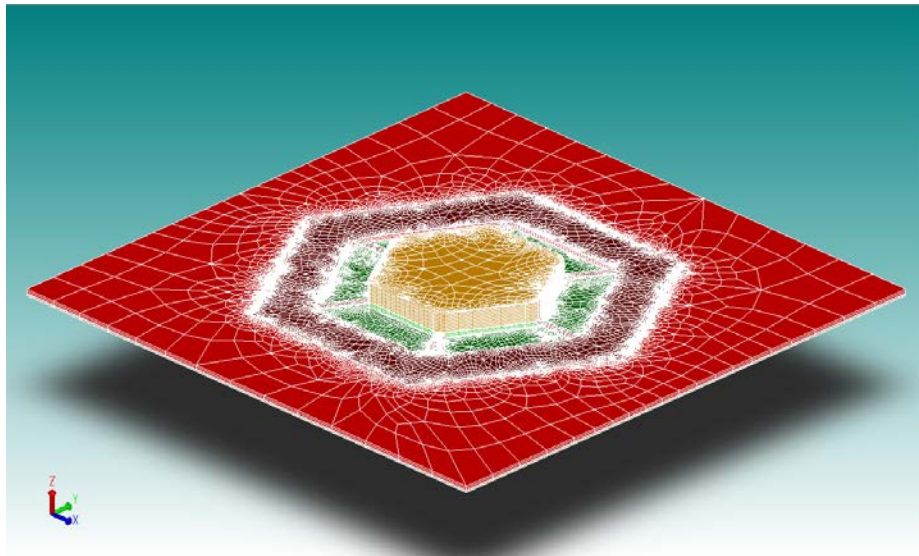


Figure 4-5 HEXA 3 model meshed with extruded brick elements

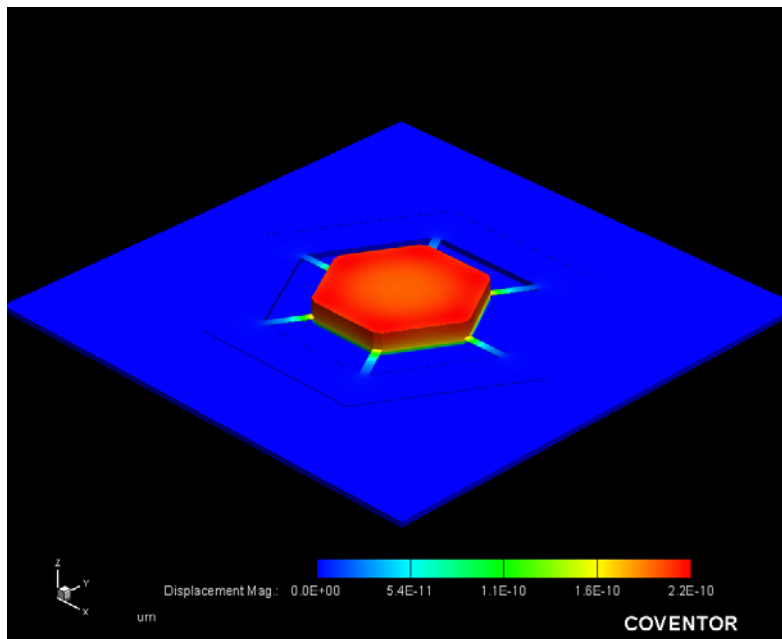


Figure 4-6 Simulated displacement for HEXA 3 Model under 2 g  $-ve$  z - direction acceleration



The meshing of thousands of nanoscale structures (nanorod array) concurrently with the larger membrane, proof - mass etc. presented a computational challenge in terms of number of elements required. To resolve this issue, the nanorod array was modeled as a solid block composed of an isotropic material whose Young's modulus and Poisson's ratio were adjusted to match that of a nanorod array with a similar thickness and occupying the same area. The formulation for the adjustment of the Young's modulus is presented next.

The relationship between number of nanorods in an array and the stiffness represented by that array was found by multiple FEM simulations involving a nanorod array put under compression by means of a proof - mass subjected to -ve z - axis acceleration. In each simulation, the number of nanorods in the array was increased from the previous one; with a corresponding increase in the area of the proof - mass. The thickness of the proof - mass and the height of the nanorods were kept constant for all simulations. The stiffness was found from the force applied (known) and the displacement obtained from the simulation. A representative simulation result (Fig. 4-7) and the results from all simulations (Fig. 4-8) are shown below.

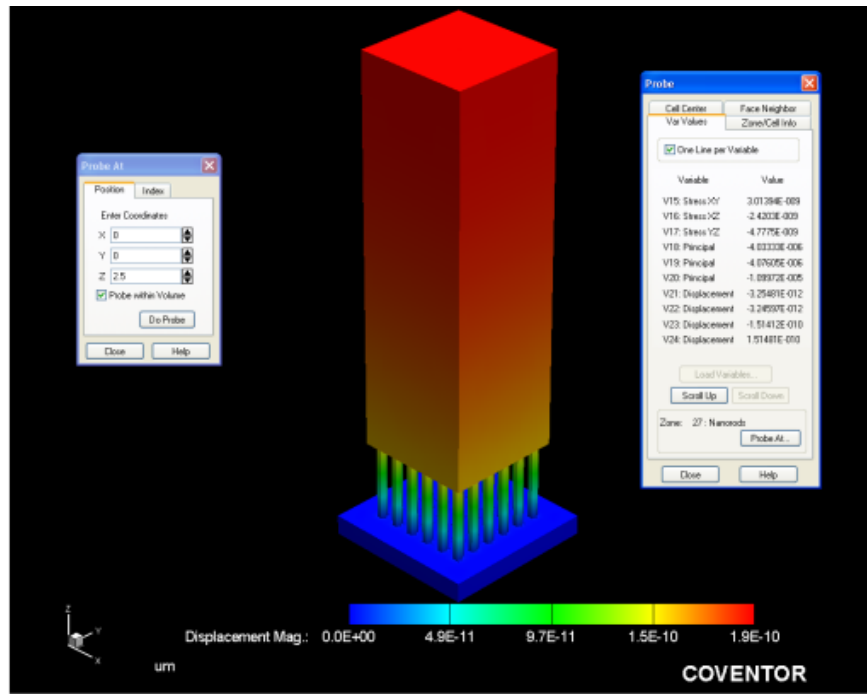


Figure 4-7 A proof - mass compressing a nanorod array of 6 x 6 nanorods

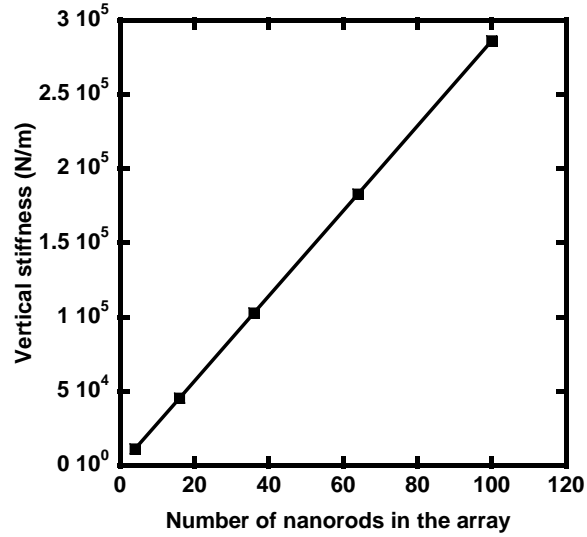


Figure 4-8 Stiffness of nanorod array vs. number of nanorods

From the graph it is evident that the stiffness of the nanorod array varies linearly with the number of nanorods in the array. The assumption here is that the pitch of the array and the dimensions of individual nanorods do not change. This means that, to match the stiffness of the representative block and the nanorod array, one only has to account for the empty space between individual nanorods. Accordingly, an equivalent Young's modulus for the block can be easily calculated from the following simple formulation.

$$\sigma = Y * \epsilon \tag{4-3}$$

$$\frac{F}{A} = Y * \frac{\Delta x}{x} \tag{4-4}$$

$$\frac{k * \Delta x}{A} = Y * \frac{\Delta x}{x} \tag{4-5}$$

$$k = \frac{Y * A}{x} \tag{4-6}$$

Where,

$\sigma$  : Stress

$\epsilon$  : Strain

$Y$  : Young's Modulus

$k$  : Stiffness

$A$  : Area of cross section

$x$  : length

$\Delta x$  : change in length

Putting  $k$  as the required stiffness from the representative nanorod block,  $A$  and  $x$  as the area and height respectively of the block, one can calculate the Young's modulus ( $Y$ ) necessary to achieve the same stiffness as the nanorod array the block is intended to replace. From calculations, the  $Y$  was found to be 22.9 GPa. All further simulations were done using this  $Y$  and 0.3 as the Poisson's ratio. It was found that the difference in FEM results from a nanorod array and its representative block differed by 0.7 %. This can be attributed to the fact that the block was modeled as an isotropic material while ZnO nanorod array was modeled with anisotropic material properties. As such, the error is insignificant and therefore the use of this formulation for further simulation of large area nanorod arrays is justified due to the enormous reduction in computation time.

#### 4.2.1.3 Z – axis energy harvester - device behavior results and discussion

Accordingly, the designs HEXA 3, HEXA 4A and HEXA 4B were simulated with representative nanorod blocks. The displacement of the structure under a known force was found using simulation and the resulting spring constants for each case were calculated. The resonance frequency in each case was calculated using the formula mentioned earlier (Eqn. 4.2).

Table 4-2 Calculation of spring constants and resonance frequencies for the z – axis harvester designs

Design name	HEXA 3	HEXA 4A	HEXA 4B	Units
Area of the proof - mass	$6.47 \times 10^{-9}$	$1.60 \times 10^{-9}$	$1.60 \times 10^{-9}$	$m^2$
Thickness of the proof - mass	$1.00 \times 10^{-5}$	$1.00 \times 10^{-5}$	$1.00 \times 10^{-5}$	m
Volume of proof - mass	$6.47 \times 10^{-14}$	$1.60 \times 10^{-14}$	$1.60 \times 10^{-14}$	$m^3$
Density of proof - mass (electroplated Ni)	$8.91 \times 10^{-3}$	$8.91 \times 10^{-3}$	$8.91 \times 10^{-3}$	$kg/m^3$
Mass of the proof - mass	$5.77 \times 10^{-10}$	$1.43 \times 10^{-10}$	$1.43 \times 10^{-10}$	kg
Acceleration	$1.96 \times 10^{-1}$	$1.96 \times 10^{-1}$	$1.96 \times 10^{-1}$	$m/s^2$
Force (as a result of acceleration)	$1.13 \times 10^{-8}$	$2.80 \times 10^{-9}$	$2.80 \times 10^{-9}$	N
Displacement without the NW block (obtained from simulation)	$7.60 \times 10^{-10}$	$1.70 \times 10^{-11}$	$3.30 \times 10^{-11}$	m
Spring constant k without NW block	$1.49 \times 10^1$	$1.65 \times 10^2$	$8.48 \times 10^1$	N/m
Displacement with the NW block (obtained from simulation)	$2.20 \times 10^{-16}$	$2.10 \times 10^{-16}$	$2.10 \times 10^{-16}$	m
Spring constant k with NW block	$5.14 \times 10^7$	$1.33 \times 10^7$	$1.33 \times 10^7$	N/m
Resonance frequency without NW block	$2.56 \times 10^4$	$1.71 \times 10^5$	$1.23 \times 10^5$	Hz
Resonance frequency with NW block	$4.75 \times 10^7$	$4.86 \times 10^7$	$4.86 \times 10^7$	Hz

From the results in Table 4-2, the resonance frequency for all three designs is seen to be in the megahertz range. This is over three orders of magnitude more than the target resonant frequency of 1 kHz. The main cause of such a high resonance frequency is the large stiffness of the ZnO nanorod array. One approach to solve this issue is to either increase the volume of the proof - mass or to reduce the dimensions of the nanorod array or both. However, a significant reduction in the nanorod array area or increase in the proof - mass size would be necessary, which would result in a corresponding decrease in the normalized energy, which is the energy generated/unit volume. Clearly, a different design approach is needed to reduce the stiffness of the nanorod array, to achieve the required reduction in the resonant frequency.

#### 4.2.2 Lateral motion vibration energy harvester

##### 4.2.2.1 Principle of operation and design

The lateral axis design employs a spring suspended proof - mass that can translate in the lateral direction in response to vibration in – plane with the substrate. An electrode attached to the proof - mass, bends individual nanorods in an array, thereby inducing bending stress in the nanorods. The  $d_{31}$  piezoelectric coefficient causes opposing potentials to be developed on opposite sides of the nanorod. The electrode is designed such that it encircles each nanorod and makes contact with only the side under tensile stress. This resolves the issue associated with the nanorod “shorting” across its cross section. An added advantage is that the generated output voltage has a single polarity and hence the device does not need an external rectifier for signal conditioning. The structure of the lateral energy harvester is shown in Figure4-9 and Figure 4-10.

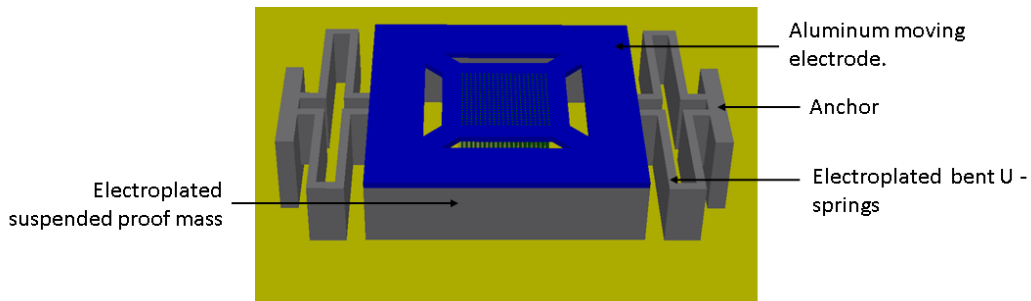


Figure 4-9 Lateral motion energy harvester design

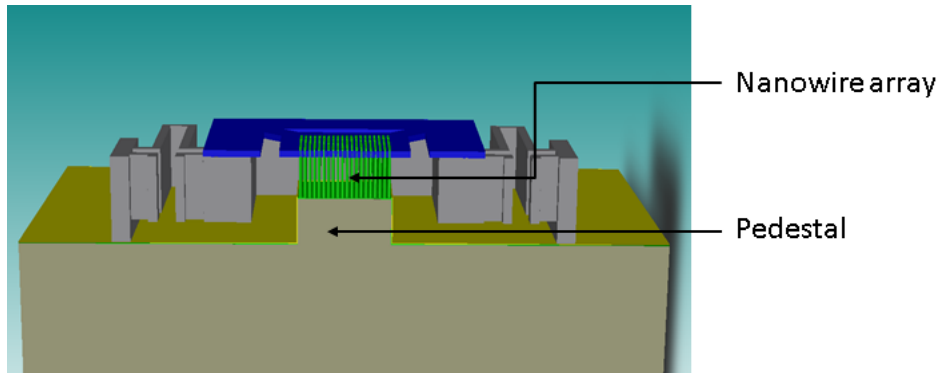


Figure 4-10 Cross sectional view of lateral motion energy harvester showing the position of the nanorod array

Figure 4-11 shows a zoomed in top view and a cross section view of the electrode – nanorod arrangement. At rest position, the electrode does not make contact with the nanorods. When the device is excited with in plane vibrations, the proof - mass translates in-plane dragging the electrode along with it. The electrode then makes contact with the nanorods which are in turn bent. The bending results in voltage generation across the opposite surface of the nanorod as explained previously, which is then extracted by the electrode.

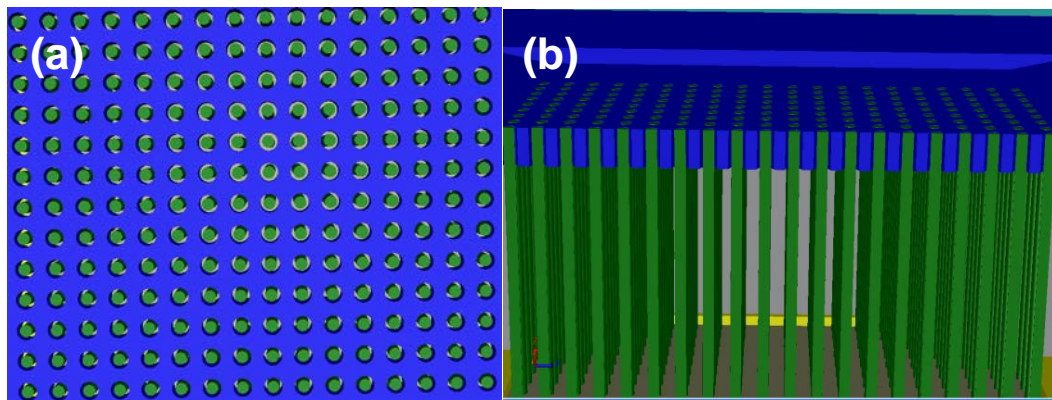


Figure 4-11 (a) Top view of nanorod array (green) and electrode (blue) (b) Cross sectional side – view of the nanorod array and electrode.

#### 4.2.2.2 Evaluation of device performance using finite element modeling.

As was observed in the case of z - axis energy harvester, the significant stiffness of the nanorod array was a deciding factor in driving up the resonance frequency. Since the bending

stiffness of an elastic bar is less than stiffness under compression or tension, it was expected that the nanorod array would present a reduced overall stiffness and hence a reduced resonant frequency. Therefore, with a view to obtain an initial estimate of the reduction in resonant frequency, a simplified model of the lateral energy harvester was constructed, as shown in Figure 4-12 and 4-13.

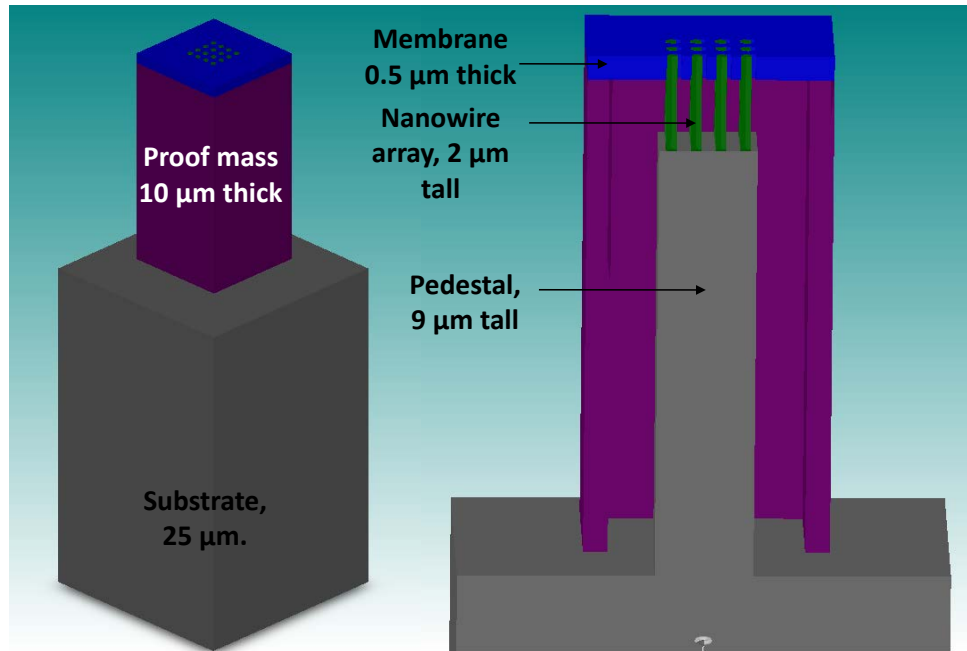


Figure 4-12 Left - Simplified solid model for simulation of the lateral motion energy harvester.

Right – Cross section

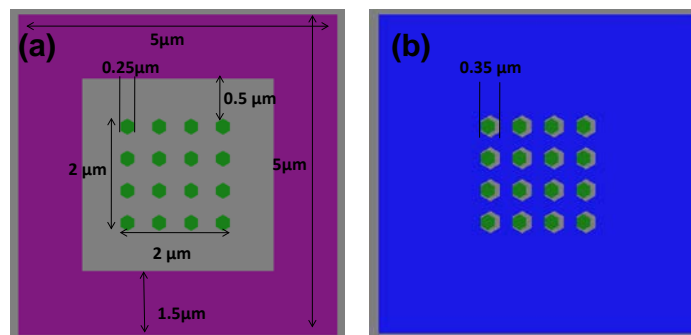


Figure 4-13 (a) Top view of the simplified solid model of lateral motion energy harvester with membrane electrode hidden (b) with membrane electrode

The structure was meshed and simulated to obtain the displacement under an applied acceleration of 1 G in the +X direction. The mesh and boundary conditions are shown in Figure 4-14.

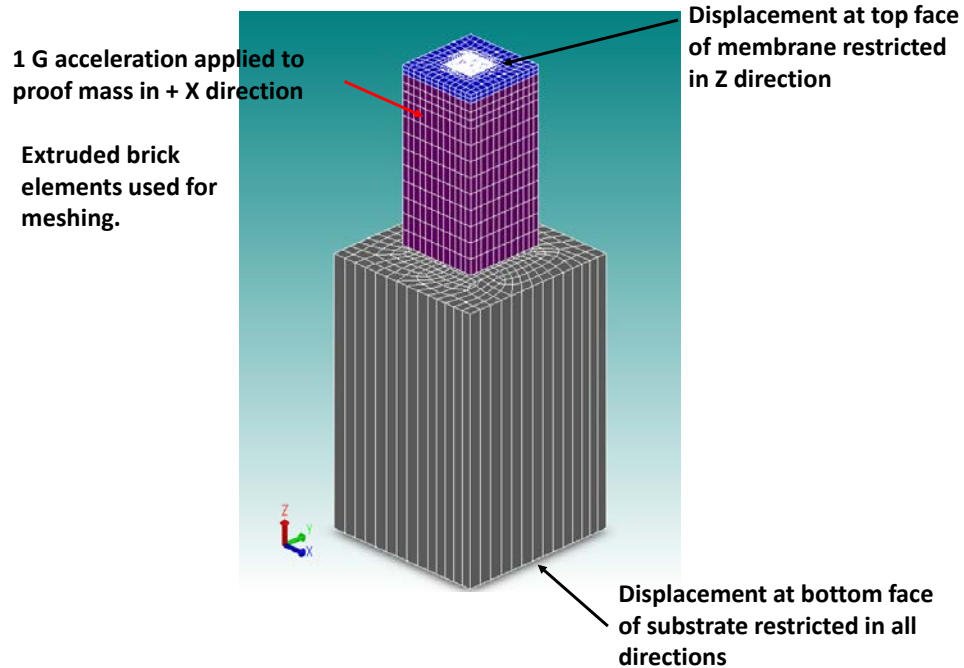


Figure 4-14 FEM boundary conditions, meshing and loading for the simplified lateral energy harvester model

To compare this lateral bending design with the z - axis design, in terms of stiffness, the same nanorod array was compressed using a proof - mass having the same volume (as the lateral bending design proof - mass). An acceleration of 1 g was applied in the -ve z direction and the model was simulated for displacement (Fig. 4-15). Knowing the force in each case, the stiffness of each design was calculated from the simulated displacements.

#### 4.2.2.3 Lateral motion energy harvester - device behavior results and discussion

The results are presented in Table 4-3.



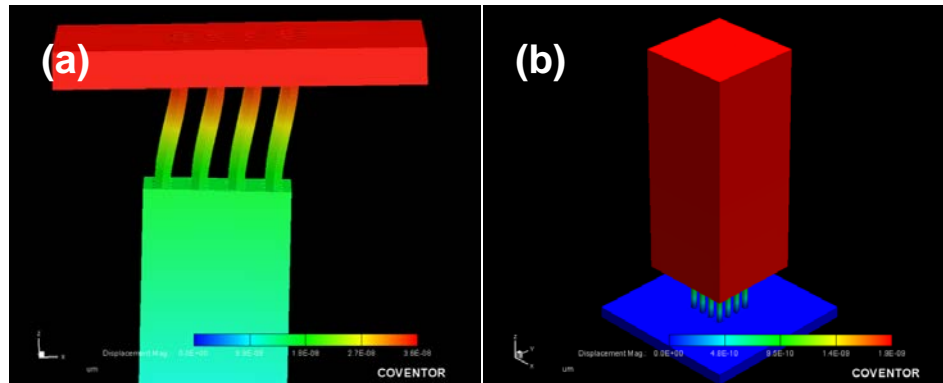


Figure 4-15 (a) Lateral motion design under 1 g acceleration in +ve x direction (The proof - mass is hidden) (b) Displacement simulation for a simplified z - axis design for comparison

The lateral bending design provides approximately an order of magnitude reduction in the resonance frequency over the z - axis design. The lateral bending design was therefore further explored via FEM simulation to observe the effects of nanorod length, proof - mass size, nanorod array area and nanorod array pitch on the resonance frequency of the structure.

To study the effect of nanorod length and proof - mass size, the nanorod array area was kept constant at  $2 \mu\text{m} \times 2 \mu\text{m}$ . The thickness of the proof - mass was also kept constant at  $10 \mu\text{m}$ . The stiffness and resonance frequency were calculated as before, from the simulated displacement and known applied force (1 g +ve x acceleration). The results are shown in Figure 4-16.

Table 4-3 Calculation of spring constants and resonance frequencies for the z – axis and lateral energy harvester designs

	<b>Z - Axis</b>	<b>Lateral</b>	<b>Units</b>
Volume of proof - mass in $\text{m}^3$	$1.60 \times 10^{-16}$	$1.60 \times 10^{-16}$	$\text{m}^3$
Density of proof - mass (electroplated Ni)	$8.91 \times 10^{-3}$	$8.91 \times 10^{-3}$	$\text{kg}/\text{m}^3$
Mass of the proof - mass	$1.43 \times 10^{-12}$	$1.43 \times 10^{-12}$	kg
Acceleration applied to the structure	9.80	9.80	$\text{m}/\text{s}^2$
Force as a result of the acceleration	$1.40 \times 10^{-11}$	$1.40 \times 10^{-11}$	N
Displacement of the proof - mass (from simulation)	$1.90 \times 10^{-15}$	$3.60 \times 10^{-14}$	m
Spring constant	$7.35 \times 10^3$	$3.88 \times 10^2$	N/m
<b>Resonance frequency</b>	<b><math>1.14 \times 10^7</math></b>	<b><math>2.63 \times 10^6</math></b>	<b>Hz</b>

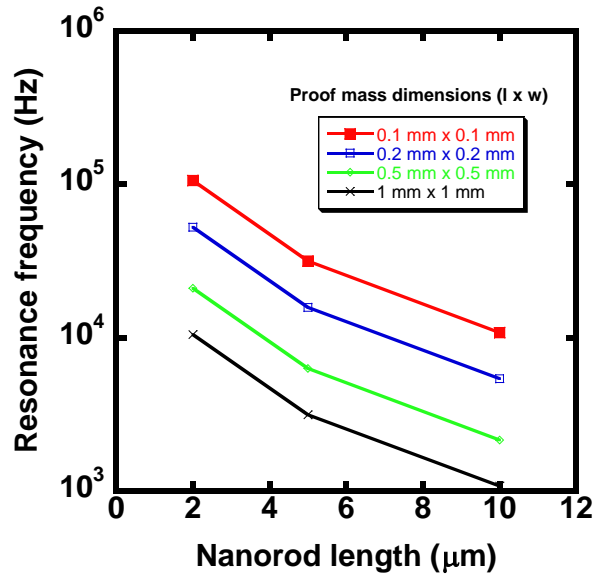


Figure 4-16 Calculated resonance frequency for different nanorod lengths and different proof - mass sizes.

It was observed that the resonance frequency reached the target value of 1 kHz for a proof - mass size of 1000 x 1000 x 10 μm for a nanorod length of 10 μm. However, this configuration is not practically feasible because it entails a drastic reduction in the energy generated/volume. In addition, based on present fabrication results, growth of 10 μm ZnO nanorods and subsequent processing are expected to present serious fabrication challenges.

The effect of nanorod array pitch, i.e. the pitch between individual ZnO nanorods grown using a template assisted nanorod growth process (Fig. 4-17) and nanorod array area (Fig. 4-18) on the stiffness was also studied via simulation. Here the proof - mass dimensions were kept constant (the resulting reduction in proof - mass volumes between simulations was negligible). In each case the proof - mass was subjected to 1 g +ve x acceleration. The stiffness in each case was calculated from the known force and simulated displacement.

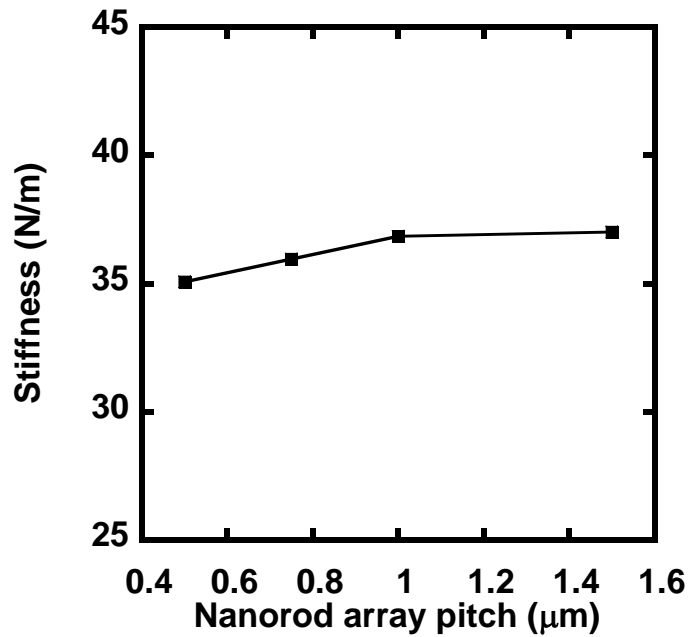


Figure 4-17 Nanorod array stiffness as a function of array pitch

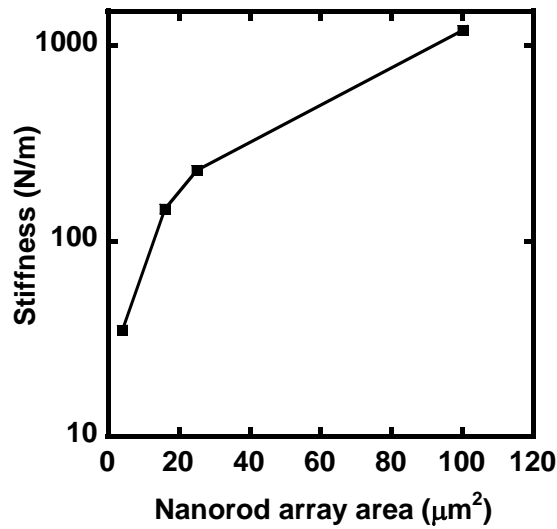


Figure 4-18 Nanorod array stiffness as a function of Nanorod array area for an array pitch of 0.5  $\mu\text{m}$

It was observed that the pitch of the nanorod array did not influence the stiffness significantly. This rules out pitch as a design parameter for optimizing the resonance frequency. Moreover, it was found that the stiffness of the nanorod array increases with increase in the array area. Hence, although this information is useful from a design perspective, it also means

that the resonance frequency will also scale up if the area of the proof - mass and nanorod array are kept same.

#### *4.2.3 Vibration energy harvester with bulk - micromachined proof - mass*

##### 4.2.3.1 Principle of operation and design

As mentioned previously, the resonance frequency of the structure is determined by the mass of the proof - mass used, and the spring constant of the springs holding the proof - mass. The springs in this case consist of micromachined structures that support the proof - mass, in addition to the ZnO nanorods themselves. In both designs described previously, it was observed that the nanorod stiffness dominates the overall structural stiffness. Hence, the nanorod stiffness needed to be optimized by controlling the nanorod length, placement and density. This has been shown to be possible previously using NIL and surface micromachining.

The other component affecting the resonance frequency is the mass of the proof - mass. The higher the mass of the proof - mass, lower the resonance frequency of the structure. Using surface - micromachined, electroplated nickel proof - mass limits the maximum thickness of the proof - mass to ~100  $\mu\text{m}$  due to limitations of the lithography process. As a result, any further increase in the mass is only possible through increase in the lateral dimensions. This approach uses up valuable real estate on the wafer surface and reduces the energy harvested to device volume metric. Residual stress in the electroplated proof - mass can cause unwanted deformations. This problem would be especially severe in a proof - mass with larger lateral dimensions as compared to the thickness.

To overcome this issue, bulk silicon was used as the material for proof - mass. Although, the density of silicon ( $2.32 \text{ g/cm}^3$ ) is much lower than nickel ( $8.91 \text{ g/cm}^3$ ), a much higher thickness of the bulk silicon (~450 – 600  $\mu\text{m}$ ) results in a much higher mass of the proof - mass without significantly increasing the lateral dimensions. Additionally, a larger proof - mass is simpler to fabricate using standard silicon bulk micromachining techniques. Finally, the single crystalline nature of the bulk silicon means fewer issues of deformation due to residual stress.

The energy harvester design consists of a bulk - micromachined silicon proof - mass suspended over a ZnO nanorod array. In response to vibration, the proof - mass is designed to move in a direction perpendicular to the plane of the substrate. The vertical motion of the proof - mass is translated into lateral motion of individual nanorods in the array by means of micromachined triangular “tooth” structures. The nanorods experience bending stress that results in a proportionate build-up of voltage on their surfaces. This voltage is harvested to drive a current through an external circuit (Fig. 4-19 and Fig. 4-20).

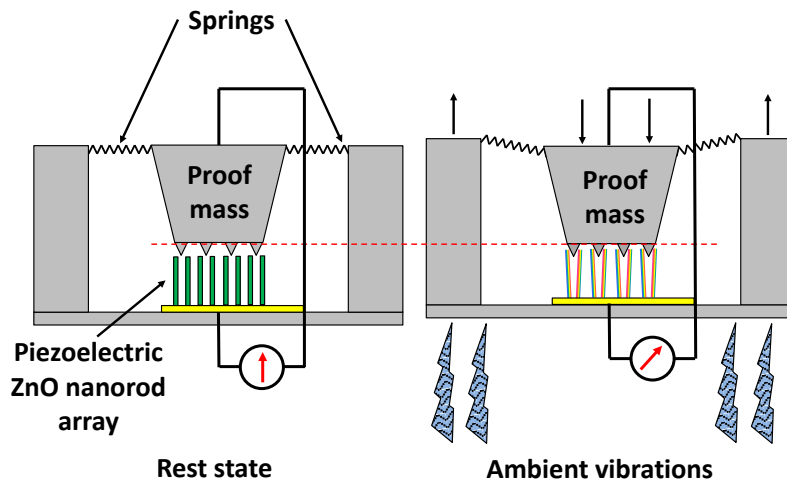


Figure 4-19 Schematic of the bulk micromachined proof - mass energy harvester design, showing operation under applied vibrations.

A model of the energy harvester is shown in Figure 4-21 and Figure 4-22. It comprises of two 420 -  $\mu\text{m}$  thick (100) silicon substrates that are bonded together using polymer bonding [139]. The top substrate wafer contains the pyramidal silicon proof - mass, springs and metallization for electrical contacts. The proof - mass is bulk micromachined using a KOH wet etch, and hence shows a characteristic  $54.7^\circ$  internal angle. It is held in place by four 1 -  $\mu\text{m}$  thick silicon nitride arms that serve as linear springs for vertical motion of the proof - mass. The bottom substrate contains an array of ZnO nanorods arranged in four rows and grown perpendicular to the substrate. Individual nanorods in the array are 5  $\mu\text{m}$  tall, 250 nm in diameter with a separation of 250 nm. The rows are 2  $\mu\text{m}$  wide, 10  $\mu\text{m}$  long, with a separation of

2  $\mu\text{m}$ . The arrayed nanorod rows are patterned using a combination of photolithography and thermal nanoimprint lithography.

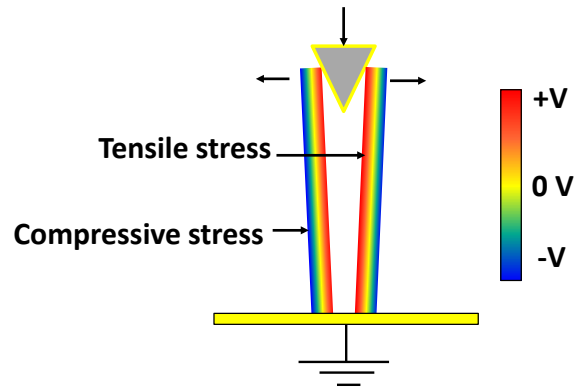


Figure 4-20 Schematic of the nanorod – tooth interaction. Ambient vibrations drive the nanorods towards the triangular tooth and are bent laterally as shown. The resultant tensile stress causes a positive voltage to develop on the surface of the nanorod which is extracted by a conductive coating on the tooth surface.

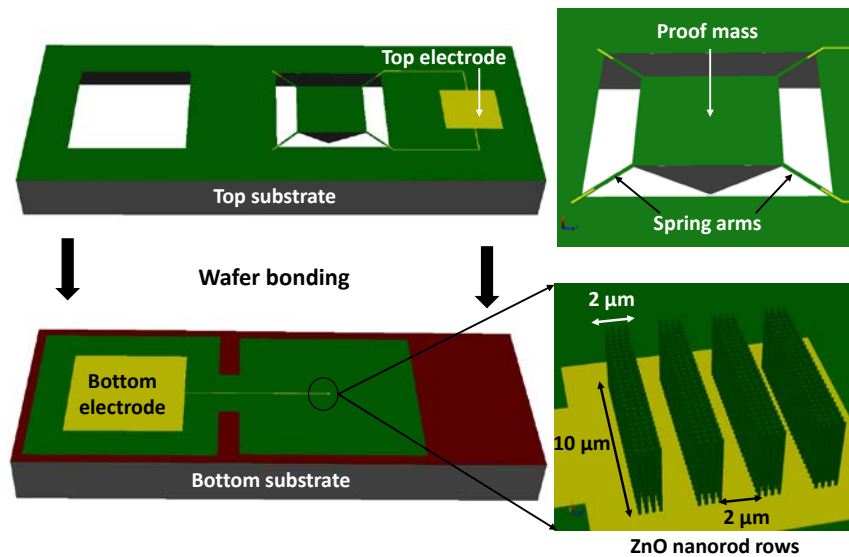


Figure 4-21 Structure and assembly of the bulk micromachined proof - mass energy harvester design. Also shown are zoomed in views of the proof - mass, springs and nanorod array placement

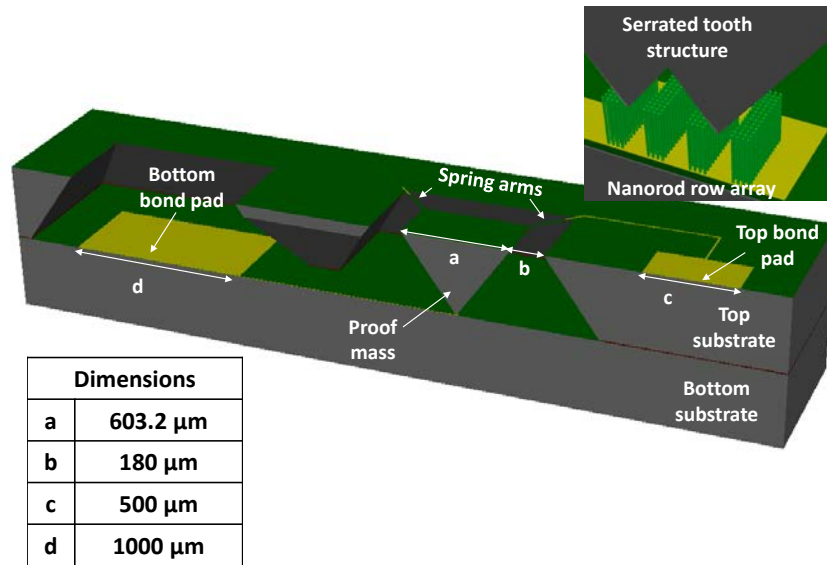


Figure 4-22 Cross section view of the assembled bulk micromachined proof - mass energy harvester design with dimensions. Inset shows zoomed in view of the teeth structure and nanorod arrays

The pyramidal proof mass has a serrated “tooth” structure at the bottom Figure 4-22 (inset). This is also accomplished using a KOH wet etch and hence the teeth have a 54.7° internal angle. This tooth structure translates the vertical motion of the proof mass into lateral bending of the ZnO nanorods. It also extracts the generated voltage and makes it available between the top and bottom bond pads. The underside of the top substrate is coated with a thin layer of gold for electrical contacts. This underlayer is accessed from the top using a micromachined via in the silicon nitride arm. A gold contact at the bottom of the ZnO nanorods serves as the second electrode. The bond pad connecting to this electrode is accessed by means of a bulk micromachined hole through the top substrate.

#### 4.2.3.2 Evaluation of device performance using finite element modeling

The silicon nitride spring arms dictate the maximum possible vertical deflection of the proof - mass in response to vibration. Since the nanorod rows have a pitch of 2  $\mu\text{m}$ , it was calculated that the proof - mass would need to displace vertically by 1.06  $\mu\text{m}$  to make initial

contact with the nanorod array. Accordingly, four different designs were evaluated to determine the vertical stiffness using finite element analysis (FEA). A quarter model of the top substrate was modeled and meshed as shown in Fig.4-23(a). The dimensions of the bridge arms were varied for the different designs Fig.4-23(b). An acceleration of 2 g ( $19.8 \text{ m/s}^2$ ) was applied to the proof - mass. This corresponds to the weight of the proof - mass in addition to a 1 g vibration amplitude. Symmetry boundary conditions were applied to the quarter faces. All motion was restricted on the bottom face of the substrate. Fig.4-24(a) and Fig. 4-24(b) show displacement and von Mises stress for design EH\_Z\_L254W20. Vertical displacement, von Mises stress and stiffness for different designs are tabulated in Table 4-4.

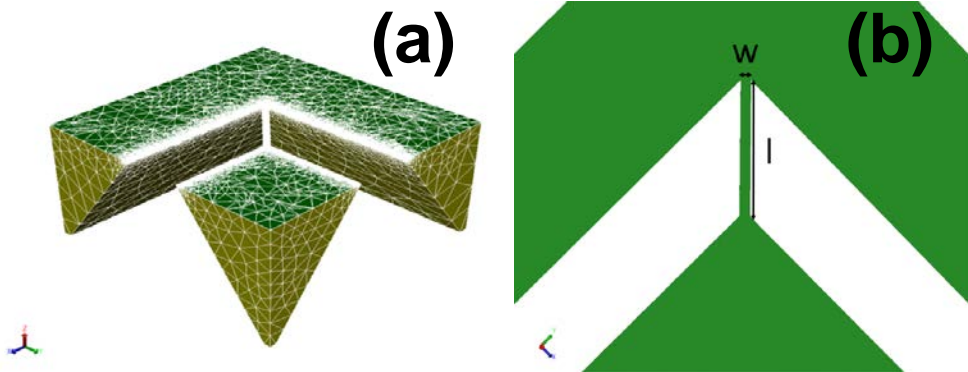


Figure 4-23 (a) Quarter model of top substrate, meshed. (b) Spring arm dimensions, displayed in Table 4-4.

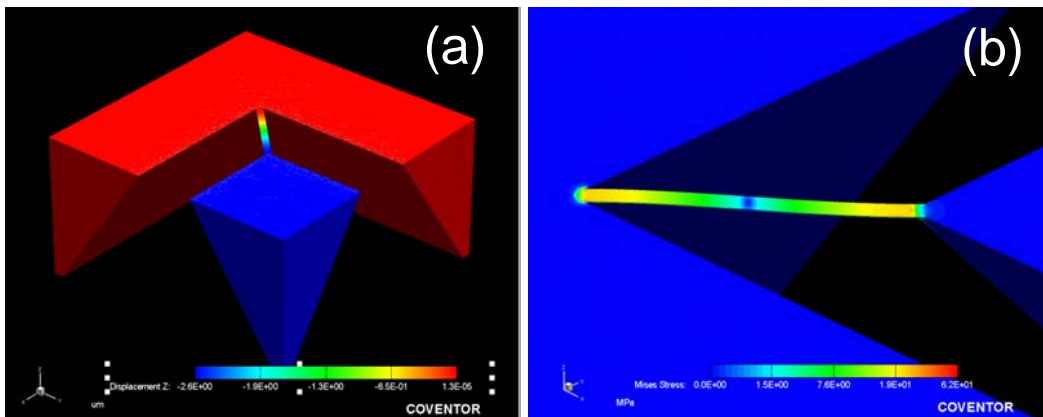


Figure 4-24 (a) Vertical displacement (b) von Mises stress in response to 2 g acceleration applied to proof - mass.



Table 4-4 Spring arm design – simulation results

Design name	l (μm)	w (μm)	Displacement (μm)	k(stiffness) N/m	von Mises stress (MPa)
EH_Z_L141W50	141	50	$1.20 \times 10^{-1}$	$2.31 \times 10^1$	$1.10 \times 10^1$
EH_Z_L141W20	141	20	$3.90 \times 10^{-1}$	7.11	$2.00 \times 10^1$
EH_Z_L211W20	211	20	1.50	1.85	$4.30 \times 10^1$
EH_Z_L254W20	253	20	2.60	1.07	$6.20 \times 10^1$

Design EH\_Z\_L254W20 was found to have the least vertical stiffness. Moreover, since the obtained von Mises stress is much lower than the published values for thin film silicon nitride tensile strength (6.4 GPa), [140] the device is expected to operate satisfactorily at expected vibration amplitudes. To further test the survivability of the device, an acceleration of 10 g was applied to the proof - mass. The maximum von Mises stress obtained using FEA was 310 MPa, which is still lower than the reported yield strength.

As mentioned previously, the vertical motion of the proof - mass in response to vibration is translated into lateral bending of the nanorods by means of micromachined “teeth” at bottom of the proof - mass. The interaction of these teeth with the nanorod rows was modeled and analyzed using FEA. Figure 4-25 shows the lateral bending of two ZnO nanorod rows when a single tooth is driven between them under an applied vertical force. The vertical displacement of the tooth ( $d_z$ ) and the lateral displacement of the nanorods ( $d_x$ ) were noted and used to calculate the vertical stiffness ( $K_z$ ) and lateral stiffness ( $K_x$ ) for a unit consisting of a single tooth and two nanorod rows. The variation of  $K_z$  and  $K_x$  with the length of the nanorod rows, ( $L_r$ ) was examined. Only nanorods in direct contact with the tooth were included in the simulation. The results are presented in Table 4-5.

Table 4-5 Vertical, lateral displacement, and spring constants for different row lengths

$L_r$ ( $\mu\text{m}$ )	$d_z$ ( $\mu\text{m}$ )	$d_x$ ( $\mu\text{m}$ )	$K_z$ (N/m)	$K_x$ (N/m)
4.000	0.183	0.105	0.865	38.095
6.000	0.178	0.102	1.381	39.216
8.000	0.175	0.099	1.870	40.237
10.000	0.171	0.097	2.380	41.399
12.000	0.167	0.094	2.899	42.571

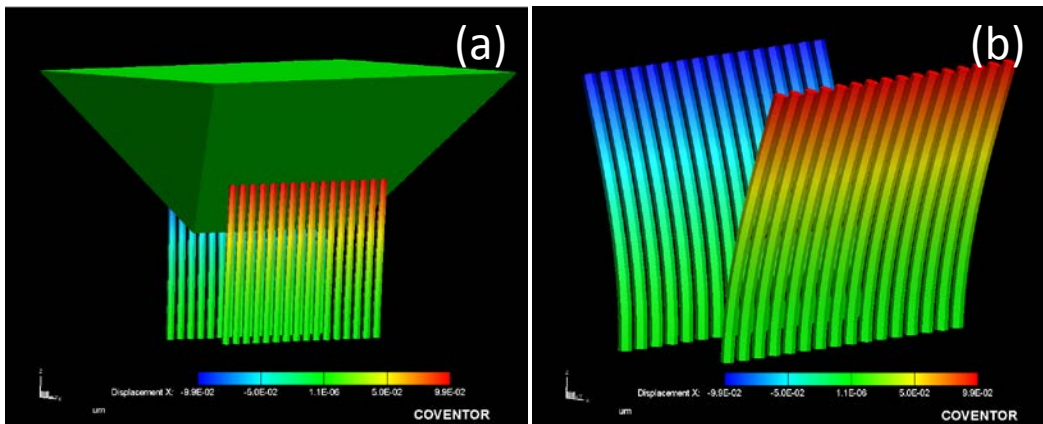


Figure 4-25 (a) Lateral bending of 8  $\mu\text{m}$  long nanorod rows (b) Nanorod deformation exaggerated, tooth hidden.

The lateral displacement of the nanorods was found to vary between 94 nm to 105 nm. The spacing between individual nanorods in the row is much greater (250 nm). This means that only the nanorods in direct contact with the tooth were subjected to bending. The rest of the nanorods in the 2  $\mu\text{m}$  wide row are not bent. Hence the simulation results with a single row of nanorods are also applicable to the 2  $\mu\text{m}$  wide row in the designed structure. Fig. 4-26 shows that  $K_z$  and  $K_x$  vary linearly with nanorod row length.

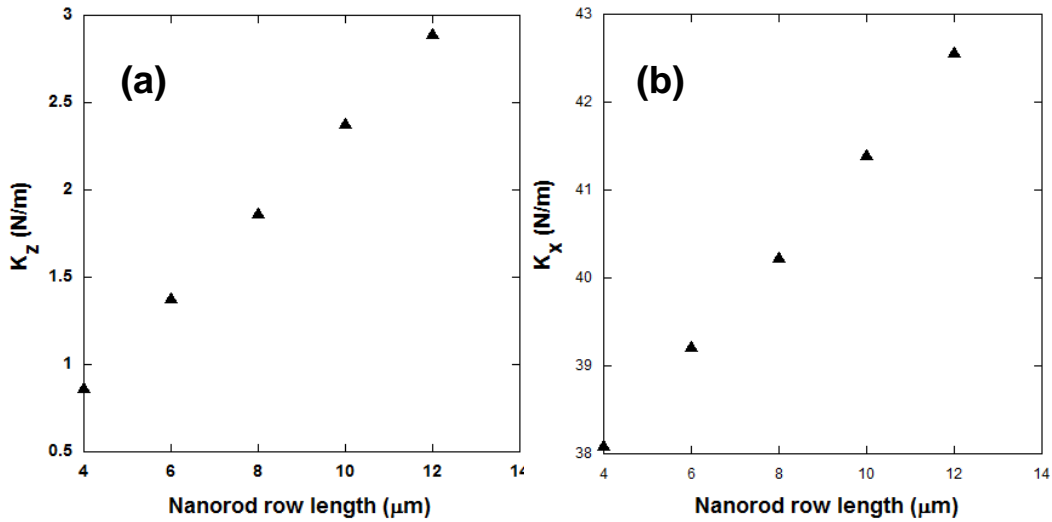


Figure 4-26 (a) Variation of vertical stiffness and (b) lateral bending stiffness with nanorod row length

The results from the foregoing analysis were used to calculate the vertical displacement of the proof - mass and lateral bending of the nanorods in response to a vibration excitation of amplitude 2 g for the designed device. The vertical and lateral displacements were calculated from the vertical and lateral stiffness respectively, knowing the force exerted by the proof - mass under 2 g acceleration. The vertical stiffness for the device is the summation of the stiffness presented by the spring arms and the nanorod array. Since there are two teeth and four rows in the design, the total stiffness of the array was found by doubling the stiffness of a single tooth – nanorod row pair unit. Similarly, the total lateral stiffness was also calculated by doubling the  $K_x$  for a single unit. Knowing the mass of the proof - mass, the total vertical stiffness for the device was then used to calculate the resonant frequency. The results are presented in Table 4-6.

Table 4-6 Calculation of lateral displacement and resonance frequency

Number of teeth-row units	2	
$K_z$ for a single unit (Nanorod row length 10 $\mu\text{m}$ )	2.38	N/m
Vertical stiffness for nanorod row array	4.76	N/m
$k$ for Design L254W20	1.07	N/m
Total vertical stiffness for the entire device	5.83	N/m
Mass of the proof - mass	$1.20 \times 10^{-7}$	Kg
Force applied by the proof - mass when subjected to 2g vibration	$2.36 \times 10^{-6}$	N
Resonant frequency	1107.51	Hz
$K_x$ for a single unit	41.40	N/m
Total lateral stiffness for the nanorod array	82.80	N/m
Lateral displacement of nanorods when subjected to a vibration of amplitude 2 g	28	nm

The lateral displacement thus computed was further used to evaluate the generated piezoelectric voltage by an individual nanorod in the row. A single nanorod of diameter 250 nm and length 5  $\mu\text{m}$  was modeled and meshed in ANSYS®. Displacement was restricted at the bottom of the nanorod in addition to an electrical ground boundary condition. The displacement obtained from the previous FEA, (28 nm) was applied to the top surface of the nanorod. The model was solved using the ANSYS® FEA solver and the result is presented in Figure 4-27. It is observed that a piezoelectric potential of 14.2 mV is generated on the nanorod surface. The polarity of the generated potential is positive on the side under tensile stress while it is negative on the side under compressive stress. Since the micromachined tooth makes contact only with the tensile side, the voltage obtained at the output is always positive. This feature eliminates the necessity of an additional rectifier that could potentially consume some of the harvested energy.

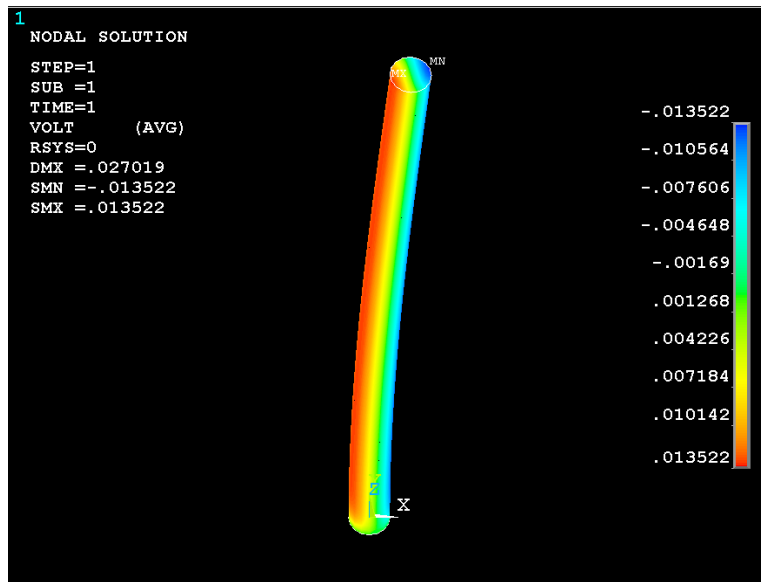


Figure 4-27 Electric potential generated on a single ZnO nanorod when subjected to lateral bending.

#### 4.3 Fabrication process development for bulk - micromachined proof - mass energy harvester

The bulk - micromachined proof - mass energy harvester design is composed of microstructures fabricated on two separate silicon wafers that are then aligned and bonded together to realize the full device. A tentative process flow showing the main fabrication steps involved is shown in Figure 4-28 (Top wafer containing the proof - mass) and Figure 4-29 (bottom wafer containing the ZnO nanorod array.

As seen from the FEM simulations in the previous section, a specific length, diameter of nanorods along with preferential placement and control over growth density yields performance that is satisfactory for harvesting vibration energy in a real world environment. This can be achieved using NIL and conventional photolithography techniques to obtain template assisted hydrothermal nanorod growth. Additionally, large area patterned growth of nanorods is also enabled using NIL, thus facilitating batch fabrication of energy harvester devices. The aforementioned work therefore plainly demonstrates the usefulness of NIL for development and realization of improved nano devices.

#### 4.4 Summary

Technological advancements in microsystem design, materials and fabrication have produced devices that are smaller, offer improved performance while being more power efficient. In the world of portable electronics, standalone devices have given way to integrated systems that have multifold subsystems and capabilities. Most systems still rely on on – board batteries. Advancements in battery technology however have not kept up with the devices that they power and as such represent a bottleneck in further improvement in device performance. Considering that various sources of energy are freely available for tapping in the immediate vicinity of a majority of systems, devices that transduce such energy into usable electrical power i.e. energy harvesters have caught the interest of industry and academia in recent years. Development of a NEMS energy harvester that can convert ambient vibrations into electrical power was the focus of this research. Three different device designs were developed and evaluated for performance using finite element modeling techniques. The finalized device uses piezoelectric crystalline ZnO nanorods that are put under bending stress by means of a bulk micromachined proof - mass when subjected to vibration. Finite element analysis shows that the device generates up to 14.2 mV of potential under vibration having amplitude of 1 g. The device has a resonant frequency of 1.10 kHz, which falls within the range of observed ambient vibrations. This is accomplished by tailoring the placement and growth density of the ZnO nanorods, which is made possible using NIL. A salient feature of the device architecture is that, the generated voltage is unipolar, thus eliminating the need of a rectifier. A process flow for microfabrication of the finalized design is proposed.

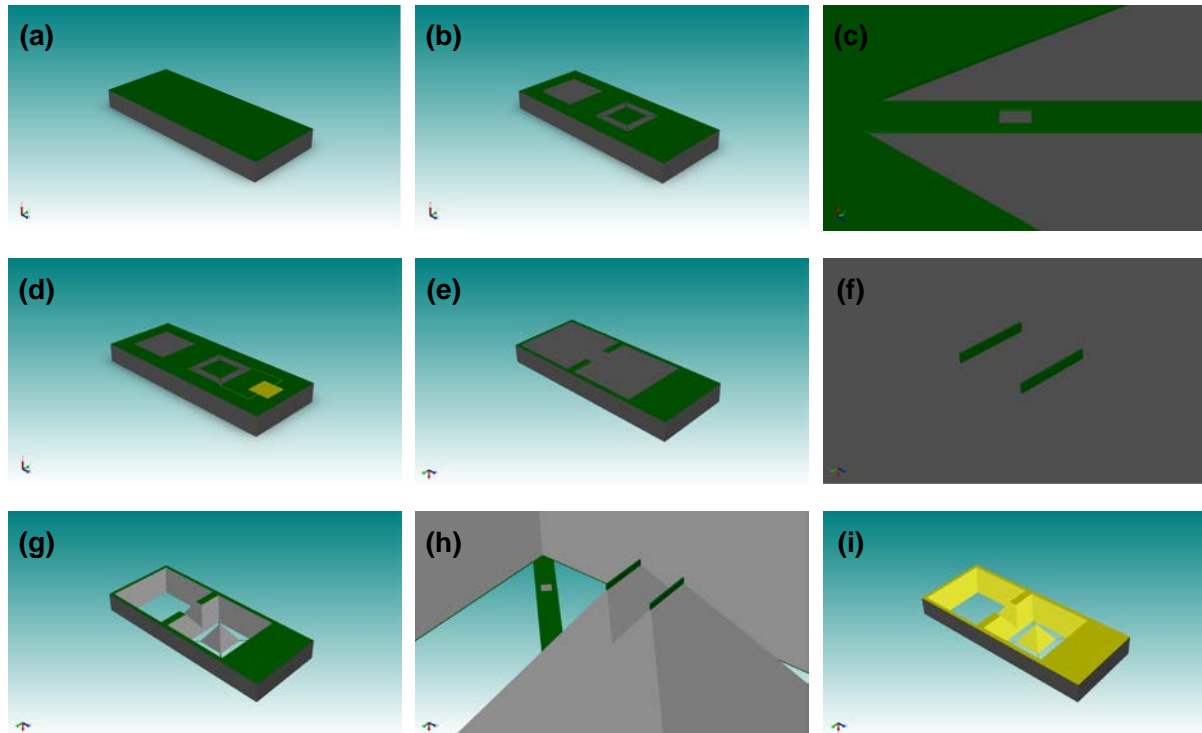


Figure 4-28 Top wafer fabrication process flow. Figures a-d show fabrication processes on the top side of the wafer. Figures e-i show fabrication on the bottom side of the wafer. (a) Deposition of 1  $\mu\text{m}$  thick  $\text{Si}_3\text{N}_4$  on both sides of a (100) Si wafer using LPCVD (b) Patterning of  $\text{Si}_3\text{N}_4$  using photolithography and RIE to define springs and openings for subsequent KOH etch (c) Zoomed in view of the spring arm showing the via for electrical contact through the arm (d) Deposition and patterning of 100 nm Au top electrode metallization layer using photolithography and lift-off (e) Patterning of wafer bottom side using photolithography and RIE to define openings for KOH etch and masking for serrated tooth structure (f) Zoomed in view of the open Si area showing masking for the serrated tooth structure (g) Anisotropic etching using KOH solution. The features on the top side are protected using Pro-Tek B3 polymer (h) Zoomed in view of the serrated tooth structure realized after KOH etch (i) 100 nm Au deposition on the bottom side of the KOH etched wafer to form a conductive coating on the proof - mass.

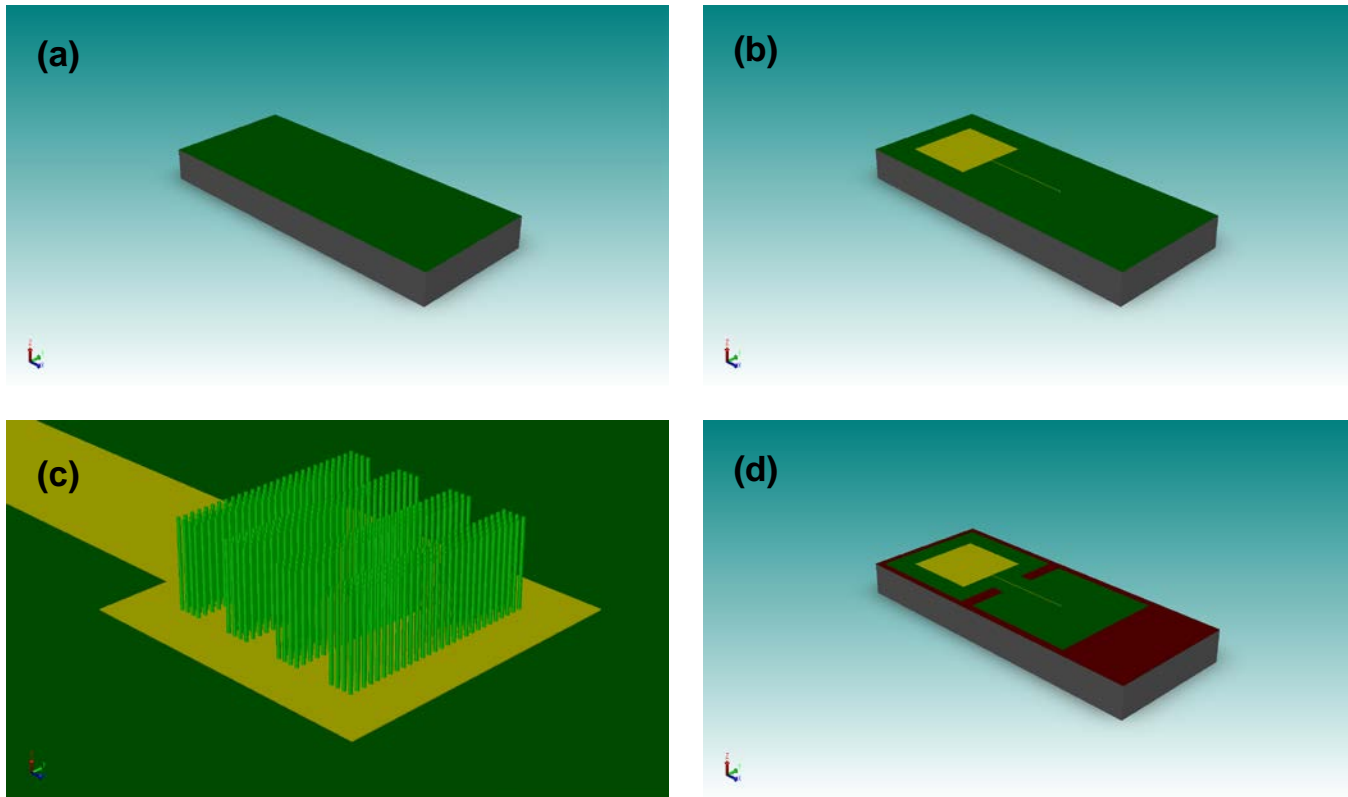


Figure 4-29 Fabrication of bottom wafer (a) Sputter deposition of  $0.5 \mu\text{m}$   $\text{Si}_3\text{N}_4$  on (100) Si substrate for passivation/planarization (b) Deposition and patterning of  $100 \text{ nm}$  Au using photolithography and lift-off patterning to define bottom electrode (c) NIL assisted hydrothermal growth of ZnO nanorods according to process described in Chapter 3 (d) Spin coating and photo-defining of polyimide layer to serve as a bonding interface to the top wafer.



## Chapter 5

### Self-powered tactile pressure sensors using NIL – ordered arrays of piezoelectric ZnO nanorods on flexible substrates

#### 5.1 Introduction to tactile pressure sensing, review of the current state-of-the-art

Tactile sensory input is a vital source of information for robot systems. It is frequently desired that a robot, especially one that is involved in human interaction, acquire tactile information from a large area on its surface for safe and effective operation within its environment. As a result, any sensor network on the robot surface needs to cover a large area, conform to various topographical features on the robot and provide tactile information to the robot with minimal energy consumption from the robot's limited power resources. Additionally, depending on the environment the robot is operating in, the sensor system needs to be resistant to dust, moisture, mechanical shock and temperature extremes.

Each sub – system on the robot presents an additional load to the robot's limited power resources. Tactile sensors currently under development could be grouped into two categories on the basis of the necessity to provide external power for transduction. Tactile sensors based on resistive [141] piezoresistive [142], capacitive [143] and optical [144] sensing principles require a source of power for operation. A large area network comprised of such sensors with a high sensor density to maintain sufficient spatial resolution represents a significant load to the robot's batteries. To mimic human skin, the robot surface needs to be draped in a large area network of tactile sensors. Another important requirement is maintaining sufficient spatial resolution, which necessitates a network of numerous micro-scale sensors for coverage of the macro – scale robot surface area. Sensor systems that require a bias - DC or AC - (capacitive and piezoresistive) are disadvantageous in such a scenario as they present a significant additional load to the robot's limited power resources as well as adding weight [145].

The tactile sensor system described in this research is a self-powered system that does not need an external source of power for transduction of applied pressure into measurable

voltage. The primary sensing element is a piezoelectric crystalline ZnO nanostructure (nanorod) that generates a measurable quantity of charge in proportion to applied mechanical stress [146, 147]. Piezoelectric properties of ZnO nanorods have been utilized in the development of several nano - devices that harvest mechanical energy from the ambient environment and convert it into usable power for powering sensor systems [148]. Advantages of piezoelectric ZnO nanorods are higher sensitivity to small forces, mechanical robustness and improved piezoelectric properties as compared to bulk or thin film materials [149].

Tactile sensing for robotics dictates that the sensors be positioned on the robot's surface. Robot surfaces are frequently designed to be non-planar in order to accomplish various tasks. An example of such a non-planar surface is the humanoid end - effector on the iCub robot [150]. The sensors developed in the present work are fabricated on flexible, polyimide substrates. This allows the sensor array to be mounted in intimate contact to the robot surface, in a conformal fashion. This ensures that there aren't any tactile sensing "blind spots" and lets the robot receive tactile information from all portions of the surface regardless of its planarity

Crystalline ZnO nanorods are central to the development of the tactile sensors described in this disclosure. A novelty of this work is the incorporation of thermal nanoimprint lithography and hydrothermal growth to achieve large area ordered growth of crystalline ZnO nanorods on polyimide substrates. A low temperature nanofabrication process has been developed for compatibility with flexible polyimide substrates. The process also allows nanoscale nanorods to be seamlessly incorporated into a microscale sensor structure. The ordered nanorod arrays improve repeatability of sensor performance and fabrication yield.

Another novelty of this work is that the tactile sensor systems are fully self - packaged on flexible substrates. The robot surface frequently encounters an environment where it is subject to dust, moisture, temperature extremes, and mechanical shock. Any tactile sensor network on the robot surface therefore, needs to withstand the aforementioned hazards while maintaining satisfactory operation. The sensor network developed in the present work is

designed to fully withstand dust and moisture and temperature extremes and mechanical shock within reasonable limits. This is accomplished by embedding the sensor structure in a chemically inert, impervious, temperature resistant polyimide that provides mechanical robustness and environmental protection. The packaging process is built-in to the sensor fabrication process resulting in a one-piece tactile pressure sensing “skin” that can be draped over the robot surface. A significant advantage of using flexible polyimide substrate is the ability to conform the sensor network to non-planar areas, resulting in sensor coverage in virtually all areas on the surface.

A sensor system employing a similar structure has been reported by Choi et al. [151]. Another device with a similar structure, an energy harvesting system has been demonstrated [148]. Both of these devices require the top electrode to be added after fabrication of the remaining system. As such these systems are not compatible with large scale integrated fabrication. The sensor system described in this dissertation is fabricated with all components integrated into the flexible skin structure using a CMOS compatible nanofabrication process. Fabrication of a sensor network on a large area (3” diameter wafer) has been demonstrated and the possibility of fabrication on even larger areas is expected. Additionally, the systems demonstrated in literature are fabricated with little to no control over ZnO nanorod density. As mentioned previously, a uniform and controllable nanorod density is essential for sensor performance repeatability. This has been addressed in the present work by means of development of a novel template assisted nanorod growth process.

## 5.2 Sensor structure, principle of operation and FEM simulation

The tactile sensor structure consists of an array of ZnO nanorods sandwiched between two layers of polyimide, namely the substrate and the superstrate. The nanorod array is embedded in an additional layer of polyimide for mechanical support and environmental protection. Tactile pressure applied to the sensor causes the nanorods to undergo axial compression resulting in generation of voltage at their extremities. Voltage generated by the

nanorods in response to applied tactile pressure is extracted by means of Au/Ti electrodes deposited on the top and bottom surfaces (lengthwise) of the nanorods. Figure 1 shows the structure and illustrates the operation of the tactile sensor.

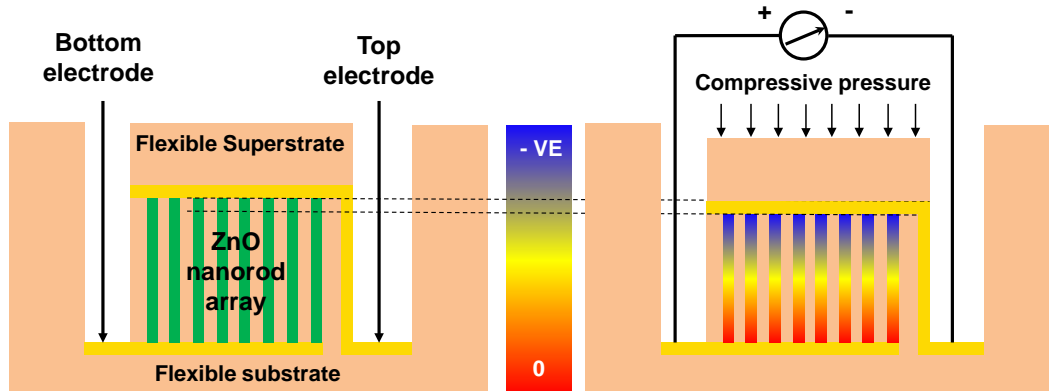


Figure 5-1 Tactile sensor structure consisting of a substrate, superstrate, fill layer, nanorod array and electrodes. Voltage is generated in response to an axial compressive pressure applied to the sensor. The generated voltage is proportional to the applied pressure

Considering the novelty of the sensor structure, FEM simulations were performed to determine the effect of various design variables such as lateral dimensions and substrate thickness on sensor performance. Additionally, finite element analysis using coupled field elements in ANSYS was used to estimate the voltage generated by the sensor in response to applied tactile pressure.

A section of the nanorod array along with the flexible polyimide substrate and superstrate was modeled using CoventorWare. The substrate and the superstrate are 5  $\mu\text{m}$  thick. The nanorods are 5  $\mu\text{m}$  tall, 160 nm diameter and are arranged in a regular array of 500 nm pitch. The nanorod array is embedded in polyimide, 5  $\mu\text{m}$  in thickness.

It was found that, under a constant applied pressure, changing the lateral dimension of the sensor array does not affect the nanorod compression, and consequently generated voltage. This result permits flexibility of design of the nanorod array lateral dimensions for ease of fabrication assembly on the robot surface and optimizing resolution. Simulation results are

shown in Figure 5-2. Note that the deformation is exaggerated 10000 times and the fill polyimide is hidden.

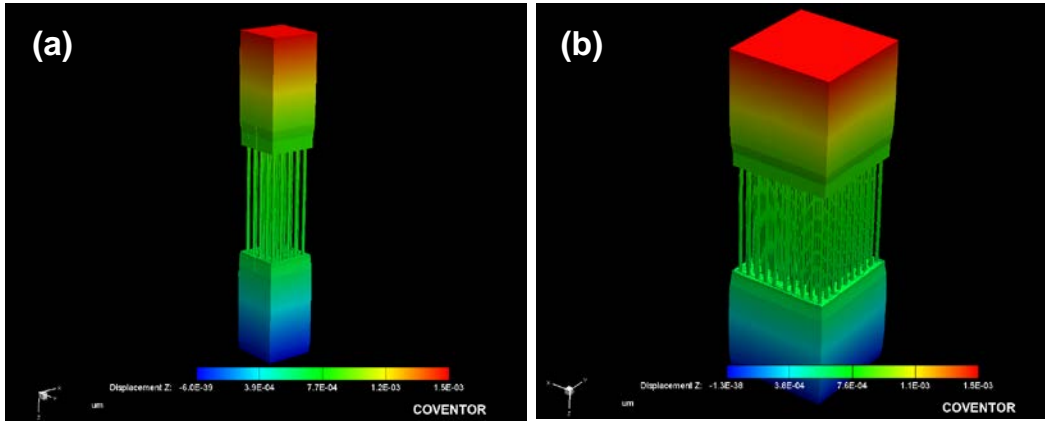


Figure 5-2 Simulation results showing nanorod compression in response to applied pressure for different sensor cross section area (a)  $2.15 \mu\text{m} \times 2.15 \mu\text{m}$  (b)  $5.13 \mu\text{m} \times 5.13 \mu\text{m}$ . Note that the fill polyimide is included in the simulation and hidden.

As mentioned previously, the sensors are fabricated on a flexible polyimide substrate. Hence, the substrate polyimide forms the focus of the next finite element simulation. The thickness of the substrate polyimide was varied to observe the effect on nanorod compression under uniform tactile pressure. The solid model was subjected to a pressure of 5 kPa and 500 kPa. The results are presented in Figure 5-3.

A net nanorod axial compression of  $1.41 \times 10^{-6} \mu\text{m}$  for the 5 kPa case and  $1.41 \times 10^{-4} \mu\text{m}$  for the 500 kPa case was observed for all substrate thicknesses. The results show that nanorod compression is independent of the substrate thickness. This allows for substrate thickness to be optimized for fabrication and robustness.

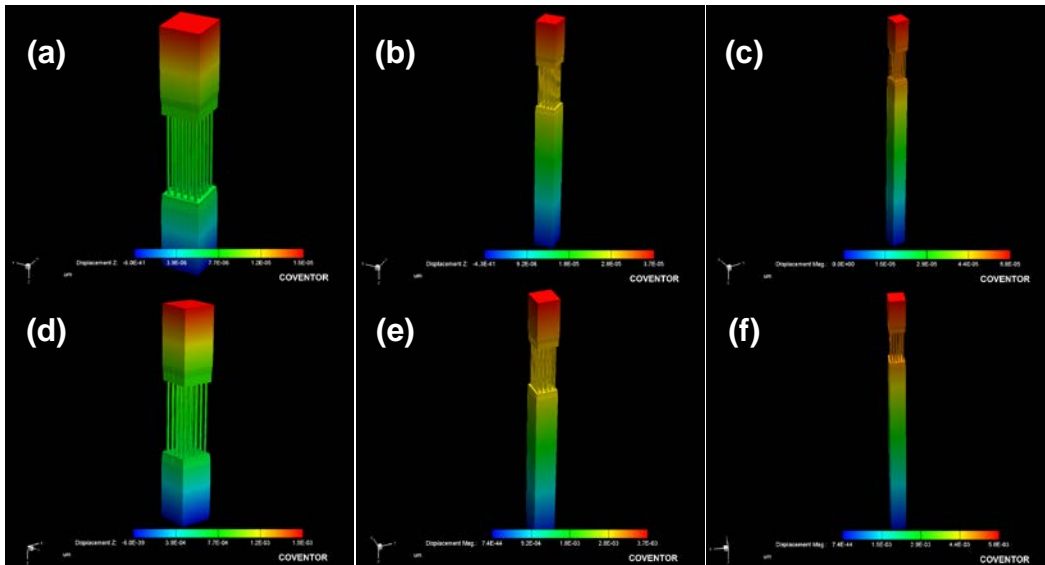


Figure 5-3 Nanorod compression in response to applied tactile pressure for different thicknesses of flexible substrate. (a) 5  $\mu\text{m}$  substrate – 5 kPa pressure (b) 20  $\mu\text{m}$  substrate – 5 kPa pressure (c) 35  $\mu\text{m}$  substrate – 5 kPa pressure (d) 5  $\mu\text{m}$  substrate – 500 kPa pressure (e) 20  $\mu\text{m}$  substrate – 500 kPa pressure (f) 35  $\mu\text{m}$  substrate – 500 kPa pressure

The nanorod compression results from the foregoing discussion were used to estimate the voltage generated by ZnO nanorods in response to applied tactile pressure. A single ZnO nanorod 160 nm in diameter and 5  $\mu\text{m}$  in height was modeled in ANSYS and meshed using coupled field elements. The nanorod compression in response to the corresponding pressure was applied as a load to the solid model, and the problem was solved to determine generated voltage. The results are shown in Figure 5-4.

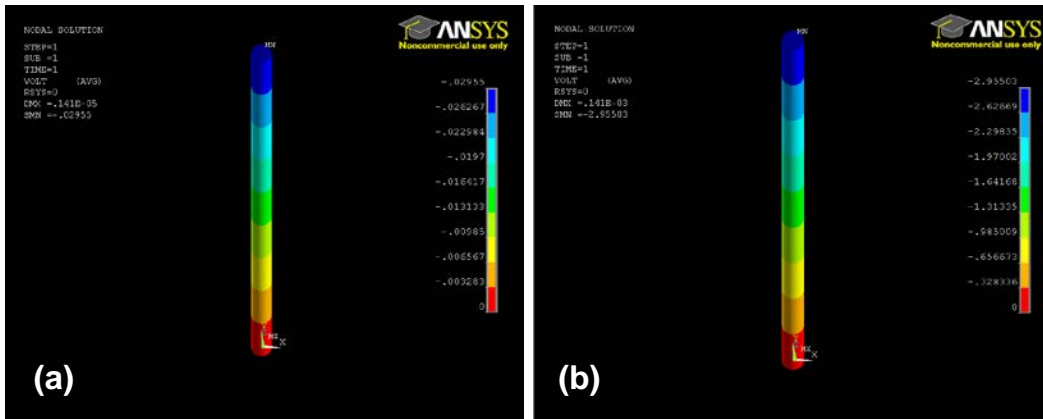


Figure 5-4 Voltage generated by a single nanorod in response to axial compression (a) 5 kPa  
(b) 500 kPa

According to the FEM results, a voltage of 29.5 mV – 2.95 V is generated in response to an applied pressure in the range of 5 kPa - 500 kPa.

Four different tactile sensor designs are developed as shown in Figure 5-5. The sensor TSS is a single array of ZnO nanorods sandwiched between two electrodes and enclosed in polyimide. The sensors TS9\_100, TS25\_50 and TS49\_30 consist of multiple ZnO nanorod arrays connected in series. Since all series connected arrays experience the same tactile pressure, they generate higher voltage than an individual array, and therefore are expected to exhibit higher sensitivity. Details about the sensor designs are presented in Table 5-1.

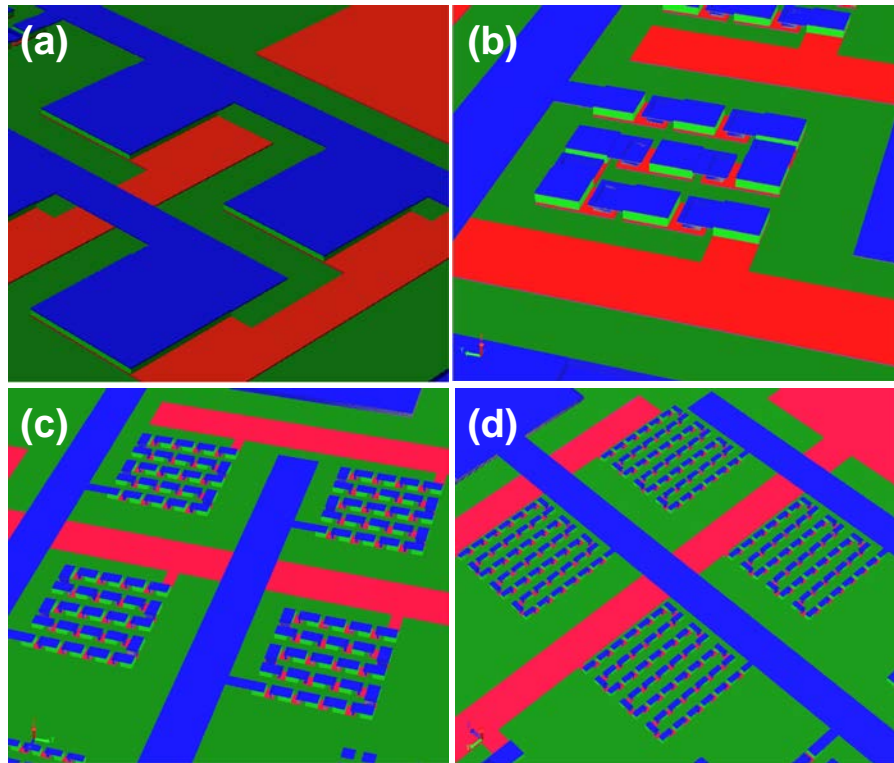


Figure 5-5 CoventorWare solid model showing the different sensor designs (a) TSS (b) TS9\_100 (c) TS25\_50 (d) TS49\_30. The polyimide layers are hidden. The top electrode is represented in red while the bottom electrode is represented in blue

Table 5-1 Sensor designs, nomenclature and dimensions

Sensor design name	Sensor type	No. of nanorod arrays in series	Dimensions of a single nanorod array
TSS	Single	1	500 $\mu\text{m}$ x 500 $\mu\text{m}$
TS9_100	Series connected	9	100 $\mu\text{m}$ x 100 $\mu\text{m}$
TS25_50	Series connected	25	50 $\mu\text{m}$ x 50 $\mu\text{m}$
TS49_30	Series connected	49	30 $\mu\text{m}$ x 30 $\mu\text{m}$

The wafer is divided into a number of rectangular dies (18.75 mm x 8.5 mm). Each die contains 3 sensor arrays namely, AAL44, SD16 and AAS44. The arrays AAL44 and AAS44 are addressable arrays, each containing 16 sensors. The array AAL44 contains 16 TSS type sensors arranged in a 4 x 4 addressable array. AAS44 contains 4 sensors of each type i.e. TSS, TS9\_100, TS25\_50 and TS49\_30 for a total of 16 sensors arranged in a 4 x 4



addressable array. The array SD16 is actually a single large device that consists of 16, 500  $\mu\text{m}$  x 500  $\mu\text{m}$  TSS type sensors connected in series. Figure 5-6 shows the die configuration and the individual arrays.

As mentioned previously, the sensors generate a voltage signal, proportional in magnitude to the pressure applied. This signal can be captured by attaching the measurement apparatus to the pair of electrodes unique to the sensor experiencing tactile pressure. Figure 5-7 shows the bondpad nomenclature. The individual sensors in the AAL44 and AAS44 arrays are to be identified using the nomenclature presented in Figure 5-8. Finally, Table 5-2 contains information for addressing and sensing signal from individual sensors. The values under the terminal columns in Table 5-2 refer to the bondpad numbers shown in Fig 5-7. Device SD16 is a single device that can be addressed using bondpads 5 and 14.

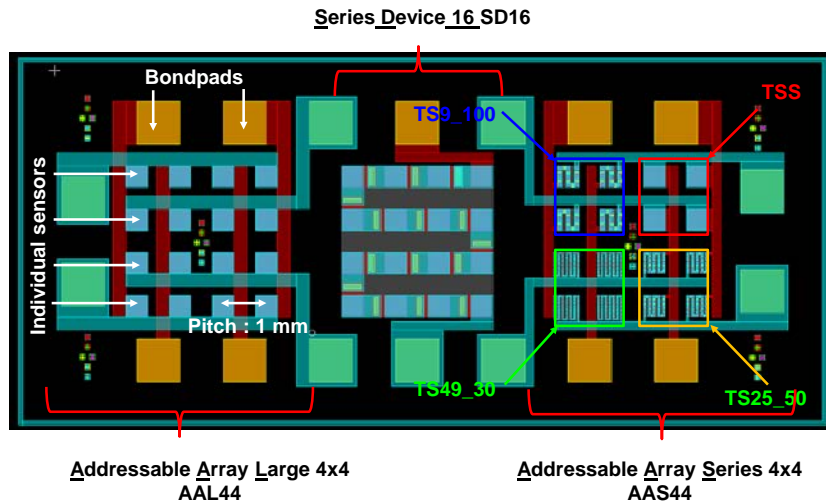


Figure 5-6 Single die layout showing the AAL44, SD16 and AAS44 arrays. The die is 18.75 mm long and 8.5 mm wide. Each die has 18, 1 mm x 1mm bondpads for sensor addressing. The sensor pitch in AAL44 and AAS44 is 1 mm resulting in 1 mm tactile sensing resolution

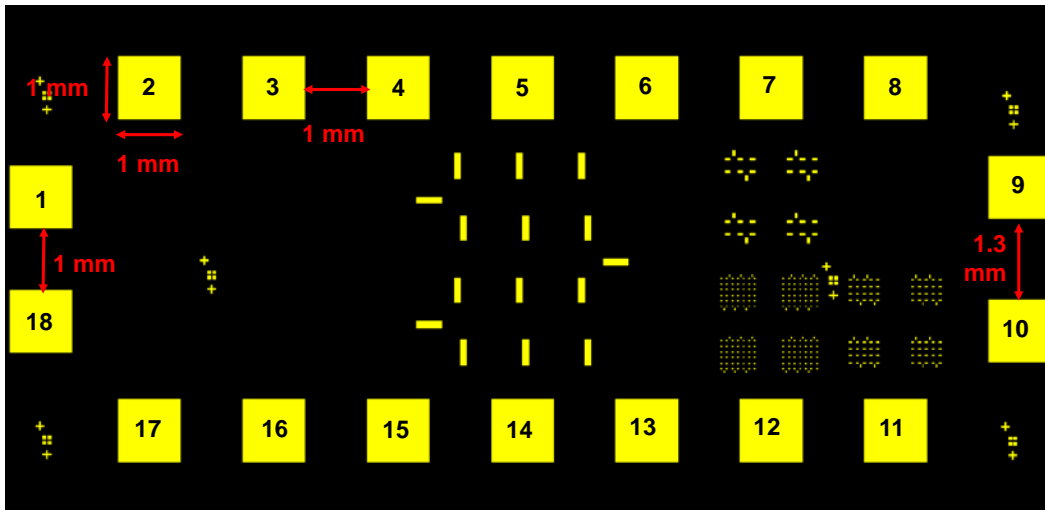


Figure 5-7 Bondpad nomenclature for individual sensor addressing

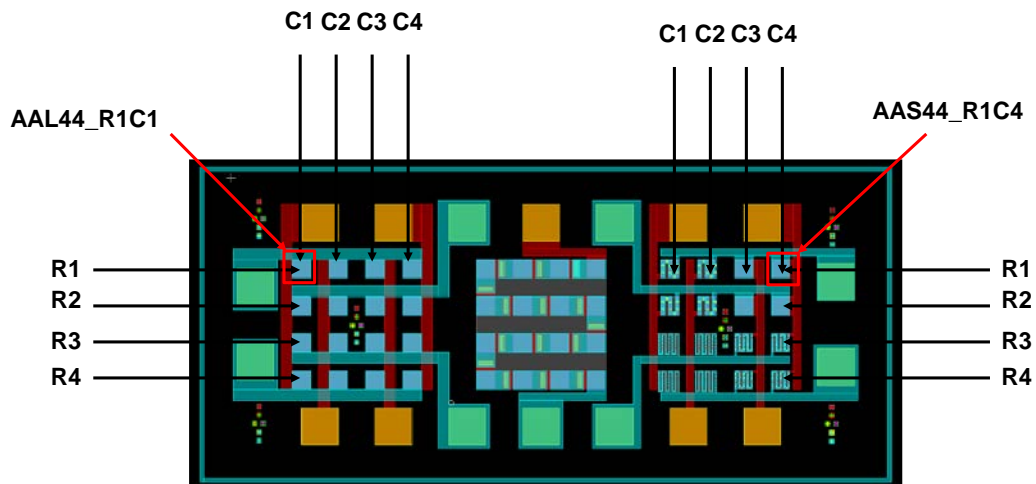


Figure 5-8 Sensor nomenclature. Each sensor is identified by its row and column number within the array. The row and column numbers, appended to the array the sensor belongs to, make the complete device name

Table 5-2 Sensor addressing for a single die

Array AAL44			Array AAS44		
Sensor name	Terminal 1	Terminal 2	Sensor name	Terminal 1	Terminal 2
AAL44_R1C1	1	2	AAS44_R1C1	9	7
AAL44_R1C2	1	17	AAS44_R1C2	9	12
AAL44_R1C3	1	16	AAS44_R1C3	9	11
AAL44_R1C4	1	3	AAS44_R1C4	9	8
AAL44_R2C1	4	2	AAS44_R2C1	6	7
AAL44_R2C2	4	17	AAS44_R2C2	6	12
AAL44_R2C3	4	16	AAS44_R2C3	6	11
AAL44_R2C4	4	3	AAS44_R2C4	6	8
AAL44_R3C1	15	2	AAS44_R3C1	13	7
AAL44_R3C2	15	17	AAS44_R3C2	13	12
AAL44_R3C3	15	16	AAS44_R3C3	13	11
AAL44_R3C4	5	3	AAS44_R3C4	13	8
AAL44_R4C1	4	2	AAS44_R4C1	10	7
AAL44_R4C2	4	17	AAS44_R4C2	10	12
AAL44_R4C3	4	16	AAS44_R4C3	10	11
AAL44_R4C4	4	3	AAS44_R4C4	10	8

### 5.3 Fabrication of tactile pressure sensors on a polyimide based flexible substrate

The tactile pressure sensors are fabricated using a bottom – up approach to simplify fabrication. Accordingly, the thin superstrate (5  $\mu\text{m}$ ) is deposited first, followed by the top electrode, ZnO nanorods and fill layer. After exposing the tips of the nanorods for electrical contact using plasma etching, the bottom electrode is deposited. This is followed by deposition of a thick polyimide layer (60  $\mu\text{m}$ ) to serve as the flexible substrate. A schematic of the process flow is shown in Figure 5-9.

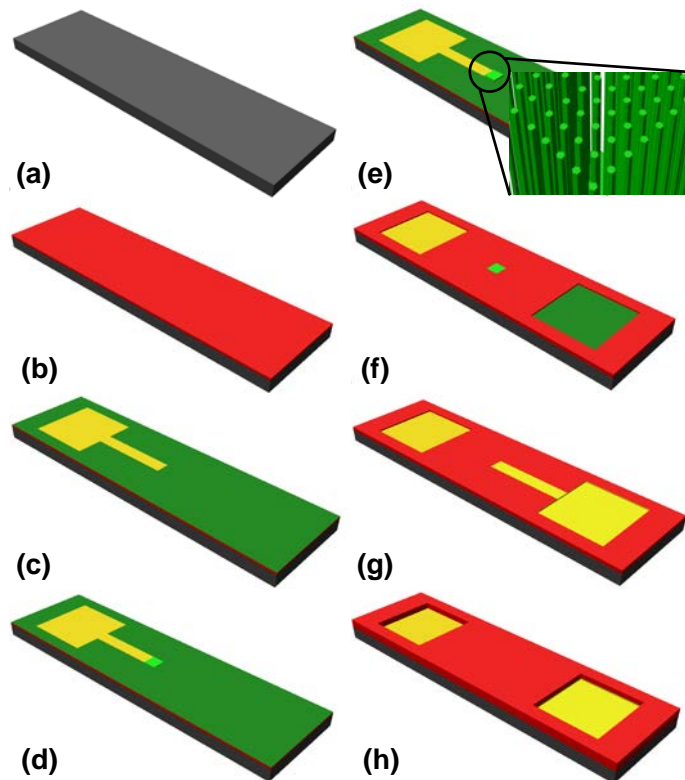


Figure 5-9 (a) (100) silicon wafer as base for fabrication (b) Deposition of  $\text{Si}_3\text{N}_4$  followed by superstrate polyimide (c) Deposition and patterning of Au/Cr top electrode metallization (d) Deposition and patterning of ZnO/Ti seed/ohmic layer (e) Ordered growth of ZnO nanorods using hydrothermal growth and NIL (f) Deposition of fill polyimide and etching to expose ZnO tips (g) Deposition and patterning of Au/Ti bottom electrode metallization (h) Deposition and patterning of flexible substrate polyimide layer

A 3" (100) SSP silicon wafer was used as the base for fabrication of tactile sensors. A thin layer of  $\text{Si}_3\text{N}_4$  (0.2  $\mu\text{m}$ ) was sputter deposited to serve as a planarizing layer. The thin (5  $\mu\text{m}$ ) superstrate layer is deposited in three steps. A 2  $\mu\text{m}$  polyimide layer is spin - coated and cured. Next, a 0.3  $\mu\text{m}$  layer of  $\text{Al}_2\text{O}_3$  is deposited and patterned to form a pressure distribution plate on top of each tactile sensor (Fig 5-10). Finally, a 3  $\mu\text{m}$  layer of polyimide is coated and cured to complete the fabrication of the superstrate. This is followed by sputter deposition of a thin layer of  $\text{Si}_3\text{N}_4$  (0.2  $\mu\text{m}$ ) to serve as a planarization and adhesion promoter for the next layer.

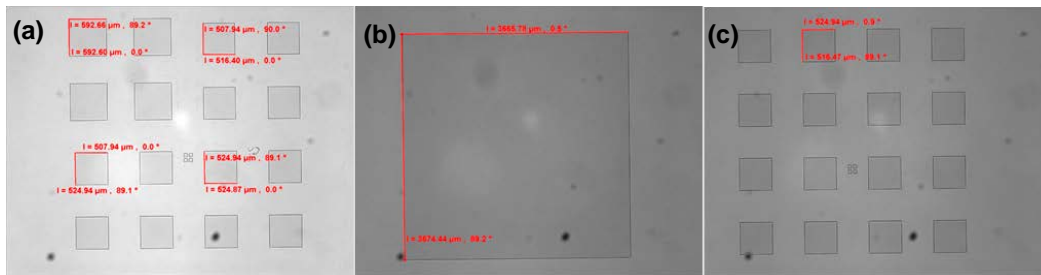


Figure 5-10 Deposition and patterning of  $\text{Al}_2\text{O}_3$  pressure distribution plate (a) AAL44 (b) SD16  
(c) AAS44

The next fabrication step consists of deposition and patterning of the top electrode. A thin layer of Cr (30 nm, adhesion promoter) followed by Au (100 nm) is deposited in an electron beam evaporator, and patterned with a lift-off process (Fig. 5-11).

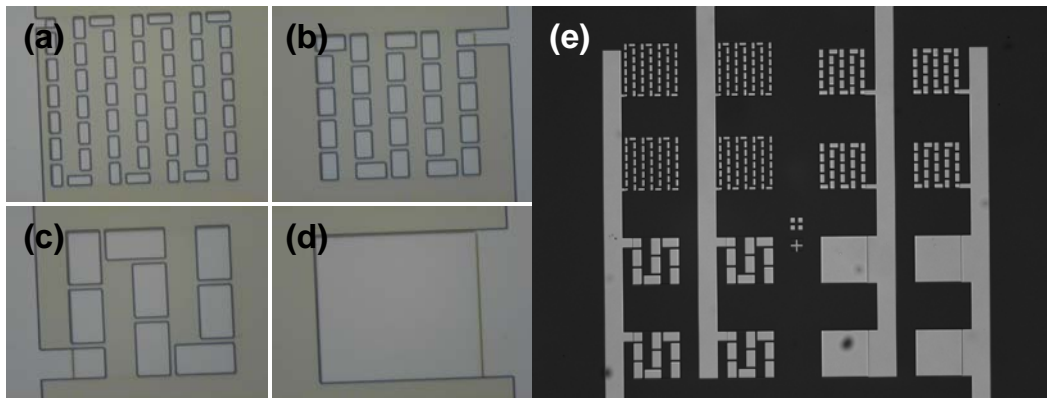


Figure 5-11 Photolithography for definition of the top electrode using negative photoresist NR9 1500PY (a) 30  $\mu\text{m}$  (b) 50  $\mu\text{m}$  (c) 100  $\mu\text{m}$  (d) 500  $\mu\text{m}$  (e) Patterned Cr/Au layer after lift-off

A thin layer of Ti (30 nm, ohmic contact layer) is evaporated in an electron beam evaporator. Next, 0.4  $\mu\text{m}$  of ZnO is deposited using pulsed laser ablation to serve as the seed layer for nanorod growth. The wafer temperature (300°C) and chamber conditions (100 mTorr  $\text{O}_2$ ) are optimized for obtaining a polycrystalline c-plane oriented ZnO thin film. The Ti/ZnO layer is subsequently masked using photolithography, and patterned using a dilute HF based wet etch process to define the sensor areas (Fig-5-12).

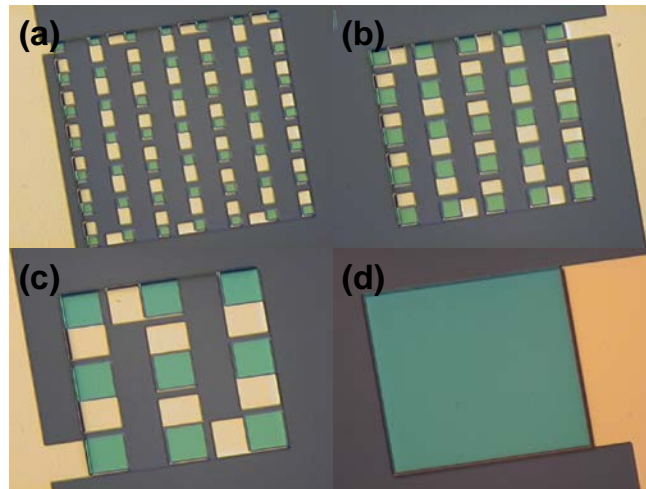


Figure 5-12 Patterned ZnO/Ti layer (a) 30  $\mu\text{m}$  x 30  $\mu\text{m}$  (b) 50  $\mu\text{m}$  x 50  $\mu\text{m}$  (c) 100  $\mu\text{m}$  x 100  $\mu\text{m}$   
(d) 500  $\mu\text{m}$  x 500  $\mu\text{m}$  area

The ZnO seed areas are next coated with a thermoplastic polymer and patterned with thermal NIL (The NIL process and the residual layer etch process has been described previously in Chapter 2). This step results in a regular array of 0.2  $\mu\text{m}$  diameter, 0.5  $\mu\text{m}$  pitch circular openings on the ZnO layer, which serve as growth sites for the subsequent ZnO nanorod hydrothermal growth (Fig 5-13).

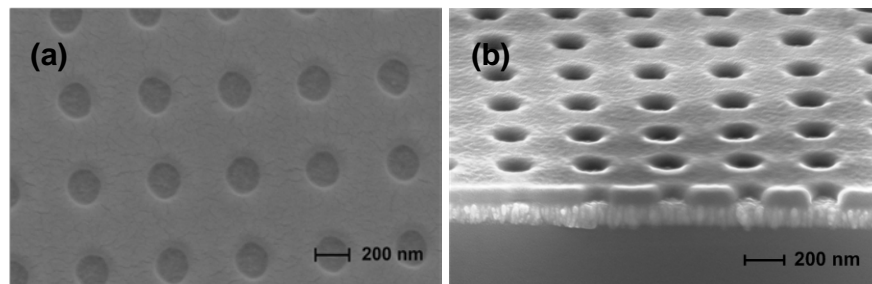


Figure 5-13 SEM image of NIL patterned nanoimprint resist template on ZnO seed layer (a) Top view (b) Side view

Crystalline ZnO nanorods are grown utilizing the low temperature (85°C) hydrothermal growth process described previously. The growth solution is an equimolar (20 mM) mixture of Zinc Acetate and Hexamethylenetetramine (HMTA) that results in nanorod growth with an average diameter 100 nm and length of 4  $\mu\text{m}$ . Nanorod growth is restricted in areas covered by

the nanoimprint resist. This results in a regular array of ZnO nanorods (Fig. 5-14). The nanoimprint resist is subsequently removed in an organic solvent.

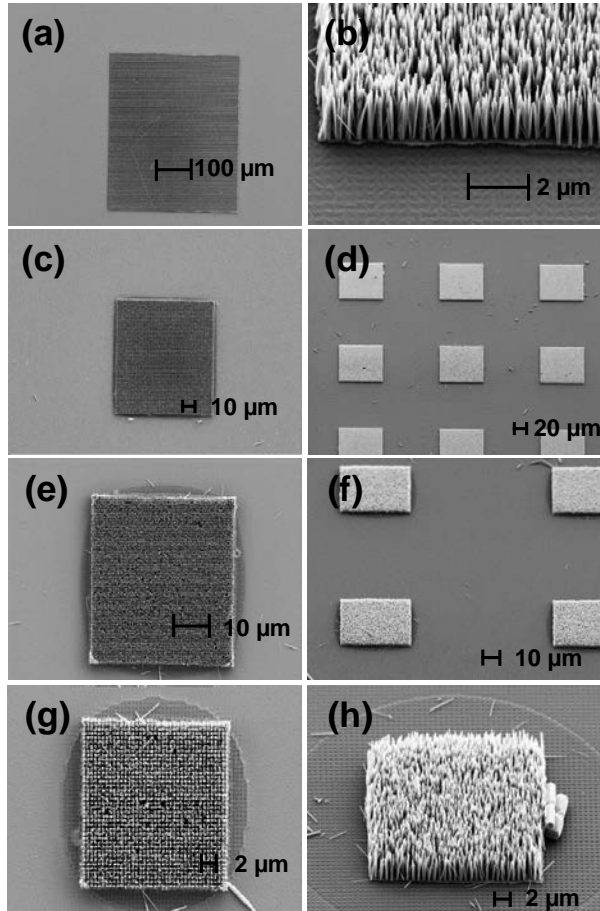


Figure 5-14 SEM images of ordered ZnO nanorod arrays Left – Top view, Right – Side view. (a-b) 500  $\mu\text{m}$  x 500  $\mu\text{m}$  (c-d) 100  $\mu\text{m}$  x 100  $\mu\text{m}$  (e-f) 50  $\mu\text{m}$  x 50  $\mu\text{m}$  (g-h) 30  $\mu\text{m}$  x 30  $\mu\text{m}$

The ZnO nanorods are subsequently encased in a layer of polyimide which provides mechanical and environmental protection, in addition to serving as support for deposition of the bottom electrode. The hydrothermally grown ZnO nanorod arrays are primed with a monolayer of NMP (N-Methylpyrrolidone) to enhance the surface wettability. Next, a layer of polyimide is spin coated and patterned with conventional photolithography to define bondpad areas for electrical connection to the top and bottom electrodes. The polyimide is then cured (5  $\mu\text{m}$ ) and

subjected to an anisotropic oxygen plasma etch process to expose the tips of the nanorods for electrical contact (Fig. 5-15).

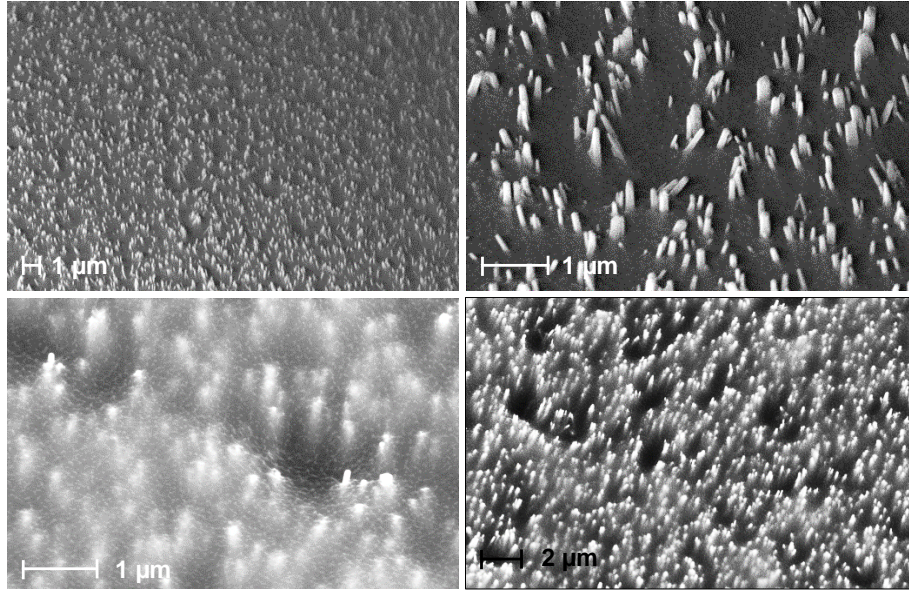


Figure 5-15 SEM images of exposed nanorod tips embedded in polyimide after plasma etch

The bottom electrode layer is deposited and patterned next. 30 nm of Ti and 100 nm of Au are E – beam - evaporated and patterned using a lift –off process (Fig. 5-16).

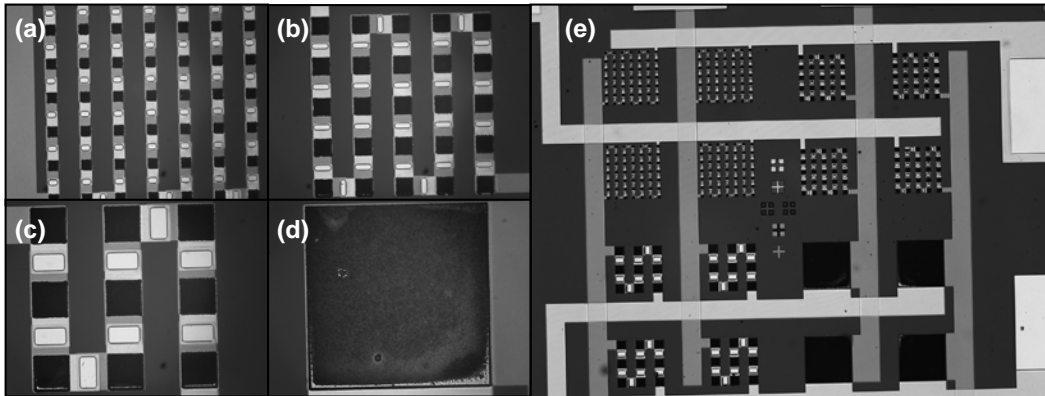


Figure 5-16 Microscope images after Au/Ti bottom electrode deposition and lift-off(a) TS49\_30

(b) TS25\_50 (c) TS9\_100 (d) TSS (e) AAS44 array

As discussed previously, a 60 μm thick layer of polyimide is subsequently coated and patterned to define bondpads. The Si wafer with the fabricated devices is then inverted, and



subjected to a fluorine - based plasma etch. The silicon wafer is completely etched away to release the sensors embedded within the flexible substrate (Fig. 5-17).

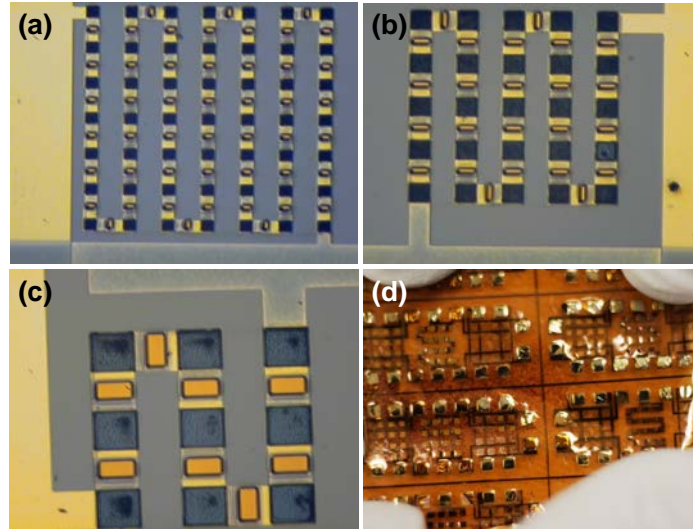


Figure 5-17 Microscope images after deposition of flexible substrate (a) TS49\_30 (b) TS25\_50 (c) TS9\_100 (d) Photograph of tactile sensor arrays on flexible substrate after removal of silicon base wafer

#### 5.4 Frequency domain and time domain characterization of ZnO nanorods

The as-fabricated sensors were subjected to pressure loading with a custom - devised measurement setup. A micromanipulator station was modified to accept an assembly consisting of a 500  $\mu\text{m}$  diameter, laser cut, flat - tipped tungsten probe, a sensitive load cell (10 gm. max range, 1 mg. resolution) and a single axis piezoelectric nanopositioner (50  $\mu\text{m}$  max travel, <1 nm resolution). These elements were connected in series to apply a precise tactile pressure on top of the fabricated sensors. The assembly was attached to the microscope platform of the micromanipulator station whereby it was possible to translate the assembly with fine motion control in X, Y and Z directions. The characterization setup is shown in Figure 5-18.

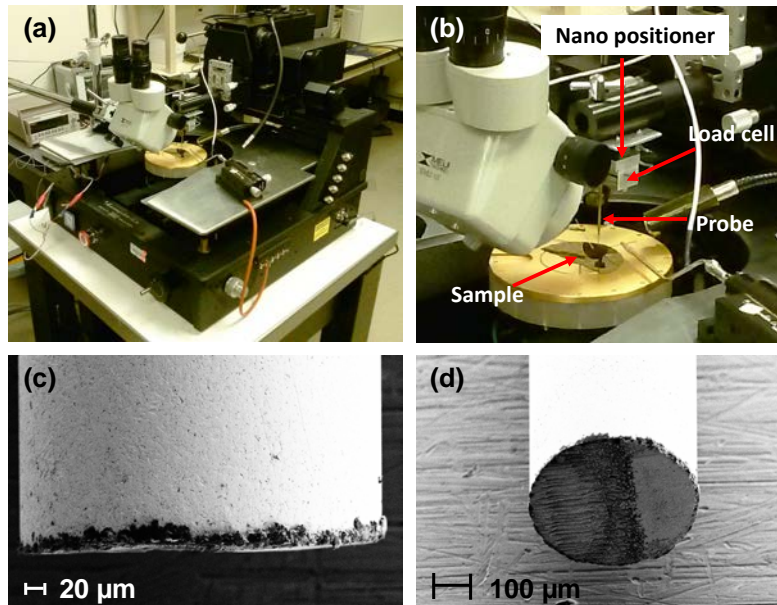


Figure 5-18 (a) Modified micromanipulator station used for characterization of tactile pressure sensors (b) Zoomed in photograph showing a sample under test along with the nano positioner, load cell and probe (c) SEM image, top view of flat - tipped tungsten probe (d) SEM image side view of tungsten probe

In order to clearly evaluate the sensor output with respect to the background noise such as environmental pick-up, line voltage and harmonics, the sensor response was characterized in frequency domain using a Agilent 35670 dynamic signal analyzer (Fig. 5-19(a)). The nanopositioner module was driven using a 50% duty cycle square wave signal from a signal generator. The amplitude of the signal is set such that the tungsten probe applies the desired tactile pressure to the tactile sensor. The load cell displays the force applied to the tactile sensor in grams, from which, knowing the cross sectional area of the tungsten tip, the applied pressure can be calculated. The tactile sensor response, at an amplitude corresponding to the pressure applied and at the frequency at which the nanopositioner is driven at, is registered by the signal analyzer as a voltage spike. The contributions from other noise sources are also registered as distinct voltage spikes at the corresponding noise source frequency. The tactile sensor is then probed at a frequency in a range that is free from noise sources thus allowing an accurate

measurement of the generated voltage signal. An example of such a frequency – voltage plot is shown in Figure 5-19(b). The tactile sensor is probed at a frequency of 10 Hz.

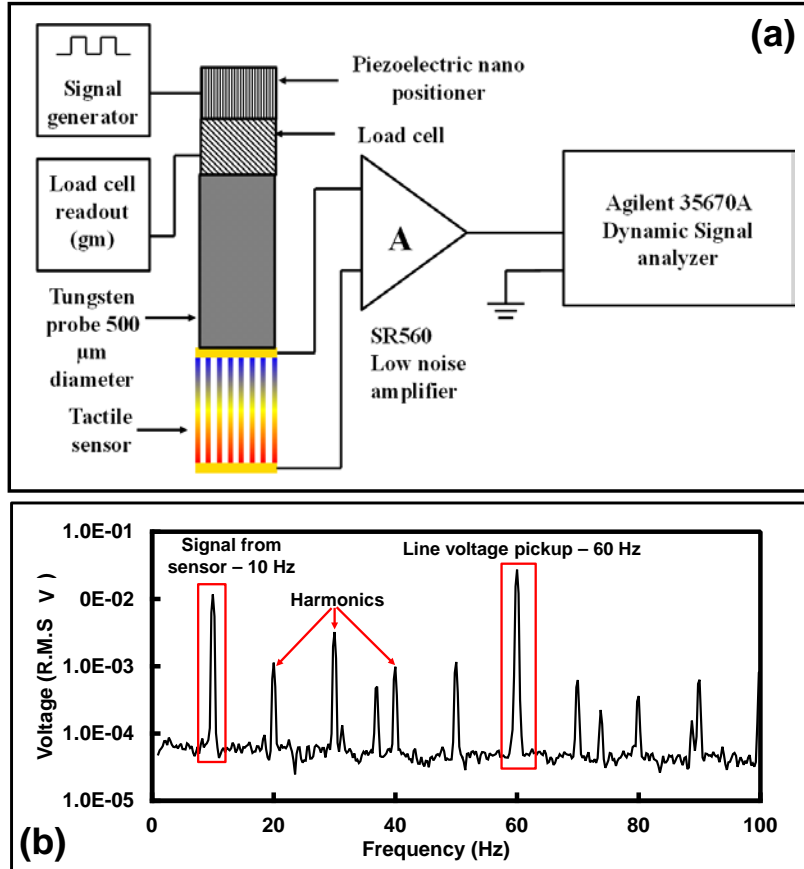


Figure 5-19 (a) Schematic of the characterization setup used for frequency domain characterization of tactile pressure sensor (b) An example plot from the signal analyzer showing sensor signal, and various noise components Note that all signals are amplified using an amplifier gain of 10000

In order to execute this experimental procedure, it was necessary to ascertain that the pressure sensor response was invariant with respect to the probe frequency. Hence, the sensor was probed at different frequencies at a fixed pressure amplitude. The results are presented in Figure 5-20. It was observed that the sensor response does not vary significantly with respect to the probe frequency up to 50 Hz. Beyond 50 Hz, the frequency spectrum contains a number of noise components, most notably the 60 Hz line voltage pickup. Additionally, the tactile sensor

response was found to be inconsistent at frequencies greater than 70 Hz. At the time of writing it is not known if the cause of the inconsistency lies with the tactile pressure sensor or the piezoelectric nano – positioner module. However, as the tactile pressure sensor is not expected to experience cyclic loading in excess of a few Hz in normal operation, further investigation into the cause was deemed unnecessary.

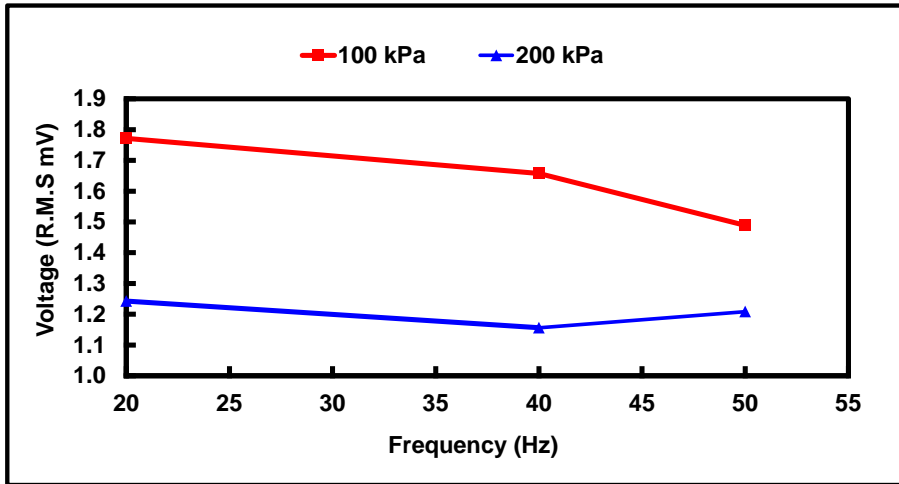


Figure 5-20 Sensor response at 100 kPa and 200 kPa at different probe frequencies Note that all signals are amplified using an amplifier gain of 10000

The next experiment aimed to verify the origin of the observed voltage signal and to observe any possible cross-talk between adjacent sensors. Accordingly, a set of four neighboring TSS type sensors were probed as shown in Figure 5-21 (a-e). Initially, none of the sensors was probed and the signal across the device TSS\_R1C1 was measured using the signal analyzer. No voltage spikes were observed. Next, TSS\_R1C1 was subjected to a cyclic tactile pressure loading at a frequency of 25 Hz. A corresponding voltage spike was observed on the signal analyzer readout at 25 Hz, thus confirming that the signal originated from the cyclic mechanical compression of the piezoelectric ZnO nanorods in the sensor. Next, with TSS\_R1C1 connected across the measurement circuit, the neighboring sensors TSS\_R1C2, TSS\_R2C1 and TSS\_R2C2 were subjected to cyclic tactile pressure loading at 25 Hz. No voltage spike was observed at 25 Hz, which indicated the complete absence of any cross-talk

between adjacent sensors (Fig. 5-21(f)). Since the sensor pitch is 1 mm, this test effectively proves that the spatial resolution of the sensor array is at least 1 mm.

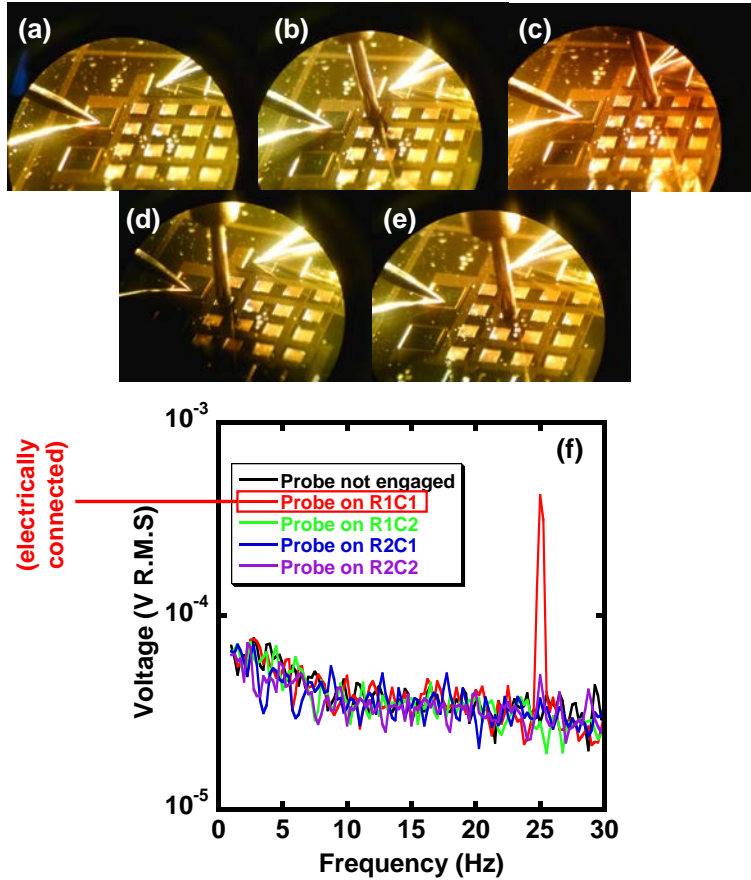


Figure 5-21 Micrographs showing the tactile sensor array being probed. R1C1 is connected to the measurement apparatus (a) Probe not engaged (b) R1C1 probed (c) R1C2 probed (d) R1C3 probed (e) R1C4 probed (f) Frequency domain plot corresponding to a-e. Note that all signals are amplified using an amplifier gain of 10000

With the origin of the observed signal verified and any possibility of cross-talk eliminated, the different sensor designs were subjected to cyclic tactile pressure loading in the 10 kPa – 200 kPa range . The applied pressure was increased in six steps and then reduced, to observe the sensor hysteresis. Initially, the sensors were probed with a 2  $\mu$ m substrate polyimide layer. Figure 5-22 shows examples of the observed response from the different types of sensors. The pressure voltage characteristic is nearly linear and hysteresis is negligible.

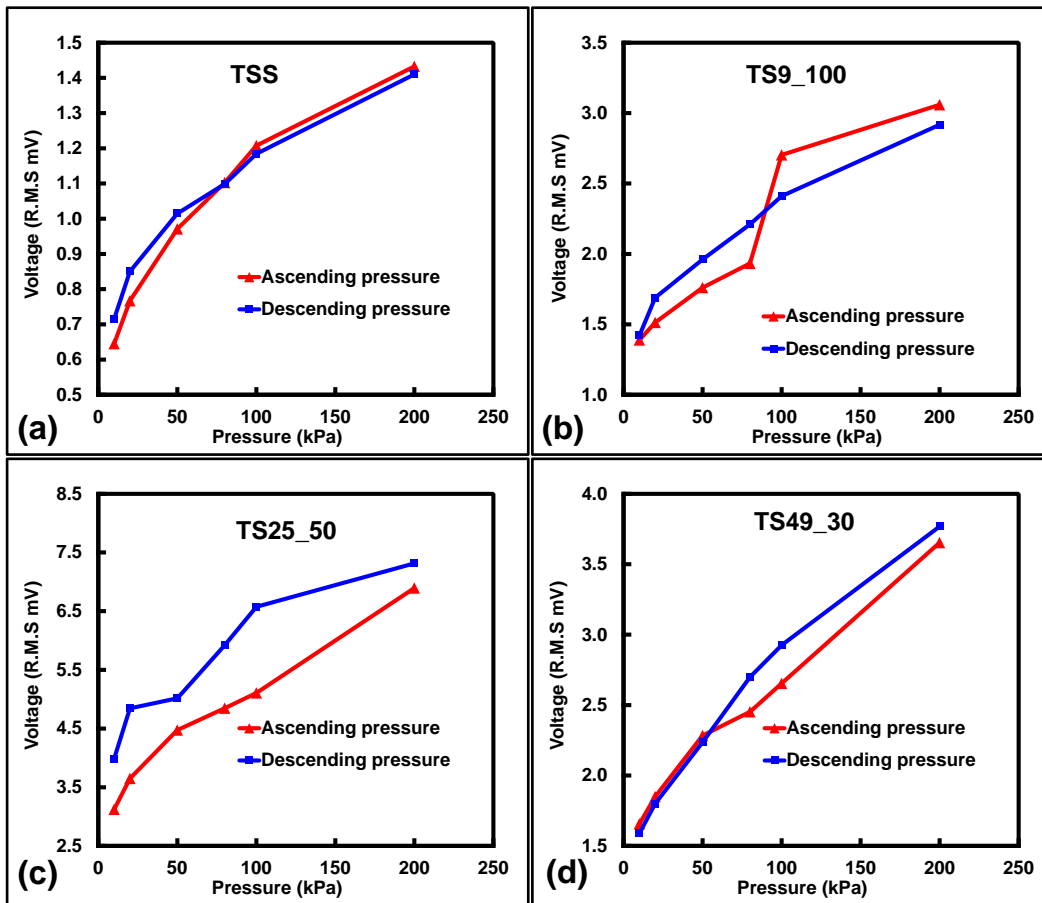


Figure 5-22 Tactile sensor response when subjected to a cyclic load in the 10 – 200 kPa range

(a)TSS (b) TS9\_100 (c) TS25\_50 (d) TS49\_30 Note that all signals are amplified using an amplifier gain of 10000

The sensor was probed multiple times at each pressure step and the average generated voltage and standard deviation was noted. The sensor response repeatability is excellent as is evident from the low standard deviation from average (Fig. 5-23).

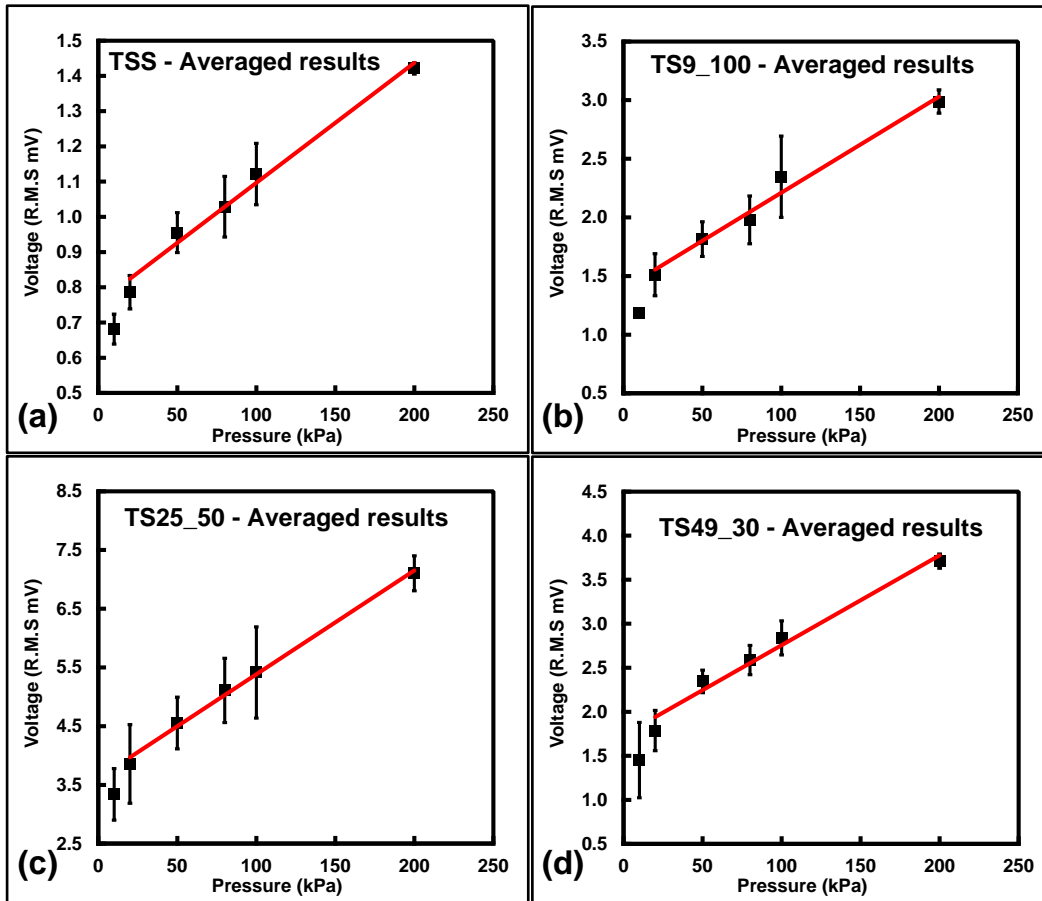


Figure 5-23 Averaged results from probing the different sensor designs at different pressure values multiple times. The error bars at each data point show standard deviation. (a) TSS (b) TS9\_100 (c) TS25\_50 (d)TS49\_30. Note that all signals are amplified using an amplifier gain of 10000

The sensitivity of each sensor was determined from the slope of the voltage – pressure graph shown in Figure 5-23. The sensitivity from fourteen different sensors is noted in Figure 5-24.

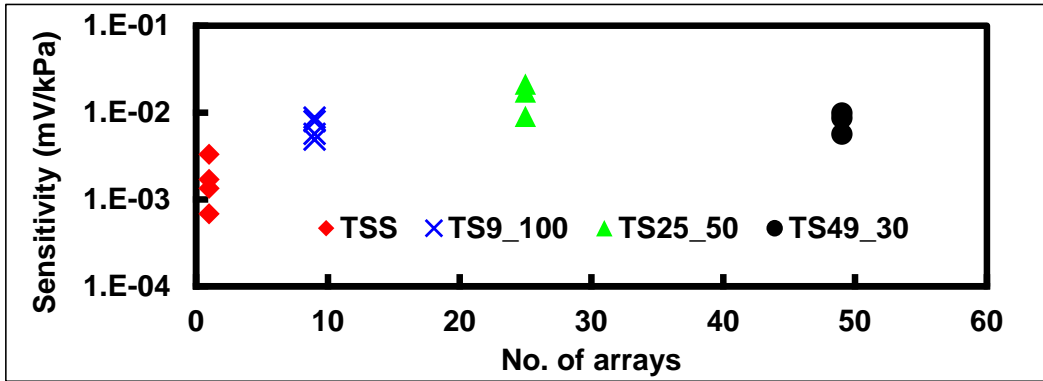


Figure 5-24 Sensitivity of tactile pressure sensors as a function of the number of nanorod arrays in each sensor design. Each data point represents the sensitivity from a single sensor. Note that all signals are amplified using an amplifier gain of 10000

Next, 18  $\mu\text{m}$  of substrate polyimide layer was coated on the sensors and the sensors were probed as before. This was done to observe the effect of the polyimide fabrication process in addition to the polyimide thickness on sensor performance, specifically hysteresis and repeatability. The sensor pressure-voltage characteristic is once again observed to be nearly linear with negligible hysteresis (Fig. 5-25) and excellent repeatability (Fig. 5-26). An expected reduction in sensitivity is observed, due to the change in mechanical stiffness caused by the addition of the thick polyimide substrate (Fig. 5-27).



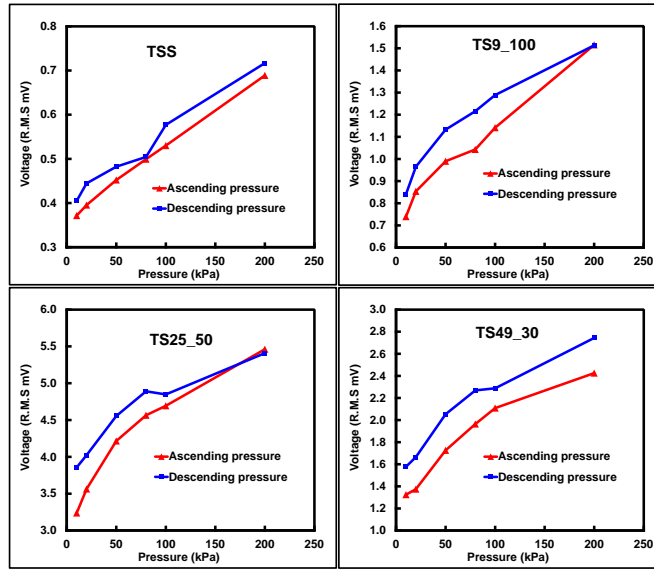


Figure 5-25 Tactile sensor response when subjected to a cyclic load in the 10 – 200 kPa range after deposition of 18  $\mu\text{m}$  substrate polyimide (a)TSS (b) TS9\_100 (c) TS25\_50 (d) TS49\_30.

Note that all signals are amplified using an amplifier gain of 10000

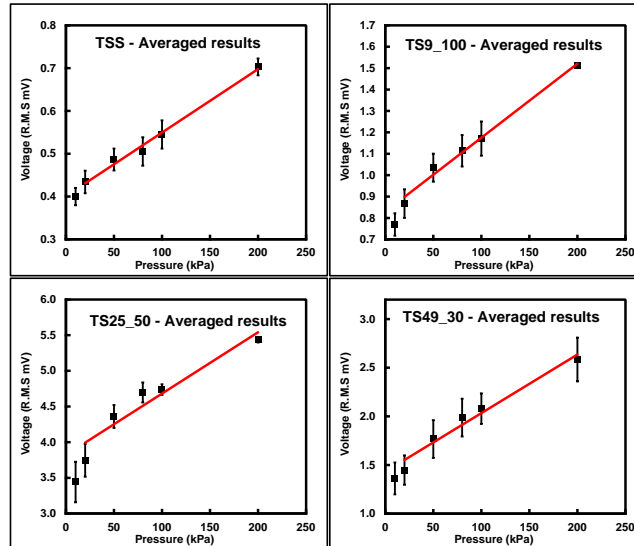


Figure 5-26 Averaged results from probing the different sensor designs after deposition of 18  $\mu\text{m}$  substrate polyimide at different pressure values multiple times. The error bars at each data point show standard deviation. (a) TSS (b) TS9\_100 (c) TS25\_50 (d)TS49\_30. Note that all signals are amplified using an amplifier gain of 10000

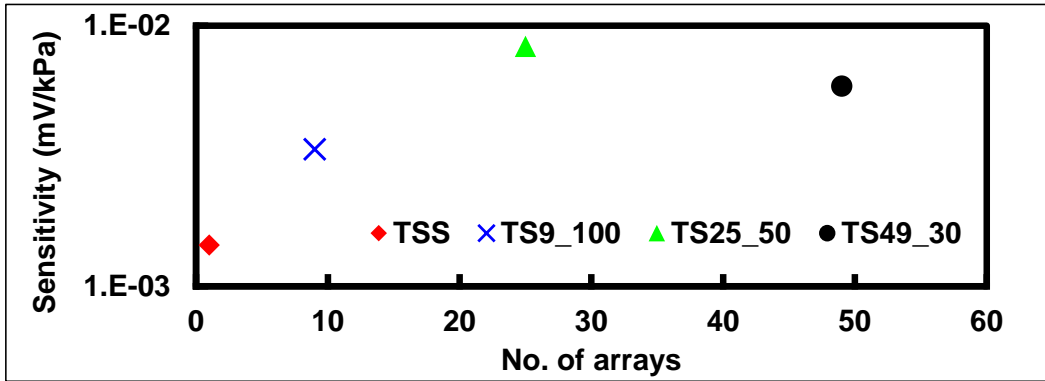


Figure 5-27 Sensitivity of tactile pressure sensors as a function of the number of nanorod arrays in each sensor design after deposition of 18  $\mu\text{m}$  thick substrate. Each data point represents the sensitivity from a single sensor. Note that all signals are amplified using an amplifier gain of 10000

Finally, in order to mimic the real world operation, the tactile sensors were probed in time domain. The sensors were probed at a frequency of 1 Hz and the sensor output was amplified using a SR 560 low noise amplifier at a gain of 10000. The output from the amplifier was fed to a Keithley 2182a nanovoltmeter that was continuously sampled using a Labview program. Results from the time domain characterization are presented in Figures 5-29 and 5-30. The observed sensor response mirrors the observation from frequency domain testing. The series - connected sensor designs, namely TS9\_100, TS25\_50 and TS49\_30 generate higher voltage for the same applied pressure than the TSS design. This results in a noticeably higher signal to noise ratio, thus allowing more accurate detection of the applied pressure.

It was observed, from both the frequency domain results as well as the time domain results, that the series - connected designs generated higher voltages than the single array design. However, contrary to expectation, it is also observed that the design TS49\_30 with 49 series connected arrays consistently generates lower voltage than the TS25\_50 design with 25 series connected arrays. A possible reason for the lower voltage generation from the TS49\_30 design lies in the fabrication process; specifically, the fabrication step that involves coating the as-grown ZnO nanorod arrays with a protecting layer of polyimide. After spin coating and curing,

the polyimide thickness on top of the larger nanorod arrays (500  $\mu\text{m}$ , 100  $\mu\text{m}$ , and 50  $\mu\text{m}$ ) was found to be slightly higher ( $< 1\mu\text{m}$ ) as compared to that on the smallest nanorod arrays (30  $\mu\text{m}$ , used in the TS49\_30 design). This difference in thickness could be attributed to differences in spin coating dynamics of the viscous polyimide as applied to nanorod arrays of different areas. For the same area ( $\sim 500\ \mu\text{m} \times 500\ \mu\text{m}$ ), the TSS, TS9\_100 and TS25\_50 designs have a higher percentage of the area occupied by nanorods as compared to the TS49\_30 design. Consequently, the sensor designs with the larger areas would present a higher resistance to the free flow of polyimide during the spin coating process, resulting in a slightly more quantity of polyimide being 'trapped' between the arrays. This could contribute to a higher thickness of the polyimide in these areas after coating and curing. Conversely, the TS49\_30 design has smaller nanorod arrays that would present a comparatively less resistance to the polyimide flow during spin coating which could result in a slightly thinner polyimide layer after coating and curing. The different sensor designs with dissimilar fill polyimide thicknesses were then subjected to a single, uniform plasma etch, to expose the nanorod tips for electrical contact. This transferred the thickness dissimilarities that originated in the coating process to the etch process, resulting in a greater section of the nanorods in the 30  $\mu\text{m}$  array exposed. In comparison, the nanorod tips in the 500, 100 and 50  $\mu\text{m}$  arrays were exposed to a lesser extent. Ti/Au electrode layer that was subsequently deposited shorted out the exposed nanorod tips rendering those areas incapable of generating piezoelectric voltage. A larger section of the exposed nanorods in the 30  $\mu\text{m}$  arrays was shorted out thus reducing the effective nanorod length participating in generation of piezoelectric voltage. As a result, even though the TS49\_30 has 49 series connected arrays and does generate higher voltage than the TSS design, the lower effective length of the nanorods in the 30  $\mu\text{m}$  arrays reduces the amplitude of the generated voltage in comparison to the TS25\_50 design. This problem could be resolved by optimizing the polyimide plasma etch time to expose the nanorod tips in the 30  $\mu\text{m}$  arrays.

As mentioned previously, the device SD16 is a single large area (3.5 mm x 3.5 mm ) device containing 16 TSS type arrays connected in series. This device was fabricated to demonstrate the operation of the tactile sensor in response to tactile pressure applied using a common everyday object, as opposed to the precision nanopositioner-load cell setup. Accordingly, a tactile pressure was applied to the device by a human operator holding a hex – key that had a diameter comparable to the area of the sensor. The hex – key was tapped on the sensor at a pressure comparable to that applied when pressing a cell-phone button. The response from the sensor was recorded using in time domain using the measurement apparatus described previously (without the amplifier), and is shown in Figure 5-28. Each tap on the sensor with the hex – key correspond to a negative going pulse on the waveform.

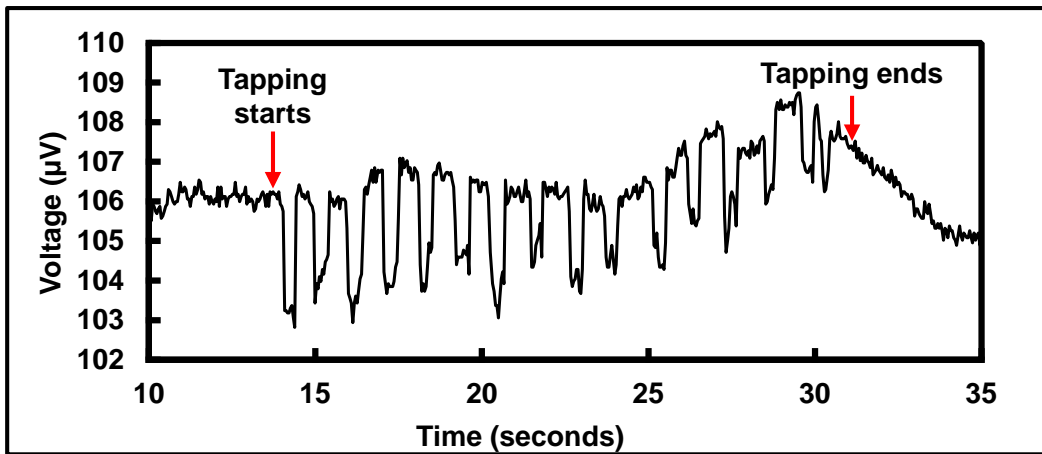


Figure 5-28 SD16 sensor response after being tapped manually using a hex key. The sensor response is unamplified.

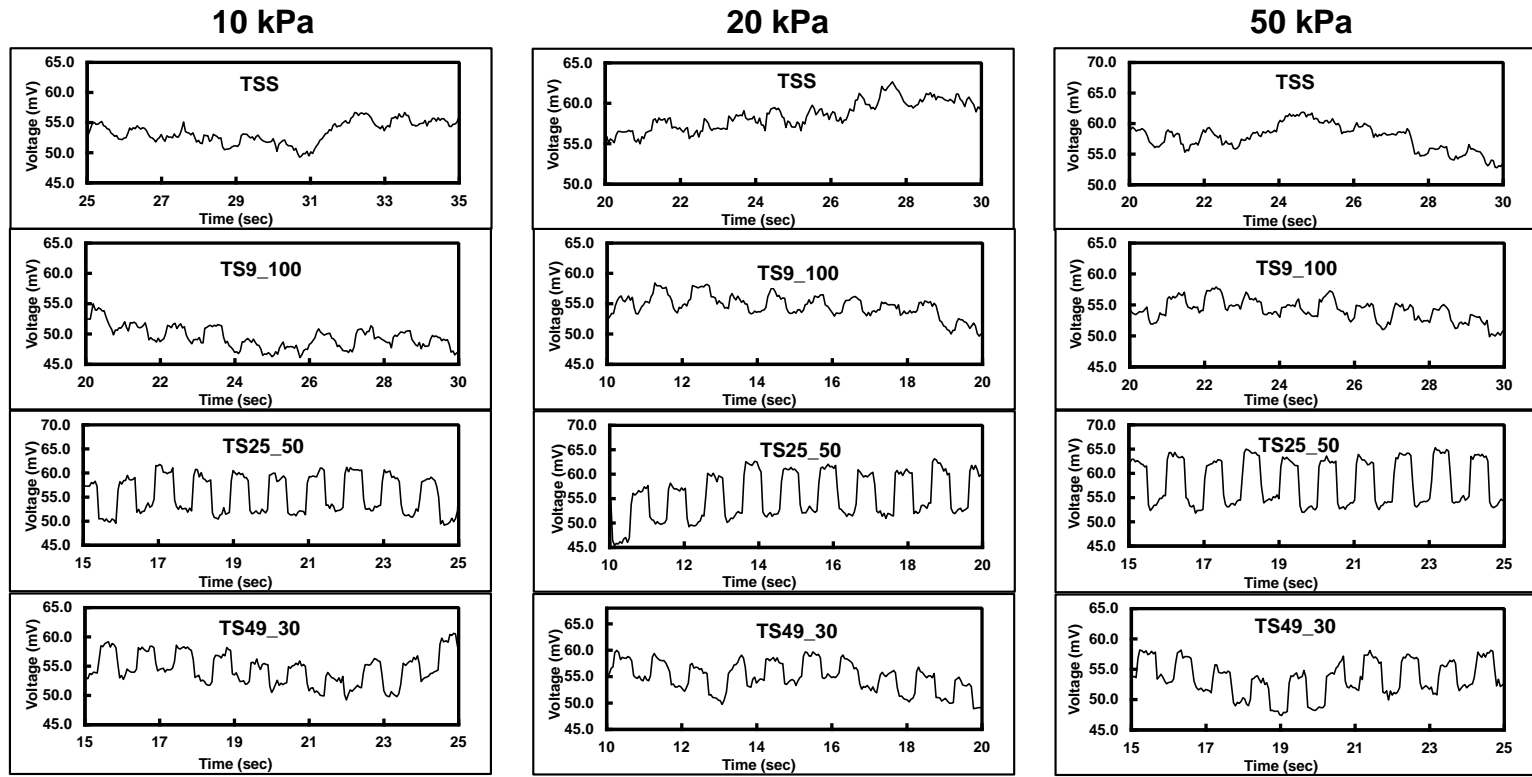


Figure 5-29 Time domain response from the different tactile sensors in the 10 – 50 kPa pressure range. All signals amplified using an amplifier with gain 10000

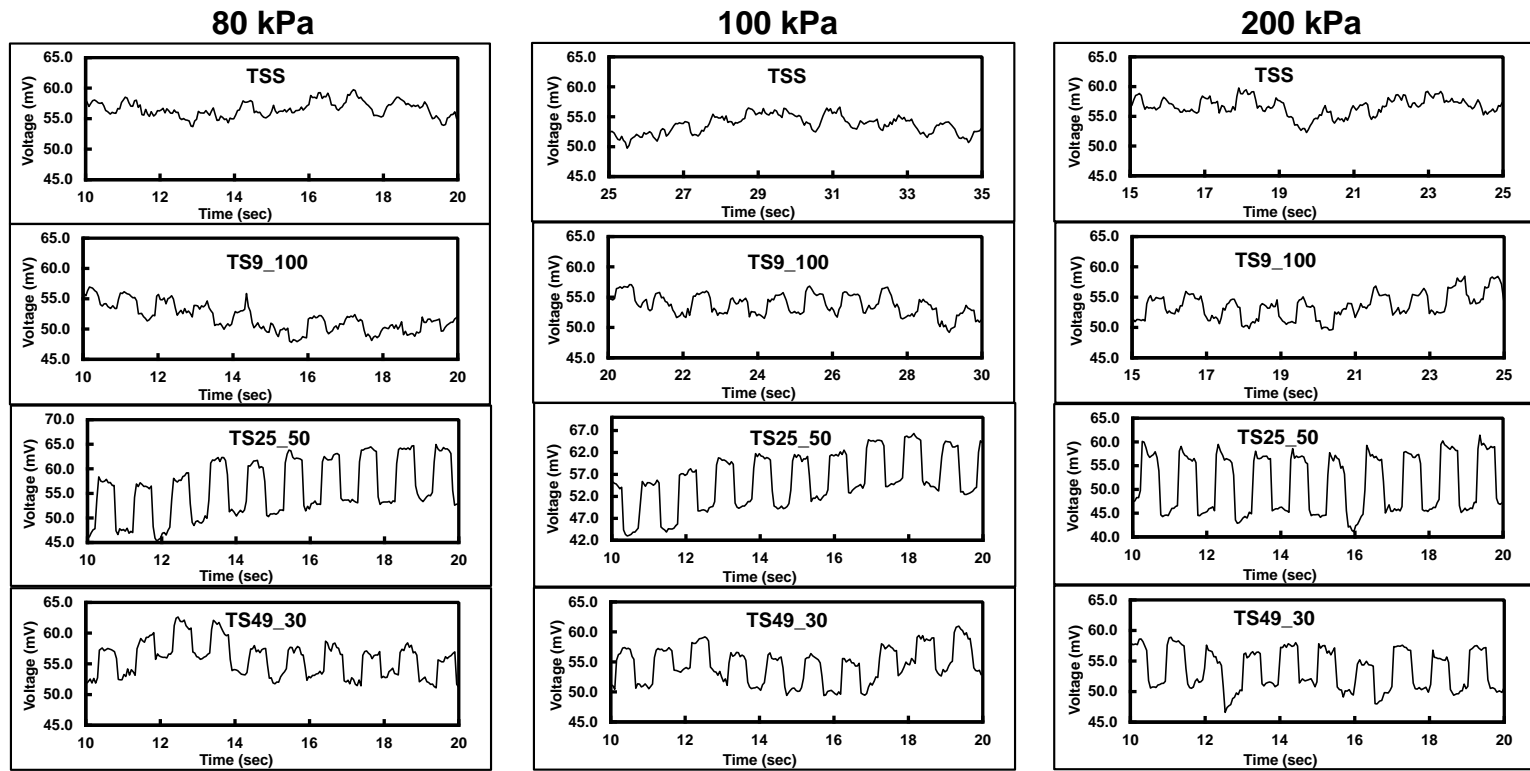


Figure 5-30 Time domain response from the different tactile sensors in the 10 – 50 kPa pressure range. All signals amplified using an amplifier with gain 10000

## 5.5 Summary

Tactile pressure sensing is of utmost importance in enhancing a robot's interaction with its environment. The addition of the human sense of touch to a robot provides it with a layer of information that simply cannot be obtained using non-contact sensors. Moreover, the benefits of tactile sensing in areas of prosthetics and human - assisted robotic object manipulation are limitless. In order to successfully adapt tactile sensing systems to robotics and prosthetics, certain unique requirements have to be fulfilled. The sensor systems developed in the present research aim to meet these requirements. Large area arrays of tactile sensors have been developed on flexible substrates. The sensor arrays are fully conformable to non-planar surfaces frequently found on robot systems. In addition, sensor systems are self-powered, which allows for effective large area coverage without presenting any additional load to the robot's power supplies. The pressure transduction element used in the sensor system is piezoelectric ZnO nanorods that generate a voltage signal in proportion to the amplitude of the applied tactile pressure. The sensor systems display near linear response with negligible hysteresis. Different sensor designs have been explored with a view to optimize sensitivity with a maximum of 2.12mV/kPa (amplified sensor output, amplifier gain 10000) being recorded for the TS25\_50 design. The sensors are arranged in an addressable array with a pitch of 1 mm and no cross-talk has been observed between adjacent sensors in the array. This translates to a spatial resolution of 1 mm or better. Furthermore, a process incorporating thermal nanoimprint lithography and photolithography has been developed for fabrication of custom sized arrays of ordered ZnO nanorods. This allows control over nanorod growth density which in turn improves sensor performance repeatability. In addition, the developed sensor systems are fully packaged in a chemical and moisture resistant polyimide that greatly enhances usability in harsh environments.

## Chapter 6

### Conclusion

#### 6.1 Nanoimprint lithography as an enabling technology

Since the first development was reported by Dr. Stephen Chou at Princeton in 1996, nanoimprint lithography has come a long way in the past decade as a noteworthy lithography technology for fabrication of submicron features. This is evident from the abundance of research articles using NIL for different applications in MEMS and NEMS systems. Large area fabrication of submicron features has been frequently demonstrated using NIL. NIL offers advantages such as process repeatability, lower equipment cost and complexity and fast process throughput. Technological advancements such as improved nanoimprint resists, mold anti-adhesion coatings and nanoimprinters with better control over process temperature and pressure have resulted in a reliable process capable of rendering features as small as 2 nm in dimension. As a result, NIL is included in the ITRS as a next generation lithography process to carry forward Moore's law beyond the capabilities of diffraction limited optical lithography techniques. The aforementioned advantages and capabilities of NIL have been extensively explored to realize and improve the different applications presented in this research.

#### 6.2 Development of a novel membrane blood oxygenator with a nanoporous silicon nitride membrane

A gas exchange module for an implantable blood oxygenator system was the focus of the research presented in Chapter 2. Central to the development of this module, was the thin nanoporous  $\text{Si}_3\text{N}_4$  membrane that serves as the gas exchange interface. Conventional gas exchange membranes are made from PCTE (polycarbonate track - etched) or porous PDMS that have widely varying porosities and irregular pore placement. As a result of the inherent random nature of the patterning process. In the present work, NIL was used to pattern a template with a large area regular array of uniform diameter nanopores, 200 nm in diameter and



500 nm pitch. In order to overcome the limited etch selectivity of the nanoimprint resist for pattern transfer, a novel two-step lift-off technique was developed and optimized. This enabled pattern transfer from the resist to a  $\text{Al}_2\text{O}_3$  thin film. The  $\text{Al}_2\text{O}_3$  layer was used as a hard mask to transfer the nanoscale pattern from the resist to a 1  $\mu\text{m}$  thick LPCVD deposited  $\text{Si}_3\text{N}_4$  thin film, using a tailor-made high - selectivity, anisotropic RIE process. The nanoporous  $\text{Si}_3\text{N}_4$  thin film was transformed into a suspended membrane using conventional bulk micromachining.

A microfluidic channel structure for transport of blood through the oxygenator has been developed. The branched channel structure allows for a uniform, constant flow rate, laminar flow of blood with minimal turbulence and is designed to significantly reduce cell trauma. The channel structure was realized using silicon bulk micromachining, and in combination with nanoporous membrane forms the membrane oxygenator module.

The two stage lift-off and the anisotropic RIE processes have been optimized for a 100 % yield of membranes from a 3" diameter Si wafer. It has been observed that only 13 % of nanopores show some kind of damage or deformation across the wafer. The percent standard deviation in nanopore diameter is as low as 0.71%. These statistics effectively prove the usefulness of NIL for large area fabrication of nanostructures.

### 6.3 Characterization of piezoelectric response of crystalline ZnO nanorods and low temperature NIL assisted hydrothermal growth

Low temperature growth and characterization of piezoelectric response of crystalline ZnO nanorods was discussed in Chapter 3. ZnO is a wide – bandgap II-VI semiconductor that also exhibits piezoelectric and pyroelectric properties. It has been suggested in literature that high aspect ratio nanostructures of ZnO i.e. nanorods may exhibit enhanced piezoelectric characteristics as compared to bulk ZnO. This makes ZnO nanorods an attractive candidate in applications involving piezoelectric transduction of mechanical energy to an electrical signal.

A low temperature process for growth of crystalline ZnO nanorods has been demonstrated. The process is fully compatible with conventional CMOS processing and also meets the low temperature requirements for fabrication on flexible substrates. The as-grown nanorods were probed using the force spectroscopy mode of an atomic force microscope. A mechanical force of the order of few tens of nN was applied to the nanorods as mechanical excitation for piezoelectric transduction. The corresponding generated voltage was recorded using a sensitive low noise measurement apparatus. Voltage generation up to few tens of mV was recorded.

It was observed that the interaction between the nanorod and the AFM tip was highly irregular due to the random nature of nanorod growth on the substrate. Variation in nanorod dimensions and density made it impossible to accurately determine the force applied by the AFM tip. The nanoscale patterning techniques using NIL developed in the previous work were employed as a solution. By selectively masking the ZnO seed layer with an array of submicron patterns, a corresponding ordered array of ZnO nanorods was obtained using the same low temperature growth process. NIL allowed some degree of control over nanorod placement. Additional control over placement was achieved using conventional photolithography. Rows of NIL ordered nanorods with up to 2  $\mu\text{m}$  spacing have been thus fabricated. The effects of growth process variables such as solution concentration and seed layer deposition temperature on nanorod morphology was also examined.

It is expected that a combination of placement, density and morphology control techniques will alleviate the issue associated with random nanorod growth. These techniques could be further extended to grow a regular ordered array of nanorods. Currently, the size of a single grain in the PLD deposited polycrystalline ZnO seed layer is  $\sim 40$  nm. The size of the opening in the NIL template is 200 nm, dictated by the nanoimprint mold. As a result, multiple seed layer grains are exposed per opening resulting in multiple nanorods growing per growth

site. This could be remedied by matching the diameter of the opening in the template to the individual grain which could result in growth of a single crystalline nanorod per site.

Finally in order to apply a precise magnitude of force using force spectroscopy, accurate tip placement with nanometer accuracy is desirable. This could be accomplished with the latest AFM systems incorporating closed-loop tip position control

#### 6.4 Development of a NEMS vibration energy harvester using ordered ZnO nanorods

Microelectronic devices and systems have increasingly grown more capable in the past few decades. Advancements in semiconductor manufacturing technologies have given rise to multifunctional portable devices. Energy storage technology however, has not progressed in tandem and represents a bottleneck in furthering device improvement. Extracting energy from the ambient environment represents an alternative approach to powering mobile and remote systems. Harvesting vibration energy from the environment for conversion to usable electrical power was the focus of the work presented in Chapter 4. The principle of operation of device is based on a proof-mass system that converts ambient vibrations into mechanical excitation for a piezoelectric ZnO nanorod array. In response, the nanorods generate a voltage due to the piezoelectric effect, which can be harvested. The experiments with AFM probing and NIL - assisted ordered growth of crystalline ZnO nanorods described in Chapter 3 formed the basis of the NEMS energy harvester design.

A survey of literature revealed that an energy harvester system would need to harvest energy from vibrations  $\sim 1$  g in amplitude at  $\sim 1$  kHz frequency for effective operation. Two different design approaches were considered to realize such a device. In the first approach, a NEMS device was designed to be fabricated using surface micromachining techniques involving fabrication of the proof-mass using electroplating. The proof-mass thickness is limited to few tens of  $\mu\text{m}$  using this approach which results in a minimum resonance frequency of 2.63 MHz. This is over three orders of magnitude higher than the desired operation frequency. Since the

resonance frequency varies inversely with the square root of the mass of the proof-mass, a wide area proof-mass would be necessary to achieve the desired operation frequency. This would complicate fabrication and occupy a large footprint on the device.

The second approach utilized a bulk - micromachined proof-mass having thickness up to 600  $\mu\text{m}$  (Si wafer thickness). This approach allowed the mass of the proof-mass to be increased while occupying a smaller area on the wafer. A NEMS device designed using a bulk - micromachined proof-mass and an ordered ZnO nanorod array was shown to generate up to 14.2 mV at a vibration frequency of 1.1 kHz and 1 g amplitude using finite element modeling. A fabrication process flow for realization of the bulk - micromachined harvester design is proposed.

#### 6.5 Design, fabrication and characterization of tactile pressure sensors on flexible substrates using piezoelectric ZnO nanorods

Chapter 6 demonstrates a tactile pressure sensor system developed on flexible substrates for mobile robotic applications. Robot systems present a set of unique requirements for sensor design. In order to achieve a human – like sense of touch, the robot system needs to be draped in a large area sensing “skin” of tactile sensors. This requirement, coupled with the need to maintain sufficient spatial resolution necessitate a large number of sensors.

A large area network of pressure sensors based on the piezoresistive or capacitive sensing principles require a constant bias for operation which represents a significant load to the robot’s limited power resources. The sensor system developed in the present research is based on piezoelectric ZnO nanorods that generate an electrical signal proportional to the magnitude of the applied pressure. As such, the sensor is completely self-generating in nature, requiring no external bias for transduction. Moreover, the sensors are fabricated on flexible polyimide substrates to conform to non-planar surfaces on the robot. Additionally, the nanorod

array is fully packaged in impervious polyimide for protection against dust, moisture and mechanical shock.

NIL – assisted ordering of the nanorod array has been instrumental in simplifying fabrication, along with improving performance repeatability and resulting in a near linear response with negligible hysteresis. The tactile sensors have been demonstrated to detect tactile pressure in the 10 kPa – 200 kPa pressure range. No cross-talk is observed in sensors spaced at a pitch of 1 mm in an array confirming the minimum spatial resolution of the array to be 1mm. Different sensor designs were explored with a view to improve sensitivity. Accordingly a peak sensitivity of 2.12 mV/kPa has been recorded for the series –connected TS25\_50 design.

## References

- [1] R. P. Feynman. There's plenty of room at the bottom [data storage]. *Microelectromechanical Systems, Journal Of* 1(1), pp. 60-66. 1992.
- [2] J. Arlett, E. Myers and M. Roukes. Comparative advantages of mechanical biosensors. *Nature Nanotechnology* 6(4), pp. 203-215. 2011.
- [3] V. T. Moy, E. Florin and H. E. Gaub. Intermolecular forces and energies between ligands and receptors. *Science-new york then washington-* pp. 257-257. 1994.
- [4] J. M. Fernandez and H. Li. Force-clamp spectroscopy monitors the folding trajectory of a single protein. *Science* 303(5664), pp. 1674-1678. 2004.
- [5] Y. Yang, C. Callegari, X. Feng, K. Ekinici and M. Roukes. Zeptogram-scale nanomechanical mass sensing. *Nano Letters* 6(4), pp. 583-586. 2006.
- [6] A. de la Escosura-Muñiz and A. Merkoçi. Nanochannels preparation and application in biosensing. *ACS Nano* 6(9), pp. 7556-7583. 2012.
- [7] C. T. Lim, J. Han, J. Guck and H. Espinosa. Micro and nanotechnology for biological and biomedical applications. *Med. Biol. Eng. Comput.* 48(10), pp. 941-943. 2010.
- [8] X. Hou and L. Jiang. Learning from nature: Building bio-inspired smart nanochannels. *ACS Nano* 3(11), pp. 3339-3342. 2009.
- [9] S. Nagarajan, Z. Li, V. Marchi-Artzner, F. Grasset and Y. Zhang. Imaging gap junctions with silica-coated upconversion nanoparticles. *Med. Biol. Eng. Comput.* 48(10), pp. 1033-1041. 2010.
- [10] T. Qian and Y. Wang. Micro/nano-fabrication technologies for cell biology. *Med. Biol. Eng. Comput.* 48(10), pp. 1023-1032. 2010.

- [11] C. M. Bruinink, M. Buresi, M. J. de Boer, F. B. Segerink, H. V. Jansen, E. Berenschot, D. N. Reinhoudt, J. Huskens and L. Kuipers. Nanoimprint lithography for nanophotonics in silicon. *Nano Letters* 8(9), pp. 2872-2877. 2008.
- [12] C. Duan, W. Wang and Q. Xie. Review article: Fabrication of nanofluidic devices. *Biomicrofluidics* 7pp. 026501. 2013.
- [13] "ITRS Lithography 2011," [Online] Available: <http://www.itrs.net/Links/2011ITRS/2011Chapters/2011Lithography.pdf> Accessed November 15 2013.
- [14] R. Lawes. Future trends in high-resolution lithography. *Appl. Surf. Sci.* 154pp. 519-526. 2000.
- [15] B. J. Lin. Optical lithography—present and future challenges. *Comptes Rendus Physique* 7(8), pp. 858-874. 2006.
- [16] B. Fay. Advanced optical lithography development, from UV to EUV. *Microelectronic Engineering* 61pp. 11-24. 2002.
- [17] M. C. Peckerar and J. R. Maldonado. X-ray lithography-an overview. *Proc IEEE* 81(9), pp. 1249-1274. 1993.
- [18] R. Hughes and T. Heinrichs. A quantum information science and technology roadmap. *Universidad De California (En Línea)* [Http://Qist.Lanl.Gov](http://Qist.Lanl.Gov) 2004.
- [19] P. Gargini, G. Edwards, K. Dean, P. Seidel, K. Toyoda, V. Bakshi, S. Wurm, Y. Takamori, G. Dao and S. Tedesco. International EUV initiative (IEUVI) overview; challenges and collaborative efforts. *Future Fab Intl* 212006.
- [20] C. Vieu, F. Carcenac, A. Pepin, Y. Chen, M. Mejias, A. Lebib, L. Manin-Ferlazzo, L. Couraud and H. Launois. Electron beam lithography: Resolution limits and applications. *Appl. Surf. Sci.* 164(1), pp. 111-117. 2000.

- [21] J. Huh, M. Shepard and J. Melngailis. Focused ion beam lithography. *Journal of Vacuum Science & Technology B: Microelectronics and Nanometer Structures* 9(1), pp. 173-175. 1991.
- [22] L. Heyderman, H. Schiff, C. David, J. Gobrecht and T. Schweizer. Flow behaviour of thin polymer films used for hot embossing lithography. *Microelectronic Engineering* 54(3), pp. 229-245. 2000.
- [23] S. Minne, P. Flueckiger, H. Soh and C. Quate. Atomic force microscope lithography using amorphous silicon as a resist and advances in parallel operation. *Journal of Vacuum Science & Technology B: Microelectronics and Nanometer Structures* 13(3), pp. 1380-1385. 1995.
- [24] G. M. Whitesides, J. P. Mathias and C. T. Seto. *Molecular Self-Assembly and Nanochemistry: A Chemical Strategy for the Synthesis of Nanostructures* 1991.
- [25] S. Srivastava and N. A. Kotov. Nanoparticle assembly for 1D and 2D ordered structures. *Soft Matter* 5(6), pp. 1146-1156. 2009.
- [26] N. C. Seeman. DNA in a material world. *Nature* 421(6921), pp. 427-431. 2003.
- [27] D. Kim, J. Ahn, W. M. Choi, H. Kim, T. Kim, J. Song, Y. Y. Huang, Z. Liu, C. Lu and J. A. Rogers. Stretchable and foldable silicon integrated circuits. *Science* 320(5875), pp. 507-511. 2008.
- [28] G. M. Whitesides. The origins and the future of microfluidics. *Nature* 442(7101), pp. 368-373. 2006.
- [29] A. J. Hoffman, L. Alekseyev, S. S. Howard, K. J. Franz, D. Wasserman, V. A. Podolskiy, E. E. Narimanov, D. L. Sivco and C. Gmachl. Negative refraction in semiconductor metamaterials. *Nature Materials* 6(12), pp. 946-950. 2007.



- [30] S. Y. Chou, P. R. Krauss and P. J. Renstrom. Nanoimprint lithography. *Journal of Vacuum Science & Technology B: Microelectronics and Nanometer Structures* 14(6), pp. 4129-4133. 1996.
- [31] F. Hua, Y. Sun, A. Gaur, M. A. Meitl, L. Bilhaut, L. Rotkina, J. Wang, P. Geil, M. Shim and J. A. Rogers. Polymer imprint lithography with molecular-scale resolution. *Nano Letters* 4(12), pp. 2467-2471. 2004.
- [32] M. D. Austin, W. Zhang, H. Ge, D. Wasserman, S. Lyon and S. Y. Chou. 6 nm half-pitch lines and 0.04  $\mu\text{m}^2$  static random access memory patterns by nanoimprint lithography. *Nanotechnology* 16(8), pp. 1058. 2005.
- [33] L. J. Guo. Nanoimprint lithography: Methods and material requirements. *Adv Mater* 19(4), pp. 495-513. 2007.
- [34] W. J. Federspiel and K. A. Hench. Lung, artificial: Basic principles and current applications. *Encyclopedia of Biomaterials and Biomedical Engineering* 9pp. 910. 2004.
- [35] M. Demling Robert H. The modern version of adult respiratory distress syndrome. *Annu. Rev. Med.* 46(1), pp. 193-202. 1995.
- [36] M. D. Zilberberg and S. K. Epstein. Acute lung injury in the medical ICU: Comorbid conditions, age, etiology, and hospital outcome. *American Journal of Respiratory and Critical Care Medicine* 157(4), pp. 1159-1164. 1998.
- [37] L. B. Ware and M. A. Matthay. The acute respiratory distress syndrome. *N. Engl. J. Med.* 342(18), pp. 1334-1349. 2000.
- [38] M. Halpern, R. Stanford and R. Borker. The burden of COPD in the USA: Results from the confronting COPD survey. *Respir. Med.* 97pp. S81-S89. 2003.

- [39] J. Lee, M. Kung, H. Kung and L. Mockros. Microchannel technologies for artificial lungs:(3) open rectangular channels. *ASAIO Journal (American Society for Artificial Internal Organs: 1992)* 54(4), pp. 390. 2008.
- [40] A. Esteban, A. Anzueto, F. Frutos, I. Alía, L. Brochard, T. E. Stewart, S. Benito, S. K. Epstein, C. Apezteguía and P. Nightingale. Characteristics and outcomes in adult patients receiving mechanical ventilation. *JAMA: The Journal of the American Medical Association* 287(3), pp. 345-355. 2002.
- [41] G. Kim, S. Kim, M. Kim, C. Hong and H. Kang. Development of a hollow fiber membrane module for using implantable artificial lung. *J. Membr. Sci.* 326(1), pp. 130-136. 2009.
- [42] B. D. Kozower, B. F. Meyers, M. A. Smith, N. C. De Oliveira, S. D. Cassivi, T. J. Guthrie, H. Wang, B. J. Ryan, K. R. Shen and T. M. Daniel. The impact of the lung allocation score on short-term transplantation outcomes: A multicenter study. *J. Thorac. Cardiovasc. Surg.* 135(1), pp. 166-171. 2008.
- [43] R. Sreenivasan, E. K. Bassett, D. M. Hoganson, J. P. Vacanti and K. K. Gleason. Ultra-thin, gas permeable free-standing and composite membranes for microfluidic lung assist devices. *Biomaterials* 32(16), pp. 3883-3889. 2011.
- [44] J. H. Gibbon Jr. Application of a mechanical heart and lung apparatus to cardiac surgery. *Minn. Med.* 37(3), pp. 171-85; passim. 1954.
- [45] W. S. Haworth. The development of the modern oxygenator. *Ann. Thorac. Surg.* 76(6), pp. S2216-S2219. 2003.
- [46] J. A. Wegner. Oxygenator anatomy and function. *J. Cardiothorac. Vasc. Anesth.* 11(3), pp. 275-281. 1997.
- [47] J. Kaar, H. Oh, A. Russell and W. Federspiel, "Towards improved artificial lungs through biocatalysis," *Biomaterials*, pp. 3131-3139, 2007.

- [48] M. T. Newhouse. Tennis anyone? the lungs as a new court for systemic therapy. *Can. Med. Assoc. J.* 161(10), pp. 1287-1288. 1999.
- [49] E. R. Weibel, *The Pathway for Oxygen : Structure and Function in the Mammalian Respiratory System*. Cambridge: Harvard University Press, 1984.
- [50] W. J. Federspiel, P. J. Sawzik, H. S. Borovetz, G. D. Reeder and B. G. Hattler, "Temporary support of the lungs - the artificial lung," in *The Transplantation and Replacement of Thoracic Organs*, D. K. C. Cooper, L. W. Miller and G. A. Patterson, Eds. Boston: Kluwer Academic Publishers, 1996, pp. 717-728.
- [51] K. A. Burgess, H. Hu, W. R. Wagner and W. J. Federspiel. Towards microfabricated biohybrid artificial lung modules for chronic respiratory support. *Biomed. Microdevices* 11(1), pp. 117-127. 2009.
- [52] J. A. Potkay. A high efficiency micromachined artificial lung. Presented at Solid-State Sensors, Actuators and Microsystems Conference, 2009. TRANSDUCERS 2009. International. 2009, .
- [53] T. A. Desai, D. J. Hansford, L. Leoni, M. Essenpreis and M. Ferrari. Nanoporous anti-fouling silicon membranes for biosensor applications. *Biosensors and Bioelectronics* 15(9), pp. 453-462. 2000.
- [54] S. Y. Yang, I. Ryu, H. Y. Kim, J. K. Kim, S. K. Jang and T. P. Russell. Nanoporous membranes with ultrahigh selectivity and flux for the filtration of viruses. *Adv Mater* 18(6), pp. 709-712. 2006.
- [55] W. Fissell, H. Humes, A. Fleischman and S. Roy. Dialysis and nanotechnology: Now, 10 years, or never? *Blood Purif.* 25(1), pp. 12-17. 2006.
- [56] E. A. Heins, Z. S. Siwy, L. A. Baker and C. R. Martin. Detecting single porphyrin molecules in a conically shaped synthetic nanopore. *Nano Letters* 5(9), pp. 1824-1829. 2005.

- [57] Q. Li, G. Luo, J. Feng, Q. Zhou, L. Zhang and Y. Zhu. Amperometric detection of glucose with glucose oxidase absorbed on porous nanocrystalline TiO<sub>2</sub> film. *Electroanalysis* 13(5), pp. 413-416. 2001.
- [58] S. Singh, S. K. Arya, P. Pandey, B. Malhotra, S. Saha, K. Sreenivas and V. Gupta. Cholesterol biosensor based on rf sputtered zinc oxide nanoporous thin film. *Appl. Phys. Lett.* 91(6), pp. 063901-063901-3. 2007.
- [59] I. Oh, C. Monty, M. A. Shannon and R. Maset. Microfabricated electrochemical sensor for chemical warfare agents: Smaller is better. Presented at Solid-State Sensors, Actuators and Microsystems Conference, 2007. Transducers 2007. International. 2007, .
- [60] M. M. Deshmukh, D. Ralph, M. Thomas and J. Silcox. Nanofabrication using a stencil mask. *Appl. Phys. Lett.* 75(11), pp. 1631-1633. 1999.
- [61] V. Ambravaneswaran, S. Uttamaraj, Z. Celik-Butler, R. C. Eberhart, C. J. Chuong, R. E. Billo and M. A. Savitt. Micromachined nanoporous membranes for blood oxygenation systems. Presented at Nanotechnology, 2008. NANO'08. 8th IEEE Conference On. 2008, .
- [62] E. Ferain and R. Legras. Characterisation of nanoporous particle track etched membrane. *Nuclear Instruments and Methods in Physics Research Section B: Beam Interactions with Materials and Atoms* 131(1), pp. 97-102. 1997.
- [63] T. Mele, J. Nulman and J. Krusius. Selective and anisotropic reactive ion etch of LPCVD silicon nitride with CHF<sub>3</sub> based gases. *Journal of Vacuum Science & Technology B: Microelectronics and Nanometer Structures* 2(4), pp. 684-687. 1984.

- [64] B. Kastenmeier, P. Matsuo and G. Oehrlein. Highly selective etching of silicon nitride over silicon and silicon dioxide. *Journal of Vacuum Science & Technology A: Vacuum, Surfaces, and Films* 17(6), pp. 3179-3184. 1999.
- [65] Z. L. Wang. Zinc oxide nanostructures: Growth, properties and applications. *Journal of Physics: Condensed Matter* 16(25), pp. R829. 2004.
- [66] Z. L. Wang and J. Song. Piezoelectric nanogenerators based on zinc oxide nanowire arrays. *Science* 312(5771), pp. 242-246. 2006.
- [67] H. Xiang, J. Yang, J. Hou and Q. Zhu. Piezoelectricity in ZnO nanowires: A first-principles study. *Appl. Phys. Lett.* 89(22), pp. 223111-223111-3. 2006.
- [68] A. Mitrushchenkov, R. Linguerrri and G. Chambaud. Piezoelectric properties of AlN, ZnO, and  $\text{Hg}_x\text{Zn}_{1-x}\text{O}$  nanowires by first-principles calculations. *The Journal of Physical Chemistry C* 113(17), pp. 6883-6886. 2009.
- [69] S. Dai, M. Gharbi, P. Sharma and H. S. Park. Surface piezoelectricity: Size effects in nanostructures and the emergence of piezoelectricity in non-piezoelectric materials. *J. Appl. Phys.* 110(10), pp. 104305-104305-7. 2011.
- [70] M. Zhao, Z. Wang and S. X. Mao. Piezoelectric characterization of individual zinc oxide nanobelt probed by piezoresponse force microscope. *Nano Letters* 4(4), pp. 587-590. 2004.
- [71] R. Agrawal, B. Peng, E. E. Gdoutos and H. D. Espinosa. Elasticity size effects in ZnO nanowires- a combined experimental-computational approach. *Nano Letters* 8(11), pp. 3668-3674. 2008.
- [72] S. Dai and H. S. Park. Surface effects on the piezoelectricity of ZnO nanowires. *J. Mech. Phys. Solids* 61(2), pp. 385-397. 2013.
- [73] E. Lai, W. Kim and P. Yang. Vertical nanowire array-based light emitting diodes. *Nano Research* 1(2), pp. 123-128. 2008.

- [74] Y. Zhang, R. E. Russo and S. S. Mao. Quantum efficiency of ZnO nanowire nanolasers. *Appl. Phys. Lett.* 87(4), pp. 043106-043106-3. 2005.
- [75] P. Yang, R. Yan and M. Fardy. Semiconductor nanowire: What's next? *Nano Letters* 10(5), pp. 1529-1536. 2010.
- [76] Q. Wan, Q. Li, Y. Chen, T. Wang, X. He, J. Li and C. Lin. Fabrication and ethanol sensing characteristics of ZnO nanowire gas sensors. *Appl. Phys. Lett.* 84(18), pp. 3654-3656. 2004.
- [77] T. Hsueh, S. Chang, C. Hsu, Y. Lin and I. Chen. Highly sensitive ZnO nanowire ethanol sensor with pd adsorption. *Appl. Phys. Lett.* 91(5), pp. 053111-053111-3. 2007.
- [78] T. Hsueh, C. Hsu, S. Chang and I. Chen. Laterally grown ZnO nanowire ethanol gas sensors. *Sensors Actuators B: Chem.* 126(2), pp. 473-477. 2007.
- [79] Q. Li, Y. Liang, Q. Wan and T. Wang. Oxygen sensing characteristics of individual ZnO nanowire transistors. *Appl. Phys. Lett.* 85(26), pp. 6389-6391. 2004.
- [80] Z. Fan, D. Wang, P. Chang, W. Tseng and J. G. Lu. ZnO nanowire field-effect transistor and oxygen sensing property. *Appl. Phys. Lett.* 85pp. 5923. 2004.
- [81] J. Law and J. Thong. Improving the NH<sub>3</sub> gas sensitivity of ZnO nanowire sensors by reducing the carrier concentration. *Nanotechnology* 19(20), pp. 205502. 2008.
- [82] S. D. Senturia, *Microsystem Design* Norwell, MA: Kluwer Academic Publishers 2001, pp. 571-572.
- [83] C. Jagadish and S. J. Pearton, *Zinc Oxide Bulk, Thin Films and Nanostructures: Processing, Properties, and Applications* Oxford UK: Elsevier 2011.

- [84] Y. Gao and Z. L. Wang. Electrostatic potential in a bent piezoelectric nanowire. the fundamental theory of nanogenerator and nanopiezotronics. *Nano Letters* 7(8), pp. 2499-2505. 2007.
- [85] C. Majidi, M. Haataja and D. Srolovitz. Analysis and design principles for shear-mode piezoelectric energy harvesting with ZnO nanoribbons. *Smart Mater. Struct.* 19(5), pp. 055027. 2010.
- [86] P. Gao and Z. L. Wang. Self-assembled nanowire-nanoribbon junction arrays of ZnO. *The Journal of Physical Chemistry B* 106(49), pp. 12653-12658. 2002.
- [87] X. Wang, X. Wang, C. J. Summers and Z. L. Wang. Large-scale hexagonal-patterned growth of aligned ZnO nanorods for nano-optoelectronics and nanosensor arrays. *Nano Letters* 4(3), pp. 423-426. 2004.
- [88] H. J. Fan, W. Lee, R. Scholz, A. Dadgar, A. Krost, K. Nielsch and M. Zacharias. Arrays of vertically aligned and hexagonally arranged ZnO nanowires: A new template-directed approach. *Nanotechnology* 16(6), pp. 913. 2005.
- [89] H. T. Ng, J. Han, T. Yamada, P. Nguyen, Y. P. Chen and M. Meyyappan. Single crystal nanowire vertical surround-gate field-effect transistor. *Nano Letters* 4(7), pp. 1247-1252. 2004.
- [90] P. Yang, H. Yan, S. Mao, R. Russo, J. Johnson, R. Saykally, N. Morris, J. Pham, R. He and H. Choi. Controlled growth of ZnO nanowires and their optical properties. *Advanced Functional Materials* 12(5), pp. 323. 2002.
- [91] L. Vayssieres. Growth of arrayed nanorods and nanowires of ZnO from aqueous solutions. *Adv Mater* 15(5), pp. 464-466. 2003.
- [92] L. Schmidt-Mende and J. L. MacManus-Driscoll. ZnO-nanostructures, defects, and devices. *Materials Today* 10(5), pp. 40-48. 2007.

- [93] S. Baruah and J. Dutta. Hydrothermal growth of ZnO nanostructures. *Science and Technology of Advanced Materials* 10(1), pp. 013001. 2009.
- [94] M. N. Ashfold, R. P. Doherty, N. G. Ndifor-Angwafor, D. J. Riley and Y. Sun. The kinetics of the hydrothermal growth of ZnO nanostructures. *Thin Solid Films* 515(24), pp. 8679-8683. 2007.
- [95] A. Sugunan, H. C. Warad, M. Boman and J. Dutta. Zinc oxide nanowires in chemical bath on seeded substrates: Role of hexamine. *J. Sol Gel Sci. Technol.* 39(1), pp. 49-56. 2006.
- [96] D. Chen, X. Jiao and G. Cheng. Hydrothermal synthesis of zinc oxide powders with different morphologies. *Solid State Commun.* 113(6), pp. 363-366. 1999.
- [97] K. Govender, D. S. Boyle, P. O'Brien, D. Binks, D. West and D. Coleman. Room-temperature lasing observed from ZnO nanocolumns grown by aqueous solution deposition. *Adv Mater* 14(17), pp. 1221-1224. 2002.
- [98] M. C. Akgun, A. Afal and H. E. Unalan. Hydrothermal zinc oxide nanowire growth with different zinc salts. *J. Mater. Res.* 1(1), pp. 1-7. 2012.
- [99] D. Yuan, R. Guo, Y. Wei, W. Wu, Y. Ding, Z. L. Wang and S. Das. Heteroepitaxial patterned growth of vertically aligned and periodically distributed ZnO nanowires on GaN using laser interference ablation. *Advanced Functional Materials* 20(20), pp. 3484-3489. 2010.
- [100] K. S. Kim, H. Jeong, M. S. Jeong and G. Y. Jung. Polymer-Templated hydrothermal growth of vertically aligned Single-Crystal ZnO nanorods and morphological transformations using structural polarity. *Advanced Functional Materials* 20(18), pp. 3055-3063. 2010.



- [101] Y. Wei, W. Wu, R. Guo, D. Yuan, S. Das and Z. L. Wang. Wafer-scale high-throughput ordered growth of vertically aligned ZnO nanowire arrays. *Nano Letters* 10(9), pp. 3414-3419. 2010.
- [102] S. Xu, Y. Wei, M. Kirkham, J. Liu, W. Mai, D. Davidovic, R. L. Snyder and Z. L. Wang. Patterned growth of vertically aligned ZnO nanowire arrays on inorganic substrates at low temperature without catalyst. *J. Am. Chem. Soc.* 130(45), pp. 14958-14959. 2008.
- [103] P. Gao, Y. Ding and Z. Wang. Crystallographic orientation-aligned ZnO nanorods grown by a tin catalyst. *Nano Letters* 3(9), pp. 1315-1320. 2003.
- [104] H. Fan, F. Bertram, A. Dadgar, J. Christen, A. Krost and M. Zacharias. Self-assembly of ZnO nanowires and the spatial resolved characterization of their luminescence. *Nanotechnology* 15(11), pp. 1401. 2004.
- [105] "HD-4100 Series - HD Microsystems," [Online] Available: [http://hdmicrosystems.com/HDMicroSystems/en\\_US/pdf/HD-4100\\_ProcessGuide.pdf](http://hdmicrosystems.com/HDMicroSystems/en_US/pdf/HD-4100_ProcessGuide.pdf). Accessed 11/13/2013.
- [106] P. X. Gao, J. Song, J. Liu and Z. L. Wang. Nanowire piezoelectric nanogenerators on plastic substrates as flexible power sources for nanodevices. *Adv Mater* 19(1), pp. 67-72. 2007.
- [107] S. Sundararajan and B. Bhushan. Static friction and surface roughness studies of surface micromachined electrostatic micromotors using an atomic force/friction force microscope. *Journal of Vacuum Science & Technology A: Vacuum, Surfaces, and Films* 19(4), pp. 1777-1785. 2001.
- [108] E. K. Dimitriadis, F. Horkay, J. Maresca, B. Kachar and R. S. Chadwick. Determination of elastic moduli of thin layers of soft material using the atomic force microscope. *Biophys. J.* 82(5), pp. 2798-2810. 2002.

- [109] W. Han and F. M. Serry. Force spectroscopy with the atomic force microscope. *Application Note/www.agilent.com* 2011.
- [110] W. Park, G. Yi, J. Kim and S. Park. Schottky nanocontacts on ZnO nanorod arrays. *Appl. Phys. Lett.* 82(24), pp. 4358-4360. 2003.
- [111] J. Song, J. Zhou and Z. L. Wang. Piezoelectric and semiconducting coupled power generating process of a single ZnO belt/wire. A technology for harvesting electricity from the environment. *Nano Letters* 6(8), pp. 1656-1662. 2006.
- [112] J. Zhou, P. Fei, Y. Gao, Y. Gu, J. Liu, G. Bao and Z. L. Wang. Mechanical-electrical triggers and sensors using piezoelectric micowires/nanowires. *Nano Letters* 8(9), pp. 2725-2730. 2008.
- [113] B. D. Cullity, *Elements of X-Ray Diffraction*, Reading, MA: Addison-Wesley, 1978.
- [114] Y. Zhao, Y. Jiang and Y. Fang. The influence of substrate temperature on ZnO thin films prepared by PLD technique. *J. Cryst. Growth* 307(2), pp. 278-282. 2007.
- [115] M. Rahimi, H. Shah, G. S. Sukhatme, J. Heideman and D. Estrin. Studying the feasibility of energy harvesting in a mobile sensor network. Presented at Robotics and Automation, 2003. Proceedings. ICRA'03. IEEE International Conference On. 2003, .
- [116] M. A. Wood and K. A. Ellenbogen. Cardiac pacemakers from the patient's perspective. *Circulation* 105(18), pp. 2136-2138. 2002.
- [117] H. Beck, W. E. Boden, S. Patibandla, D. Kireyev, V. Gupta, F. Campagna, M. E. Cain and J. E. Marine. 50th anniversary of the first successful permanent pacemaker implantation in the united states: Historical review and future directions. *Am. J. Cardiol.* 106(6), pp. 810-818. 2010.

- [118] A. M. Crespi, S. K. Somdahl, C. L. Schmidt and P. M. Skarstad. Evolution of power sources for implantable cardioverter defibrillators. *J. Power Sources* 96(1), pp. 33-38. 2001.
- [119] M. C. Frost and M. E. Meyerhoff. Implantable chemical sensors for real-time clinical monitoring: Progress and challenges. *Curr. Opin. Chem. Biol.* 6(5), pp. 633-641. 2002.
- [120] J. A. Paradiso and T. Starner. Energy scavenging for mobile and wireless electronics. *Pervasive Computing, IEEE* 4(1), pp. 18-27. 2005.
- [121] A. Lewandowski and M. Galinski. Practical and theoretical limits for electrochemical double-layer capacitors. *J. Power Sources* 173(2), pp. 822-828. 2007.
- [122] S. K. Kamarudin, W. R. W. Daud, S. Ho and U. A. Hasran. Overview on the challenges and developments of micro-direct methanol fuel cells (DMFC). *J. Power Sources* 163(2), pp. 743-754. 2007.
- [123] B. A. Warneke, M. D. Scott, B. S. Leibowitz, L. Zhou, C. L. Bellew, J. A. Chediak, J. M. Kahn, B. E. Boser and K. S. Pister. An autonomous 16 mm<sup>2</sup> solar-powered node for distributed wireless sensor networks. Presented at Sensors, 2002. Proceedings of IEEE. 2002, .
- [124] J. B. Lee, Z. Chen, M. G. Allen, A. Rohatgi and R. Arya. A miniaturized high-voltage solar cell array as an electrostatic MEMS power supply. *Microelectromechanical Systems, Journal Of* 4(3), pp. 102-108. 1995.
- [125] M. Stordeur and I. Stark. Low power thermoelectric generator-self-sufficient energy supply for micro systems. Presented at Thermoelectrics, 1997. Proceedings ICT'97. XVI International Conference On. 1997, .

- [126] P. D. Mitcheson, E. M. Yeatman, G. K. Rao, A. S. Holmes and T. C. Green. Energy harvesting from human and machine motion for wireless electronic devices. *Proc IEEE* 96(9), pp. 1457-1486. 2008.
- [127] E. D. Mantipliy, K. R. Pohl, S. W. Poppell and J. A. Murphy. Summary of measured radiofrequency electric and magnetic fields(10 kHz to 30 GHz) in the general and work environment. *Bioelectromagnetics* 18(8), pp. 563-577. 1997.
- [128] S. Roundy, P. K. Wright and J. Rabaey. A study of low level vibrations as a power source for wireless sensor nodes. *Comput. Commun.* 26(11), pp. 1131-1144. 2003.
- [129] H. A. Sodano, D. J. Inman and G. Park. A review of power harvesting from vibration using piezoelectric materials. *Shock Vib Dig* 36(3), pp. 197-206. 2004.
- [130] S. Roundy, P. K. Wright and K. S. Pister. Micro-electrostatic vibration-to-electricity converters. *Fuel Cells (Methanol)* 220pp. 22. 2002.
- [131] S. Beeby, M. Tudor, R. Torah, S. Roberts, T. O'Donnell and S. Roy. Experimental comparison of macro and micro scale electromagnetic vibration powered generators. *Microsystem Technologies* 13(11-12), pp. 1647-1653. 2007.
- [132] S. Lee and B. D. Youn. A new piezoelectric energy harvesting design concept: Multimodal energy harvesting skin. *Ultrasonics, Ferroelectrics and Frequency Control, IEEE Transactions On* 58(3), pp. 629-645. 2011.
- [133] J. W. Gardner, V. K. Varadan and O. O. Awadelkarim, *Microsensors, MEMS and Smart Devices*, West Sussex England: John Wiley and Sons, 2005
- [134] Z. L. Wang and J. Song. Piezoelectric nanogenerators based on zinc oxide nanowire arrays. *Science* 312(5771), pp. 242-246. 2006.
- [135] X. Wang. Piezoelectric nanogenerators—harvesting ambient mechanical energy at the nanometer scale. *Nano Energy* 1(1), pp. 13-24. 2012.

- [136] S. Xu, Y. Qin, C. Xu, Y. Wei, R. Yang and Z. L. Wang. Self-powered nanowire devices. *Nature Nanotechnology* 5(5), pp. 366-373. 2010.
- [137] X. Wang, J. Song, J. Liu and Z. L. Wang. Direct-current nanogenerator driven by ultrasonic waves. *Science* 316(5821), pp. 102-105. 2007.
- [138] L. Wang, R. A. Wolf Jr, Y. Wang, K. K. Deng, L. Zou, R. J. Davis and S. Trolier-McKinstry. Design, fabrication, and measurement of high-sensitivity piezoelectric microelectromechanical systems accelerometers. *Microelectromechanical Systems, Journal Of* 12(4), pp. 433-439. 2003.
- [139] V. Dragoi, E. Cakmak, E. Capsuto, C. McEwen and E. Pabo. Adhesive wafer bonding using photosensitive polymer layers. Presented at SPIE Europe Microtechnologies for the New Millennium. 2009, .
- [140] A. Kaushik, H. Kahn and A. H. Heuer. Wafer-level mechanical characterization of silicon nitride MEMS. *Microelectromechanical Systems, Journal Of* 14(2), pp. 359-367. 2005.
- [141] H. Zhang and E. So. Hybrid resistive tactile sensing. *Systems, Man, and Cybernetics, Part B: Cybernetics, IEEE Transactions On* 32(1), pp. 57-65. 2002.
- [142] H. Takao, K. Sawada and M. Ishida. Monolithic silicon smart tactile image sensor with integrated strain sensor array on pneumatically swollen single-diaphragm structure. *Electron Devices, IEEE Transactions On* 53(5), pp. 1250-1259. 2006.
- [143] P. A. Schmidt, E. Maël and R. P. Würtz. A sensor for dynamic tactile information with applications in human–robot interaction and object exploration. *Robotics and Autonomous Systems* 54(12), pp. 1005-1014. 2006.
- [144] Y. Ohmura, Y. Kuniyoshi and A. Nagakubo. Conformable and scalable tactile sensor skin for curved surfaces. Presented at Robotics and Automation, 2006. ICRA 2006. Proceedings 2006 IEEE International Conference On. 2006, .

- [145] Y. Mei, Y. Lu, Y. C. Hu and C. G. Lee. A case study of mobile robot's energy consumption and conservation techniques. Presented at Advanced Robotics, 2005. ICAR'05. Proceedings., 12th International Conference On. 2005, .
- [146] Y. Gao and Z. L. Wang. Electrostatic potential in a bent piezoelectric nanowire. the fundamental theory of nanogenerator and nanopiezotronics. *Nano Letters* 7(8), pp. 2499-2505. 2007.
- [147] R. Yang, Y. Qin, L. Dai and Z. L. Wang. Power generation with laterally packaged piezoelectric fine wires. *Nature Nanotechnology* 4(1), pp. 34-39. 2008.
- [148] S. Xu, Y. Qin, C. Xu, Y. Wei, R. Yang and Z. L. Wang. Self-powered nanowire devices. *Nature Nanotechnology* 5(5), pp. 366-373. 2010.
- [149] X. Wang. Piezoelectric nanogenerators—harvesting ambient mechanical energy at the nanometer scale. *Nano Energy* 1(1), pp. 13-24. 2012.
- [150] A. Schmitz, M. Maggiali, L. Natale, B. Bonino and G. Metta. A tactile sensor for the fingertips of the humanoid robot iCub. Presented at Intelligent Robots and Systems (IROS), 2010 IEEE/RSJ International Conference On. 2010, .
- [151] M. Choi, D. Choi, M. Jin, I. Kim, S. Kim, J. Choi, S. Y. Lee, J. M. Kim and S. Kim. Mechanically powered transparent flexible Charge-Generating nanodevices with piezoelectric ZnO nanorods. *Adv Mater* 21(21), pp. 2185-2189. 2009.

### Biographical Information

Bhargav Nabar received his B.E in Electronics Engineering from the University of Mumbai in August 2007. He received his Ph.D in Electrical Engineering from the University of Texas at Arlington in 2013. He has authored three journal publications and two conference papers. He was the first recipient of the Nanofab Best Citizen Award from the College of Engineering at UTA. His research interests include next - generation lithography, nano-scale systems and devices, MEMS and semiconductor fabrication.